



TECHNISCHE  
UNIVERSITÄT  
WIEN

Vienna University of Technology

Diese Dissertation haben begutachtet:

Prof. Dr. Günther Rupprechter

Prof. Dr. Josef Redinger

# DISSERTATION

---

## In Situ Spectroscopy on Cu and Ceria Modified Ni-Zirconia Catalysts for Methane Reforming

ausgeführt zum Zwecke der Erlangung des akademischen Grades einer  
Doktorin der technischen Wissenschaften unter der Leitung von

Univ. Prof. Dr. rer. nat. Günther Rupprechter  
und  
Ass. Prof. Dr. techn. Karin Föttinger

E165 Institut für Materialchemie

eingereicht an der Technischen Universität Wien  
Technische Chemie

von

Dipl.-Ing. Astrid Wolfbeisser

0625342

Treustraße 52/1/7

1200 Wien

Wien, 1. Juni 2015

# Kurzfassung der Dissertation

---

Ni/ZrO<sub>2</sub> Katalysatoren werden für die Reformierung von Methan, einem wichtigen Prozess für die industrielle Wasserstoffproduktion und in Festoxidbrennstoffzellen, eingesetzt. Obwohl Nickelkatalysatoren generell eine hohe Aktivität für diverse Methanreformierungsreaktionen aufweisen, führen Kohlenstoffablagerungen, die den Katalysator rasch deaktivieren, zu großen Problemen. Das Ziel dieser Arbeit war, Ni/ZrO<sub>2</sub> dahingehend zu modifizieren, dass die Bildung von Kohlenstoffablagerungen unterdrückt wird. Dazu wurde zwei Ansätze verfolgt und untersucht: Der Einfluss der Zumischung von Kupfer zur metallischen Nickel-Komponente des Katalysators und der Modifizierung des Trägermaterials mit Ceroxid. Durch die Zugabe von Kupfer wird eine erhöhte Beständigkeit gegenüber Kohlenstoffablagerungen auf Nickel aufgrund elektronischer Wechselwirkung und durch die Veränderung der Oberflächenzusammensetzung erwartet. Aufgrund der besseren Verfügbarkeit von Oberflächensauerstoff eines CeO<sub>2</sub>/ZrO<sub>2</sub>-Mischoxides gegenüber ZrO<sub>2</sub> kann bereits abgelagerter Kohlenstoff leichter von der Katalysatoroberfläche weg-oxidiert werden.

Kupfer und Nickel wurde mittels Ko-Imprägnierung auf das ZrO<sub>2</sub>-Trägermaterial aufgebracht. CeO<sub>2</sub>/ZrO<sub>2</sub>-Mischoxide wurden auf verschiedenen Wegen, darunter Imprägnierung, Verbrennung der Ausgangsstoffe, Ko-Fällung und Tensid-unterstützter Ko-Fällung, hergestellt. Nickel wurde mittels Imprägnierung und einer nominellen Beladung von 5 % w/w. auf die Trägermaterialien aufgebracht.

Die Katalysatoren wurden mittels Transmissionselektronenmikroskopie (TEM), Wasserstoffchemisorption, Infrarotspektroskopie mit CO als Sondenmolekül, Röntgendiffraktion (XRD) und Röntgenabsorptionsspektroskopie (XAS) charakterisiert. Um die Aktivität für partielle Methanoxidation, Methanzersetzung, -dampfreformierung und -kohlendioxidreformierung zu untersuchen, wurden die Katalysatoren in einem Durchflussreaktor getestet.

*In situ* Spektroskopie liefert Informationen über den Katalysator unter relevanten Reaktionsbedingungen wie hohe Temperaturen und eine reaktive Gasatmosphäre. Die Katalysatoren in dieser Arbeit wurden mittels *in situ* Infrarotspektroskopie, *in situ* XAS und Röntgenphotoelektronen-spektroskopie (XPS) unter Drücken nahe Atmosphärendruck (NAP-XPS) untersucht. Nach der Reaktion wurden mittels temperaturprogrammierter Oxidation (TPO) Informationen über die Menge der Kohlenstoff-ablagerungen sowie der

Temperatur, die für deren Entfernung durch Oxidation erforderlich ist, gewonnen. Mittels TEM konnten Kohlenstoff-ablagerungen auf den Proben direkt beobachtet werden.

Auf den ZrO<sub>2</sub>-geträgerten bi-metallischen Katalysatoren konnte die Bildung einer CuNi-Legierung während der Reduktion mehrfach bestätigt werden. Auf den TEM Bildern von zuvor reduzierten Proben konnten etwa 20 nm große Teilchen, die sowohl Kupfer als auch Nickel enthalten, beobachtet werden. Diese bimetallischen Partikel enthielten mehr Nickel als Kupfer, während zusätzlich fein verteilt reine Kupfer-Partikel am Trägermaterial gefunden wurden. Informationen über die Cu:Ni Zusammensetzung der Oberfläche wurden mittels Wasserstoff-chemisorption gewonnen. In Einklang mit den Ergebnissen der mit Infrarotspektroskopie untersuchten CO-Adsorption wurde eine Anreicherung der Oberfläche mit Kupfer beobachtet.<sup>[1]</sup>

In einem temperaturprogrammierten Experiment konnte gezeigt werden, dass Nickel deutlich aktiver als Kupfer für Methanzerersetzung in Abwesenheit von Sauerstoff hinsichtlich der Wasserstoffproduktion war. Die Aktivität des bi-metallischen Cu/Ni Katalysators war zunächst so gering wie von Cu-ZrO<sub>2</sub>, bis die H<sub>2</sub>-Bildung schlagartig bei einer spezifischen Temperatur zwischen 650 und 735 K einsetzte. Im gleichen Temperaturbereich konnte mittels *in situ* NAP-XPS ein Konzentrations-anstieg reduzierter Nickel-Atome an der Katalysatoroberfläche beobachtet werden. Die Zugabe von Kupfer führte zur Verringerung der Kohlenstoffablagerung, jedoch ist die Stabilität der CuNi-Legierung unter relevanten Reaktionsbedingungen stark limitiert.<sup>[2]</sup>

Die strukturellen Eigenschaften der verschiedenen hergestellten CeO<sub>2</sub>/ZrO<sub>2</sub> Trägermaterialien zeigten große Unterschiede. Tetragonale und kubische Mischoxidphasen mit unterschiedlichen Kristallitgrößen und spezifischen Oberflächen wurden gefunden. Die größten spezifischen Oberflächen wurden für die Trägermaterialien, welche mittels Ko-Fällung und Tensid-unterstützter Ko-Fällung hergestellt wurden, gemessen. Die Nickel-Katalysatoren wurden für Dampfreformierung und Kohlendioxidreformierung von Methan getestet. Außer dem mittels Tensid-unterstützter Ko-Fällung hergestellten Katalysator waren alle für diese Reformierungsreaktionen aktiv. Die größte Aktivität unter den Mischoxid-geträgerten Proben zeigte der mittels Ko-Fällung hergestellte Katalysator. Obwohl die katalytische Aktivität im Vergleich zu Ni-ZrO<sub>2</sub> nicht erhöht wurde, wurde eine stark verringerte Kohlenstoffablagerung, insbesondere von faser-artigem Kohlenstoff, im Vergleich zu Ni-ZrO<sub>2</sub> auf dem aktiven Kofällungsträger Katalysator beobachtet.

# Abstract

---

Ni/ZrO<sub>2</sub> is used as a catalyst for methane reforming reactions, which are key processes for hydrogen production in industry and in solid oxide fuel cells. Nickel shows high activity but is rapidly deactivated by coke formation, which is a major problem. Aim of this thesis was to modify Ni/ZrO<sub>2</sub> in order to prevent coke formation. Two approaches of catalyst modification were studied: The influence of copper addition to nickel and the modification of the zirconia support material by adding ceria were investigated. The promotion of nickel is expected to stabilize nickel electronically or via an ensemble effect against carbon deposition while the ceria-zirconia mixed oxide support releases surface oxygen more easily which oxidizes surface carbon.

Copper and nickel were loaded on the zirconia support via co-impregnation followed by calcination. Ceria-Zirconia mixed oxide support materials were prepared via different synthesis routes including impregnation, combustion of precursors, co-precipitation and surfactant assisted co-precipitation. Ni was deposited on these support materials via impregnation with a nominal loading of 5 % w/w.

The catalysts were characterized using techniques such as transmission electron microscopy (TEM), H<sub>2</sub>-Chemisorption, infrared spectroscopy with CO as a probe molecule, X-ray diffraction (XRD), and X-ray absorption spectroscopy (XAS). To study the catalytic performance, the catalysts were tested in a continuous flow setup for partial oxidation of methane, methane decomposition, steam reforming and dry reforming. *In situ* spectroscopy provides information about the catalyst under relevant reaction conditions such as high temperature and reactive gas atmosphere. In this thesis, the catalysts were studied via *in situ* infrared spectroscopy, *in situ* XAS and near ambient pressure (NAP-)XPS. After reaction, the used catalysts were further studied via temperature programmed oxidation (TPO), in order to get information about the amount of carbon deposition and the temperature needed to remove these carbon species via oxidation, and by TEM, where carbon deposition was visible.

Formation of a copper-nickel alloy on the zirconia supported bimetallic catalysts during reduction was confirmed by various techniques. TEM images of catalysts reduced prior to microscopy revealed particles of about 20 nm size containing both copper and nickel. These alloy particles were enriched in nickel. Additionally, much smaller particles containing mainly or only copper were found finely distributed over the zirconium oxide support. In order to

get information about the Cu:Ni ratio on the surface, chemisorption of hydrogen as adsorbing agent was performed. The results of these experiments showed, that the surface was enriched in copper, in agreement with FTIR spectroscopy of CO adsorption.<sup>[1]</sup>

Temperature Programmed Reaction with mass spectrometry (MS) detection showed that the methane decomposition rate towards hydrogen in absence of oxygen was much higher on nickel than on the copper catalyst. The bimetallic Cu/Ni catalysts showed low initial activity, similar to Cu-ZrO<sub>2</sub>, until a sudden strong increase of the H<sub>2</sub> formation rate was observed at a certain temperature between 650 and 735 K. In the same temperature range, an increase of the concentration of reduced Ni atoms at the catalyst surface in the active state, likely as a consequence of the interaction with C and CH<sub>x</sub>, was observed by *in situ* NAP-XPS. Cu addition to the Ni catalyst caused decreased coke formation but the CuNi alloy shows limited stability under relevant reaction conditions.<sup>[2]</sup>

The textural properties of the CeO<sub>2</sub>/ZrO<sub>2</sub> support materials prepared by different synthesis routes were strongly different. Tetragonal and cubic mixed oxide phases with different crystallite size and surface area were observed. The highest specific surface area was observed for the catalysts prepared by co-precipitation and surfactant assisted co-precipitation. The catalytic performance of the supported nickel catalysts was evaluated for methane dry reforming and methane steam reforming. Except of the catalyst prepared by surfactant assisted co-precipitation, all catalysts were active for these methane reforming reactions. The highest activity among the mixed oxide supported catalysts was observed on the catalyst prepared by co-precipitation. Even though the catalytic activity compared to Ni-ZrO<sub>2</sub> was not increased, strongly decreased coke formation after methane dry reforming was observed on the active co-precipitation catalyst compared to Ni-ZrO<sub>2</sub>.

# Danksagung

---

An dieser Stelle möchte ich mich bei einigen Personen bedanken, die zur Entstehung der vorliegenden Arbeit beigetragen haben.

Professorin Karin Föttinger für die Betreuung der Arbeit, die wertvollen Anregungen und Diskussionen zur Interpretation der Ergebnisse.

Professor Günther Rupprechter für die interessante Themenstellung und für die Möglichkeit, meine Dissertation in seiner Arbeitsgruppe durchführen zu dürfen.

Professor Josef Redinger für die Bereitschaft als Gutachter für diese Arbeit zur Verfügung zu stellen.

Dem FWF (Fonds zur Förderung wissenschaftlicher Forschung) für die finanzielle Förderung der Dissertation durch den Spezialforschungsbereich (SFB) F45 "Functional Oxide Surfaces and Interfaces FOXSI".

Dem ASEA-UNINET (European Academic University Network) für ein Stipendium für meinen einmonatigen Forschungsaufenthalt in Thailand.

Professor Jatuporn Wittayakun für die Betreuung an der Suranaree University of Technology in Nakhon Ratchasima und besonders Onsulang Sophiphun für sämtliche Unterstützung und Hilfestellungen auch außerhalb der Universität während meiner Zeit in Thailand.

Allen Mitarbeitern des Instituts für Materialchemie, besonders meinen Kollegen der Arbeitsgruppe Katalyse und den Mädels aus dem Viererbüro für das hervorragende Arbeitsklima, die Hilfsbereitschaft und die gute Zusammenarbeit.

Besonderen Dank verdienen mein Mann Georg und meine Eltern, bei denen ich in allen Lebenslagen den nötigen Rückhalt finde und die mich mit viel Geduld auch in schwierigen Zeiten ermuntert und unterstützt haben.

# Content

## Chapter 1 Introduction..... 1

1.1	Methane Reforming Catalysts.....	2
1.2	Methane Decomposition.....	3
1.3	Methane Steam Reforming.....	4
1.4	Partial Oxidation of Methane.....	4
1.5	Methane Dry Reforming.....	5
1.6	Objectives and Outline.....	6

## Chapter 2 Sample Preparation..... 8

2.1	Preparation of the Support Material.....	8
2.2	Preparation of Supported Ni and Cu Catalysts.....	9

## Chapter 3 Methods ..... 11

3.1	Characterization.....	11
3.1.1	X-Ray Diffraction Measurements.....	11
3.1.2	Surface Area Analysis.....	11
3.1.3	Metal Dispersion Measurements.....	11
3.1.4	Transmission Electron Microscopy.....	12
3.1.5	Temperature Programmed Desorption.....	13
3.2	<i>In situ</i> Infrared Spectroscopy.....	13
3.2.1	Spectra Acquisition.....	14

## Content

3.2.2	Pretreatment Procedure in the Vacuum Cell .....	14
3.2.3	Adsorption of CO as a Probe Molecule.....	14
3.2.4	Operando FTIR during Methane Steam Reforming.....	14
3.3	Catalytic Testing.....	15
3.3.1	Temperature Programmed Methane Decomposition.....	15
3.3.2	Partial Oxidation of Methane .....	16
3.3.3	Methane Dry Reforming .....	16
3.3.4	Equations used for Calculation of Catalytic Results .....	16
3.3.5	Temperature Programmed Oxidation.....	17
3.4	X-Ray Absorption Spectroscopy .....	17
3.4.1	<i>In situ</i> XAS of Ni, Cu and CuNi Supported Catalysts .....	18
3.4.2	Ex-situ XAS of Dry Reforming Catalysts.....	19
3.4.3	Data Acquisition and Analysis.....	19
3.5	<i>In situ</i> X-Ray Photoelectron Spectroscopy .....	19

## **Chapter 4 Results .....** **22**

4.1	Characterization of ZrO <sub>2</sub> .....	22
4.2	Monometallic Zirconia Supported Catalysts .....	27
4.2.1	Ni-ZrO <sub>2</sub> .....	27
4.2.2	Cu-ZrO <sub>2</sub> .....	30
4.3	Bimetallic CuNi Catalysts .....	32
4.3.1	<i>In situ</i> X-ray Absorption During Reduction .....	32
4.3.2	Transmission Electron Microscopy .....	33

## Content

4.3.3	X-Ray Diffraction .....	35
4.3.4	<i>In situ</i> FTIR Studies .....	35
4.3.5	Partial Oxidation of Methane .....	42
4.3.6	Methane Decomposition .....	43
4.3.7	<i>In situ</i> X-Ray Photoelectron Spectroscopy .....	46
4.3.8	Temperature Programmed Oxidation.....	52
4.4	Ceria Promoted Ni-ZrO <sub>2</sub> .....	54
4.4.1	Textural and Structural Properties .....	54
4.4.2	TEM Study .....	56
4.4.3	Adsorption Properties .....	58
4.4.4	Methane Steam Reforming .....	59
4.4.5	Methane Dry Reforming .....	62
4.4.6	Post-MDR-studies .....	65
<b>Chapter 5 Discussion .....</b>		<b>71</b>
<b>Chapter 6 Summary and Conclusions.....</b>		<b>75</b>
<b>List of Abbreviations .....</b>		<b>78</b>
<b>List of Figures.....</b>		<b>79</b>
<b>List of Tables .....</b>		<b>83</b>
<b>References .....</b>		<b>84</b>

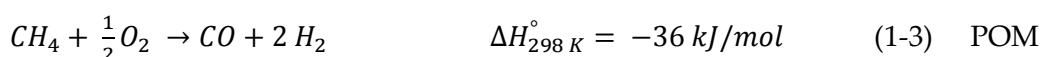
# Chapter 1

## Introduction

---

In recent years, the global need of energy and rising oil prices increased the interest in alternative energy generation. Besides this, considerable attention has been paid to global warming due to the greenhouse effect. The reduction of greenhouse gas emission as well as utilization of greenhouse gases such as methane and carbon dioxide is therefore becoming more and more important. Methane exists in enormous quantity on our planet as it occurs as the main component of natural gas. Nevertheless, its use as chemical raw material is still underrepresented. The major amount of natural gas is burned to create energy for heating, cooking, transportation or electricity production while only a minor amount is used for direct conversion into chemicals and fuels.

The production of  $H_2$  or synthesis gas, a mixture of CO and  $H_2$ , can occur via catalytic methane steam reforming<sup>[3-5]</sup>, (1-1), dry reforming<sup>[6-11]</sup>, (1-2), partial oxidation<sup>[12, 13]</sup>, (1-3) or decomposition of methane<sup>[14-16]</sup>.



A review presenting recent results and developments in heterogeneous catalytic methane conversion to synthesis gas, hydrogen, cyanide, ethylene, methanol, formaldehyde, methyl chloride, methyl bromide and aromatics has been published this year by Horn and Schlögl<sup>[17]</sup>.

Besides of methane, methanol has been intensively studied as a feedstock for hydrogen and syngas via methanol steam reforming<sup>[18-20]</sup>. Considering environmental catalysis, catalytic CO oxidation<sup>[21, 22]</sup> and hydrodechlorination<sup>[23, 24]</sup> of organic waste were investigated.

## 1.1 Methane Reforming Catalysts

Fischer and Tropsch showed already in 1928 that most group VIII metals display activity for methane dry reforming<sup>[25]</sup>. Many years later various transition metals (Ni, Ru, Rh, Pd, Ir, Pt) have been tested<sup>[26-30]</sup>. Even though Rh was observed to be the most stable and active of group VIII metals Pt catalysts have been developed as excellent methane dry reforming catalysts<sup>[9, 31-34]</sup>. Besides highly active noble metal catalysts, nickel based catalysts with their relatively high availability, low cost and activity comparable to that of noble metal catalysts is becoming the metal of choice for industrial applications<sup>[35]</sup>. However, the active nickel particles tend to form coke, leading to deactivation of the catalyst<sup>[36]</sup>. The effect of carbon deposition is a major problem and may lead to catalyst deactivation<sup>[10, 17]</sup> by decoration of the active metallic sites and or physical blockage of the tubes in fixed bed reformers<sup>[37]</sup>. Hence, intense research efforts have been focused on the development of catalysts that show high activity but are also resistant to carbon formation and sintering. It has been reported, that smaller nickel particle size leads to less coke deposition<sup>[38, 39]</sup>. Therefore, increasing the nickel dispersion should help to improve the catalyst's stability. An improvement of the catalyst's stability against coke formation can also be achieved by modification of the metal component or modification of the support material.

Nickel based catalysts have been shown to be sensitive to doping and structure modification by other metals, such as Cu or Au, or other promoters such as boron, which affect the structure and morphology of the produced carbon<sup>[40]</sup>. Xu and Saeys<sup>[41]</sup> studied the effect of boron promotion on Ni-based catalysts towards coke formation using first-principles density functional theory calculations. Addition of small amounts of boron to the Ni catalyst was found to inhibit the formation of bulk carbide and weaken the on-surface carbon binding energies<sup>[41]</sup>. Improved stability against deactivation has been achieved by adding a second metal component, e.g. Au<sup>[42-44]</sup> and Cu<sup>[1, 2, 15, 16, 45-51]</sup> have been studied for this aim. Since neighbouring Ni atoms are necessary for coke formation the resistance against coke formation can be achieved by exchanging the Ni neighbours by Cu or Au (ensemble effect). On the other hand, the formation of an alloy leads to a lower nickel reduction temperature because of electron donation of Au or Cu to Ni (electronic effect). Copper was chosen as alloying component in this thesis because of its lower price compared to gold and the high probability of gold to sinter. The Ni-Au surface alloy was active for steam reforming and more resistant towards carbon formation than pure Ni, which was explained by blocking of highly reactive Ni edge and kink sites by Au atoms<sup>[43]</sup>. The addition of Cu to nickel-based catalysts has several effects such as an easier reducibility of Ni. Cu is rich in d-electrons which may exert an electronic effect on Ni and furthermore affect the affinity of the metal surface to graphite<sup>[14]</sup>. Ashok et al. observed that addition of Cu to Ni enhanced the methane decomposition activity of hydrotalcite-like Ni-Cu-Al catalysts when added in an appropriate amount<sup>[45]</sup>. Suelves et al. showed that doping of Cu has a strong influence on the dispersion of nickel and enhances the catalyst's activity<sup>[47]</sup>. Similarly, Monzón found that promoting Ni

with a small amount of Cu improves the activity and stability of the catalyst<sup>[49]</sup>. Cunha et al. observed, that doping with Cu improves the catalyst stability<sup>[50]</sup>. Li et al. observed, that in  $\text{Cu}_{0.25}\text{Ni}_{0.75}\text{Al}_2\text{O}_4$  Cu is acting as a dispersive agent to prevent Ni particles from growing<sup>[51]</sup> and enhances the catalyst stability when employed in a suitable amount<sup>[52]</sup>. Lazaro et al. found that the presence of copper in NiCu-SiO<sub>2</sub> catalysts led to higher methane conversion<sup>[16]</sup>, and Park et al. observed that on Cu-Ni-YSZ anode materials for direct use of methane fuel in solid oxide fuel cells (SOFC) the carbon deposition decreased compared to the amount of carbon on Ni-YSZ<sup>[46]</sup>. DFT based computational studies by Liu et al. compared the methane dissociation on NiCu(111) bimetallic alloy surfaces. Their calculations indicated that C is easily formed on a uniform 1:1 NiCu surface but unfavourable on a Cu-rich NiCu surface<sup>[53]</sup>. Therefore, the surface composition on a NiCu alloy catalyst under reaction conditions is expected to play the key role in determining the catalytic activity and stability.

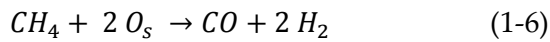
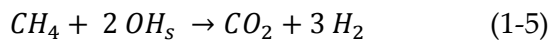
In general, bimetallic nanoparticles are key to many catalytic reactions, due to their beneficial catalytic properties, as reported for Pd-Zn<sup>[20, 54-56]</sup>, PdGa<sup>[18, 19, 56-58]</sup> and Pd(Pt)-Cu<sup>[23, 56, 59]</sup> in comparison to Pd<sup>[60-62]</sup>.

Various materials have been tested as support for nickel catalysts such as MgO<sup>[10, 35, 63-65]</sup>, Al<sub>2</sub>O<sub>3</sub><sup>[8, 10, 66-68]</sup>, SiO<sub>2</sub><sup>[10, 35, 69]</sup>, TiO<sub>2</sub><sup>[10, 35]</sup>, La<sub>2</sub>O<sub>3</sub><sup>[66, 67]</sup>, CeO<sub>2</sub><sup>[67, 70]</sup>, ZrO<sub>2</sub><sup>[8, 67, 71]</sup> and Ce<sub>1-x</sub>Zr<sub>x</sub>O<sub>2</sub><sup>[6, 7, 72-79]</sup>. Ce<sub>1-x</sub>Zr<sub>x</sub>O<sub>2</sub> solid solution is considered as a promising support<sup>[6, 7, 72-77]</sup> for Ni-based methane dry reforming catalysts. Adding ZrO<sub>2</sub> to CeO<sub>2</sub> has been found to improve the oxygen storage capacity, redox property, which can be related to the ability to deliver oxygen from the lattice to the gas phase or solid carbon,, thermal stability and catalytic activity.<sup>[5, 7, 72]</sup> Several methods have been used to prepare Ce<sub>1-x</sub>Zr<sub>x</sub>O<sub>2</sub> solid solutions for catalytic applications. These include the high-temperature milling of a mixture of the oxides<sup>[80]</sup>, co-precipitation<sup>[5, 6, 72, 73, 76, 81-85]</sup>, surfactant-assisted co-precipitation<sup>[72, 74, 75, 77, 86, 87]</sup>, thermal hydrolysis<sup>[88-90]</sup>, sol-gel<sup>[7, 91, 92]</sup> and pseudo-sol-gel techniques<sup>[78, 79]</sup>. Among these methods, combustion, co-precipitation and surfactant-assisted co-precipitation were applied to study the influence of catalyst modification towards catalytic activity and stability.

## 1.2 Methane Decomposition

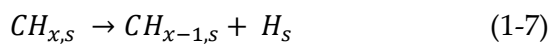
By production of hydrogen via steam reforming or partial oxidation of methane, CO or CO<sub>2</sub> is formed as a by-product. For many applications such as the use of hydrogen in PEM fuel cells CO needs to be removed because it is a catalyst poison. To overcome the problem of CO or CO<sub>2</sub> formation, direct production of hydrogen by catalytic methane decomposition (MD) in absence of air or oxygen can be applied. The by-product of this process is carbon in form of layers, filaments, fibres or nanotubes. Especially the formation of useful nanocarbons<sup>[40, 52, 93-98]</sup> is of high interest. Li et al.<sup>[14]</sup> published a comprehensive review about this topic discussing the effect of the nature of the catalyst and feed composition on the catalytic activity, stability and the influence on the morphology of the produced carbon.

Besides of dissociation of methane (1-4) surface reactions with hydroxyl groups (1-5) and oxygen of the catalyst surface (1-6) take place during methane decomposition.



The index  $s$  indicates that the molecule/fragment is adsorbed on the surface.

Liao et al.<sup>[99]</sup> calculated dissociation enthalpies and activation energies of the sequential dehydrogenation and oxygen-assisted dissociation of methane for various transition metals, including nickel and copper. Nickel was found to be one of the most efficient catalysts for the methane dissociation described by sequential dehydrogenation of CH<sub>4</sub>:



The total dissociation of methane on Cu and the other coinage metals was found to be very endothermic. The presence of adsorbed oxygen however promoted methane dissociation<sup>[99, 100]</sup> because oxygen located at metal on-top sites increases the adsorption energy of hydrogen<sup>[100]</sup>. Besides, the ability to catalyse the reaction of carbon produced by (1-6) with surface oxygen is rather high for Cu compared to other transition metals<sup>[100]</sup>.

### 1.3 Methane Steam Reforming

In methane steam reforming (MSR), the reaction of CH<sub>4</sub> with H<sub>2</sub>O to a mixture of CO, CO<sub>2</sub> and H<sub>2</sub> is endothermic. It is used for H<sub>2</sub> production or to produce synthesis gas with a high H<sub>2</sub>:CO ratio. The reaction is limited by thermodynamic equilibrium, and besides steam reforming (1-1) reverse water-gas-shift (WGS) reaction (1-8) is involved.



Since the WGS reaction is an exothermic reaction, it is favoured at low temperatures. Jones et al.<sup>[101]</sup> reported an elementary step mechanism for MSR on transition metals and found that CO formation is the rate limiting step at the investigated temperature of 773 K but dissociative methane adsorption becomes rate limiting at higher temperatures. These results are in agreement with experimental results obtained by Wei and Iglesia at 823-1023 K<sup>[102]</sup>.

### 1.4 Partial Oxidation of Methane

Another method for converting methane to synthesis gas is catalytic partial oxidation. Besides H<sub>2</sub> and CO formed by (1-3), H<sub>2</sub>O and CO<sub>2</sub> are formed as by-products via (1-8) or (1-4) and several other side reactions. Enger et al.<sup>[103]</sup> listed reactions that are expected to play a role in catalytic partial oxidation of methane.



Carbon formation is strongly suppressed due to the presence of  $O_2$  and the high affinity of  $O_2$  to oxidize surface carbon to CO or  $CO_2$ . The challenge for catalyst design is to achieving high selectivity towards  $H_2$  and CO while suppressing the total oxidation to  $CO_2$  and  $H_2O$ .

## 1.5 Methane Dry Reforming

By  $CO_2$  reforming of methane or methane dry reforming (MDR)  $CH_4$  and  $CO_2$  are converted into synthesis gas with a lower  $H_2:CO$  ratio than that of methane steam reforming (MSR). Synthesis gas produced by MDR is effective for the synthesis of long chain hydrocarbons<sup>[17]</sup> and valuable oxygenated chemicals<sup>[72, 104, 105]</sup>. Additionally, MDR has great potential to be used for energy transformation and storage due to its reversibility by methanation<sup>[106]</sup>.

However, other possible reactions such as reverse water-gas-shift (1-8), MSR (1-1), methane decomposition (1-4) and CO disproportionation (1-14) must be considered resulting in  $H_2:CO$  ratios different from 1 and carbon deposition.

The activation of  $CH_4$  and of  $CO_2$  as well as the reaction of these molecules on transition metal surfaces have been studied in great detail. Methane activation on transition metal surfaces is characterized by a high activation barrier, a low sticking coefficient and a high hydrogen kinetic isotope effect<sup>[107]</sup>. Wang et al.<sup>[108]</sup> investigated the reaction pathways for MDR on Ni(111) by density functional theory and published a simplified reaction mechanism. The rate determining step was found to be  $CH_4$  dissociative adsorption.  $CH_3$ , which is produced by  $CH_4$  dissociation prefers to dehydrogenate into  $CH_2$  which prefers to dehydrogenate to CH and CH prefers to be oxygenated into CHO. Without surface oxygen, which is formed by  $CO_2$  dissociation, dehydrogenation to C and H occurs. Dehydrogenation of CHO into H and CO has a very low energy barrier on Ni(111). The simplified mechanism proposed in this analysis is summarized in Fig. 1.

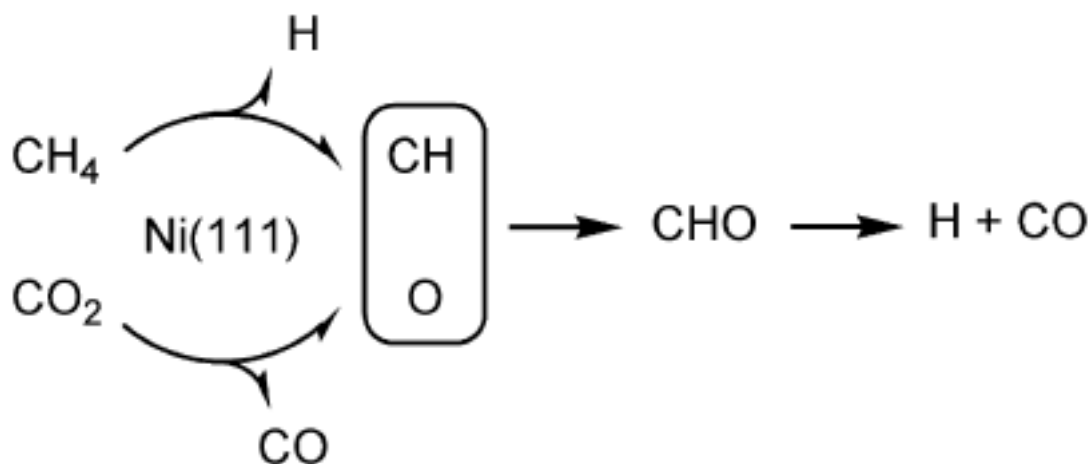


Fig. 1. Simplified mechanism of CO<sub>2</sub> reforming on Ni(111). Adopted from Wang et al.<sup>[108]</sup>

On supported catalysts, it is expected that the step of methane decomposition occurs on the metal particles while CO<sub>2</sub> activation could take place on the support, too. Thus, the reaction might take place on the metal-support interface. For MDR over Pt/ZrO<sub>2</sub>/Al<sub>2</sub>O<sub>3</sub> catalysts, a kinetic model based on this dual mechanism was successfully correlated with the experimental data<sup>[9]</sup>.

For CO<sub>2</sub> activation, support materials with basic OH species increase the interaction of CO<sub>2</sub> with the support and therefore, increase the CO<sub>2</sub> concentration on the surface in form of carbonates, and also increase CO<sub>2</sub> affinity for surface carbon which minimizes carbon accumulation<sup>[65]</sup>.

## 1.6 Objectives and Outline

In this thesis, the modification of Ni-ZrO<sub>2</sub> catalysts and the effect on methane reforming reactions was studied. This was done by modifying the metallic Ni component with Cu in order to achieve an increased stability against coke formation without decreasing the catalytic activity. As a second strategy, ZrO<sub>2</sub> was modified by CeO<sub>2</sub> and the effect of the synthesis procedure on ceria-zirconia solid solution formation and properties thereof were studied.

In the next two chapters preparation methods for Cu and/or CeO<sub>2</sub> promoted Ni-ZrO<sub>2</sub> and the applied methods for characterization and catalytic testing of the catalysts are presented.

Afterwards, the properties of pure ZrO<sub>2</sub> support and Ni supported on ZrO<sub>2</sub>, as well as the catalytic activity of Ni-ZrO<sub>2</sub> are discussed. Then, Ni-ZrO<sub>2</sub> catalysts promoted by Cu addition are studied. The bimetallic catalysts are investigated during reduction pretreatment, when alloy formation is observed. The catalytic activity for catalytic partial oxidation of methane

and methane decomposition is discussed next and after reaction these used catalysts are characterized with focus on carbon deposition.

Then, the effect of the modification of  $ZrO_2$  with  $CeO_2$  is studied. The mixed-oxide supported catalysts are characterized for their textural and structural properties as well as for their adsorption properties. Thereafter, nickel supported on  $ZrO_2$ ,  $CeO_2$  and mixed  $CeO_2/ZrO_2$  catalysts are tested for steam and dry reforming of methane. Their catalytic activity and stability during up to 24 hours time on stream are compared and after reaction the used catalyst are again characterized with focus on the amount and nature of deposited carbon.

Published results, presented in this thesis as characterization and in-situ studies of zirconia supported Ni and CuNi catalysts, are included as appendix. Two articles about CuNi- $ZrO_2$  catalysts have already appeared and a third manuscript on methane dry reforming over ceria-zirconia supported Ni catalysts is currently under preparation.

## Chapter 2

# Sample Preparation

---

The catalysts which were used during this work consisted of nickel and/or copper supported on zirconia, ceria or ceria-zirconia mixed oxide.

### 2.1 Preparation of the Support Material

As pure support materials commercial  $\text{ZrO}_2$  (prepared from  $\text{Zr}(\text{OH})_4$  from MEL chemicals XZO 880/01; calcined at 973 K) and  $\text{CeO}_2$  (commercial from Schuchardt CE026) were used.

Binary ceria-zirconia support materials were prepared by different methods including impregnation, composition and co-precipitation.

$\text{CeO}_2$  was added by impregnation of the  $\text{ZrO}_2$ . This material is labelled as CeZr.  $\text{Ce}(\text{NO}_3)_3 \cdot 6 \text{H}_2\text{O}$  was dissolved in water and  $\text{ZrO}_2$  was suspended in this solution to obtain a powder with 5.3 wt%  $\text{CeO}_2$ . The suspension was dried over night at 373 K. Then the yellowish ceria/zirconia powder (CeZr) was heated to 723 K with a heating rate of 5 K/min and held there for 2 hours. Due to the chosen preparation by impregnation ceria is expected to be enriched on the surface and no solid solution is formed.

The catalyst prepared by combustion synthesis route was obtained by mixing and melting of  $\text{ZrO}(\text{NO}_3)_2 \cdot 6 \text{H}_2\text{O}$  and  $\text{Ce}(\text{NO}_3)_3 \cdot 6 \text{H}_2\text{O}$  to achieve a Ce/Zr molar ratio 1:4. Water was admixed to the molten mass and urea was added. Only half of the urea was necessary for the reaction while the rest was used as a fuel. After the addition of urea the mixture was placed into the preheated oven, where it was kept for 15 minutes at 873 K. After the impetuous reaction greenish agglomerates with a texture different from that of the other samples were obtained. Finally, fine powder was gained by hand-milling of the agglomerates. This support is further labelled as  $\text{Ce}_x\text{Zr}_y\text{O}_2_{\text{comb}}$ .

Two further binary ceria-zirconia materials were prepared by co-precipitation method, both  $\text{Ce}_{0.6}\text{Zr}_{0.4}\text{O}_2$  with is composed of 60 mol%  $\text{CeO}_2$  and 40 mol%  $\text{ZrO}_2$ . For preparation of the mixed oxide support labelled as  $\text{Ce}_x\text{Zr}_y\text{O}_2_{\text{cp}}$  stoichiometric quantities of zirconyl nitrate hexahydrate ( $\text{ZrO}(\text{NO}_3)_2 \cdot 6 \text{H}_2\text{O}$ , Fluka), cerium(III) nitrate hexahydrate ( $\text{Ce}(\text{NO}_3)_3 \cdot 6 \text{H}_2\text{O}$ , Aldrich) were dissolved in distilled water, and the resulting solution was transferred to a

round bottom flask and stirred for 1 hour at 353 K. Then, an aqueous solution of 20 % w/w KOH was added drop-wise at 353 K with constant stirring until a pH of 10.5 was reached. After digesting the precipitate at 353 K for 72 hours, it was filtrated and washed several times with distilled water to remove any potassium impurity. Then, it was air-dried for 72 hours followed by drying at 393 K for 6 hours. Finally, the mixed oxide was heated at a ramp of 2 K/min and kept at 923 K for 2 hours. The other mixed oxide, labelled as  $Ce_xZr_yO_2$ \_ctab was prepared by a surfactant-assisted co-precipitation route. The synthesis route was adopted from Sunkonket et al.<sup>[77]</sup>. Zirconyl nitrate hexahydrate ( $ZrO(NO_3)_2 \cdot 6 H_2O$ , Fluka) and cerium(III) nitrate hexahydrate ( $Ce(NO_3)_3 \cdot 6 H_2O$ , Aldrich) precursor salts were dissolved in deionized water. Separately, cetyltrimethylammonium bromide (CTAB, Roth) was dissolved in deionized water at 333 K. The metal nitrate solution was added to the surfactant solution to obtain a mixed solution with a molar ratio  $c(CTAB)/c(Ce+Zr) = 1$ . Aqueous ammonia was gradually added to the mixture solution under vigorous stirring until precipitation was complete. The addition of ammonia induced precipitation of a yellow-brown colloidal slurry which was further stirred for 60 min in a quartz reactor and aged "hydrothermally" for 5 days at 363 K. After this timeframe, the bottles were cooled and the resulting precipitate was filtered and washed repeatedly with deionized water. The resulting cakes were oven-dried at 393 K overnight and finally calcined at 923 K for 2 hours. dropwise addition of aqueous ammonia for precipitation.

## 2.2 Preparation of Supported Ni and Cu Catalysts

Ni, Cu and CuNi catalyst were prepared by impregnation of  $ZrO_2$  and CeZr with  $Cu(NO_3)_2 \cdot 3 H_2O$  and  $Ni(NO_3)_2 \cdot 6 H_2O$  to obtain the following Cu:Ni ratios: 1:0, 3:1, 1:1, 1:3 and 0:1. The total metal weight content was kept at 5 % w/w. After dissolving the nitrates in water,  $ZrO_2$  or CeZr powder was suspended in the solution, which was dried at 373 K overnight. Then the powder was heated to 723 K with a heating rate of 5 K/min and held there for 2 hours.

For *in situ* X-Ray Photoelectron Spectroscopy (XPS) investigations an additional CuNi sample was prepared via impregnation of copper and nickel nitrates but with a higher overall metal loading of 50 wt% with a Cu:Ni ratio of 1:3 in order to prevent sample charging.

The other mixed oxide support materials and  $CeO_2$  were impregnated with nickel nitrate in order to obtain 5% w/w. All catalysts and their compositions are listed in Table 1.

**Table 1.** Composition of Cu/Ni-CeO<sub>2</sub>/ZrO<sub>2</sub> catalysts.

Name	ZrO <sub>2</sub> (wt %)	CeO <sub>2</sub> (wt %)	Cu (wt %)	Ni (wt %)
Cu-ZrO <sub>2</sub>	95	-	5	-
31CuNi-ZrO <sub>2</sub>	95	-	3.75	1.25
11CuNi-ZrO <sub>2</sub>	95	-	2.5	2.5
13CuNi-ZrO <sub>2</sub>	95	-	1.25	3.75
Ni-ZrO <sub>2</sub>	95	-	-	5
Cu-CeZr	90	5	5	-
31CuNi-CeZr	90	5	3.75	1.25
11CuNi-CeZr	90	5	2.5	2.5
13CuNi-CeZr	90	5	1.25	3.75
Ni-CeZr	90	5	-	5
Ni-Ce <sub>x</sub> Zr <sub>y</sub> O <sub>2</sub> _comb	75.4	24.6		5
Ni-Ce <sub>x</sub> Zr <sub>y</sub> O <sub>2</sub> _cp	53.5	46.5		5
Ni-Ce <sub>x</sub> Zr <sub>y</sub> O <sub>2</sub> _ctab	53.5	46.5		5
Ni-CeO <sub>2</sub>	-	95		5
13CuNi-ZrO <sub>2</sub> 50	50		12.5	37.5

## Chapter 3

# Methods

---

### 3.1 Characterization

Common methods for catalyst characterization are shortly described in the following.

#### 3.1.1 X-Ray Diffraction Measurements

Powder X-ray diffraction (XRD) patterns were recorded on a XPERT-PRO diffractometer with Cu K $\alpha$  radiation operating at 40 kV and 40 mA with a  $2\theta$  scanning from 5 to 90° and a step size of 0.02°. The crystallite size  $t$  was determined from X-ray line broadening studies using the Scherrer's formula<sup>[109]</sup>  $t = 0.9 \cdot \lambda / (B \cdot \cos(\theta))$ , where  $\lambda$  is the X-ray wavelength (Cu K $\alpha$  radiation: 0.154 nm) and  $B$  the full-width half-maximum of the Bragg diffraction angle  $\theta$ .

#### 3.1.2 Surface Area Analysis

The Brunauer-Emmet-Teller (BET) specific surface area for all catalysts was obtained by N<sub>2</sub> physisorption acquired at liquid N<sub>2</sub> temperature using a Micromeritics ASAP 2020 apparatus. Prior to analysis, all the powders were outgassed at 573 K and < 13  $\mu$ bar for 1 hour to ensure a clean surface prior to acquisition of the adsorption isotherm. The average pore size and average pore volume were analysed using the adsorption branch of the N<sub>2</sub> isotherm.

#### 3.1.3 Metal Dispersion Measurements

The nickel dispersion and metallic nickel surface area of the catalyst samples were estimated by H<sub>2</sub> chemisorption at 308 K using a Micromeritics ASAP 2020 C instrument. An amount of 0.5 g sample was used for these measurements. Prior to analysis, the samples were heated in an oxygen flow at 773 K for 1 hour. After cooling down in vacuum to 573 K the samples were reduced in hydrogen flow up to 673 K. After 20 minutes reduction, the samples were evacuated for 30 min at 673 K. Chemisorption was performed at 308 K at hydrogen pressures between 75 and 775 mbar and repeated once in order to isolate the chemisorption isotherm. Between the first and the repeated analysis the samples were evacuated at 308 K for 30 min to remove reversibly adsorbed H<sub>2</sub>. For the Ni samples, the same analysis procedure was applied after reducing at 873 K since reduction prior to reaction was at 873 K, too. The

difference of the first isotherm data (reversible + irreversible adsorption) and the repeated isotherm data (only reversibly adsorption) was utilized to calculate the quantity of irreversible adsorbed hydrogen. For determination of the nickel dispersion hydrogen pressures of 274, 341, 408, 474, 541 and 608 mbar were selected. H<sub>2</sub> was chosen as analysis gas because it adsorbs irreversibly on nickel but not on copper.

The active nickel area  $A_m$  at the surface and thus accessible to gases was calculated from

$$A_m(m^2/g) = 6.022 \times 10^{23} F_s n_a A_g \quad (3-1)^{[110]}$$

where  $F_s$  is the stoichiometry factor, obtained from the ratio of the atoms or molecules in the balanced chemical equation between the active gas and active surface, which therefore is 2 for H<sub>2</sub> on Ni,  $n_a$  is the number of moles of gas adsorbed (in cm<sup>3</sup>/g STP) determined at the monolayer coverage and  $A_g$  is the cross-sectional area of the adsorptive atom.<sup>[110]</sup> In case of Ni  $A_g$  is 0.0649 nm<sup>2</sup>.<sup>[111]</sup>

The metal dispersion  $\gamma\%$  is the fraction of the total of active metal accessible to the reactant molecules  $N_T$ . It is expressed as a percentage,

$$\gamma\% = \frac{V_m N_A F_s}{N_T V_{mol}} \times 100\% \quad (3-2)^{[110]}$$

where  $V_m$  is the monolayer volume,  $N_A$  is Avogadro's number and  $V_{mol}$  is the molar volume of the adsorptive.<sup>[110]</sup>

### 3.1.4 Transmission Electron Microscopy

Transmission Electron Microscopy (TEM) was utilized to obtain information about the size, morphology and distribution of the nickel particles on the supported catalysts. Prior to the microscopy the catalysts were oxidized at 773 K and reduced at 673 K or 873 K. To characterize the nickel catalysts after MDR reaction, samples exposed to CH<sub>4</sub> and CO<sub>2</sub> at 873 K for three hours were explored. All treatments were performed in a quartz flow reactor in the kinetic setup which is described in 3.3. For TEM measurements the samples were suspended in ethanol and one drop of the suspension was deposited on carbon coated Cu grids. TEM measurements were performed on an analytical TECNAI F20 instrument connected to an EDX detector. EDX was used to identify the metal particles on the support materials.

The structural analysis of the recorded images has been performed using ImageJ 1.48. The digital diffractograms reported in the results section correspond to the long-scaled power spectrum of the corresponding fast Fourier transforms.

### 3.1.5 Temperature Programmed Desorption

Temperature Programmed Desorption (TPD) was applied on  $\text{ZrO}_2$  to study the absorption properties of  $\text{H}_2\text{O}$ ,  $\text{D}_2\text{O}$ ,  $\text{CO}$  and  $\text{CO}_2$ . Therefore, 0.5 g  $\text{ZrO}_2$  was placed in a quartz tube and after oxidation at 773 K followed by cooling down to room temperature in vacuum 100 mbar of the desired gas or vapour was introduced. After 10 minutes in the gas/vapour atmosphere, the tube was evacuated for 30 minutes and then heated up to 1173 K with a heating rate of 5 K/min. The species which desorbed during heating were analysed by a mass spectrometer (Pfeiffer QMS 200).

## 3.2 In situ Infrared Spectroscopy

Fourier transformed infrared (FTIR) Spectra were recorded in transmission using a Vertex 70 spectrometer (Bruker Optics) with a globar as radiation source, a mercury cadmium telluride (MCT) detector and a HeNe laser as internal wavelength standard. The resolution of the spectra is  $4\text{ cm}^{-1}$ . A scheme of the FTIR apparatus is shown in Fig. 2.

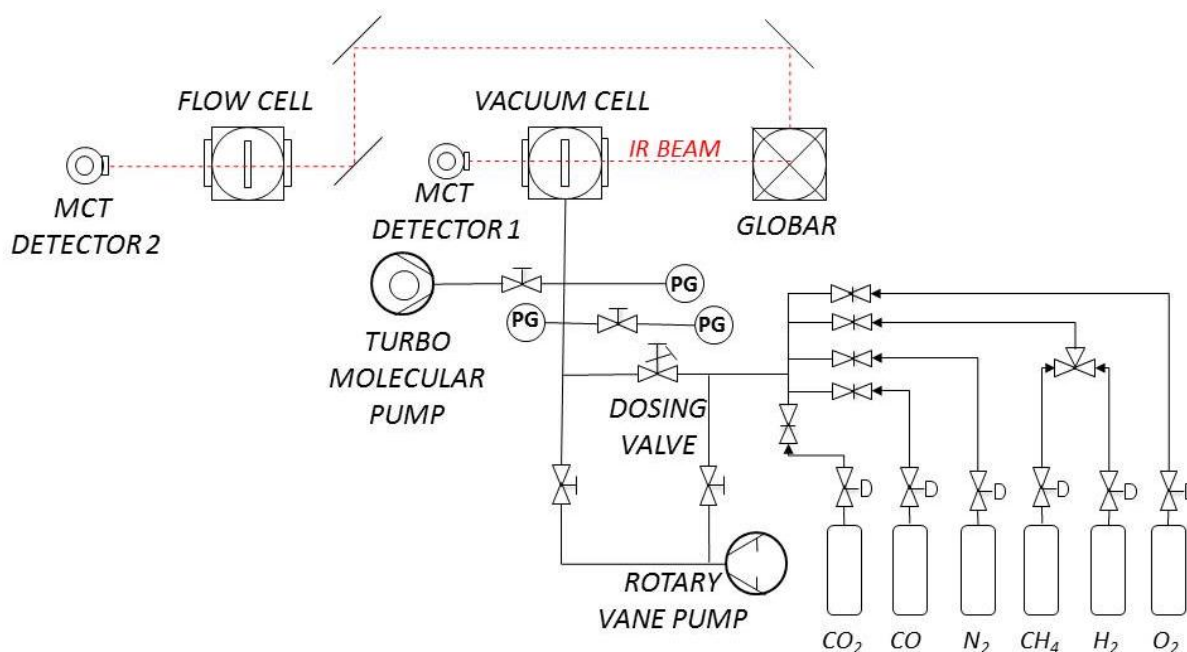


Fig. 2. Schematic illustration of the experimental setup for FTIR measurement.

The Infrared apparatus is equipped with a vacuum cell and a flow cell and records infrared spectra in transmission mode. The samples were pressed to small discs before placing in the sample holder. The vacuum cell is connected to a turbomolecular pump which allows pressures down to  $10^{-6}$  mbar. A rotary vane pump is used to achieve the fine vacuum needed for the turbomolecular pump. Gases are introduced into the chamber via a leak valve. The pressure in the chamber is monitored by a MKS type 626 pressure gauge for pressures above 1 mbar, a Pfeiffer Vacuum type CMR 264 compact capacitance gauge for the fine vacuum range and by a Balzers type IKR 260 compact cold cathode gauge for pressures in the high

vacuum range. The sample temperature is measured by a type K thermocouple positioned around the edges of the sample holder holding the sample disc. The thermocouple is connected to a Eurotherm temperature controller, which is used to power the heating wire to heat the sample up to 773 K. Cooling of the sample to temperatures until 163 K is possible by keeping liquid nitrogen in a cooling loop around the sample holder. The flow cell is connected to the apparatus used for kinetic measurements.

### **3.2.1 Spectra Acquisition**

All spectra were obtained by averaging 128 scans to achieve good signal to noise ratios. A spectrum of the sample holder was used as a background for all spectra. Spectra were obtained in the range of 4000 to 900  $\text{cm}^{-1}$  with an aperture of 1.5 mm.

The area of peaks on different samples cannot be compared quantitatively because of the strong dependence on the thickness of the sample discs.

### **3.2.2 Pretreatment Procedure in the Vacuum Cell**

After installing the sample in the cell, it was closed and evacuated for a few minutes. Then 100 mbar  $\text{O}_2$  were introduced and the sample was heated to 773 K at a rate of 10 K/min in the oxygen atmosphere. After 60 minutes the chamber was evacuated again and the sample was cooled down to 303 K where experiments on the oxidized samples were performed. For reduction 5 mbar  $\text{H}_2$  and 900 mbar  $\text{N}_2$  were introduced into the evacuated chamber after oxidation and the sample was heated to 673 K at a rate of 10 K/min. After 30 minutes in hydrogen atmosphere the chamber was evacuated and kept at 673 K for another 30 minutes to remove chemisorbed hydrogen and water before cooling down to 303 K to perform experiments on the reduced sample.

### **3.2.3 Adsorption of CO as a Probe Molecule**

Infrared spectroscopy of adsorbed carbon monoxide as a probe molecule is a common technique for the characterization of supported metal catalysts. In this work it was applied to get information about the oxidation states of copper and nickel after oxidation and reduction and to compare the bimetallic with the monometallic catalysts.

### **3.2.4 Operando FTIR during Methane Steam Reforming**

The supported nickel catalysts were tested for methane steam reforming (MSR) reaction. After oxidation at 773 K in  $\text{O}_2/\text{Ar}$  flow and reduction in  $\text{H}_2/\text{Ar}$  flow at 673 K the tested catalysts were cooled down in Ar flow. Then, the samples were heated in a mixture of 15 mbar  $\text{H}_2\text{O}$  and 5 mbar  $\text{CH}_4$  in Ar with a total flow rate of 50 ml/min with 5 K/min up to 673 K and kept at 673 K for 2 hours. The reactants and product were detected by mass spectrometer (MS) simultaneously to recording of IR spectra.

### 3.3 Catalytic Testing

Activity evaluation studies were carried out in a quartz flow reactor. A small amount of 25-50 mg catalyst was placed in the quartz glass reactor in-between two plugs of quartz wool. The flow rates of the reactants were set with mass flow controllers (MFC). For quantitative detection, the reaction products were analysed under steady state conditions by a gas chromatograph (GC) equipped with a thermal conductivity detector (TCD) and a flame ionization detector (FID). The FID is equipped with a Ni-catalyst (METHANIZER) to hydrogenate CO and CO<sub>2</sub> to CH<sub>4</sub> to enable FI detection of these gases. Via a differentially pumped capillary directed to a mass spectrometer (Pfeiffer OMNIStar) with Faraday detector a semi quantitative detection of the products was possible, too. A diagram of the kinetic setup is shown in Fig. 3.

A second setup with quartz flow reactor was used for temperature programmed studies. Part of the effluent was directed to a mass spectrometer (Pfeiffer QMS 200) via a differentially pumped capillary to detect the reactants and products during heating in reactive gas flow.

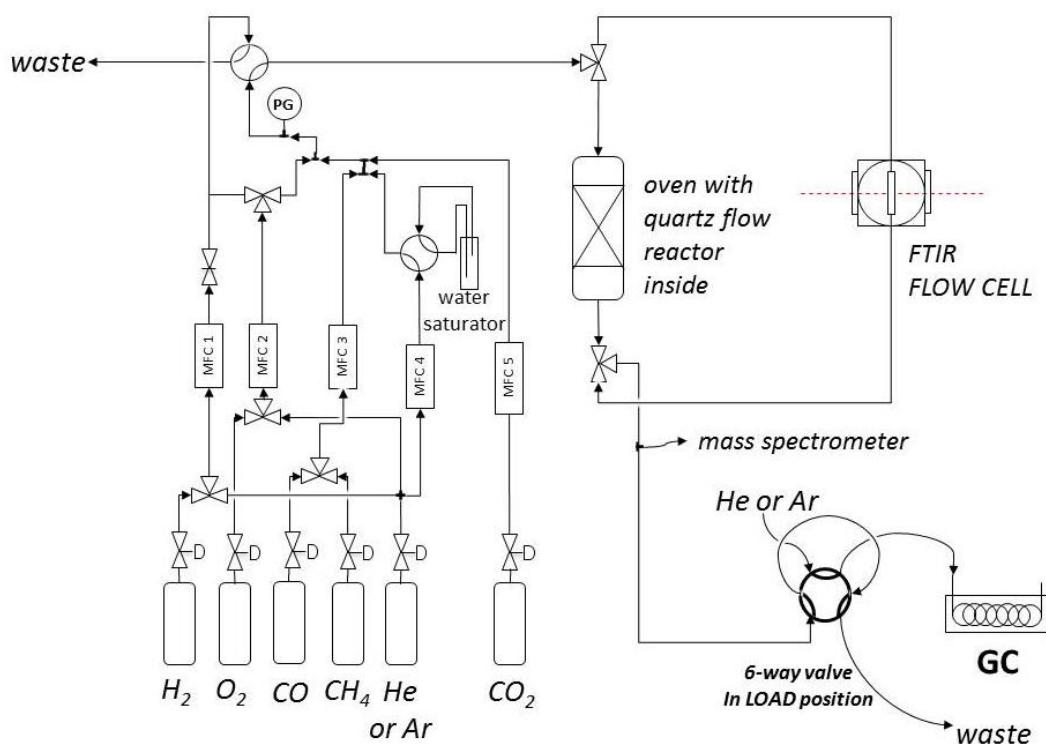


Fig. 3. Scheme of the Kinetic setup

#### 3.3.1 Temperature Programmed Methane Decomposition

For temperature programmed methane decomposition (TPMD) experiments 50 mg catalyst was placed in the quartz flow reactor. The zirconia supported Ni, Cu and CuNi samples

were tested for methane decomposition. The main products ( $H_2$ ,  $CO$ ,  $CO_2$  and  $CH_4$ ) were detected with the mass spectrometer. The catalysts were oxidized at 727 K and reduced at 673 K prior to the reaction. Then the samples were heated up to 727 K and cooled down to 573 K in a mixture of 5 %  $CH_4$  and 95 % Ar with a total flow of 50 ml/min. The heating and cooling rate was set to 5 K/min and the heating-cooling cycle was repeated twice. After the TPMD experiment the sample was cooled down to room temperature in Ar.

For quantitative determination of the reaction rates the reaction products were analysed under steady state conditions by GC.

### 3.3.2 Partial Oxidation of Methane

To test the catalytic activity during partial oxidation of methane, 50 mg catalyst was placed in the quartz flow reactor. The zirconia supported Ni, Cu and CuNi samples were tested for this reaction. The main products and reactants ( $H_2$ ,  $CO$ ,  $CO_2$ ,  $H_2O$  and  $CH_4$ ) were detected via mass spectrometer. The catalysts were oxidized at 727 K and reduced at 673 K prior to the reaction. Then the samples were heated up to 727 K, kept at 727 K for 30 minutes and then cooled down to 573 K in a mixture of 5 %  $CH_4$ , 10 %  $O_2$  and 95 % Ar with a total flow of 50 ml/min. The heating and cooling rate was set to 5 K/min and the heating-cooling cycle was repeated twice. After the temperature programmed experiment the samples were cooled down to room temperature in Ar.

### 3.3.3 Methane Dry Reforming

Activity evaluation studies in the methane dry reforming (MDR) reaction were carried out in a quartz flow reactor. 25 mg catalyst was mixed with 75 mg quartz sand and loaded into the glass reactor in-between two plugs of quartz wool. The catalysts were oxidized in an  $O_2/Ar$  mixture at 773 K for 30 min and reduced in a  $H_2/Ar$  mixture at 873 K for 30 min. Before exposure to the reaction mixture the sample was kept in Ar at 873 K for 30 min. Then, the sample was exposed to a mixture of 10 %  $CH_4$ , 10 %  $CO_2$  and 80 % Ar with a total flow of 25 ml/min at 873 K for 24 hours. The reaction products and reactants were quantitatively analysed by GC.

### 3.3.4 Equations used for Calculation of Catalytic Results

The  $CH_4$  and  $CO_2$  conversion,  $H_2$  formation and  $CH_4$  reaction rates,  $H_2:CO$  ratio, carbon balance,  $H_2$  selectivity and turn-over-frequency (TOF) based on the metallic Ni surface area ( $A_{Ni}$ ) after reduction at 873 K

$$\% CH_4 \text{ conversion: } X_{CH_4} = \frac{f(CH_{4,in}) - f(CH_{4,out})}{f(CH_{4,in})} \times 100\% \quad (3-3)$$

$$\% CO_2 \text{ conversion: } X_{CO_2} = \frac{f(CO_{2,in}) - f(CO_{2,out})}{f(CO_{2,in})} \times 100\% \quad (3-4)$$

$$\text{H}_2 \text{ production rate: } r_{\text{H}_2} = \frac{f(\text{H}_{2,\text{out}}) \times p}{R \times T \times m_{\text{cat}}} \frac{\text{mol H}_2}{\text{g catalyst} \times \text{s}} \quad (3-5)$$

$$\text{CO production rate: } r_{\text{CO}} = \frac{f(\text{CO}_{\text{out}}) \times p}{R \times T \times m_{\text{cat}}} \frac{\text{mol CO}}{\text{g catalyst} \times \text{s}} \quad (3-6)$$

$$\text{H}_2:\text{CO ratio: } R = \frac{r_{\text{H}_2}}{r_{\text{CO}}} \quad (3-7)$$

$$\text{Carbon balance: } C_{\text{balance}} = \frac{f(\text{CH}_{4,\text{out}}) + f(\text{CO}_{2,\text{out}}) + f(\text{CO}_{\text{out}})}{f(\text{CH}_{4,\text{in}}) + f(\text{CO}_{2,\text{in}})} \quad (3-8)$$

$$\% \text{ H}_2 \text{ selectivity: } S_{\text{H}_2} = \frac{f(\text{H}_{2,\text{out}})}{2(f(\text{CH}_{4,\text{in}}) - f(\text{CH}_{4,\text{out}}))} \times 100\% \quad (3-9)$$

$$\text{Turn-over-frequency: } TOF = \frac{N_{\text{CH}_4}}{N_{\text{Ni}}} \quad (3-10)$$

Number of converted CH<sub>4</sub> molecules:

$$N_{\text{CH}_4} = f(\text{CH}_{4,\text{in}}) \times X_{\text{CH}_4} \times \rho(\text{CH}_4) \times M(\text{CH}_4) \quad (3-11)$$

$$\text{Number of surface nickel atoms: } N_{\text{Ni}} = m_{\text{cat}} \times A_{\text{Ni}} \times N_{\text{Ni}/\text{m}^2} \quad (3-12)$$

where  $f(i_{\text{in}})$  and  $f(i_{\text{out}})$  are the flow rates of each component in the feed or effluent in m<sup>3</sup>/s,  $p$  is the pressure in the quartz reactor,  $R$  is the universal gas constant with 8.314 J/(K mol),  $T$  is the reaction temperature in Kelvin,  $m_{\text{cat}}$  is the mass of the catalyst in the reactor,  $\rho(\text{CH}_4)$  the density of methane,  $M(\text{CH}_4)$  the molar mass of methane and  $N_{\text{Ni}/\text{m}^2}$  the number of surface nickel atoms per square meter.

### 3.3.5 Temperature Programmed Oxidation

After testing the catalyst's performance the amount of coke deposited on the catalyst, was determined by a temperature programmed oxidation (TPO) in 20% O<sub>2</sub> in Ar applying a heating rate of 5 K/min up to 673 K. The amount of CO<sub>2</sub> formed by (1-17) is monitored by mass spectrometry detection.



## 3.4 X-Ray Absorption Spectroscopy

X-ray absorption spectroscopy (XAS) is used for the determination of the local electronic and/or geometric structure of materials. In principle, an X-ray photon is absorbed and excites a core electron to an unoccupied level or an unbound state. In both cases, a core hole is created. X-ray Absorption Near Edge Structure (XANES) is in the region where a core electron is photo-excited into an unoccupied valence level. Its shape and intensity is characteristic of the oxidation state and other species bonded to the excited atom. Therefore,

the XANES region is often used to determine the formal oxidation state of the element. The region above the core-level binding energies of the atom is called Extended Absorption Fine Structure (EXAFS) and provides local information about the number and type of neighbouring atoms and their distance to the absorbing atom. Since each element has specific characteristic absorption edges, X-ray absorption spectroscopy provides specific information about the element, depending on the X-ray photon energy range. Since gas phase and a quartz flow reactor are transparent for hard X-rays, XAS is adoptable for *in situ* measurements.

### 3.4.1 *In situ* XAS of Ni, Cu and CuNi Supported Catalysts

*In situ* X-ray absorption spectroscopy (XAS) measurements were carried out in fluorescence mode at the SuperXAS beamline at the Swiss Light Source (SLS) in Villigen, Switzerland using a single-photon-counting pixel detector. The catalyst was placed between two plugs of quartz wool in a quartz glass flow reactor which was heated by an air blower. A schematic illustration of the measurement setup is shown in Fig. 4.

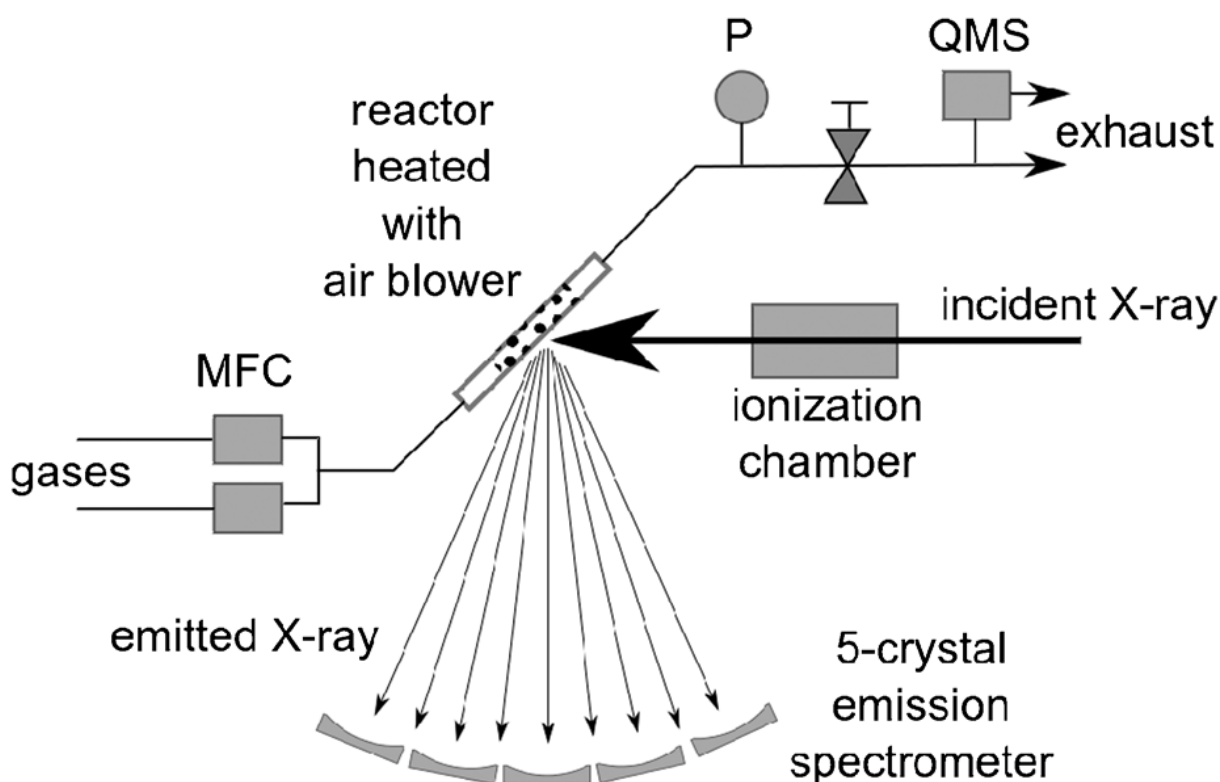


Fig. 4. Schematic illustration of the setup for *in situ* XAS measurements. Adopted from Kleymenov et al.<sup>[112]</sup>

High energy resolution fluorescence detected X-ray absorption spectroscopy (HERFD-XAS) was applied at the Cu  $K_{\alpha}$  edge ( $E_0 = 8980$  eV) and X-ray near edge structure (XANES) measurements were performed at the Ni K edge ( $E_0 = 8333$  eV). The spectrometer and experimental setup are described in detail in<sup>[112-114]</sup>. The catalyst was heated in a mixture of 5 % hydrogen in helium with a heating rate of 10 K/min from room temperature up to 660 K in

case of Ni-ZrO<sub>2</sub> and up to 560 K for Cu-ZrO<sub>2</sub> and CuNi-ZrO<sub>2</sub>. Spectra were recorded at 300, 360, 430, 500, 560 and in case of Ni-ZrO<sub>2</sub> at 660 K. The sample was kept for about 20 minutes at each temperature while spectra were recorded. After cooling down to room temperature another spectrum at 300 K was recorded.

### 3.4.2 Ex-situ XAS of Dry Reforming Catalysts

XAS spectra were recorded at the Ni K-edge ( $E_0 = 8333$  eV) at Beamline 8 of the Synchrotron Light Research Center, Thailand. Spectra of the catalysts Ni-ZrO<sub>2</sub>, Ni-CeO<sub>2</sub>, Ni-Ce<sub>x</sub>Zr<sub>y</sub>O<sub>2\_cp</sub> and Ni-Ce<sub>x</sub>Zr<sub>y</sub>O<sub>2\_ctab</sub> pre-reduced in H<sub>2</sub>/Ar at 873 K (labeled as: "red.") and samples after exposure to the MDR-reaction mixture (CH<sub>4</sub>/CO<sub>2</sub>/Ar) at 600°C (labeled as: "used") were recorded at room temperature in fluorescence mode. Each sample was pressed into a frame covered by polyimide tape and mounted onto a sample holder. The experimental setup and the measurement procedure are described in<sup>[115]</sup>.

### 3.4.3 Data Acquisition and Analysis

X-ray absorption data were processed and analyzed using the IFEFFIT<sup>[116, 117]</sup> software package (version 1.2.11 and version 0.9.21). With each recorded XAS spectrum, the absorption edge position ( $E_0$ ) was set equal to the position of the highest maximum of the 1<sup>st</sup> derivative of  $\mu(E)$  in the X-ray energy  $E$ . Data processing was done by fitting a linear and a polynomial function to the pre- and post-edge region, respectively. The fraction of Ni present in respective phase of the background-subtracted and normalized XANES spectra of the catalysts were determined by linear combination of normalized Ni K-edge XANES spectra of Ni foil and NiO references in case of Ni K-edge spectra and by linear combination of normalized Cu K-edge HERFD-XAS spectra of Cu foil, Cu<sub>2</sub>O and CuO references in case of Cu K-edge spectra.

The EXAFS signal of the used MDR catalysts were converted into k-space and the resulting  $\chi(k)$  functions were then weighted by  $k^2$  to compensate for dampening of EXAFS oscillations at increasing  $k$  and Fourier transformed in k-range 2 to 12 Å<sup>-1</sup>. The spectra of the used catalysts were fitted in R-space in the R-range 1 to 5 Å with multiple k-weightenings ( $k=1,2,3$ ), using theoretical models built from Ni<sup>0</sup> (JCPDS 04-0850), NiO (JCPDS 44-1159) and Ni<sub>3</sub>C (JCPDS 06-0697). Data fitting allowed the estimation of the coordination numbers (CN), absorber-scatter distance (R) and Debye-Waller factors ( $\sigma^2$ ).

## 3.5 In situ X-Ray Photoelectron Spectroscopy

X-Ray Photoelectron Spectroscopy (XPS) is a well established non-destructive method for studying the chemical composition of surfaces based on the photoelectric effect. The absorption of an X-ray photon with energy  $h\nu$  leads to excitation and emission of an electron from the core level. The kinetic energy  $E_{kin}$  of the emitted photoelectron is equal to the

difference between photon energy  $h\nu$  and the sum of the binding energy  $E_b$  of the photoelectron and the work function  $\psi$ . Since every element is characterized by unique energy levels, XPS can be used for elemental analysis. Additionally, small shifts of the detected binding energy provide information about the chemical environment of the atom.

The detected photoelectrons originate only from the upper atomic layers of the sample because of the mean free path of the electrons which is in the nm-range. The mean free path depends of the kinetic energy. Synchrotron based X-ray radiation can be varied in order to record XP spectra at different kinetic energies and create a depth profile of the sample's surface and surface-near region.

In the past most surface sensitive spectroscopy techniques such as XPS were restricted to high-vacuum conditions<sup>[118, 119]</sup> since inelastic scattering of photoelectrons with gas phase molecules must be avoided. However, instrumental developments have enabled XPS operation at elevated pressures up to 10 mbar<sup>[120-122]</sup>. XPS investigations at mbar pressure enable the determination of chemical species near the surface of a catalyst, including the gas-phase reaction products while the reaction takes place<sup>[123, 124]</sup>.

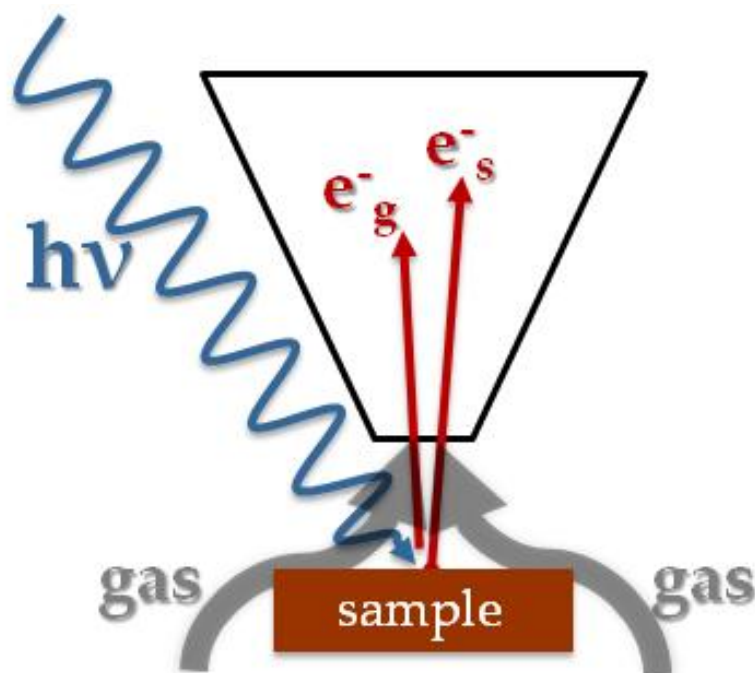


Fig. 5. Schematic illustration of near-ambient pressure XPS. The incident X-rays interact both with the sample surface (photoelectrons  $e^-_s$ ) and part of the gas phase molecules in front of the sample (photoelectrons  $e^-_g$ ) which are directed via a differentially pumped electrostatic lens system to the electron detector.

*In situ* synchrotron-based near ambient pressure (NAP-)XPS measurements were carried out at the ISSIS-PGM beamline at the Helmholtz-Zentrum Berlin using a high pressure XPS station constructed at the FHI Berlin. Details of the setup are described by Bluhm et al.<sup>[123]</sup>. The sample is mounted inside a high-pressure cell 2 mm away from a small aperture with

1 mm in diameter which is the entrance to a differentially pumped electrostatic lens system. The combination of electrostatic lenses and differentially pumped apertures allows to efficiently collect electrons while keeping a pressure differential of 9 orders of magnitude between the high-pressure cell and the hemispherical analyzer (SPECS)<sup>[123]</sup>.

The catalyst  $13\text{CuNi-ZrO}_2/50$  was used for *in situ* NAP-XPS measurement. The 50 wt% total metal loading of this catalyst was used for these experiments in order to prevent sample charging. The calcined powder was pressed onto a copper plate and reduced at 773 K prior to placing it into the *in situ* reaction cell. Measurements were performed at photon energies of 1100 eV for the Cu 2p, 1010 eV for the Ni 2p and 425 eV for the C 1s XP spectra, yielding photoelectron kinetic energies of 150 eV. For depth profiling the photon energies were varied to obtain photoelectron kinetic energies of 350 eV and 550 eV. All spectra were corrected for synchrotron beam current, incident photon flux and energy dependent photo-ionization cross sections<sup>[125]</sup>. Binding energies (BEs) were referenced to the Fermi edge recorded after each core-level measurement. The measured signal envelopes were fitted with Gauss-Lorentzian peaks by using the software Casa XPS after subtraction of a Shirley background.

## Chapter 4

# Results

### 4.1 Characterization of ZrO<sub>2</sub>

The ZrO<sub>2</sub> support material was characterized as monoclinic phase, as shown Fig. 6 with a BET surface area of 36.6 m<sup>2</sup>/g. Adsorption properties and the interaction with CO, CO<sub>2</sub>, H<sub>2</sub>, H<sub>2</sub>O and D<sub>2</sub>O were studied by FTIR and TPD.

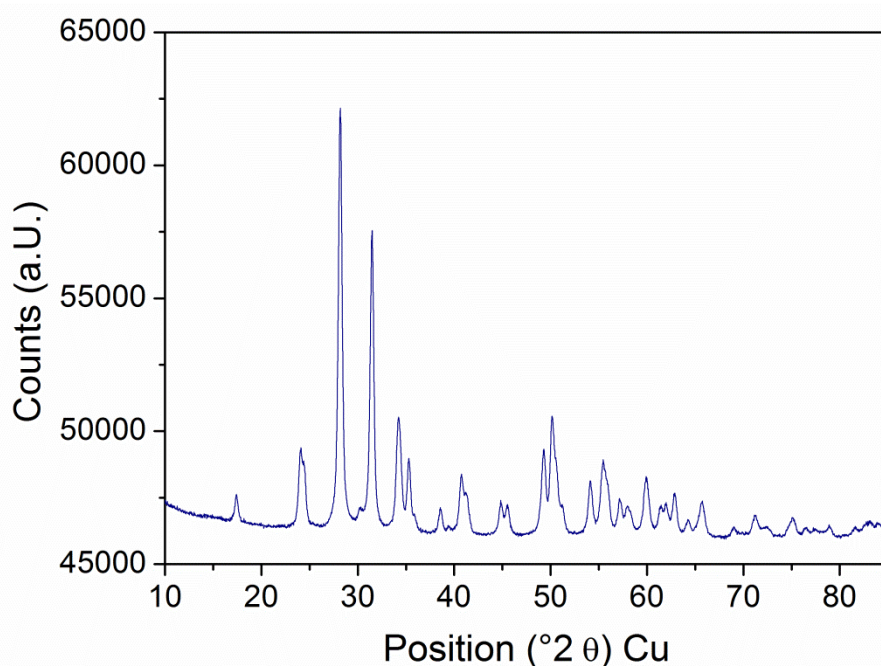


Fig. 6. XRD pattern of ZrO<sub>2</sub>.

In order to determine how ZrO<sub>2</sub> is affected by mild reduction at 673 K, FTIR spectra of oxidized and reduced ZrO<sub>2</sub> are compared in Fig. 7. As expected, only little changes are found. In the region between 3800 and 3600 cm<sup>-1</sup>, hydroxyl-bands at 3770 and 3670 and a much smaller one at 3730 cm<sup>-1</sup> are observed in the spectrum of oxidized ZrO<sub>2</sub>. The OH species above 3700 cm<sup>-1</sup> and below 3700 cm<sup>-1</sup> have been assigned by Tsyganenko et al.<sup>[126]</sup> to terminal and bridged surface OH groups, respectively. Upon reduction at 673 K the intensity of the larger OH-bands as well as the wavenumber increases for about 2 cm<sup>-1</sup> and an additional OH-band at 3610 cm<sup>-1</sup> appears. Surface OH-groups on ZrO<sub>2</sub> are stable up to 773 K.

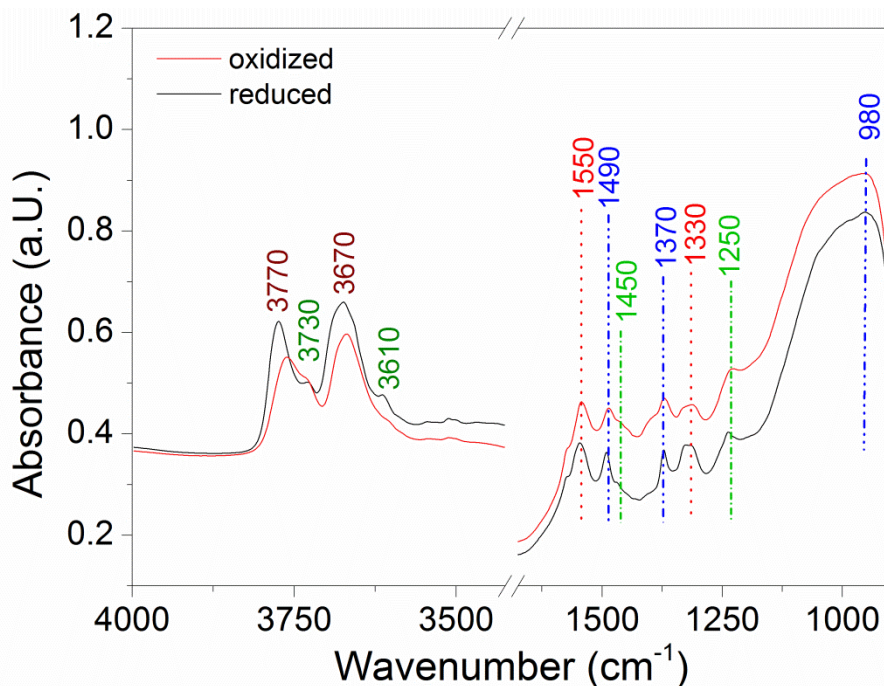


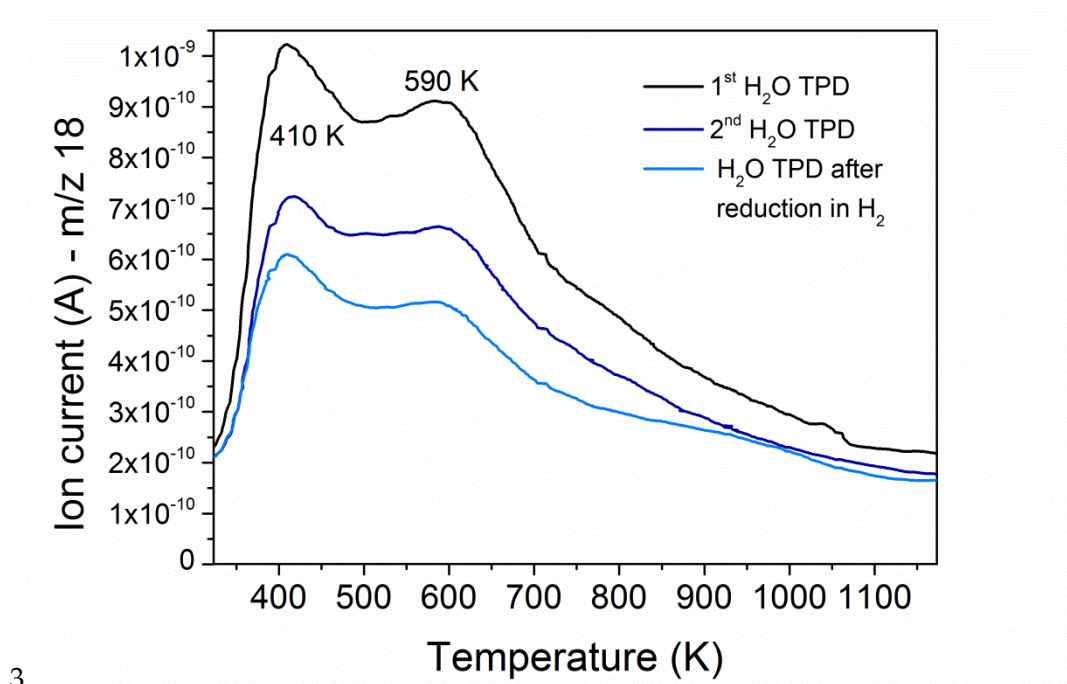
Fig. 7. FTIR spectra at room temperature of ZrO<sub>2</sub> after oxidation at 773 K and after reduction at 673 K.

In the region between 1600 and 900 cm<sup>-1</sup> several bands assigned to carbonates on the oxide surface are observed. In agreement with literature<sup>[127-129]</sup>, the bands at 1490, 1370 and 980 cm<sup>-1</sup> are assigned to monodentate carbonate. Bands at 1550 and 1330 cm<sup>-1</sup> are assigned to bidentate carbonate<sup>[128, 130, 131]</sup> and those at 1450 and 1250 cm<sup>-1</sup> are most likely bands of bidentate bicarbonate<sup>[131]</sup>.

By adsorption of H<sub>2</sub>O followed by evacuation and temperature programmed desorption (TPD) at 5 · 10<sup>-6</sup> mbar the stability of adsorbed water or hydroxyl and desorption temperatures of these species were monitored. The TPD profiles of H<sub>2</sub>O after two subsequent adsorption-desorption cycles from oxidized and once from reduced ZrO<sub>2</sub> powder are shown in Fig. 8.

In all desorption profiles two main peaks are observed. The one at 410 K is assigned to desorption of molecular water while the second desorption peak at 590 K is assigned to the associative desorption of surface hydroxide. Upon repetition, the amount of desorbed water decreases what could be ascribed to sintering due to the high temperature of 1173 K.

Fig. 5 shows a scheme of the sample in an XPS experiment under gas atmosphere. XPS experiments at elevated pressures require high-vacuum condition for the operation of electron detectors<sup>[123]</sup>.



3

Fig. 8. Temperature Programmed Desorption of H<sub>2</sub>O from ZrO<sub>2</sub> powder.

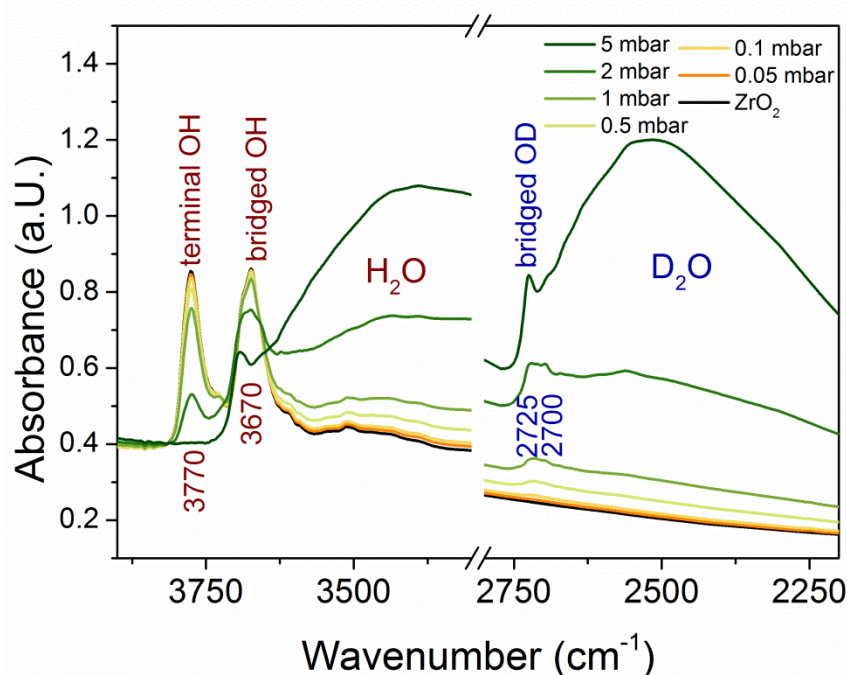


Fig. 9. FTIR Spectra of ZrO<sub>2</sub> after oxidation at 775 K and during adsorption of 0.05, 0.1, 0.5, 1, 2 and 5 mbar D<sub>2</sub>O at room temperature.

D<sub>2</sub>O was adsorbed on ZrO<sub>2</sub> followed by FTIR spectroscopy to see if surface sites for dissociative water desorption are available. FTIR spectra of ZrO<sub>2</sub> during adsorption of 0.05 up to 5 mbar D<sub>2</sub>O are shown in Fig. 9. In 1 mbar D<sub>2</sub>O atmosphere small OD-bands are observed. This indicates that sites for dissociative water adsorption are available on the pre-oxidized ZrO<sub>2</sub> surface. With increasing D<sub>2</sub>O pressure, the OD and OH bands are covered by

the broad bands of molecularly adsorbed D<sub>2</sub>O and H<sub>2</sub>O and exchange of OH against OD groups can take place.

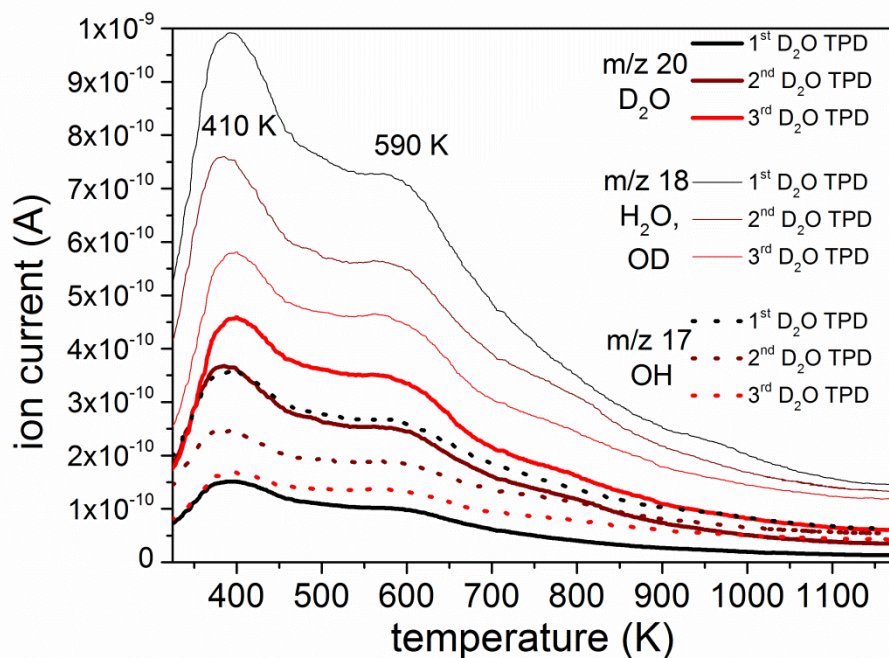


Fig. 10. TPD profiles of D<sub>2</sub>O, OD, H<sub>2</sub>O and OH desorbed from ZrO<sub>2</sub> performed 3 times in a row.

D<sub>2</sub>O was adsorbed on ZrO<sub>2</sub> followed by evacuation and heating. The TPD profiles of the desorbed species, followed by MS detection, are shown in Fig. 10. Besides of D<sub>2</sub>O and OD which desorb at the same temperatures as H<sub>2</sub>O and OH, respectively (shown in Fig. 8) still H<sub>2</sub>O and its fragment OH are detected. The ratio D:H is increasing by repetition but nevertheless the amount of OH seems to be significantly higher than the amount of OD on the surface. Anyway one needs to take in account that this result might be biased due to insufficient vacuum during cooling down in vacuum (<10<sup>-3</sup> mbar) after oxidation and in-between the TPD experiments what might allow H<sub>2</sub>O to impurify the atmosphere in the system.

Fig. 11 shows TPD profiles of CO<sub>2</sub> on ZrO<sub>2</sub>. Three main desorption peaks are observed at 380, 550 and 780 K, respectively. The profiles are identical when repeated after evacuation at 1173 K and cooling down in vacuum. In order to assign the CO<sub>2</sub> desorption peaks to carbonate species on ZrO<sub>2</sub> the experiment was repeated in the FTIR vacuum cell. The spectra recorded during heating after evacuation below 10<sup>-5</sup> mbar are shown in Fig. 12.

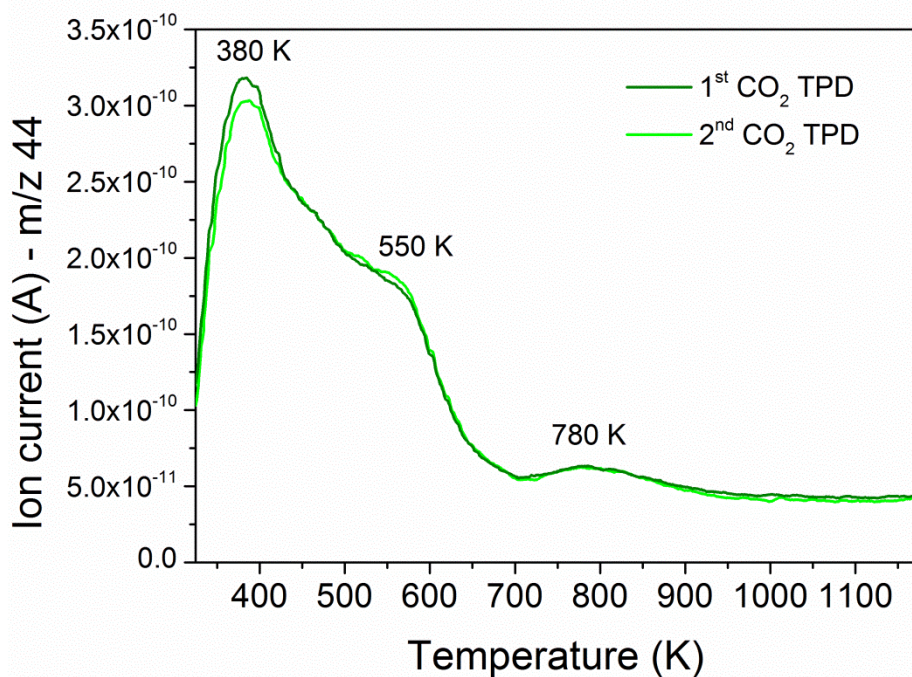


Fig. 11. TPD profiles of CO<sub>2</sub> desorbed from ZrO<sub>2</sub> two times in a row.

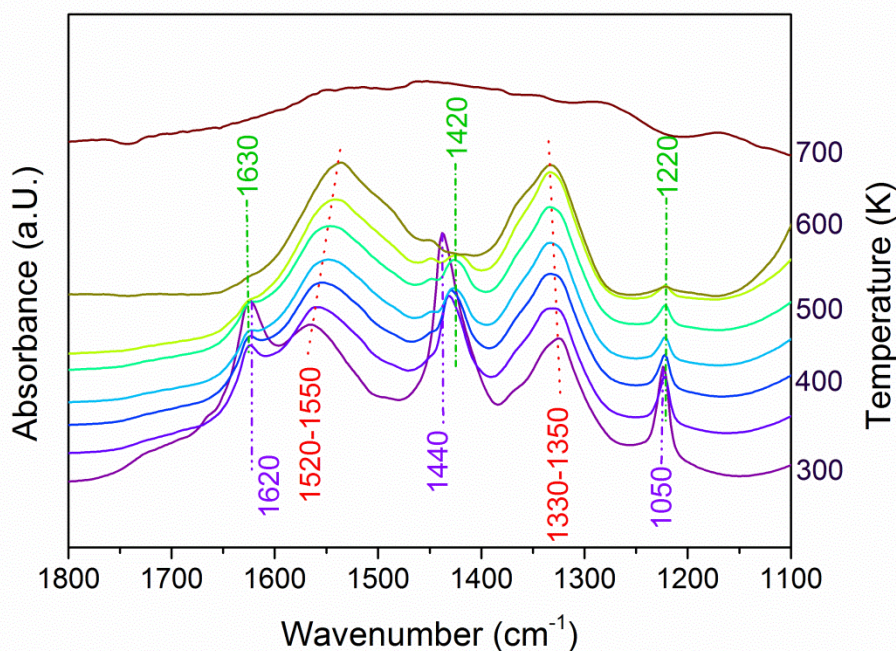


Fig. 12. Temperature programmed desorption of carbonates followed by FTIR spectroscopy on ZrO<sub>2</sub>.

According to the peaks in the region between 1800 and 1100 cm<sup>-1</sup> of FTIR spectra recorded during temperature programmed desorption of carbon dioxide shown in Fig. 12, the desorption peak at 380 K in Fig. 11 can be assigned to the desorption of bidentate bicarbonate<sup>[9, 132]</sup> which shows peaks at 1620, 1440 and 1050 cm<sup>-1</sup>. Furthermore, the desorption peak at 550 K can be assigned to the desorption of bidentate bicarbonate<sup>[131]</sup>. Bands at 1550 and 1330 cm<sup>-1</sup>, which are assigned to bidentate carbonate<sup>[128, 130, 131]</sup> shift to 1520

and 1350, respectively and possibly desorb at 780 K, where no more FTIR spectra could be recorded.

## 4.2 Monometallic Zirconia Supported Catalysts

### 4.2.1 Ni-ZrO<sub>2</sub>

Ni supported on ZrO<sub>2</sub> was studied by Transmission Electron Microscopy (TEM) both after reduction at 673 K and after reduction at 873 K.

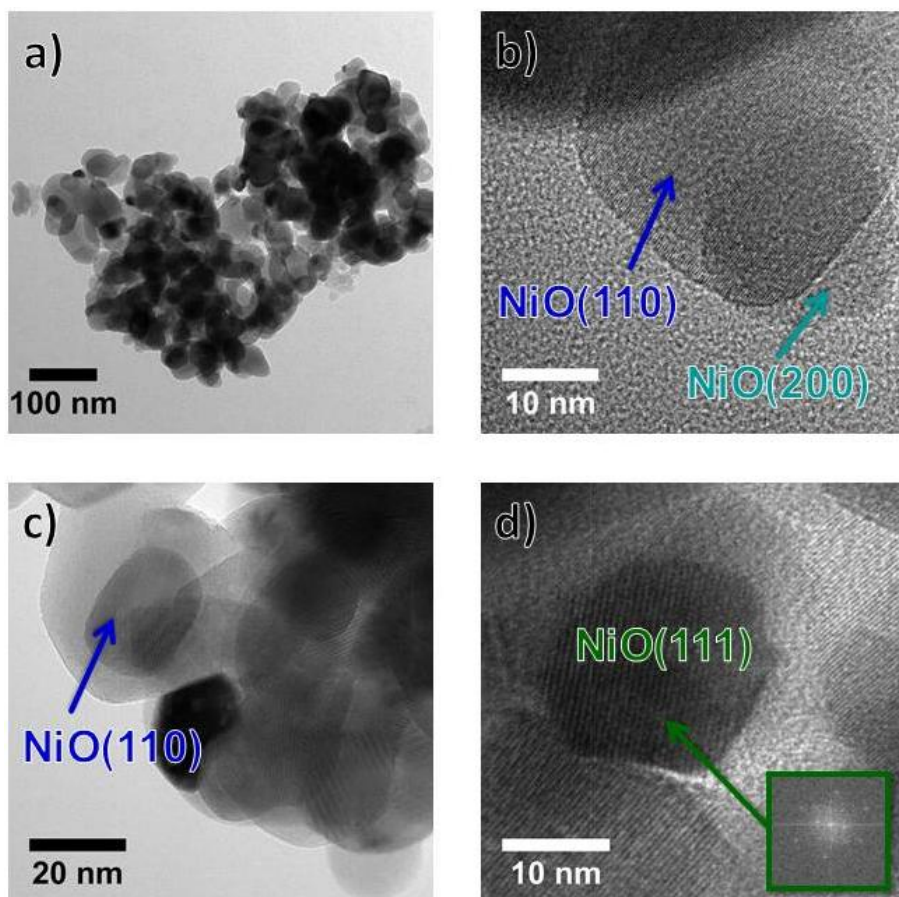


Fig. 13. TEM micrographs of Ni-ZrO<sub>2</sub> after *ex-situ* reduction at 673 K.

TEM micrographs of Ni-ZrO<sub>2</sub> after oxidation at 773 K followed by reduction at 673 K are shown in Fig. 13. After the pretreatment the samples were exposed to air for the sample preparation for TEM and therefore, Ni is not expected to remain in the metallic state due to re-oxidation. In Fig. 13 a) an overview of agglomerates of nickel oxide supported on zirconia is shown. The larger particles, which are assigned to the support have a diameter of about 50-100 nm. The Ni particles cannot be identified in this magnification due to the low Z-contrast between zirconia and nickel oxide. For identification and localisation of the nickel particles EDX was applied. At higher magnification, as shown in Fig. 13 b)-d) the lattice constants were measured and zirconia and nickel oxide particles were assigned due to the known lattice parameters of cubic NiO and monoclinic ZrO<sub>2</sub>. In Fig. 13 b) two nickel particles

with approximately 30 and 20 nm in diameter, respectively, are shown. The orientation on the larger particle is NiO(110) and that on the smaller one is NiO(200). On Fig. 13 c) several catalyst particles are monitored. The arrow directs to a 20 nm particle with NiO(110) orientation on or under a m-ZrO<sub>2</sub>(110) particle. In Fig. 13 d) a NiO(111) particle of polyhedral shape with a diameter of about 20 nm on or under monoclinic ZrO<sub>2</sub>(100) is shown.

In general, the NiO particles are evenly distributed on the support and the size of these particles ranges from about 10 up to 30 nm while the majority of the identified Ni particles had a diameter of about 20 nm. The accessible metallic Ni surface area of Ni-ZrO<sub>2</sub> after reduction at 673 K determined by H<sub>2</sub>-Chemisorption was 31.40 m<sup>2</sup>/g. That gives a calculated Ni particle size of 21.5 nm (implying spherical Ni particles) what is in good agreement with the particle size found by TEM.

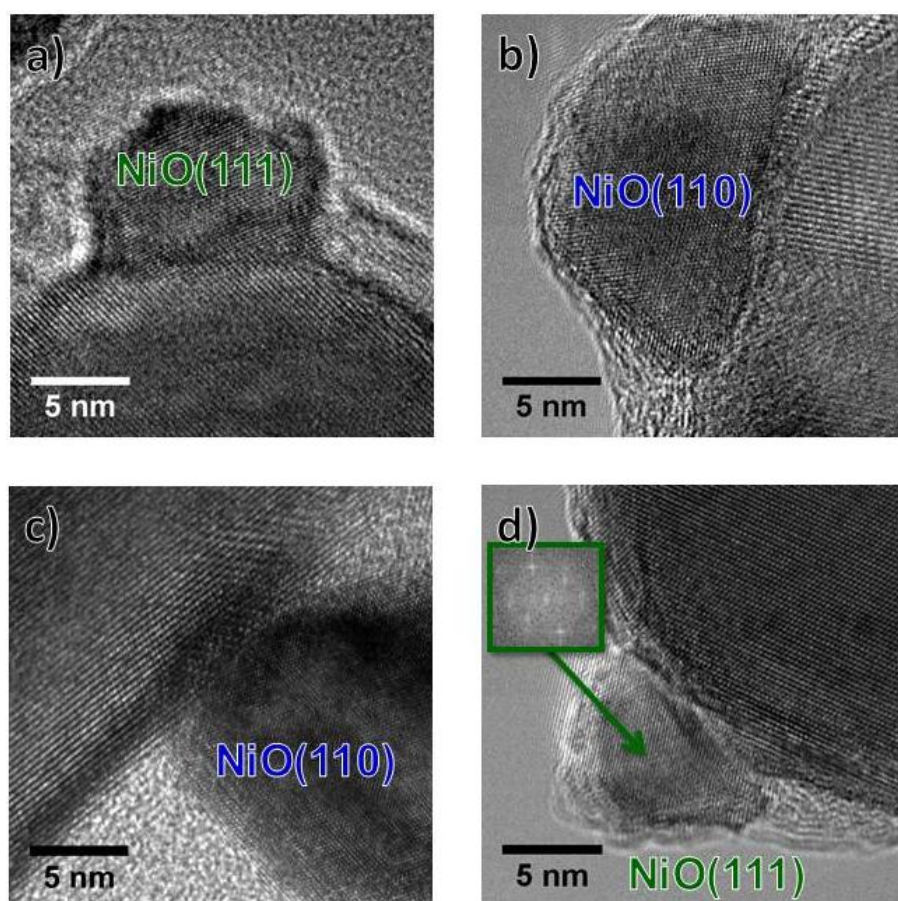


Fig. 14. TEM micrographs of Ni-ZrO<sub>2</sub> after *ex-situ* reduction at 873 K.

High resolution TEM micrographs of Ni-ZrO<sub>2</sub> after oxidation at 773 K followed by reduction at 873 K, which was the pretreatment of the samples used for MDR, are shown in Fig. 14. The particle shown in Fig. 14 a) has NiO(111) orientation and sits on m-ZrO<sub>2</sub>(002) or (020). In Fig. 14 b) it is NiO(110) on m-ZrO<sub>2</sub>(110), in c) NiO(110) on m-ZrO<sub>2</sub>(111) and in d) NiO(111) on m-ZrO<sub>2</sub>(111). In TEM, no indication for Ni particle growth after reduction at 873 K compared to the sample reduced at 673 K was found.

Infrared spectra of room temperature CO adsorption on oxidized Ni-ZrO<sub>2</sub> are shown in Fig. 15. According to literature data<sup>[8, 9, 133-135]</sup> adsorption of CO on ZrO<sub>2</sub> results in a band at about 2190 cm<sup>-1</sup>. Ni in different oxidation states can be distinguished by the vibration frequencies of adsorbed CO. Bands ascribed to Ni<sup>n+</sup>-CO surface complexes cover a broad spectral range including, besides linear monocarbonyls, also bridged, di- and tricarbonyl species. Ni<sup>2+</sup>-CO produces a weak band at around 2150-2180 cm<sup>-1</sup><sup>[8, 134, 136-138]</sup>. CO forms stable monocarbonyls with Ni<sup>+</sup> (2160-2100 cm<sup>-1</sup>)<sup>[139-142]</sup>, which may be converted into dicarbonyls ( $\nu_s(\text{CO})$ ) at 2131-2145 and  $\nu_{as}(\text{CO})$  at 2100-2083 cm<sup>-1</sup><sup>[139, 141-143]</sup> with increasing CO pressure. The stretching vibrations of Ni<sup>+</sup>(CO)<sub>3</sub> are expected at about 2156, 2124 and 2109 cm<sup>-1</sup><sup>[139]</sup>. Linear carbonyls of metallic nickel appear at 2050-2094 cm<sup>-1</sup><sup>[136, 142-148]</sup> and bridged carbonyls are visible below 1960 cm<sup>-1</sup><sup>[136, 144, 148]</sup>.

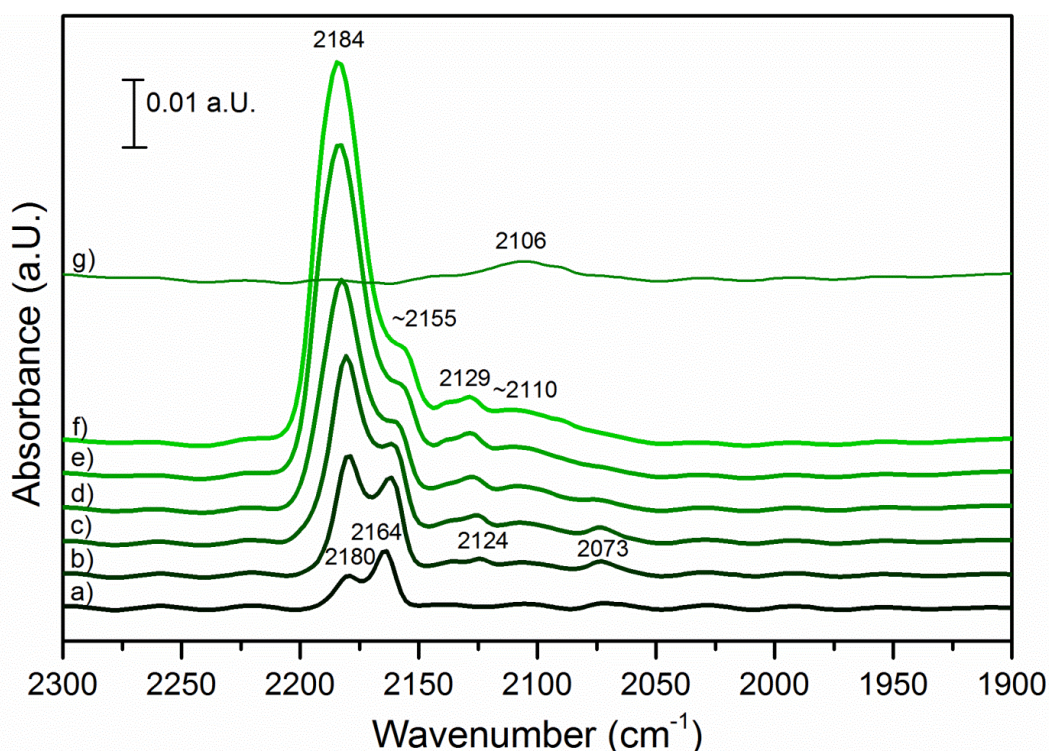


Fig. 15. IR Spectra of CO on Ni-ZrO<sub>2</sub>, oxidized in 100 mbar O<sub>2</sub> at 773 K, in a) 0.005, b) 0.2, c) 0.5, d) 1.0, e) 3.0, f) 5.0 mbar CO pressure and g) after evacuation. Published in<sup>[1]</sup>.

Fig. 15 displays spectra obtained in different CO background pressures to deduce additional information from changes with increasing CO coverage. At 0.05 mbar CO pressure two bands are visible: The Zr<sup>4+</sup>-CO interaction at 2180 cm<sup>-1</sup> and the Ni<sup>2+</sup>-CO interaction at 2164 cm<sup>-1</sup>. At 0.2 mbar besides these two bands, absorption peaks at 2124 and at 2073 cm<sup>-1</sup> can be observed. Those bands are attributed to the symmetric and antisymmetric CO stretching vibrations of Ni<sup>+</sup>(CO)<sub>2</sub>. With increasing pressure the low frequency band shifts to higher wavenumber and disappears. The three bands at about 2155, 2129 and 2110 cm<sup>-1</sup> are attributed to Ni<sup>+</sup>(CO)<sub>3</sub>. The band of the Ni<sup>2+</sup>-CO interaction is covered by the 2115 cm<sup>-1</sup>-band of Ni<sup>+</sup>(CO)<sub>3</sub> and the Zr<sup>4+</sup>-CO interaction, which increased strongly with increasing CO pressure and shifted to 2184 cm<sup>-1</sup>. After evacuation only one band at 2106 cm<sup>-1</sup> remains. This

band is attributed to Ni<sup>+</sup>-CO, which is known to be stable against evacuation<sup>[139, 141-143]</sup>. In summary, various CO on Ni<sup>2+</sup> and Ni<sup>+</sup> adsorption complexes can be observed in the spectra.

FTIR spectra of CO adsorption at various pressures obtained after reduction of Ni-ZrO<sub>2</sub> at 673 K are shown in Fig. 16. Like on the oxidized sample, a Ni<sup>2+</sup>-CO peak at 2164 cm<sup>-1</sup> and a Zr<sup>4+</sup>-CO peak at 2180 cm<sup>-1</sup> are observed at 0.05 mbar CO pressure. With increasing CO pressure, the Zr<sup>4+</sup>-CO peak grows and covers the Ni<sup>2+</sup>-CO peak.

The band at 2075 cm<sup>-1</sup> appearing in 0.05 mbar CO is attributed to linearly adsorbed CO on Ni<sup>0</sup>, while the band at 1946 cm<sup>-1</sup>, which starts to show up at 0.2 mbar, is attributed to bridge-bonded CO on Ni<sup>0</sup>. This band blue-shifts with increasing CO pressure. The vibration at 2116 cm<sup>-1</sup> shifting to 2125 cm<sup>-1</sup> with increasing pressure is attributed to Ni<sup>+</sup>-CO. The unusual oxidation state Ni<sup>+</sup> can be stabilized by the ligand CO<sup>[141]</sup>. After evacuation Ni<sup>+</sup>-CO as well as linear and bridged CO on Ni<sup>0</sup> remain on the surface. Overall, CO adsorption indicates that both reduced and oxidized Ni species are present on the surface. In agreement with the XAS measurements presented in<sup>[1]</sup>, NiO reduction is not complete at 673 K.

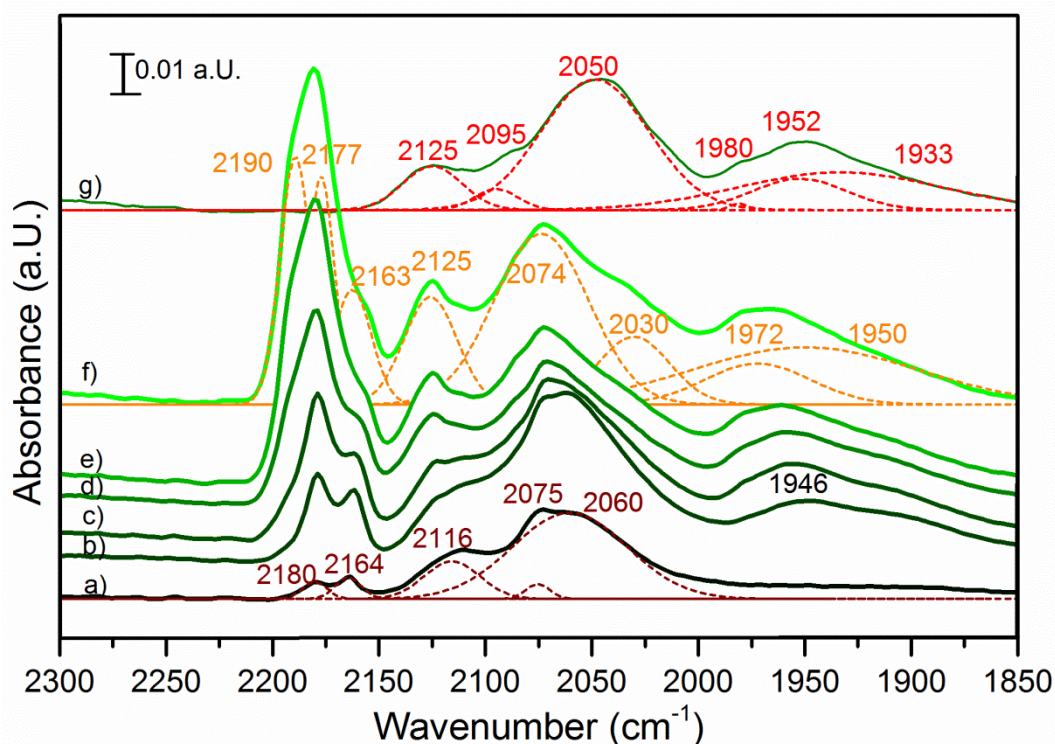


Fig. 16. IR Spectra of CO on Ni-ZrO<sub>2</sub>, reduced in 5 mbar H<sub>2</sub> at 673 K, in a) 0.005, b) 0.2, c) 0.5, d) 1.0, e) 3.0, f) 5.0 mbar CO pressure and g) after evacuation. Published in<sup>[1]</sup>.

#### 4.2.2 Cu-ZrO<sub>2</sub>

Cu-ZrO<sub>2</sub> was mainly used as a reference when comparing the bimetallic catalysts with Ni-ZrO<sub>2</sub> in order to get insights of the contribution of Cu to the CuNi-ZrO<sub>2</sub> catalyst's properties and to clarify if Cu-ZrO<sub>2</sub> showed any activity for the explored catalytic reactions.

TEM images of Cu-ZrO<sub>2</sub> after *ex-situ* pretreatment are shown in Fig. 17. The size of the Cu or CuO particles which were identified via EDX is between 5-10 nm and all these particles are spherical.

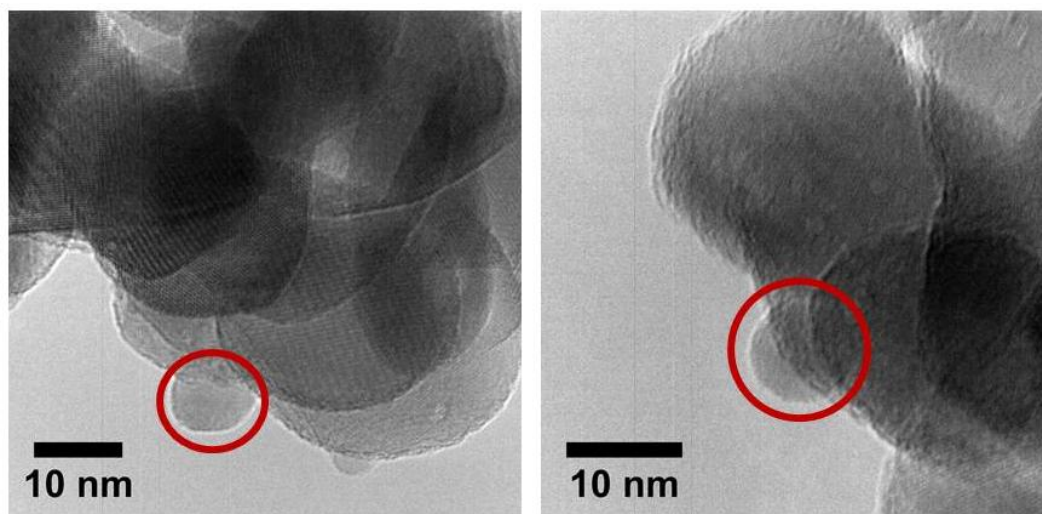


Fig. 17. TEM micrographs of Cu-ZrO<sub>2</sub> after *ex-situ* reduction at 673 K. The Cu particles identified by EDX are marked with a cycle.

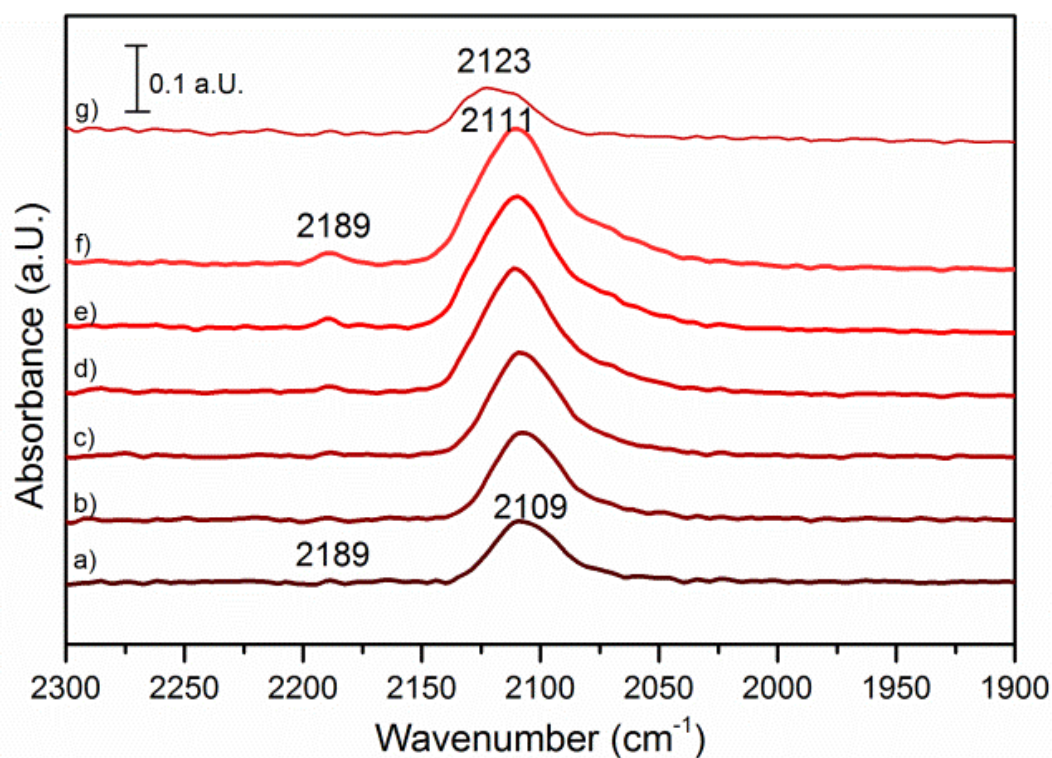


Fig. 18. IR Spectra of CO on Cu-Zr, reduced in 5 mbar H<sub>2</sub> at 673 K, in a) 0.005, b) 0.2, c) 0.5, d) 1.0, e) 3.0, f) 5.0 mbar CO pressure and g) after evacuation.

IR spectra of CO on reduced Cu-ZrO<sub>2</sub>, which are displayed in Fig. 18, show besides the Zr<sup>4+</sup>-CO interaction only one peak at around 2110 cm<sup>-1</sup>. As it shifts to 2123 cm<sup>-1</sup> after evacuation it

is expected to contain both  $\text{Cu}^0\text{-CO}$  and  $\text{Cu}^+\text{-CO}$  bands, while after evacuation only the more stable  $\text{Cu}^+\text{-CO}$  complex remains.

### 4.3 Bimetallic CuNi Catalysts

Zirconia supported bimetallic CuNi catalysts were characterized via several methods and tested for catalytic partial oxidation and methane decomposition. The major issue was to study the formation and stability of an CuNi alloy and the influence of Ni alloy formation on the catalytic performance and stability against coke formation during methane decomposition.

#### 4.3.1 *In situ* X-ray Absorption During Reduction

In order to determine the oxidation state of the analysed copper and nickel containing samples, Ni K edge XANES and Cu K $\alpha$  HERFD-XAS spectra were recorded. NiO and Ni foil as well as CuO, Cu<sub>2</sub>O and Cu foil were analysed and served as reference spectra. The spectra obtained on the catalysts during reduction were fitted by a linear combination of these reference spectra to estimate the fraction of atoms in the respective oxidation states.

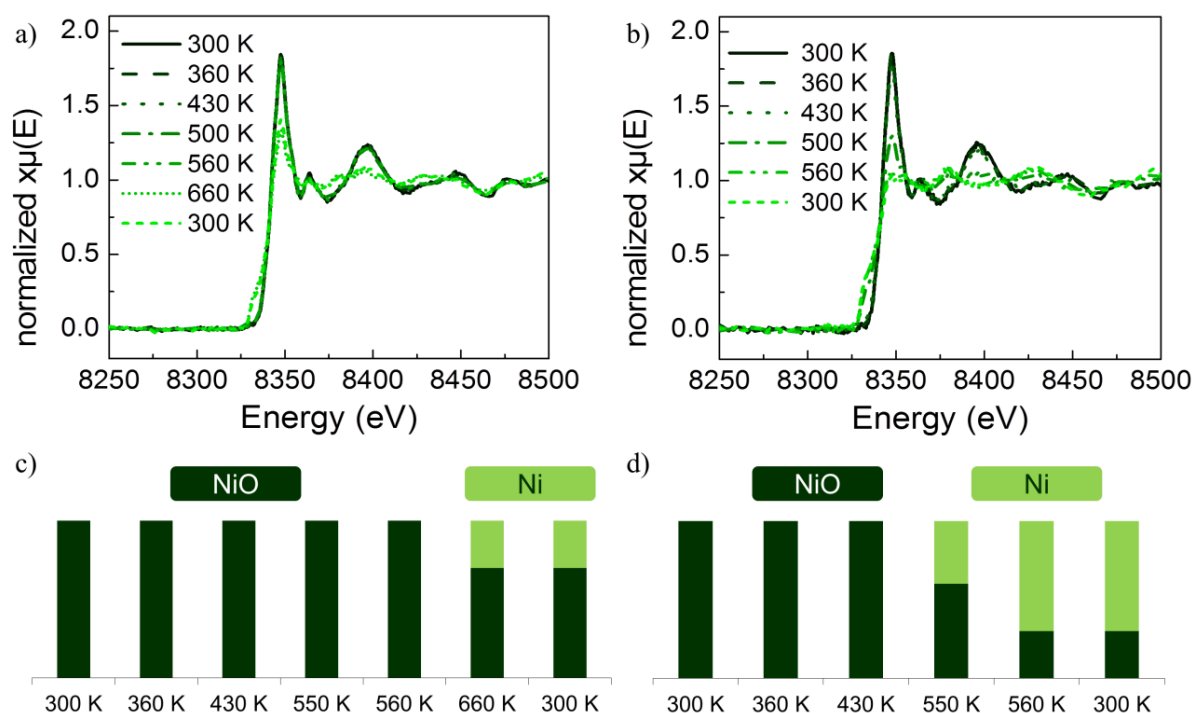


Fig. 19. XANES spectra at the Ni K edge of a) Ni-ZrO<sub>2</sub> and b) 11CuNi-ZrO<sub>2</sub> during reduction in 5% hydrogen in helium and amount of reduced versus oxidized nickel calculated by linear combination of reference spectra for c) Ni-ZrO<sub>2</sub> and d) 11CuNi-ZrO<sub>2</sub>. Published in<sup>[1]</sup>.

Fig. 19 shows XANES spectra in H<sub>2</sub>/He at different temperatures during reduction. Both the Ni in Ni-ZrO<sub>2</sub> and in 11CuNi-ZrO<sub>2</sub> is completely oxidized until 430 K. On Ni-ZrO<sub>2</sub> nickel reduction starts at 660 K and the linear combination analysis indicates about 30 % of nickel

atoms in the reduced (metallic) state. On the bimetallic catalyst 11CuNi-ZrO<sub>2</sub> reduction already sets in at 500 K. The amount of reduced nickel increases from 40 % at 500 K to 70 % at 560 K. This indicates that an alloy between Cu and Ni has formed under these conditions and Cu causes a decrease of the reduction temperature of Ni.

Considering Cu-ZrO<sub>2</sub> and CuNi-ZrO<sub>2</sub>, a similar effect of lowering the reduction temperature of Cu was found as shown in Fig. 20. Up to 360 K copper was completely in the +II oxidation state in both mono- and bimetallic samples. After reduction at 430 K about 10 % of the monometallic copper was reduced to Cu(I)oxide while on the bimetallic sample 10 % were already reduced to Cu<sup>0</sup>, 40 % were in +I and 50 % in +II oxidation state. After reduction at 550 K the amount of Cu(I)oxide increased to 30 % in the monometallic sample, whereas 50 % Cu<sup>0</sup>, 20 % Cu<sub>2</sub>O and 30 % CuO were present in the bimetallic sample. Finally, after reduction at 660 K both catalysts were reduced to the same extent with 50 % Cu<sup>0</sup>. The observation that the presence of copper improves the reducibility of nickel and lowers its reduction temperature is in agreement with TPR experiments reported in literature<sup>[45, 48, 94, 149-151]</sup>.

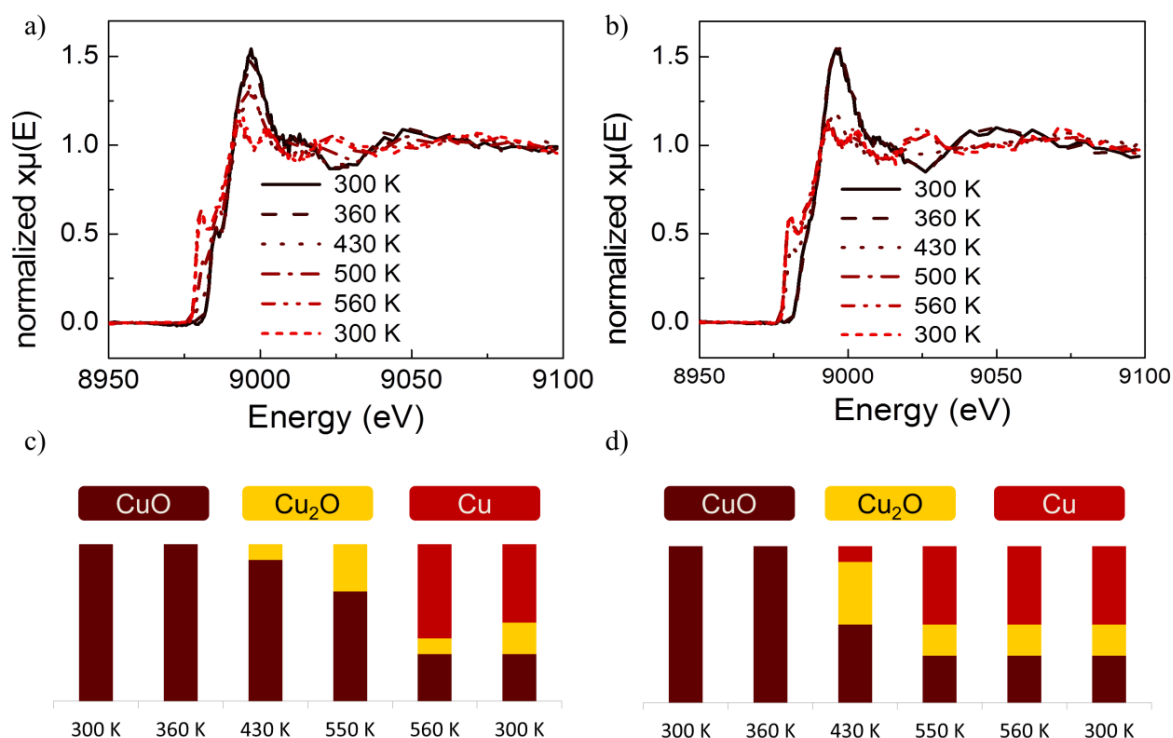


Fig. 20. HERFD-XAS spectra at the Cu K $\alpha$  edge of a) Cu-ZrO<sub>2</sub> and b) 11CuNi-ZrO<sub>2</sub> during reduction in 5% hydrogen in helium and amount of reduced versus oxidized copper calculated by linear combination of reference spectra for c) Cu-ZrO<sub>2</sub> and d) CuNi-ZrO<sub>2</sub>. Published in<sup>[1]</sup>.

### 4.3.2 Transmission Electron Microscopy

Fig. 21 shows transmission electron micrographs of 11CuNi-ZrO<sub>2</sub> after ex situ reduction. In contrast to Ni-ZrO<sub>2</sub> and Cu-ZrO<sub>2</sub>, the metal particles on the bimetallic 11CuNi-ZrO<sub>2</sub> with average sizes around 20 nm are polycrystalline and rather irregular in shape. EDX spectra showed that those particles contained both Cu and Ni, though not in the expected 1:1 ratio

but they were enriched in nickel. To get a better understanding of the Cu and Ni distribution on the bimetallic catalyst, elemental maps were recorded. The results are displayed in Fig. 22.

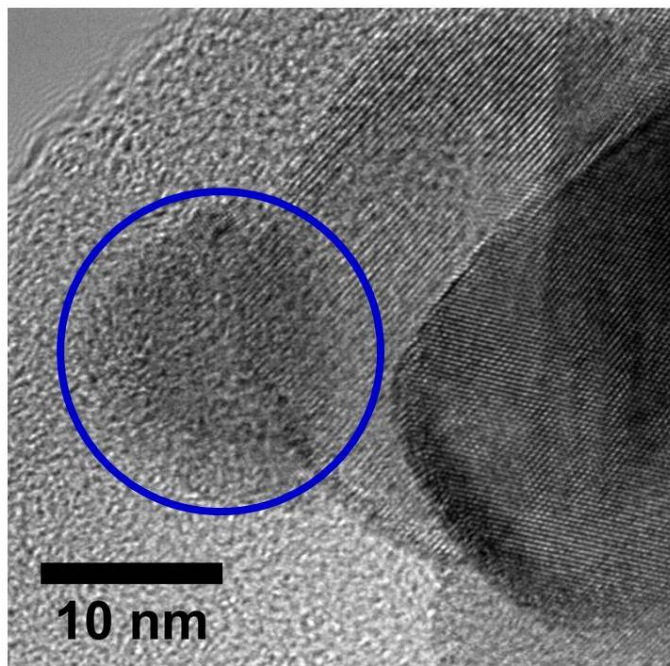


Fig. 21. TEM image of 11CuNi-ZrO<sub>2</sub>. The particle inside the circle was identified via EDX as Cu- and Ni-containing. Published in<sup>[2]</sup>.

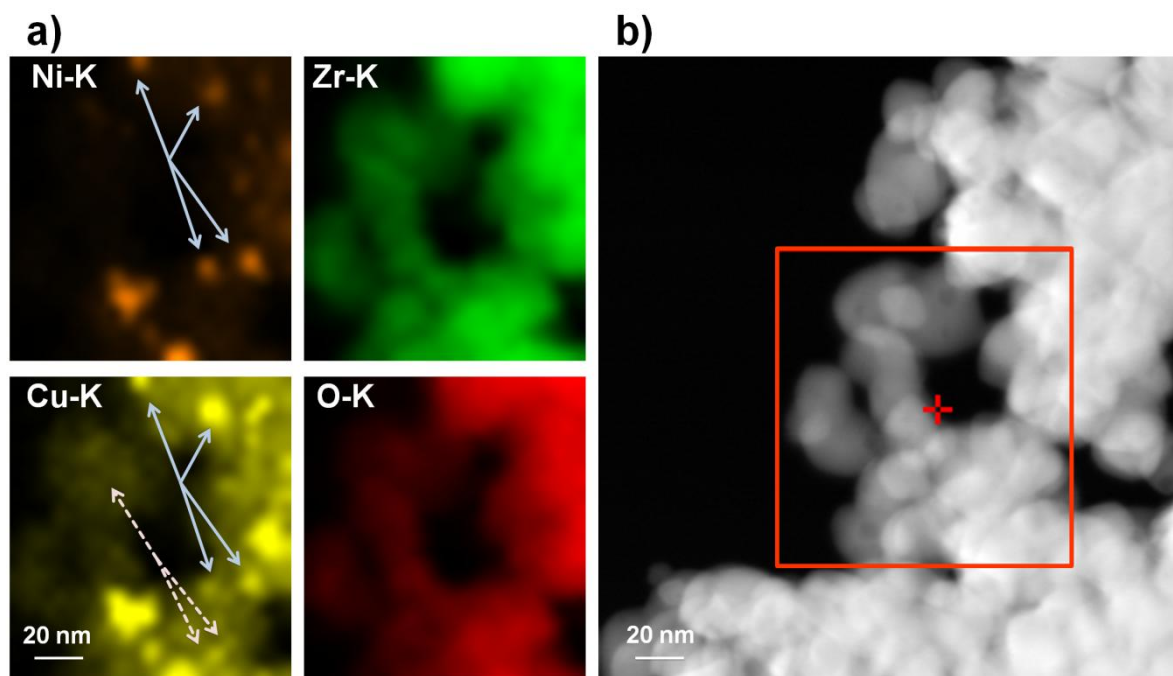


Fig. 22. a) Elemental map of the region shown in the rectangle in b) for the K edge energies of Ni, Cu, Zr and O recorded on 11CuNi-ZrO<sub>2</sub>. Full arrows: particles containing both Ni and Cu, dashed arrows: Cu but no Ni detected. Published in<sup>[2]</sup>.

While Ni was always accompanied by the simultaneous presence of Cu as demonstrated with full arrows in Fig. 22, Cu was additionally found finely distributed in regions where no

or hardly any nickel was detected (dashed arrows in Fig. 22). Thus, the elemental maps revealed the presence of Ni-rich bimetallic particles as well as monometallic Cu particles.

### 4.3.3 X-Ray Diffraction

Diffraction patterns of the samples 13CuNi-ZrO<sub>2</sub> and 13CuNi-ZrO<sub>2</sub>50 both after calcination and after ex-situ reduction at 673 K and pure ZrO<sub>2</sub> support are shown in Fig. 23. All show monoclinic ZrO<sub>2</sub> reflections.

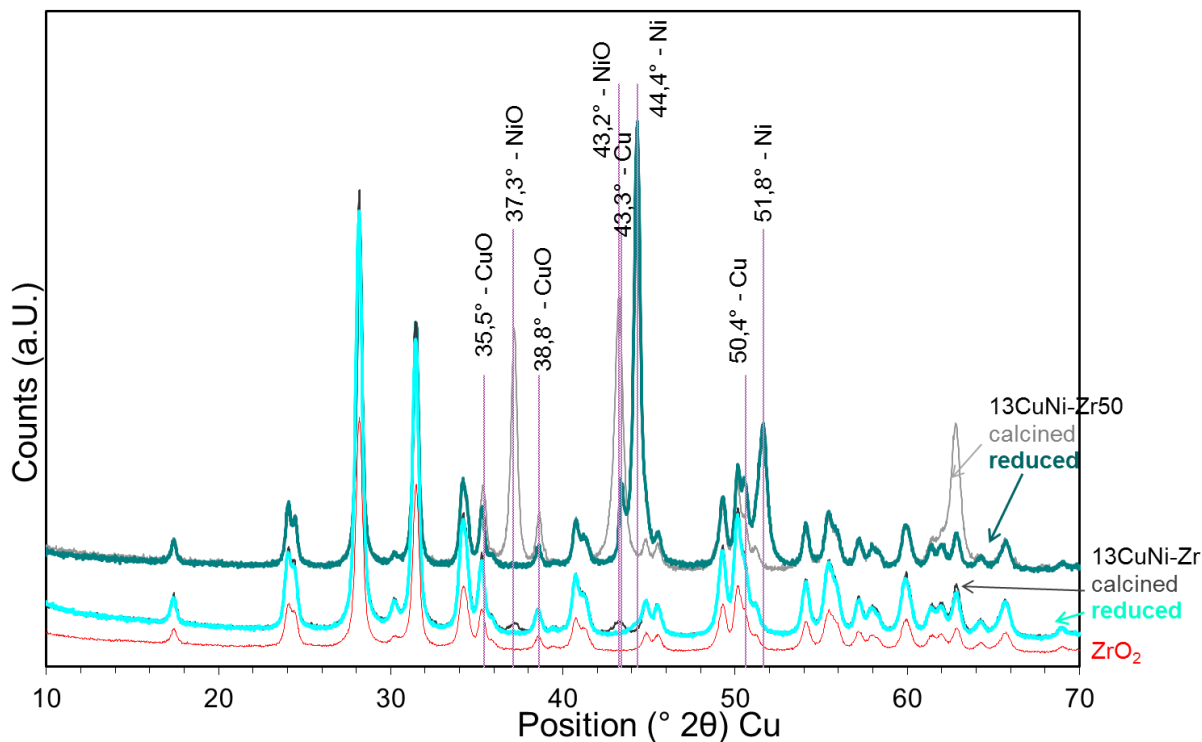


Fig. 23, XRD patterns of ZrO<sub>2</sub>, 13CuNi-Zr and 13 CuNi-Zr50

Bulk CuO has reflections very close to those of monoclinic ZrO<sub>2</sub> at 35.5 ° and 38.8°. These reflections lose intensity after reduction. The intensity of the characteristic reflections of NiO at 37.7° and 43.2° nearly vanish completely after reduction of both 13CuNi-ZrO<sub>2</sub> and 13CuNi-Zr O<sub>2</sub>50. Since we don't expect complete reduction of nickel of these catalysts under these conditions<sup>[1]</sup> we expect only small or amorphous NiO crystallites after reduction at 673 K. The reflections at 44.4° and 51.8° appearing after reduction are attributed to metallic Ni and shoulders at 43.3° and 50.4° are attributed to metallic Cu. An assignment of alloyed CuNi crystallites as found for silica supported CuNi elsewhere<sup>[152]</sup> was not possible because of the overlap with reflections of monoclinic zirconia.

### 4.3.4 *In situ* FTIR Studies

Infrared spectra of room temperature CO adsorption on the zirconia supported CuNi samples after oxidation at 773 K were published in<sup>[1]</sup>. On the bimetallic catalysts an

absorption band of strongly adsorbed CO appears at around  $2120\text{ cm}^{-1}$  like on the monometallic copper catalyst. It is attributed to  $\text{Cu}^+\text{-CO}$ , which is the strongest interaction of CO with Cu species. The  $\text{Cu}^+\text{-CO}$  band was reported in literature at around  $2120\text{-}2143\text{ cm}^{-1}$ <sup>[130, 153, 154]</sup>. It is much stronger than  $\text{Cu}^0\text{-CO}$  appearing below  $2110\text{ cm}^{-1}$ <sup>[130, 153-155]</sup> and  $\text{Cu}^{2+}\text{-CO}$  at around  $2170\text{-}2175\text{ cm}^{-1}$ <sup>[130]</sup>. On the bimetallic samples this peak appears broader indicating an interaction of copper with neighbouring nickel atoms. The broader peaks suggest that there is a distribution of Cu(I) sites with slightly different electronic properties or chemical environment on the surface. In <sup>[1]</sup> zirconia supported CuNi samples were additionally compared with CuNi samples supported on the ceria-zirconia support prepared by impregnation of cerium nitrate on zirconia. Since only little differences of these bimetallic catalysts on slightly different support materials were observed, they are only very briefly discussed in this thesis.

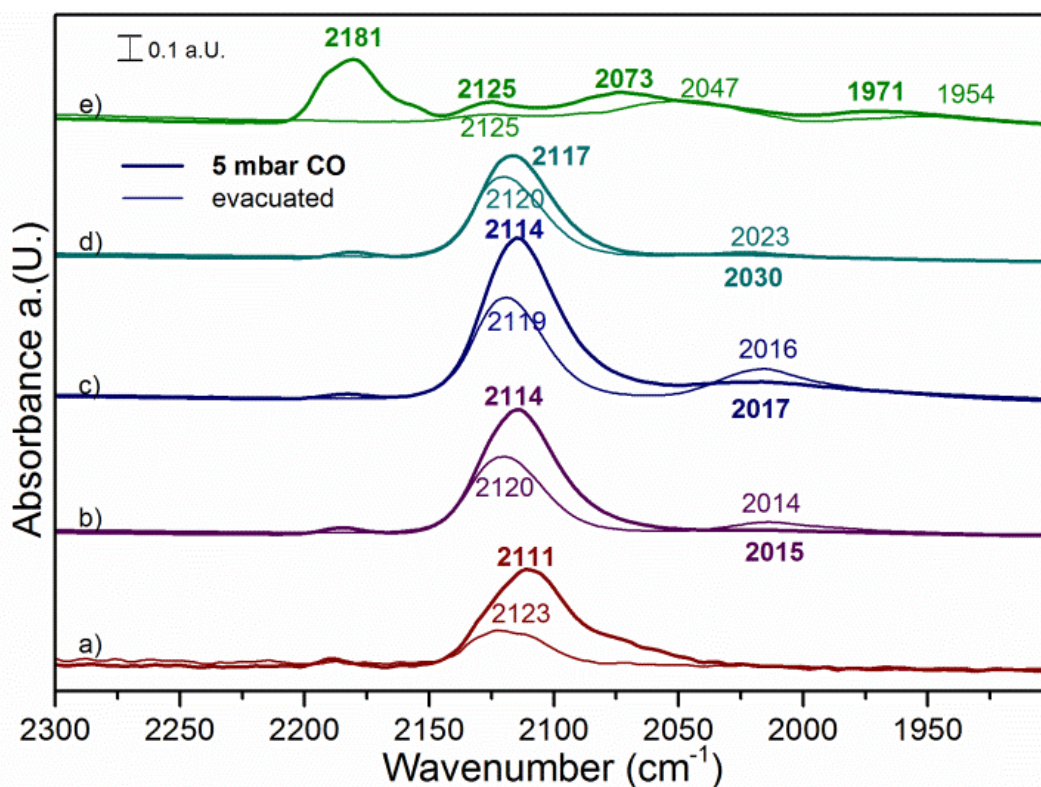


Fig. 24. Infrared carbonyl spectra of reduced catalysts under 5 mbar CO pressure and after evacuation of CO: a)  $\text{Cu-ZrO}_2$ , b)  $31\text{CuNi-ZrO}_2$ , c)  $11\text{CuNi-ZrO}_2$ , d)  $13\text{CuNi-ZrO}_2$  and e)  $\text{Ni-ZrO}_2$ . Published in<sup>[1]</sup>.

Infrared spectra of room temperature CO adsorption on reduced samples are shown in Fig. 24. Compared to the spectra of CO on oxidized samples, new bands have appeared. However, bands of CO on oxidized Cu and Ni species, which already existed on the oxidized samples are still present indicating incomplete reduction of surface Cu and Ni.

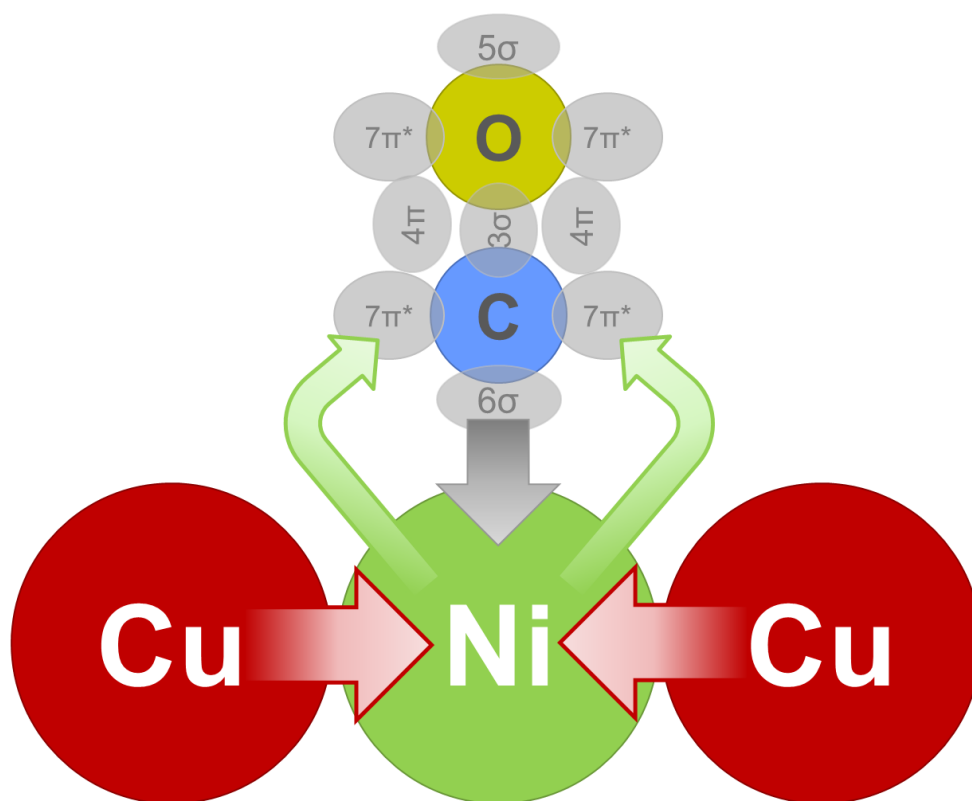


Fig. 25. Schematic illustration of CO adsorption on CuNi alloys. Donation of d-electrons from copper to nickel leads to reinforcement of the  $\pi$ -backbonding from nickel to antibonding  $7\pi^*$  orbitals of CO. This leads to a weaker C–O bond and a red-shift of the CO stretch vibration band in infrared spectra. Published in<sup>[1]</sup>.

Upon Cu addition to Ni catalysts the  $\text{Ni}^0\text{-CO}$  peak, which appears at about  $2070\text{ cm}^{-1}$  in 5 mbar CO and at about  $2050\text{ cm}^{-1}$  upon evacuation of gas phase CO on Ni-ZrO<sub>2</sub> (shown in Fig. 16), red-shifts by approximately 50 to 70  $\text{cm}^{-1}$  on the bimetallic samples to 2012–2023  $\text{cm}^{-1}$ . According to Blyholder's scheme<sup>[148]</sup>, the CO stretching vibration is predicted to shift from pure Ni as compared to Ni-Cu, because metallic Cu is expected to donate electrons to Ni. This should increase back-donation into the  $\pi^*$  orbitals of CO with consequently lowering of the CO stretching frequency. Simultaneously, the electron donation reinforces the bond between CO and Ni. This is illustrated in Fig. 25. Compared to pure Ni, the CO bands on CuNi alloy were reported to shift to lower frequencies by about  $40\text{ cm}^{-1}$ <sup>[148, 156]</sup>. Dalmon et al.<sup>[144]</sup> observed the band of irreversibly adsorbed Ni-CO at  $2058\text{ cm}^{-1}$  on monometallic nickel, at  $2028\text{ cm}^{-1}$  on a 36.6 % and at  $2005\text{ cm}^{-1}$  on a 72 % copper containing alloy, in good agreement with the present work. The fact that there is no shift of the Cu<sup>+</sup>-CO vibration with composition indicates that Ni is interacting with Cu<sup>0</sup>, but not with Cu<sup>+</sup>.

CO adsorption spectra were again recorded in different CO pressures to obtain information on coverage dependence of CO bands/species, as on the monometallic Ni-ZrO<sub>2</sub> catalyst. The band positions of the CO stretching vibrations on the bimetallic catalysts are summarized in Table 2. Beside the red-shift of CO on Ni<sup>0</sup> by 50–70  $\text{cm}^{-1}$  with increasing Cu content, as

described above, a blue-shift of 7-26  $\text{cm}^{-1}$  with increasing CO coverage is observed. The vibration frequency of CO on the alloyed  $\text{Ni}^0$  blue-shifts by 7  $\text{cm}^{-1}$  on copper-rich and up to 34  $\text{cm}^{-1}$  on nickel-rich alloys with increasing CO coverage. After evacuation the CO vibration frequency is observed in between 2012 and 2023  $\text{cm}^{-1}$  on all samples. The stretching frequency of CO on  $\text{Cu}^+$  stays at about 2110-2120  $\text{cm}^{-1}$  on all zirconia based catalysts and seems only little pressure dependent.

**Table 2.** CO stretching vibration on bimetallic CuNi-ZrO<sub>2</sub> samples at different CO pressures. Published in<sup>[1]</sup>.

Sample	CO pressure (mbar)	CO on Cu/Cu <sup>+</sup> ( $\text{cm}^{-1}$ )	CO on Ni ( $\text{cm}^{-1}$ )
<b>31CuNi-Zr</b>	0.05	2110	-
	0.2	2110	2001
	0.5	2111	2011
	1	2113	2016
	3	2113	2018
	5	2114	2015
	evacuated to $< 10^{-5}$	2120	2014
	<b>11CuNi-Zr</b>	0.05	2110
0.2		2110	2000
0.5		2110	2007
1		2113	2014
3		2114	2018
5		2114	2017
evacuated to $< 10^{-5}$		2119	2016
<b>13CuNi-Zr</b>		0.05	2111
	0.2	2111	2004
	0.5	2112	2013
	1	2113	2021
	3	2116	2025
	5	2117	2030
	evacuated to $< 10^{-5}$	2120	2023

Clearly, in all samples the CO spectra are dominated by the signals of CO adsorbed on Cu. This implies a Cu enriched surface on the bimetallic samples. This is in agreement with H<sub>2</sub>-Chemisorption measurements published in <sup>[1]</sup>, showing that the metallic Ni surface area per gram of nickel of the bimetallic sample was significantly lower compared with Ni-ZrO<sub>2</sub> indicating that the surface of the bimetallic catalysts is enriched in Cu after reduction at 673 K. The enrichment of Cu on the surface of bimetallic CuNi particles is also in agreement with theoretic calculations by Neyman et al.<sup>[157]</sup> within an ongoing cooperation. The calculations show, that Cu atoms have a preference for surface positions following the order corner > edge > terraces and the surface of CuNi nanoparticles with Cu:Ni ratios 1:3, 1:1 and 3:1, respectively is always enriched in Cu.

In order to study the temperature stability of the adsorbed CO species on different samples it was followed by recording IR spectra during heating with a rate of 10 K/min in vacuum. CO

desorbed from Ni-ZrO<sub>2</sub> at about 450 K and from Cu-ZrO<sub>2</sub> at 410 K. On all bimetallic samples the desorption temperatures were higher, as shown for 13CuNi-ZrO<sub>2</sub>, 13CuNi-ZrO<sub>2</sub> and 13CuNi-ZrO<sub>2</sub> in Fig. 26, Fig. 27 and Fig. 28, respectively.

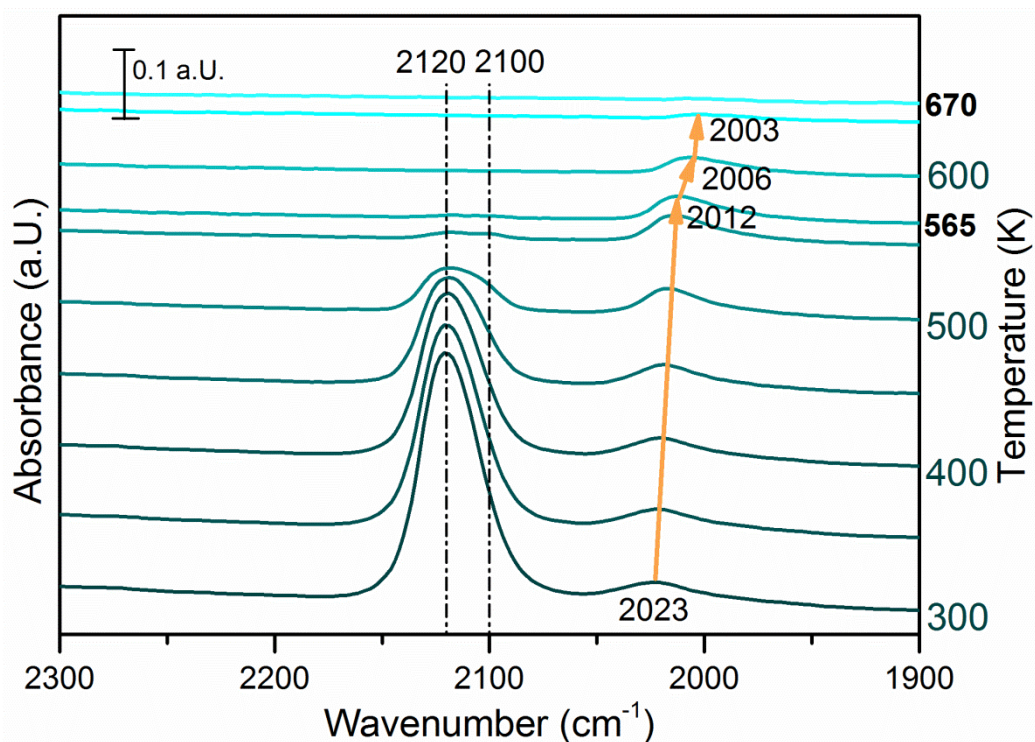


Fig. 26. Temperature programmed desorption of CO followed by FTIR spectroscopy on 13CuNi-ZrO<sub>2</sub>. Published in<sup>[1]</sup>.

With decreasing coverage the peak of CO adsorbed on copper species does not shift in frequency, but a second CO peak at about 2100 cm<sup>-1</sup> from Cu<sup>0</sup>-CO, which might be obscured by the Cu<sup>+</sup>-CO peak at about 2120 cm<sup>-1</sup> at room temperature due to the higher coverage, becomes visible with increasing temperature. On 13CuNi-ZrO<sub>2</sub> these two CO species are still present on the surface at 550 K, but disappear at about 565 K. On 11CuNi-ZrO<sub>2</sub> those peaks disappear between 540 and 550 K, and on 31CuNi-ZrO<sub>2</sub> they already vanish at about 450-460 K. Thus, with increasing copper content the CO desorption temperature is more similar to the monometallic copper sample. The usually unstable Cu-CO interaction seems to be reinforced by nickel.

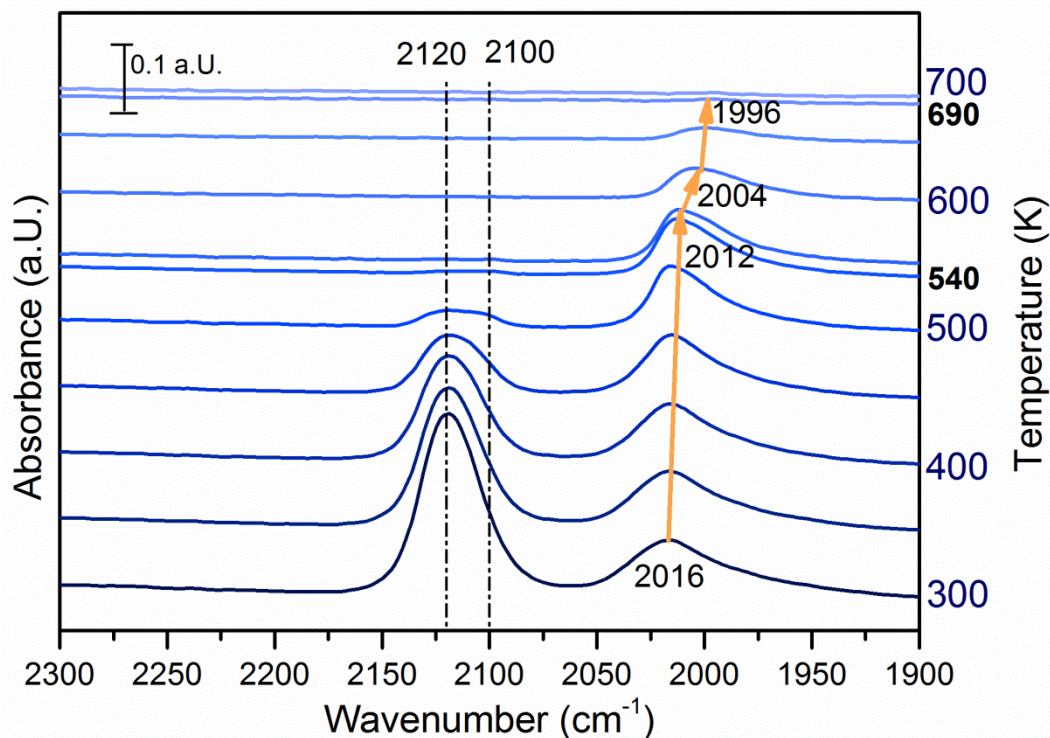


Fig. 27. Temperature programmed desorption of CO followed by FTIR spectroscopy on 11CuNi-ZrO<sub>2</sub>. Published in<sup>[1]</sup>.

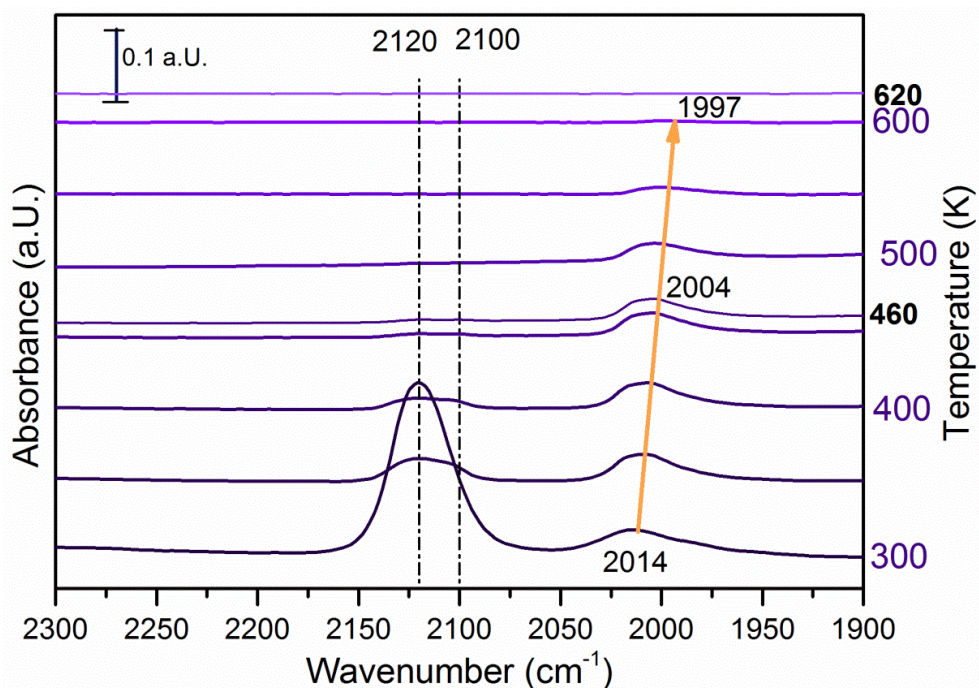


Fig. 28. Temperature programmed desorption of CO followed by FTIR spectroscopy on 31CuNi-ZrO<sub>2</sub>. Published in<sup>[1]</sup>.

To visualize the different CO desorption properties of alloyed and monometallic copper, difference quotients of the integrated peak areas of the copper peak between 2160 and 2080 cm<sup>-1</sup> are shown in Fig. 29. Most of the CO desorbs from Cu-ZrO<sub>2</sub> and the copper-rich

sample 31CuNi-ZrO<sub>2</sub> slightly above room temperature. Only a small amount of CO remains on the surface of Cu-ZrO<sub>2</sub> before desorbing at around 390 K. On the samples 11CuNi-ZrO<sub>2</sub> and 13CuNi-ZrO<sub>2</sub> most of the CO desorbs at 440 K and above, while on 31CuNi-ZrO<sub>2</sub> a small shoulder at 440 K can be observed. Beside the Cu-CO interaction of low temperature stability, which already vanishes after rising the temperature slightly above room temperature, a second Cu-CO species is observed starting to desorb at 440 K. This species might be attributed to CO on copper surrounded by nickel. As copper tends to donate d-electrons to nickel strengthening the interaction between CO and nickel<sup>[148]</sup>, the electron density in copper is reduced, which normally has its d-band completely filled. Less electrons in the d-band may reinforce the  $\sigma$ -bonding between CO and the metal and thus lead to a higher stability of this complex.

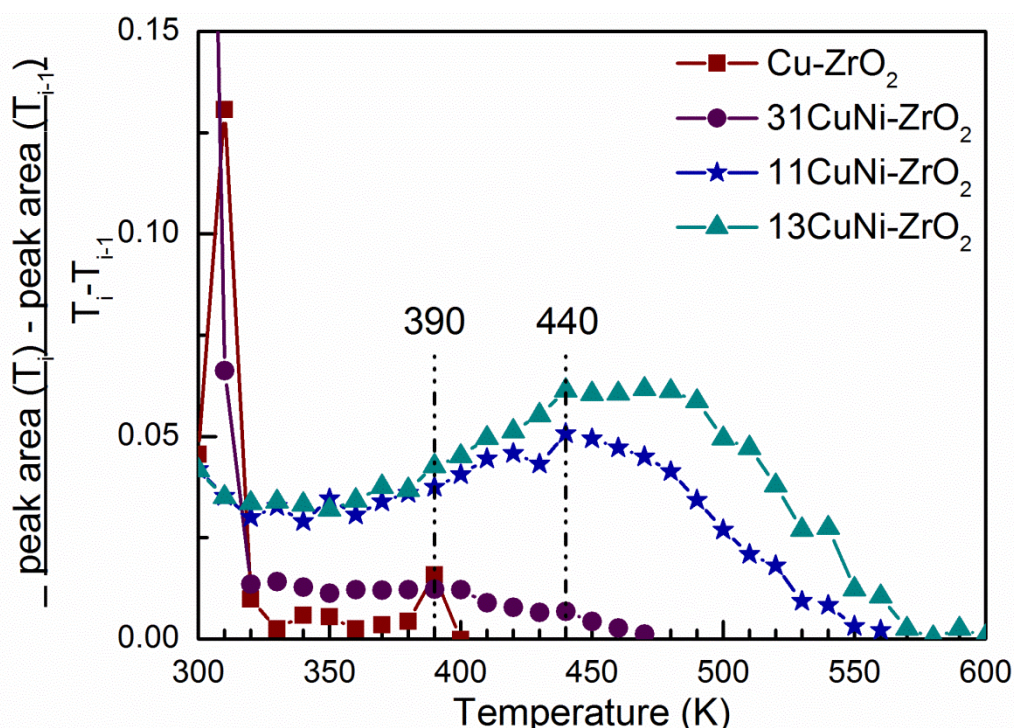


Fig. 29. Area change of the integrated Cu-CO peak area of Cu-ZrO<sub>2</sub>, 31CuNi-ZrO<sub>2</sub>, 11CuNi-ZrO<sub>2</sub> and 13CuNi-ZrO<sub>2</sub> with temperature. Published in<sup>[1]</sup>.

In parallel with the disappearance of the CO peak on copper, the CO peak on nickel shows a sudden shift to a lower wavenumber on 11CuNi-ZrO<sub>2</sub> and 13CuNi-ZrO<sub>2</sub>. This seems to be a coverage effect, as much CO desorbs from the catalyst at this stage. The Ni-CO peak completely disappears at about 670 K on 13CuNi-ZrO<sub>2</sub> and at about 700 K on 11CuNi-ZrO<sub>2</sub>. On 31CuNi-ZrO<sub>2</sub> the position of the Ni-CO band does not seem to be affected by the complete disappearance of the Cu-CO band, as only a small amount of CO is present and thus desorbs from 31CuNiZrO<sub>2</sub> at elevated temperatures. Furthermore, Ni-CO desorbs already around 620 K from this sample.

The total band shift of about  $20\text{ cm}^{-1}$  from room temperature to desorption temperature was also observed on Ni-ZrO<sub>2</sub> and is attributed to a coverage effect, probably accompanied by a temperature effect on the CO vibration frequency.

To sum up, CuNi alloy formation could be followed by FTIR spectroscopy with CO as a probe molecule. The shift of the Ni-CO vibration indicates a strong interaction between Cu and Ni. It could be shown that the adsorption strength of CO on Cu increases with decreasing copper content. The Ni-CO band shows the highest stability on the 11CuNi-ZrO<sub>2</sub> sample. On 31CuNi-ZrO<sub>2</sub> it is more stable than on Ni-ZrO<sub>2</sub>, but less stable than on the nickel-rich sample.

### 4.3.5 Partial Oxidation of Methane

The catalytic performance of the zirconia supported Cu, Ni and CuNi samples for partial oxidation of methane was investigated by temperature programmed reaction measurements. The MS detected methane during heating and cooling in CH<sub>4</sub> and O<sub>2</sub> is shown in Fig. 30 for the tested catalysts. The amount of methane was detected at  $m/z$  15, which is attributed to the CH<sub>3</sub> of methane since  $m/z$  16 includes both CH<sub>4</sub> and O, the fragment of O<sub>2</sub>. The full squares in Fig. 30 show the CH<sub>3</sub> signal during heating and the empty squares during cooling in the reaction mixture.

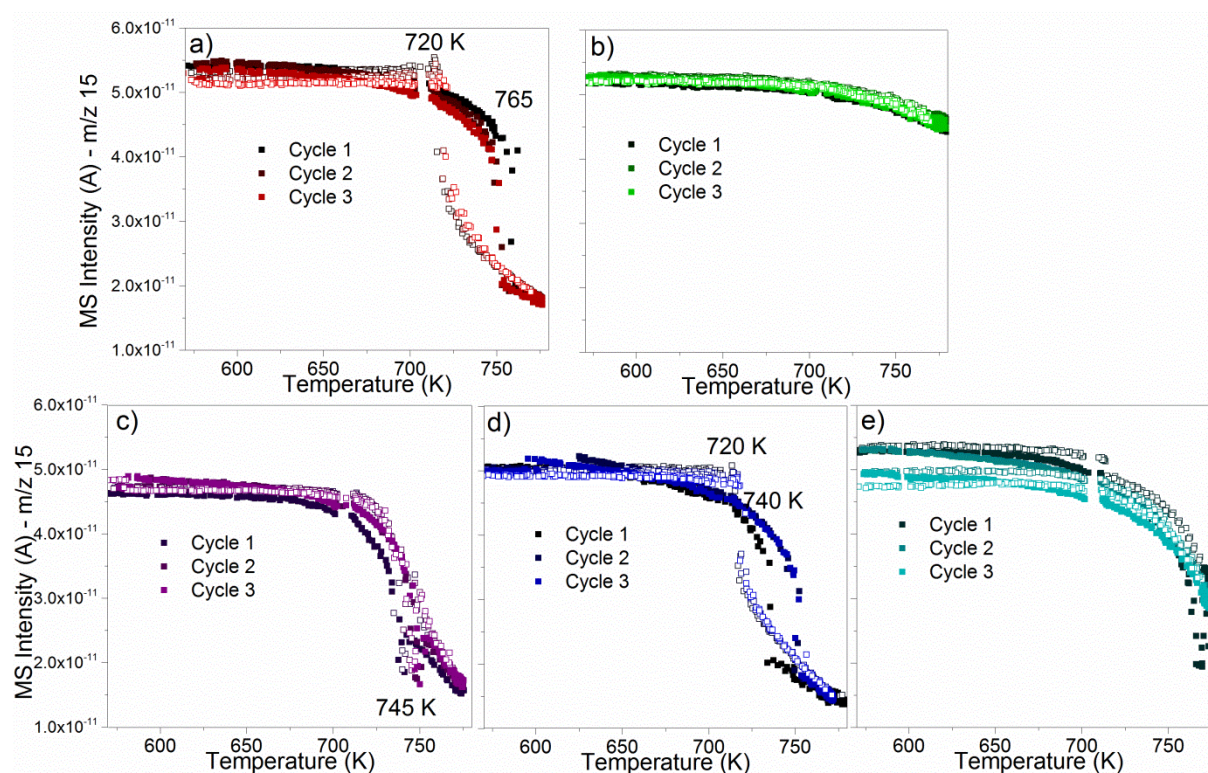


Fig. 30. Methane Conversion monitored by MS detection of CH<sub>3</sub> ( $m/z$  15) on a) Cu-ZrO<sub>2</sub>, b) Ni-ZrO<sub>2</sub>, c) 31CuNi-ZrO<sub>2</sub>, d) 11CuNi-ZrO<sub>2</sub> and e) 13CuNi-ZrO<sub>2</sub> during 3 heating-cooling cycles between 573 and 773, K in methane/oxygen/argon. The temperature was ramped with 5 K/min.

At 573 K no methane conversion as observed on any catalyst. On Cu-ZrO<sub>2</sub> methane conversion started about 765 K during the first heating cycle reaching a conversion of 70 % at 773 K. During cooling down the conversion of methane decreased and ended about 720 K. On 11CuNi-ZrO<sub>2</sub> and 31CuNi-ZrO<sub>2</sub> about the same behaviour is observed but conversion already sets in at 740-745 K. The methane conversion over Ni-ZrO<sub>2</sub> only reached about 15 % at 775 K. On the nickel-rich 13CuNi-ZrO<sub>2</sub> catalyst methane conversion was increased up to 50 % during the first heating cycle but already decreased during isothermal reaction at 773 K.

Regarding the products, over Cu-ZrO<sub>2</sub>, 11CuNi-ZrO<sub>2</sub> and 31CuNi-ZrO<sub>2</sub> mainly H<sub>2</sub>O and CO<sub>2</sub> were produced while on Ni-ZrO<sub>2</sub> and 13CuNi-ZrO<sub>2</sub> also H<sub>2</sub> and CO were produced. Thus, the addition of Cu lead to complete oxidation of methane instead of partial oxidation under the studied reaction conditions.

#### 4.3.6 Methane Decomposition

The reactivity of the zirconia supported Ni and CuNi catalysts for decomposition of methane was investigated by TPMD measurements. The amount of H<sub>2</sub> produced during this reaction was measured via MS (m/z 2) and is shown in Fig. 31 for all tested catalysts.

The results obtained over Ni-ZrO<sub>2</sub> are shown in Fig. 31 a). The production of hydrogen started at around 625 K, increased further with increasing temperature and decreased again reversibly when the sample was cooled down to 573 K. Upon heating another time to 773 K, the hydrogen production rate remained approximately the same as in the first cycle. Thus, no deactivation of the H<sub>2</sub> production activity was observed. Beside H<sub>2</sub> formation, carbon dioxide evolution occurred during the first heating cycle in methane up to ~700 K. In the second and third heating cycle a small CO<sub>2</sub> desorption peak was observed with a maximum at 630 K. The detected CO<sub>2</sub> likely originates from the reaction of methane with surface oxygen and carbonates of the zirconia or with NiO present due to incomplete reduction.

Fig. 31 b) shows the rate of hydrogen production over 13CuNi-ZrO<sub>2</sub> under the same conditions. Over this sample no catalytic activity was found up to 735 K. At this temperature, the amount of produced hydrogen increased rapidly up to a level similar to Ni-ZrO<sub>2</sub>. The onset of H<sub>2</sub> production was accompanied by a small amount of CO<sub>2</sub> evolving which occurred only in the first heating cycle. During the second and third reaction cycle about the same amount of hydrogen was detected than over Ni-ZrO<sub>2</sub>. This indicates an irreversible surface modification process on the bimetallic 13CuNi-ZrO<sub>2</sub> sample occurring during the first heating cycle in methane which significantly changed the catalytic performance of the catalyst.

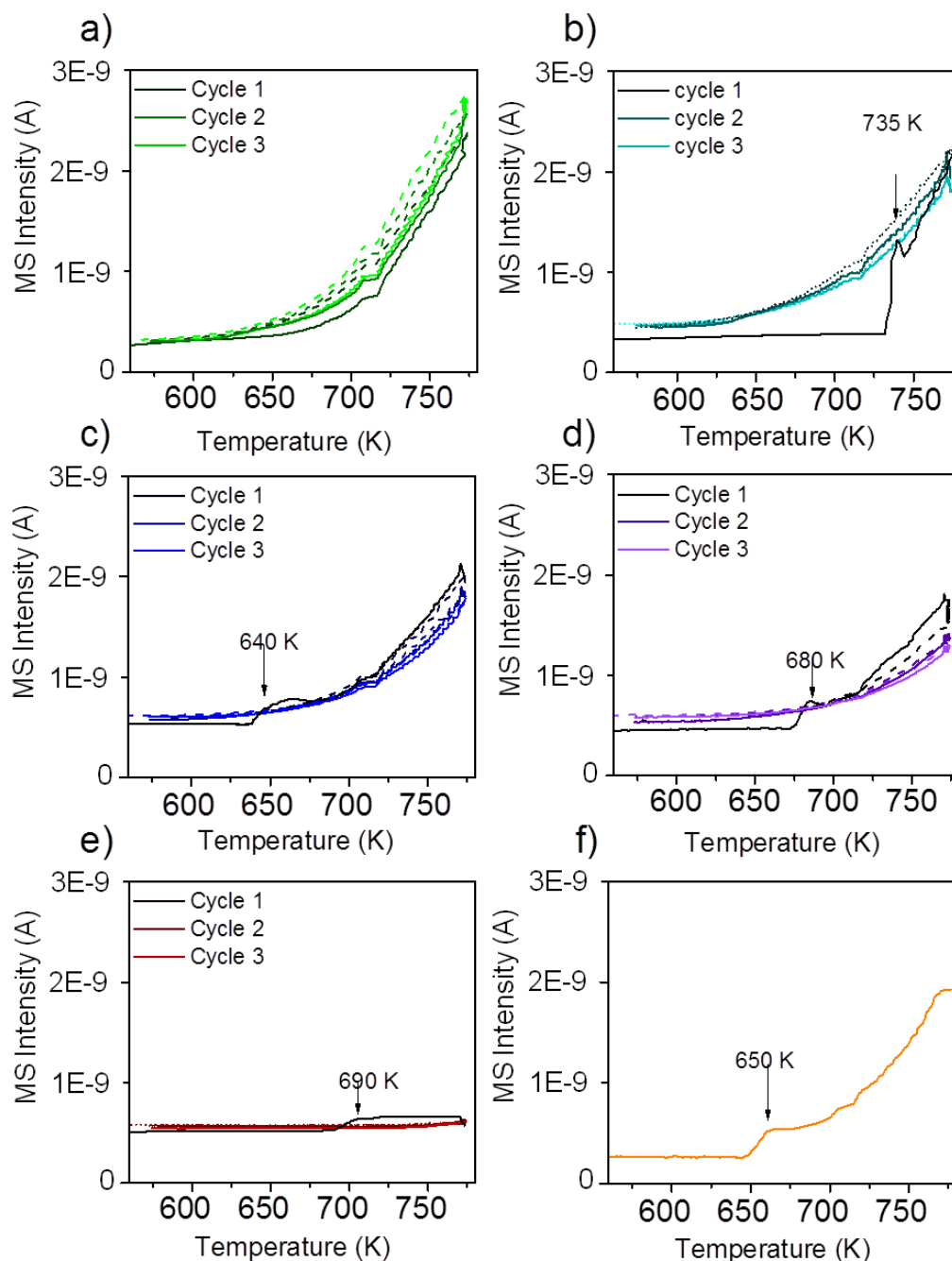


Fig. 31. Hydrogen evolution during TPMD on a) Ni-ZrO<sub>2</sub>, b) 13CuNi-ZrO<sub>2</sub>, c) 11CuNi-ZrO<sub>2</sub>, d) 31CuNi-ZrO<sub>2</sub>, e) Cu-ZrO<sub>2</sub> and f) 13CuNi-ZrO<sub>2</sub>50. The samples a)-f) were reduced at 673 K followed by 3 heating-cooling cycles between 573 and 773 K in methane/Ar. For f) only one heating cycle is shown. The temperature was ramped at 5 K/min. Published in<sup>[2]</sup>.

On 11CuNi-ZrO<sub>2</sub> and 31CuNi-ZrO<sub>2</sub> as well as 13CuNi-ZrO<sub>2</sub>50, shown in Fig. 31 c), d) and f), a similar behaviour was observed as on 13CuNi-ZrO<sub>2</sub> but the activation step occurred at 640 K, 680 K and 650 K, respectively, and the activity for H<sub>2</sub> formation was lower than on the Ni rich sample. Over Cu-ZrO<sub>2</sub>, shown in Fig. 31 e), hardly any hydrogen production was observed. During the first heating cycle a small amount of hydrogen was produced above 690 K but decreased again during the isothermal period at 773 K. A small amount of CO<sub>2</sub> was also detected during the first heating cycle. Afterwards, the Cu-ZrO<sub>2</sub> was completely inactive. The low initial activity can likely be attributed to the reaction of methane with

surface oxygen and hydroxide species from zirconia or incompletely reduced Cu species, which are not available anymore in the second and third reaction cycle. Often, CO is reported as by-product of the reaction between methane and oxygen species on the support or the incompletely reduced metal oxides<sup>[158, 159]</sup>. However, formation of various surface carbonate species was observed from CO adsorption on zirconia and all zirconia supported catalysts by IR spectroscopy, which likely decompose to CO<sub>2</sub>.

In order to find out whether hydrogen evolution occurs because of further reduction of the catalyst in methane, the measurement was repeated with the same sample but after reduction at 773 K instead of 673 K. The sudden onset in hydrogen formation accompanied by carbon dioxide evolution was observed, too, but the onset temperature was lowered to 650 K.

For quantitative comparison of the catalytic activity the amount of produced hydrogen was determined by GC-TCD. Table 3 shows the hydrogen yields and reaction rates for hydrogen production during steady state methane decomposition at 773 K.

The initial reaction rate  $r$  calculated per g catalyst decreased with decreasing overall Ni content. However, the rate  $R$  normalized per g Ni is at about the same order of magnitude for Ni and all bimetallic samples containing 5 wt% total loading. In agreement with TPMD measurements, similar rates of hydrogen formation were detected on Ni-rich 13CuNi-ZrO<sub>2</sub> compared to Ni-ZrO<sub>2</sub>. Cu is almost inactive and the reaction rate decreases fast to zero with time-on-stream while it stays constant for the other catalysts for at least one hour. The rate  $r$  of the catalyst containing 50 wt% metals, 13CuNi-ZrO<sub>2</sub>50, is about the same as that of the 13CuNi-ZrO<sub>2</sub> with 5 wt% metal loading, which results in a reaction rate  $R$  per g nickel one order of magnitude lower. This can probably be explained by a lower Ni dispersion at such high loading. In general, we did not observe an enhancement of the catalytic activity by addition of copper to the Ni/ZrO<sub>2</sub> catalyst.

**Table 3.** Hydrogen yields and initial reaction rates during methane decomposition at 773 K in 5 % CH<sub>4</sub> and 95 % Ar with a total flow of 50 ml/min.

Sample	H <sub>2</sub> yield	reaction rate $r$ per g catalyst (mol H <sub>2</sub> /(g catalyst·s))	reaction rate $R$ per g nickel (mol H <sub>2</sub> /(g nickel·s))
Ni-ZrO <sub>2</sub>	63.3 %	$2.4 \cdot 10^{-5}$	$4.8 \cdot 10^{-4}$
13CuNi-ZrO <sub>2</sub>	49.8 %	$1.9 \cdot 10^{-5}$	$5.0 \cdot 10^{-4}$
11CuNi-ZrO <sub>2</sub>	16.9 %	$6.4 \cdot 10^{-6}$	$2.6 \cdot 10^{-4}$
31CuNi-ZrO <sub>2</sub>	13.6 %	$5.1 \cdot 10^{-6}$	$4.1 \cdot 10^{-4}$
Cu-ZrO <sub>2</sub>	1.5 %	$5.6 \cdot 10^{-7}$	-
13CuNi-ZrO <sub>2</sub> 50	40.0 %	$1.5 \cdot 10^{-5}$	$3.9 \cdot 10^{-5}$

Methane Decomposition was also performed *in situ* in the FTIR vacuum cell. The results of these experiments performed with Cu-CeZr, 11CuNi-CeZr and Ni-CeZr were published in<sup>[1]</sup>.

Over Ni-CeZr a strong change in the total absorption was observed. In addition,  $\text{CH}_3$  and  $\text{CH}_2$  species were formed which proved (partial) dehydrogenation of methane. In contrast, on Cu-CeZr CO production was observed without any further changes. On 11CuNi-CeZr  $\text{CH}_2$ ,  $\text{CH}_3$  and CO formation took place coming along with strongly reduced coke formation compared to Ni-CeZr.

#### 4.3.7 *In situ* X-Ray Photoelectron Spectroscopy

In order to learn more about the surface composition, oxidation states and carbonaceous species present under reaction atmosphere *in situ* XPS at mbar pressures was employed. The bimetallic Ni-rich 1:3 composition which had shown the most pronounced increase in methane decomposition activity was investigated further by synchrotron-based *in situ* XPS aiming at understanding the nature of the irreversible surface modification process. To avoid further complication of the (already complex) spectra by charging effects a catalyst with a higher overall metal loading of 50wt% was utilized after carefully checking the comparability of this material to the respective 5 wt% sample.

##### *XP spectra during reduction in $\text{H}_2$*

Fig. 32 shows the Cu  $2p_{3/2}$  binding energy region of  $^{13}\text{CuNi-ZrO}_2$ 50 during a) oxidation in 0.10 mbar  $\text{O}_2$  and b) during reduction in 0.25 mbar  $\text{H}_2$ . The peak positions and full width at half maximum (FWHM) are listed in Table 4.

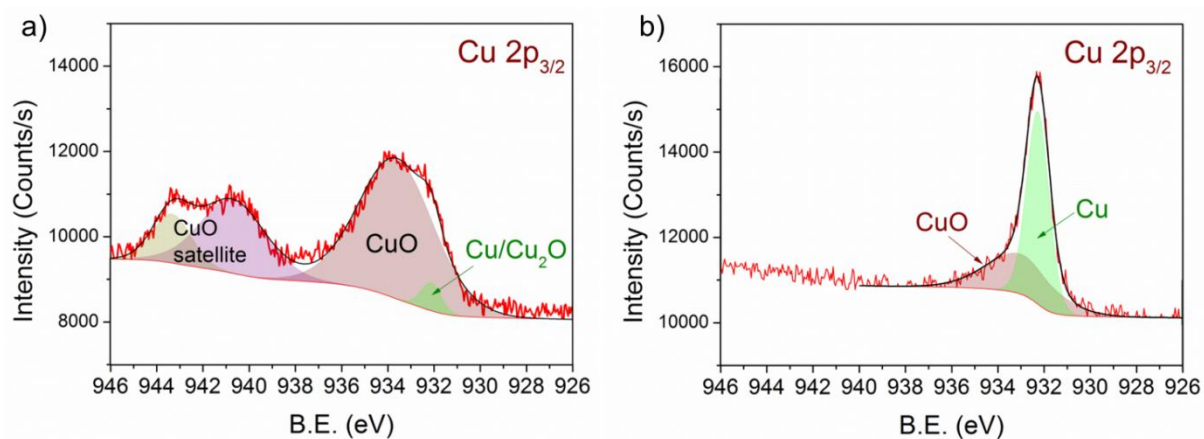


Fig. 32. Cu  $2p_{3/2}$  region of  $^{13}\text{CuNi-ZrO}_2$  50 in a) 0.10 mbar  $\text{O}_2$  at 573 K and b) 0.25 mbar  $\text{H}_2$  at 673 K for 30 min. The incident photon energy was 1100 eV. Published in<sup>[2]</sup>.

**Table 4.** Peak positions obtained in XPS measurements on 13CuNi-ZrO<sub>2</sub>50.

species	peak position (eV)	FWHM (eV)
CuO satellite 2	943.3 ± 0.2	1.9 ± 0.2
CuO satellite 1	940.7 ± 0.2	3.3 ± 0.2
CuO	933.3 ± 0.4	3.7 ± 0.3
new Cu species	933.6 ± 0.2	1.1 ± 0.1
Cu and Cu <sub>2</sub> O	932.3 ± 0.1	0.9 ± 0.1
NiO	854.2 ± 0.2	
Ni	852.6 ± 0.1	
carbonates/ carboxygenates	290.1 ± 0.1, 288.8 ± 0.1, 287.8 ± 0.2	1.1 ± 0.2
C-O or C-OH	286.3 ± 0.1	0.9 ± 0.1
C <sub>x</sub> H <sub>y</sub> species	285.4 ± 0.1	0.8 ± 0.1
C sp <sup>2</sup>	284.8 ± 0.1	0.6 ± 0.1
graphitic carbon	284.3 ± 0.1	0.8 ± 0.1
Ni <sub>x</sub> C	283.4 ± 0.1	0.9 ± 0.1

The broad peak at 933.3 eV is attributed to CuO<sup>[160-165]</sup> with two characteristic shake-up satellite peaks at 940.7 eV and 943.3 eV.

The structure seen in the satellite line is due to the multiplet splitting in the 2p 3d final state<sup>[162]</sup>. The small peak located at 932.3 eV is characteristic of Cu<sub>2</sub>O and/or metallic Cu<sup>[160, 162, 164, 165]</sup>. During reduction at 673 K the CuO peak decreased in intensity while the signal of reduced Cu species strongly increased. Since the shift of alloyed Cu in CuNi has been reported to be only about 0.2 eV compared to monometallic Cu<sup>[166-168]</sup> we could not resolve this species.

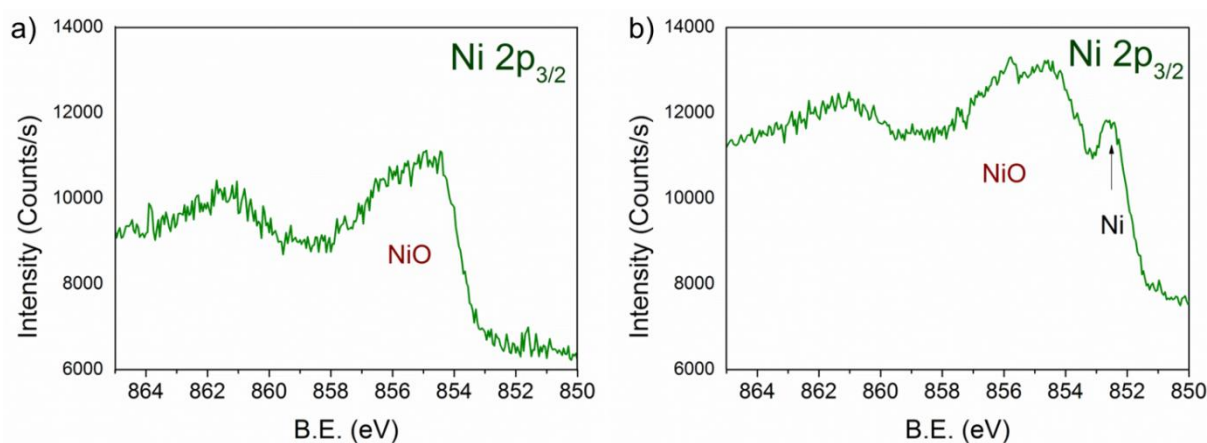


**Fig. 33.** Ni 2p<sub>3/2</sub> region of 13CuNi-ZrO<sub>2</sub> 50 in a) 0.10 mbar O<sub>2</sub> at 573 K and b) 0.25 mbar H<sub>2</sub> at 673 K for 30 min. The incident photon energy was 1010 eV. Published in<sup>[2]</sup>.

Fig. 33 shows the Ni 2p<sub>3/2</sub> core levels of 13CuNi-ZrO<sub>2</sub>50 measured during a) oxidation and b) reduction. The peak at 854.3 eV is attributed to the main line of NiO<sup>[39, 165, 169-171]</sup>. In reducing

atmosphere an additional peak appeared at 852.6 eV which is ascribed to metallic nickel<sup>[165, 172, 173]</sup>. Again, it is not possible to distinguish between nickel interacting with copper and non-interacting with copper due to the small chemical shift of about 0.2 eV<sup>[166-168]</sup> which would be expected for Ni alloyed with Cu. In agreement with previously reported findings by IR spectroscopy of CO adsorption on a reduced CuNi both oxidized and reduced Ni species are present at the surface after reduction at 673 K though the bulk consists predominantly of reduced Ni species according to XANES measurements.

Due to the high complexity of the NiO spectrum consisting of shake-up peaks and multiplet states<sup>[169, 174]</sup> we fitted Ni 2p<sub>3/2</sub> spectra by linear combination of reference spectra of NiO and completely reduced Ni. The resulting Ni to NiO ratios are summarized in Table 5.

**Table 5. Proportion of NiO and Ni in Ni 2p<sub>3/2</sub> spectra fitted by linear combination of reference spectra.**

atmosphere and temperature (K)	NiO	Ni
<b>O<sub>2</sub> - 573</b>	100%	
<b>H<sub>2</sub> - 573</b>	77 ± 3 %	23 ± 3 %
<b>CH<sub>4</sub> - 523</b>	79 ± 3 %	21 ± 3 %
<b>CH<sub>4</sub> - 573</b>	80 ± 2 %	20 ± 2 %
<b>CH<sub>4</sub> - 623</b>	79 ± 3 %	21 ± 3 %
<b>CH<sub>4</sub> - 673</b>	77 ± 3 %	23 ± 3 %
<b>CH<sub>4</sub> - 697</b>	75 ± 3 %	25 ± 3 %
<b>CH<sub>4</sub> - 723</b>	66 ± 3%	34 ± 3 %

Overall, the XP spectra reveal the coexistence of reduced Cu and a mixture of oxidized and metallic Ni species in the surface-near region after reduction.

#### *XP spectra during methane decomposition*

Fig. 34 shows a) the Cu 2p<sub>3/2</sub> region and b) the Ni 2p<sub>3/2</sub> region of 13CuNi-ZrO<sub>2</sub> during exposure to 0.25 mbar methane at temperatures from 523 to 723 K directly after reduction in H<sub>2</sub>.

At 523 K mainly metallic copper and small amounts of CuO were present in the Cu 2p<sub>3/2</sub> region. By increasing the temperature the metallic Cu peak became broader and shifted to a slightly higher binding energy indicating further alloy formation between copper and nickel. The amount of nickel oxide decreased with temperature while the signal of metallic nickel increased. At 723 K a new Cu species at 933.6 eV appeared at the highest temperature. A potential assignment of this species is Cu interacting with surface carbonates<sup>[165]</sup>, however, a larger shift to higher binding energies would be expected compared to CuO.

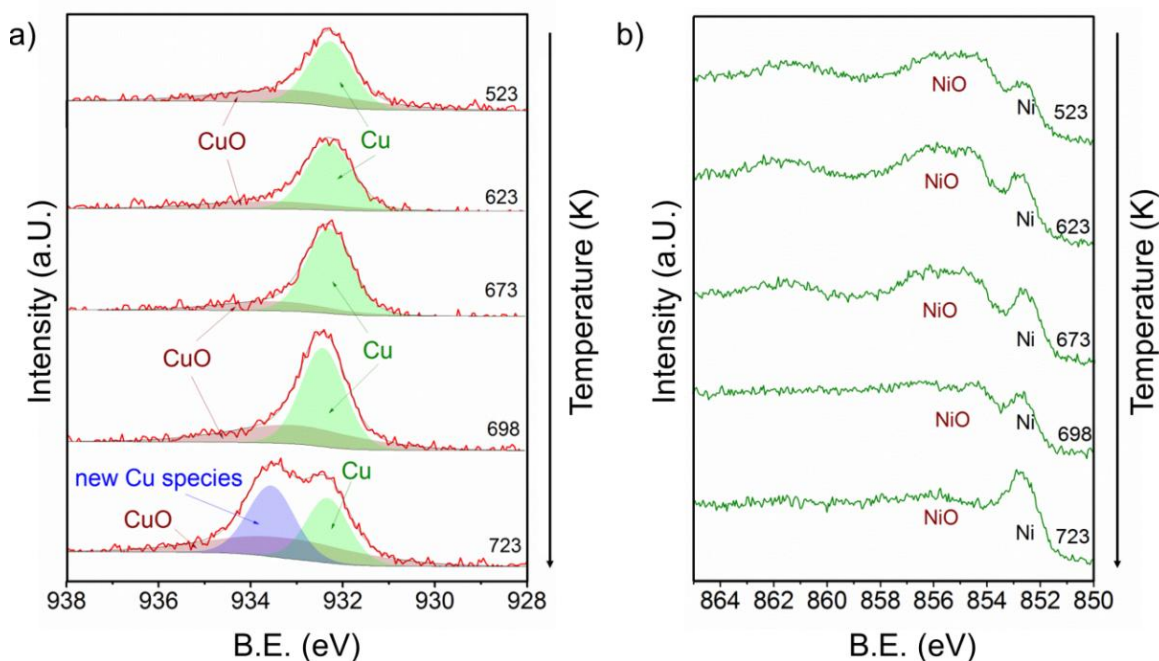


Fig. 34. a) Cu 2p<sub>3/2</sub> and b) Ni 2p<sub>3/2</sub> core level regions of <sup>13</sup>CuNi-ZrO<sub>2</sub> in 0.25 mbar CH<sub>4</sub> at rising temperature from 523 to 723 K. The incident photon energies were 1100 eV (Cu) and 1010 eV (Ni). Published in<sup>[2]</sup>.

CuO core levels have been observed over a broad binding energy range, but in the XP spectrum at 723 K no satellite peaks characteristic for CuO are found, which rather excludes the assignment of the peak at 933.6 eV to CuO. Currently, the nature of this peak remains an open question.

Between 698 and 723 K the biggest changes were observed in the Ni 2p<sub>3/2</sub> region as well. The amount of NiO decreased significantly while the concentration of metallic nickel increased in the surface near region. Note that in the temperature range

between 698 and 723 K where the strongest spectral changes occurred the catalytic activity of this catalyst increases dramatically, as shown by TPMD and in agreement with the simultaneously recorded mass spec data.

Fig. 35 shows the C 1s core level region during exposure of <sup>13</sup>CuNi-ZrO<sub>2</sub> to methane at temperatures increasing from 523 to 723 K. A number of different carbon-containing surface species were present in methane. Polycarbonates, carbonates and carbonoxygens above 287 eV hardly changed with temperature. Various carbonate species were also observed by infrared spectroscopy on ZrO<sub>2</sub>. C-O<sup>[175-178]</sup> or C-OH<sup>[176, 177]</sup> at 286.3 eV increased with temperature indicating an interaction of carbon with the oxide support or NiO and CuO which had not been reduced up to that temperature. The amount of graphitic carbon<sup>[175, 179, 180]</sup> at 284.3 eV binding energy increased until 673 K but then decreased again at 723 K. The peak at 284.8 eV attributed to C having sp<sup>2</sup> hybridization<sup>[176, 180-182]</sup> indicates the formation of carbon nanotubes (CNTs) and increased with increasing temperature. The signal at 285.4 eV corresponds to C<sub>x</sub>H<sub>y</sub> species<sup>[178, 183]</sup>. These species increased upon heating as well.

Alternatively, the signal could indicate the presence of structural defects on carbon nanotubes<sup>[182]</sup>.  $\text{Ni}_x\text{C}$ <sup>[176, 177]</sup> appeared at 283.4 eV and increased at first with rising temperature but then completely vanished at 723 K.

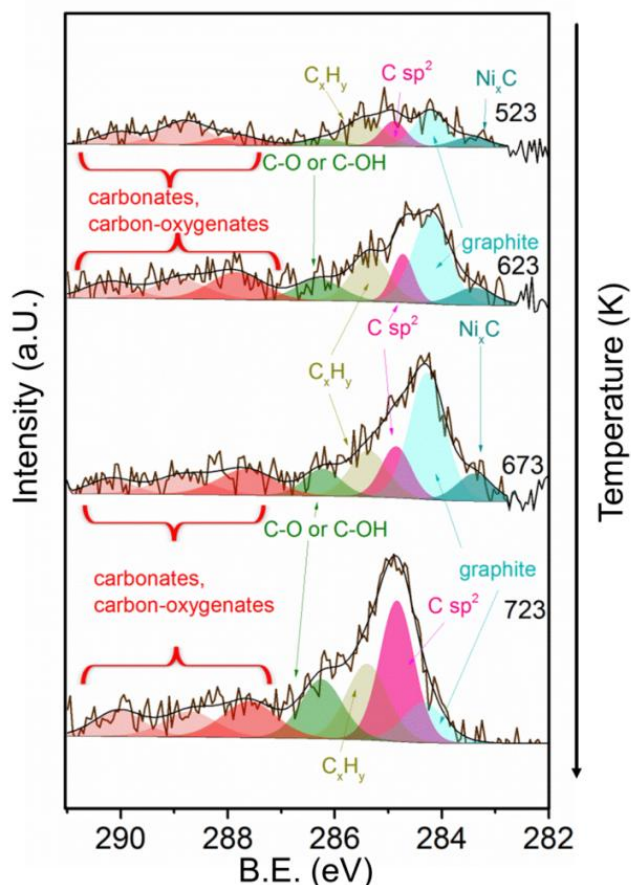


Fig. 35. C 1s core level region of  $^{13}\text{CuNi-ZrO}_2$  in 0.25 mbar  $\text{CH}_4$  at rising temperature from 523 to 723 K. The incident photon energy was 425 eV. Published in<sup>[2]</sup>

In summary, the amount of several carbon species increased during methane decomposition. In particular, the growth of CNTs is significantly enhanced at the highest temperature at which catalytic activity sets in at the same time, while graphitic carbon decreases, either by transformation to CNTs or dissolution in the bulk of the particles.

### Depth profiling

To get more insights into the distribution of Ni, Cu and C species in the surface and subsurface region XP spectra were recorded using different photon energies. The photon energies were varied to obtain photoelectron kinetic energies of 150 eV, 350 eV and 550 eV for each set of spectra of the relevant core level regions (Ni 2p, Cu 2p, C 1s). These depth profiles were performed at 523, 673 and 723 K in methane.

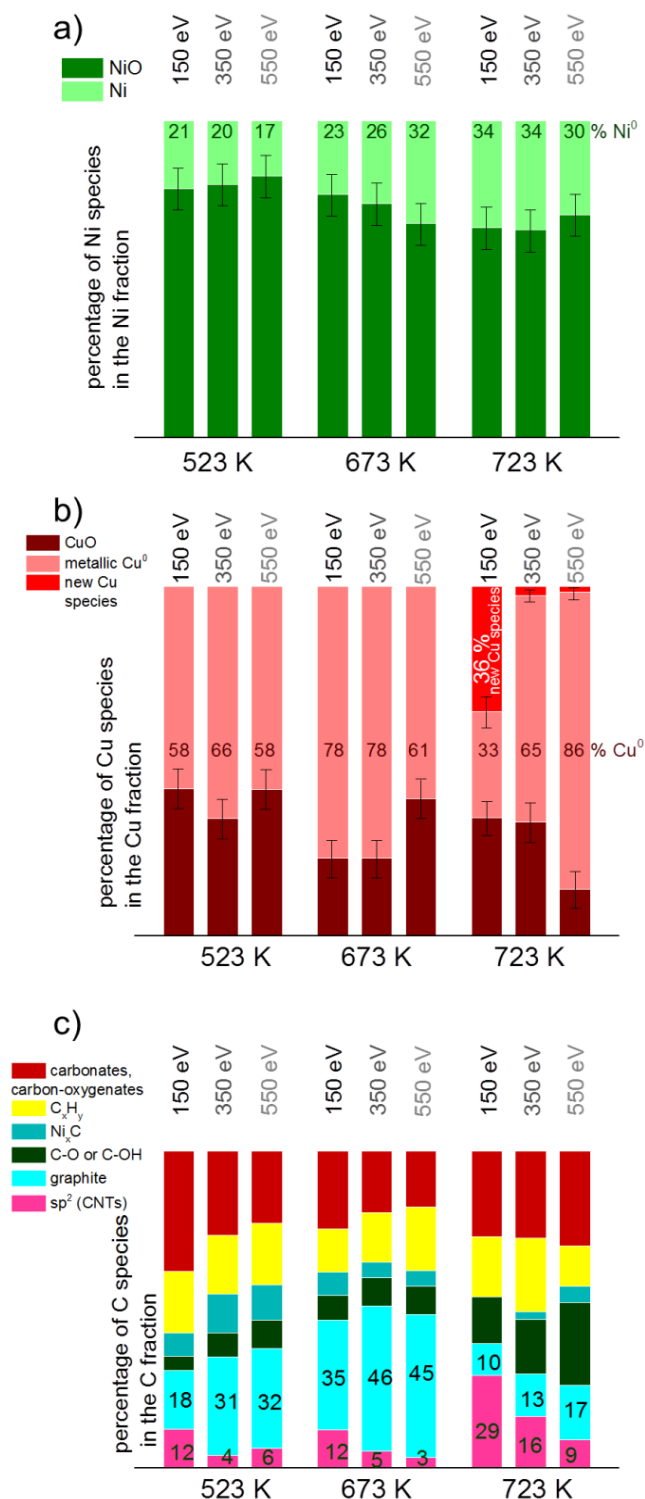


Fig. 36. Depth profile of a) Ni, b) Cu and c) C species based on the total amount of a) Ni, b) Cu and c) C, respectively. Spectra in the core level regions Ni 2p<sub>3/2</sub>, Cu 2p<sub>3/2</sub> and C 1s with kinetic energies of 150, 350 and 550 eV were consulted for the calculations. For clarity of the diagram error bars were left out in c). Published in<sup>[2]</sup>.

Fig. 36 visualizes the relative core level peak areas of the various Cu, Ni and C species based on the respective total areas of Cu, Ni and C signals. Upon heating from 523 to 673 K, the relative amount of metallic Ni increases mainly in the deeper (surface-near) layers. After

further heating from 673 to 723 K an increased amount of reduced Ni is present on the surface as well. The amount of metallic Cu increases with temperature. At 723 K the new Cu species appeared which cannot be identified yet (as discussed in the results section). Interestingly, this species is related to the surface of the catalyst, and appears only when using photon energies yielding photoelectrons of 150 eV kinetic energies, i.e. when measuring with the highest surface sensitivity.

In general, the total amount of carbon species decreases with increasing kinetic energy indicating that the carbon species are present mostly at the surface of the catalyst. As shown in Fig. 36 c), the relative proportion of CNTs increases significantly at 723 K, in particular in the surface-sensitive measurement, as shown by the strongly decreasing amount of  $sp^2$  hybridized carbon with increasing kinetic energy. Nickel carbide disappeared at 723 K in the most surface sensitive spectra recorded at 150 eV kinetic energy, while a small amount of carbide is still present in the somewhat deeper surface-near layers. The relative amount of graphitic carbon is highest at 673 K reaction temperature, and then decreases considerably at 723 K. This is observed for all photoelectron kinetic energies that were analyzed. The proportion of carbon present as carbonates, carbon-oxygenates and hydrocarbon species does not depend much on reaction temperature and photon energy.

#### 4.3.8 Temperature Programmed Oxidation

To obtain insights into coke formation, temperature programmed oxidation (TPO) was performed after reaction in methane. The amount of carbon dioxide formed during TPO provides information about the amount of coke formed during the reaction, and the temperature, which is needed to burn off the carbon species, may be characteristic for the carbon bond strength to the catalyst's surface.

Fig. 37 shows the production of carbon dioxide observed during TPO in 20 %  $O_2$  in Ar performed directly after methane decomposition (described in the previous section). Over Ni-ZrO<sub>2</sub> the highest amount of coke was formed and temperatures of 770 K were needed to oxidize most of it. On the nickel-rich bimetallic catalyst 13CuNi-ZrO<sub>2</sub> the amount of formed CO<sub>2</sub> was lower by about 50 % compared to Ni-ZrO<sub>2</sub>. Furthermore, much lower temperatures of around 700 K were required to remove carbon by oxidation. At about 750 K a second smaller CO<sub>2</sub> evolution peak was observed in the TPO. Over 11CuNi-ZrO<sub>2</sub> the amount of coke was reduced to 30 % compared to Ni-ZrO<sub>2</sub>, and the maximum of CO<sub>2</sub> formation was detected at 650 K. Over the Cu-rich catalyst 31CuNi-ZrO<sub>2</sub> the amount of carbon was reduced to only 20 % compared to Ni-ZrO<sub>2</sub>. Here, one needs to keep in mind the lower activity of the Cu-rich compositions compared to Ni-ZrO<sub>2</sub>. The maximum of CO<sub>2</sub> formation rate was observed at 660 K. When considering the differences in H<sub>2</sub> production rate (Table 3) and the CO<sub>2</sub> peak areas observed in the TPO measurements the addition of Cu lowered the amount of coke formed. A major effect of Cu was, however, the down-shift of the carbon oxidation

temperature. Since hardly any methane decomposition reaction took place over the Cu-ZrO<sub>2</sub> reference material, no coke was burnt off during TPO over this catalyst.

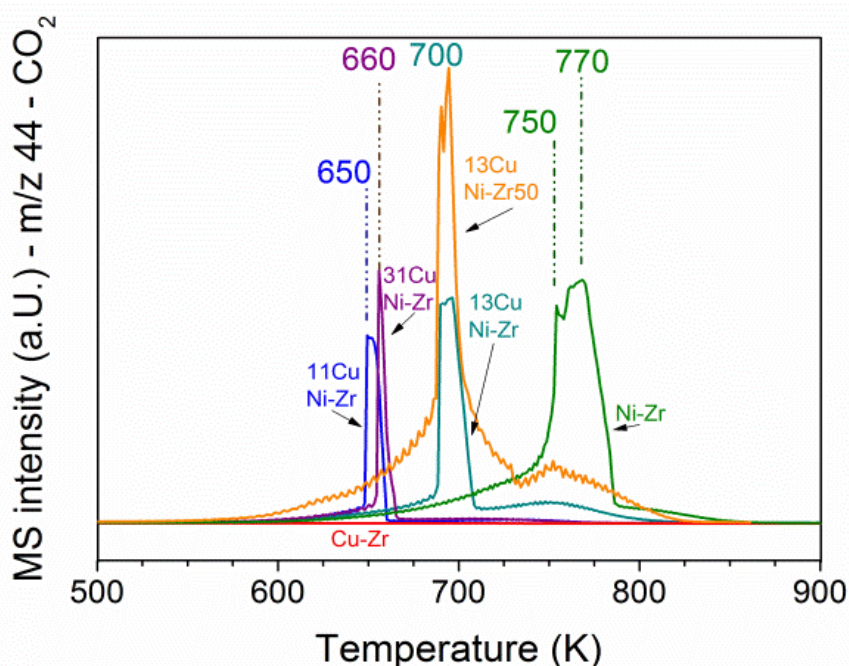


Fig. 37. TPO performed after the methane decomposition reaction over Ni and all CuNi catalysts (shown in Fig. 3). The mass spec trace of CO<sub>2</sub> (m/z 44) is displayed upon heating in 20 vol% O<sub>2</sub>/Ar at a rate of 5 K/min.

The TPO curves show large CO<sub>2</sub> desorption peaks in a narrow temperature range as well as broader peaks of CO<sub>2</sub> formation over a broad temperature range. The narrow peaks were always accompanied by a small peak of water (m/z 18) which indicates oxidation of CH<sub>x</sub> species in this temperature range. The much broader peak underneath might originate from other carbonaceous species like filamentous carbon. The presence of CH<sub>x</sub> species indicates that part of the adsorbed methane dissociated incompletely.

In summary, the highest C and CH<sub>x</sub> oxidation temperature was observed on monometallic nickel at 750-770 K. Since the oxidation temperature decreased on the bimetallic catalysts we conclude that C species are less strongly bonded to the bimetallic surface. A similar trend with composition was noticed like for the activity onset temperature described in section about TPMD. The highest temperature required to burn off coke was observed for 13CuNi-ZrO<sub>2</sub>, with a CO<sub>2</sub> evolution maximum at 700 K, while 11CuNi-ZrO<sub>2</sub> exhibited the lowest carbon oxidation temperature with a CO<sub>2</sub> evolution maximum at 650 K.

## 4.4 Ceria Promoted Ni-ZrO<sub>2</sub>

Ceria and Ceria-Zirconia supported Ni catalysts were characterized and tested for methane steam reforming and methane dry reforming.

### 4.4.1 Textural and Structural Properties

The crystalline structure of Ni-Ce<sub>x</sub>Zr<sub>y</sub>O<sub>2</sub> catalysts was determined by XRD. The X-ray diffractograms of the support materials ZrO<sub>2</sub>, CeZr, CeO<sub>2</sub>, Ce<sub>x</sub>Zr<sub>y</sub>O<sub>2\_comb</sub>, Ce<sub>x</sub>Zr<sub>y</sub>O<sub>2\_cp</sub>, Ce<sub>x</sub>Zr<sub>y</sub>O<sub>2\_cp</sub> and Ce<sub>x</sub>Zr<sub>y</sub>O<sub>2\_ctab</sub> after calcination and the catalyst samples Ni-ZrO<sub>2</sub>, Ni-CeZr, Ni-CeO<sub>2</sub>, Ni-Ce<sub>x</sub>Zr<sub>y</sub>O<sub>2\_comb</sub>, Ni-Ce<sub>x</sub>Zr<sub>y</sub>O<sub>2\_cp</sub>, Ni-Ce<sub>x</sub>Zr<sub>y</sub>O<sub>2\_cp</sub> and Ni-Ce<sub>x</sub>Zr<sub>y</sub>O<sub>2\_ctab</sub> after ex-situ reduction at 873 K are shown in Fig. 38. ZrO<sub>2</sub> and the ZrO<sub>2</sub> supported catalyst show reflections assigned to monoclinic ZrO<sub>2</sub>. No differences were found between pure ZrO<sub>2</sub> and CeZr. Since ceria was added by impregnation, no mixed oxide has formed at a moderate calcination temperature of 723 K.

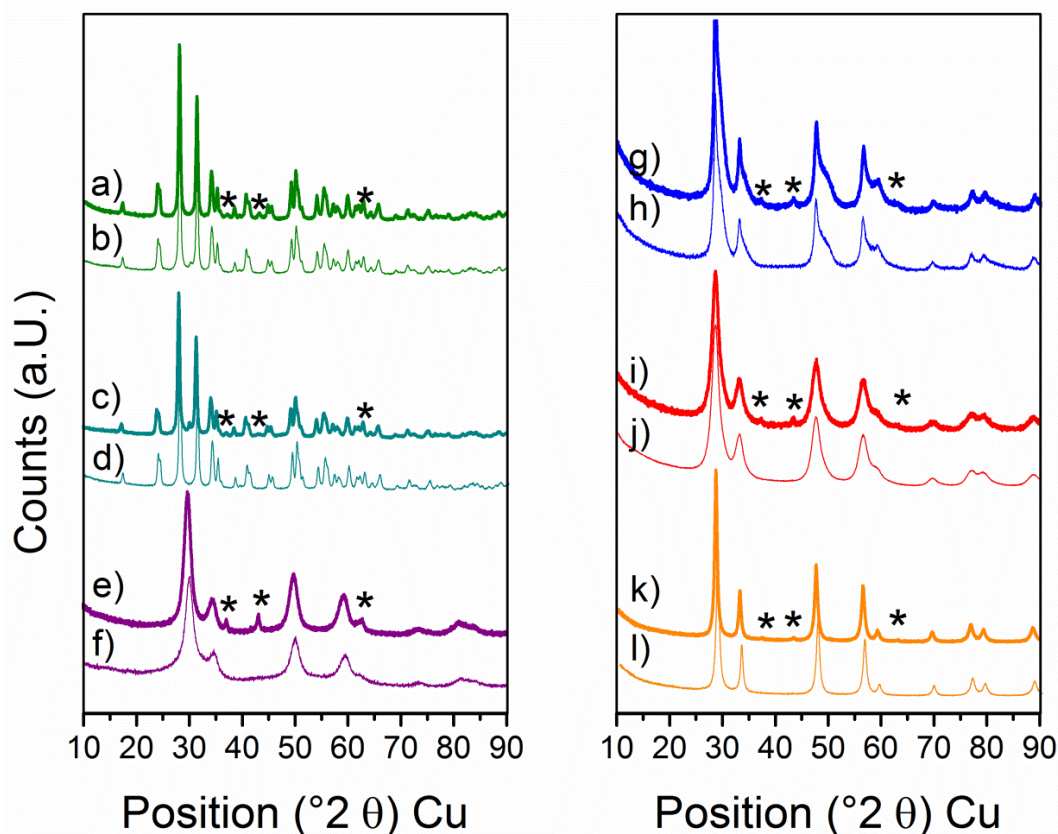


Fig. 38. XRD patterns of a) Ni-ZrO<sub>2</sub>, b) ZrO<sub>2</sub>, c) Ni-CeZr, d) CeZr, e) Ni-Ce<sub>x</sub>Zr<sub>y</sub>O<sub>2\_comb</sub>, f) Ce<sub>x</sub>Zr<sub>y</sub>O<sub>2\_comb</sub>, g) Ni-Ce<sub>x</sub>Zr<sub>y</sub>O<sub>2\_cp</sub>, h) Ce<sub>x</sub>Zr<sub>y</sub>O<sub>2\_cp</sub>, i) Ni-Ce<sub>x</sub>Zr<sub>y</sub>O<sub>2\_ctab</sub>, j) Ce<sub>x</sub>Zr<sub>y</sub>O<sub>2\_cp</sub>, k) Ni-CeO<sub>2</sub> and l) CeO<sub>2</sub>. ZrO<sub>2</sub> and CeZr support show characteristics of monoclinic zirconia, CeO<sub>2</sub> and Ce<sub>x</sub>Zr<sub>y</sub>O<sub>2\_ctab</sub> show characteristics of cubic CeO<sub>2</sub> and cubic Ce-Zr-oxide, respectively and Ce<sub>x</sub>Zr<sub>y</sub>O<sub>2\_comb</sub> shows characteristics of tetragonal Ce-Zr-oxide. Ce<sub>x</sub>Zr<sub>y</sub>O<sub>2\_cp</sub> shows both reflections of cubic and tetragonal Ce-Zr-oxides.

The diffractogram of Ni-CeO<sub>2</sub> shows reflections assigned to cubic CeO<sub>2</sub>. The ceria-zirconia mixed oxides vary in their phase composition: The support material prepared by co-precipitation without surfactant is composed of a cubic ceria-rich mixed oxide phase and a tetragonal zirconia-rich mixed oxide phase. The phase separation indicates insufficient mixing of the cerium and zirconium precursor during co-precipitation. The diffraction pattern of this sample is shown in Fig. 39 with the assignment of the two phases. The support prepared by co-precipitation with CTAB as surfactant consists of one cubic ceria-zirconia-mixed oxide phase, and the support material prepared by combustion consists of a tetragonal mixed oxide phase. Broader reflections of the mixed oxide support materials suggest smaller ceria-zirconia crystallites compared to the pure oxides. The average crystallite particle size calculated by Scherrer calculation is given in Table 6. The reflection positions of cubic NiO in the diffractograms of Ni-Ce<sub>x</sub>Zr<sub>y</sub>O<sub>2</sub>\_comb, Ni-Ce<sub>x</sub>Zr<sub>y</sub>O<sub>2</sub>\_cp, Ni-Ce<sub>x</sub>Zr<sub>y</sub>O<sub>2</sub>\_ctab and Ni-CeO<sub>2</sub> are labelled with an asterisk in Fig. 38 and observed as small reflections at 38°, 43° and 63°. The average crystallite size of NiO estimated by Scherrer-equation are 27 nm on Ni-ZrO<sub>2</sub> and Ni-CeZr, 16 nm on both mixed oxide supported catalysts prepared by co-precipitation, 29 nm on Ni-Ce<sub>x</sub>Zr<sub>y</sub>O<sub>2</sub>\_comb and 21 nm on Ni-CeO<sub>2</sub>.

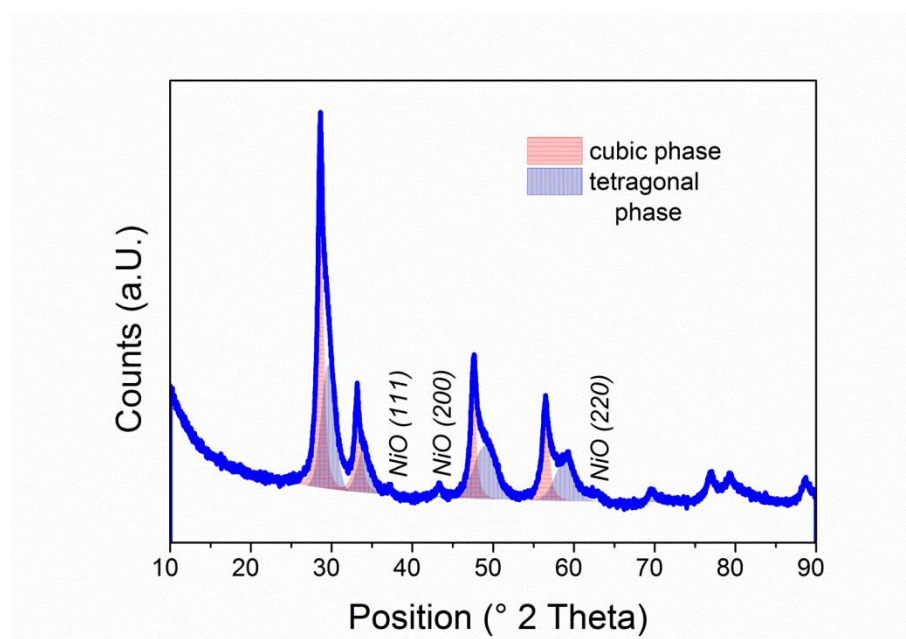


Fig. 39. XRD pattern of Ni-Ce<sub>x</sub>Zr<sub>y</sub>O<sub>2</sub>\_cp with assignment of the cubic and tetragonal phase.

The surface area analysis by nitrogen physisorption was carried out for the support samples ZrO<sub>2</sub>, CeO<sub>2</sub>, CeZr, Ce<sub>x</sub>Zr<sub>y</sub>O<sub>2</sub>\_comb, Ce<sub>x</sub>Zr<sub>y</sub>O<sub>2</sub>\_cp and Ce<sub>x</sub>Zr<sub>y</sub>O<sub>2</sub>\_ctab. The results of the calculations of the specific surface areas using the method of Brunauer, Emmet and Teller (BET)<sup>[184]</sup> and of the pore size and pore volume using the method of Barret, Joyner and Halenda (BJH)<sup>[185]</sup> are shown in Table 6. The specific surface area of both oxides prepared by co-precipitation was significantly higher than that of pure CeO<sub>2</sub> and ZrO<sub>2</sub>. The specific surface area of CeZr was slightly decreased compared to ZrO<sub>2</sub> and the smallest specific Surface area was measured for Ce<sub>x</sub>Zr<sub>y</sub>O<sub>2</sub>\_comb. The mesopore volume calculated by BJH

reached the highest value for the support prepared by surfactant assisted co-precipitation method while the lowest value was obtained for the Ce<sub>x</sub>Zr<sub>y</sub>O<sub>2</sub>\_comb support. The average pore size of ZrO<sub>2</sub> is with 21 nm clearly larger than that of the other samples.

Table 6. BET surface area, BJH average pore size and volume and crystallite size of ZrO<sub>2</sub>, CeO<sub>2</sub>, CeZr, Ce<sub>x</sub>Zr<sub>y</sub>O<sub>2</sub>\_comb, Ce<sub>x</sub>Zr<sub>y</sub>O<sub>2</sub>\_cp and Ce<sub>x</sub>Zr<sub>y</sub>O<sub>2</sub>\_ctab.

sample	BET surface area (m <sup>2</sup> /g)	BJH average pore size (nm)	BJH average pore volume (cm <sup>3</sup> /g)	average crystallite size (nm)
ZrO <sub>2</sub>	37	21	0.18	monoclinic: 36
CeO <sub>2</sub>	56	7	0.13	cubic: 30
CeZr	35	18	0.15	monoclinic: 36
Ce <sub>x</sub> Zr <sub>y</sub> O <sub>2</sub> _comb	20	11	0.05	tetragonal: 11
Ce <sub>x</sub> Zr <sub>y</sub> O <sub>2</sub> _cp	91	7	0.07	cubic: 19
Ce <sub>x</sub> Zr <sub>y</sub> O <sub>2</sub> _ctab	93	9	0.25	tetragonal: 9

#### 4.4.2 TEM Study

The catalysts Ni-Ce<sub>x</sub>Zr<sub>y</sub>O<sub>2</sub>\_cp and Ni-Ce<sub>x</sub>Zr<sub>y</sub>O<sub>2</sub>\_ctab were studied by TEM after *ex situ* reduction at 873 K. Fig. 40 shows a TEM image and an elemental map with the distribution of Ni, Ce, Zr and O. It can be observed, that some regions are enriched in Ce and others in Zr as expected from the XRD result. According to elemental maps NiO particles are located both in the Ce-rich and the Zr-rich regions. The Ni particles located by EDX are marked with cycles in Fig. 40 a). The regions labelled with I and II, respectively, are shown in Fig. 41 in more detail.

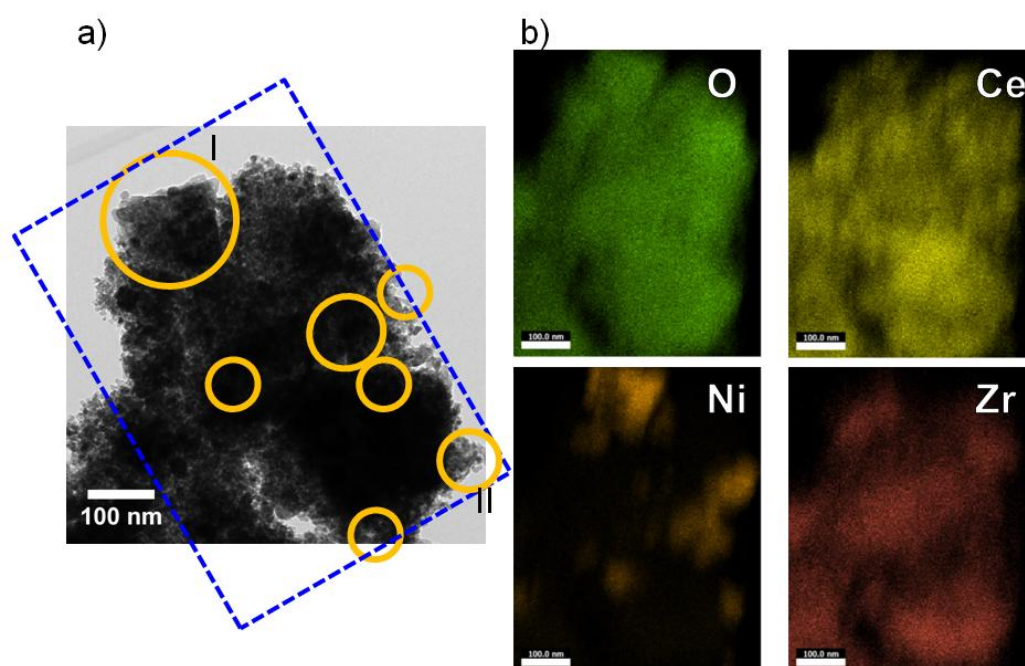


Fig. 40. a) TEM image of Ni-Ce<sub>x</sub>Zr<sub>y</sub>O<sub>2</sub>\_cp and b) Elemental map of the region shown in the rectangle in a) for the K-edge energies of O, Ce, Ni and Zr. Regions containing Ni are marked in a), I and II are shown in Fig. 41 with higher magnification.

In Fig. 41 a) two overlapping NiO particles, about 50nm in size, are shown. Besides such large particles mainly smaller NiO particles with about 10 nm diameter as shown in Fig. 41 b) were detected.

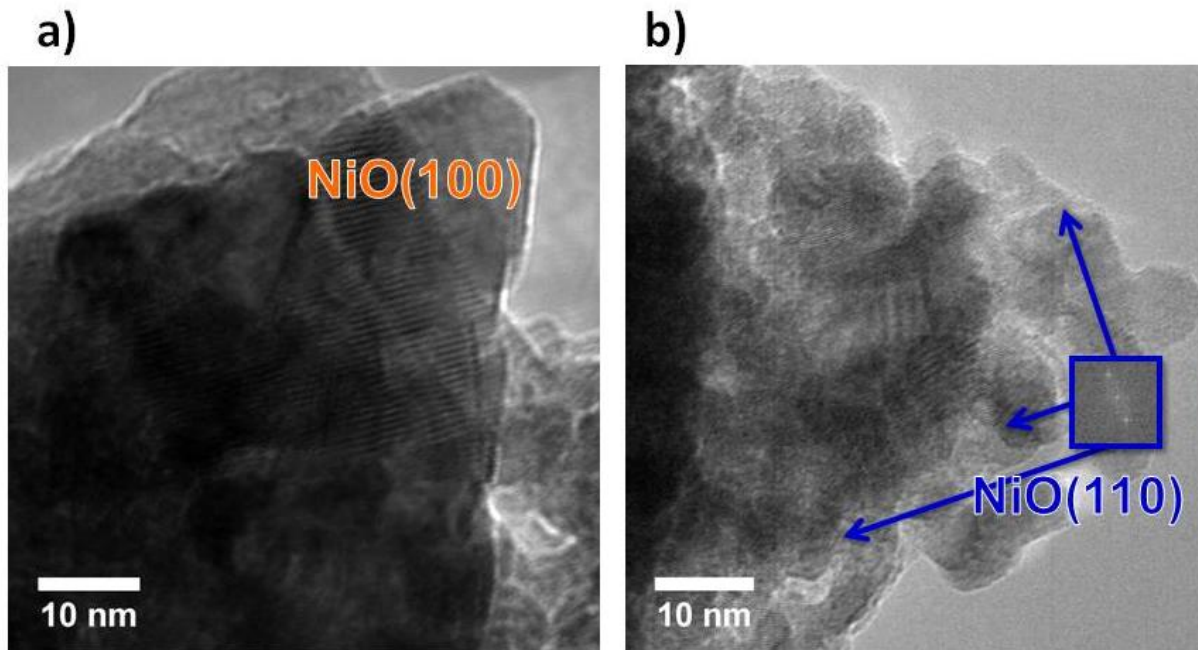


Fig. 41. TEM images of a) the region marked with I and b) the region marked with II in Fig. 40 a.

On Ni-Ce<sub>x</sub>Zr<sub>y</sub>O<sub>2</sub>\_ctab as on the other samples Ni was at first identified by EDX analysis but in contrast to the other catalysts, no NiO particles on the border of the agglomerates could be found for individual characterization. Therefore, a fast Fourier transform was applied to the whole region shown in Fig. 42 a), where Ni was detected by EDX analysis.

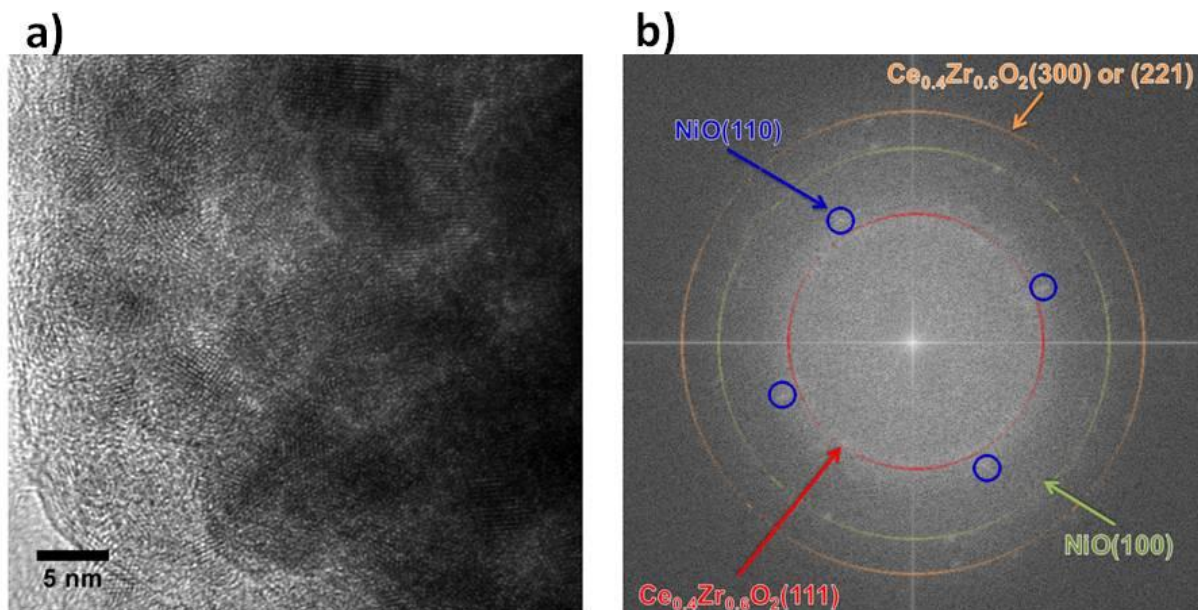


Fig. 42. a) TEM image of Ni-Ce<sub>x</sub>Zr<sub>y</sub>O<sub>2</sub>\_ctab and b) FFT of a)

The reflections in the corresponding digital diffractogram shown in Fig. 42 b) were assigned to Ce<sub>0.4</sub>Zr<sub>0.6</sub>O<sub>2</sub>(111) and (300) or (211) grains and NiO grains with (110) and (100) orientation.

#### 4.4.3 Adsorption Properties

IR spectra of room temperature CO adsorption on Ni-CeZr, Ni-CeO<sub>2</sub>, Ni-Ce<sub>x</sub>Zr<sub>y</sub>O<sub>2</sub>\_cp and Ni-Ce<sub>x</sub>Zr<sub>y</sub>O<sub>2</sub>\_ctab after oxidation at 773 K and reduction at 673 K are shown in Fig. 43. On Ni-Ce<sub>x</sub>Zr<sub>y</sub>O<sub>2</sub>\_cp Ni<sup>2+</sup>-CO is observed as a shoulder of the larger Zr<sup>4+</sup>-CO peak at 2171 cm<sup>-1</sup>, respectively. The peaks of CO adsorbed on Ni<sup>+</sup> as mono- di or -tricarbonyl can be observed on the mixed oxide supported samples, as on Ni-ZrO<sub>2</sub> (Fig. 16) but not on Ni-CeO<sub>2</sub>. On all catalysts CO peaks of linear and bridged adsorbed CO on metallic nickel are present. On Ni-CeO<sub>2</sub> CO only adsorbs on metallic nickel which indicates, that all the Ni in the surface is fully reduced at 673 K.

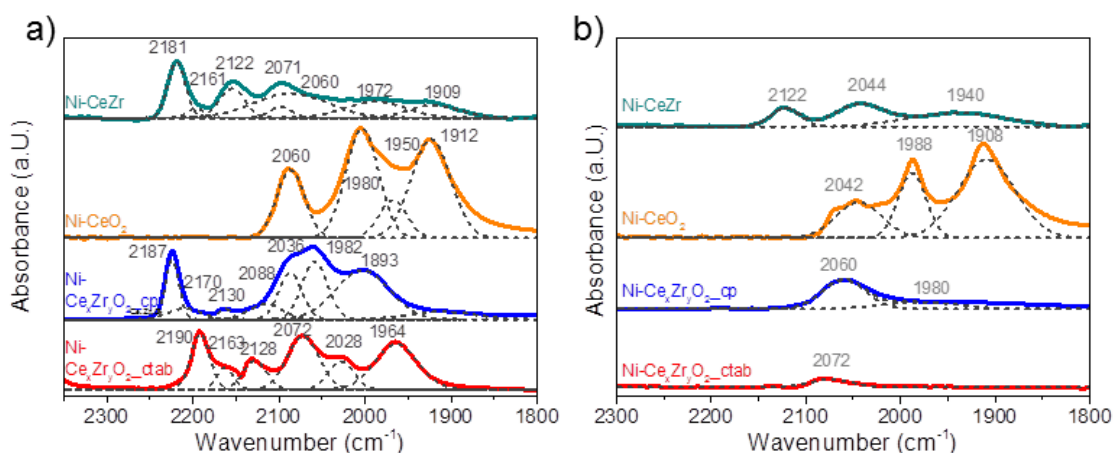


Fig. 43. IR spectra of a) 5 mbar CO adsorbed on reduced Ni-ZrO<sub>2</sub>, Ni-CeO<sub>2</sub>, Ni-Ce<sub>x</sub>Zr<sub>y</sub>O<sub>2</sub>\_cp and Ni-Ce<sub>x</sub>Zr<sub>y</sub>O<sub>2</sub>\_ctab at room temperature and b) after evacuation below 10<sup>-5</sup> mbar.

After evacuation Ni<sup>+</sup>-CO as well as linear and bridged CO on Ni<sup>0</sup> remain on the surface of Ni-CeZr, as also observed on Ni-ZrO<sub>2</sub> shown in Fig. 16. On Ni-CeO<sub>2</sub> a rather high amount of linear and bridged CO on Ni<sup>0</sup> remains on the surface in contrast to the mixed oxide supported samples, where only little CO remains on the reduced Ni surface.

The accessible nickel surface of the samples Ni-ZrO<sub>2</sub>, Ni-CeO<sub>2</sub>, Ni-Ce<sub>x</sub>Zr<sub>y</sub>O<sub>2</sub>\_cp and Ni-Ce<sub>x</sub>Zr<sub>y</sub>O<sub>2</sub>\_ctab was determined by selective chemisorption of H<sub>2</sub>. The nickel dispersion, metallic nickel surface areas per gram of sample after reduction at 673 K, the pretreatment and reaction temperature for MSR, and 873 K, the pretreatment and reaction temperature for MDR, are shown in Table 7. The highest Ni surface area upon reduction at 673 K is observed on the zirconia supported Ni catalyst while on Ni-Ce<sub>x</sub>Zr<sub>y</sub>O<sub>2</sub>\_ctab only very little H<sub>2</sub> adsorbs. After reduction at 873 K the nickel surface area decreases suggesting sintering of the supported nickel particles. The metallic Ni surface area decreases much more on Ni-ZrO<sub>2</sub>

than on Ni-CeO<sub>2</sub> and Ni-Ce<sub>x</sub>Zr<sub>y</sub>O<sub>2</sub>\_ctab indicating that the ceria support increases the stability of Ni against sintering.

Table 7. Ni dispersion and Ni surface area of Ni-ZrO<sub>2</sub>, Ni-CeO<sub>2</sub>, Ni-Ce<sub>x</sub>Zr<sub>y</sub>O<sub>2</sub>\_cp and Ni-Ce<sub>x</sub>Zr<sub>y</sub>O<sub>2</sub>\_ctab after reduction at 673 K and 873 K.

sample	Ni dispersion		Ni surface area ( $A_{Ni}$ )	
	(%)		(m <sup>2</sup> /g of catalyst)	
	673 K red.	873 K red.	673 K red.	873 K red.
Ni-ZrO <sub>2</sub>	4.7	1.75	1.57	0.14
Ni-CeO <sub>2</sub>	2.6	1.4	0.88	0.46
Ni-Ce <sub>x</sub> Zr <sub>y</sub> O <sub>2</sub> _cp	3.3	1.0	1.08	0.34
Ni-Ce <sub>x</sub> Zr <sub>y</sub> O <sub>2</sub> _ctab	0.1	-	0.03	-

#### 4.4.4 Methane Steam Reforming

Methane steam reforming (MSR) followed by MS detection of reactants and products and operando FTIR was performed at 673 K on Ni-ZrO<sub>2</sub>, Ni-CeO<sub>2</sub>, Ni-CeZr, Ni-Ce<sub>x</sub>Zr<sub>y</sub>O<sub>2</sub>\_comb, Ni-Ce<sub>x</sub>Zr<sub>y</sub>O<sub>2</sub>\_cp and Ni-Ce<sub>x</sub>Zr<sub>y</sub>O<sub>2</sub>\_ctab.

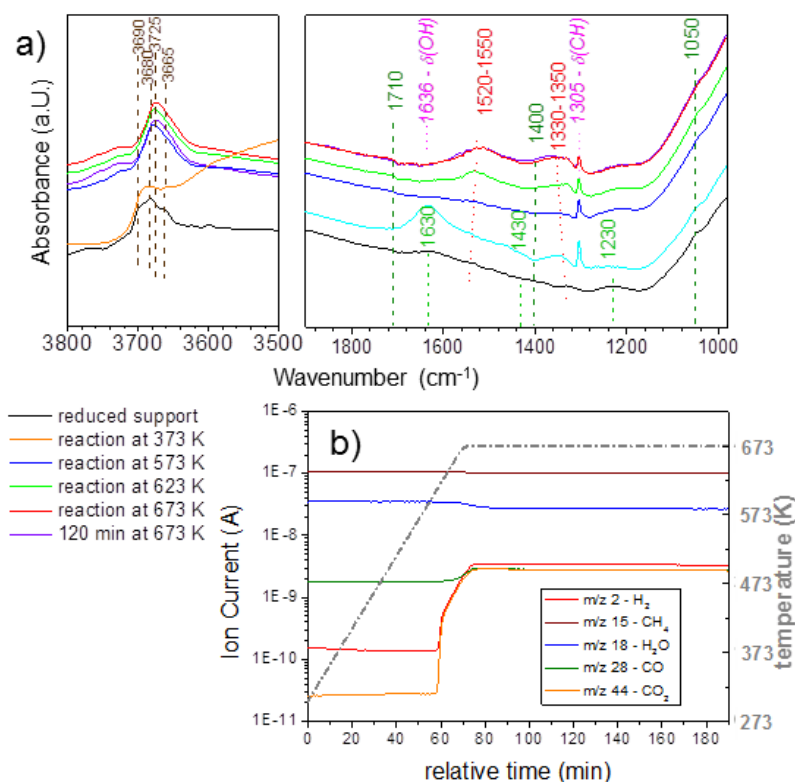


Fig. 44. a) operando FTIR and b) MS detected reactants and products during temperature programmed MSR over Ni-ZrO<sub>2</sub> up to 673 K.

Fig. 44 shows reactivity for MSR and changes on the catalyst observed by FTIR over Ni-ZrO<sub>2</sub>. Prior to the reaction only a small amount of bridged bidentate carbonates at 1630, 1430

and 1230 cm<sup>-1</sup> is observed by FTIR in the range 1900-900 cm<sup>-1</sup>. In the reaction mixture bidentate carbonates appear additionally. At about 620 K H<sub>2</sub> and CO<sub>2</sub> formation sets in and the amount of bidentate biscarbonate increases on the surface. The vibrations of bidentate carbonates shift from 1550 to 1520 and from 1330 to 1350 cm<sup>-1</sup> when reactivity sets in. During two hours of reaction at 673 K neither the catalyst nor its reactivity towards MSR are changing. Both terminal and bridged OH-groups are observed on the reduced catalyst and during reaction. The reactivity and stability of Ni-CeZr (not shown) is basically identically with that of Ni-ZrO<sub>2</sub> indicating, that the addition of a low loading of 5 % w/w ceria by impregnation doesn't influence the catalytic behaviour of the nickel catalyst.

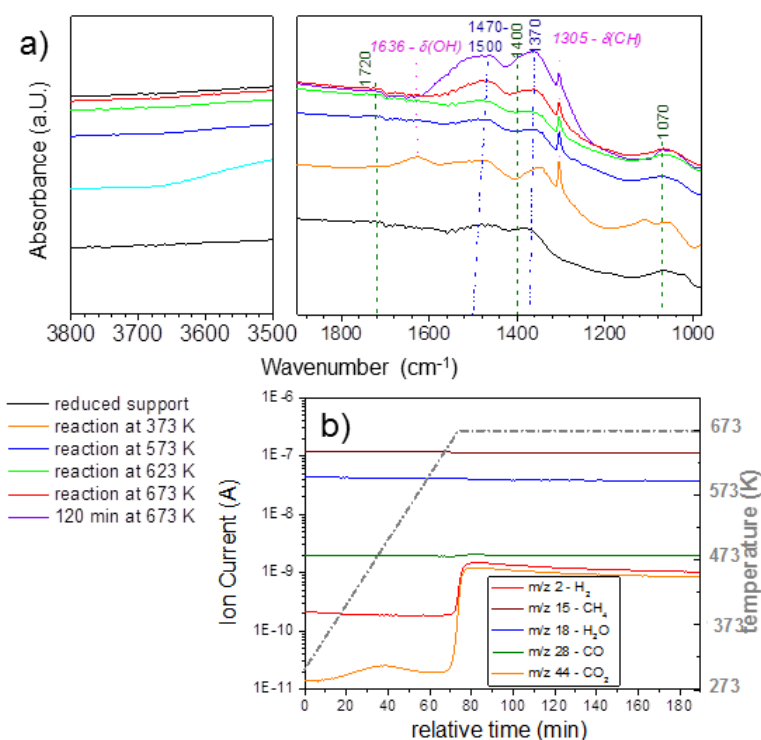


Fig. 45. a) operando FTIR and b) MS detected reactants and products during temperature programmed MSR over NiCeO<sub>2</sub> up to 673 K.

Over Ni-CeO<sub>2</sub>, as shown in Fig. 45, after little CO<sub>2</sub> evolution already at about 473 K, H<sub>2</sub> starts and CO<sub>2</sub> formation strongly increases at about 650 K. The amount of monodentate carbonates at 1470-1500 cm<sup>-1</sup> and 1370 cm<sup>-1</sup> is increasing, too in this temperature range. During reaction at 673 K the reactivity slowly decreases and the amount of monodentate carbonates further increases. No peaks are observed in the OH region of the FTIR spectra besides of molecular water at 373 K.

Over Ni-Ce<sub>x</sub>Zr<sub>y</sub>O<sub>2</sub>\_comb, as shown in Fig. 46, reactivity already sets in at about 573 K and then slowly increases with simultaneously increase of bidentate carbonates at 1510-1550 and 1330-1350 cm<sup>-1</sup>. Besides of molecular water at low temperatures, no OH bands are observed. The catalytic activity significantly decreases during reaction at 673 K.

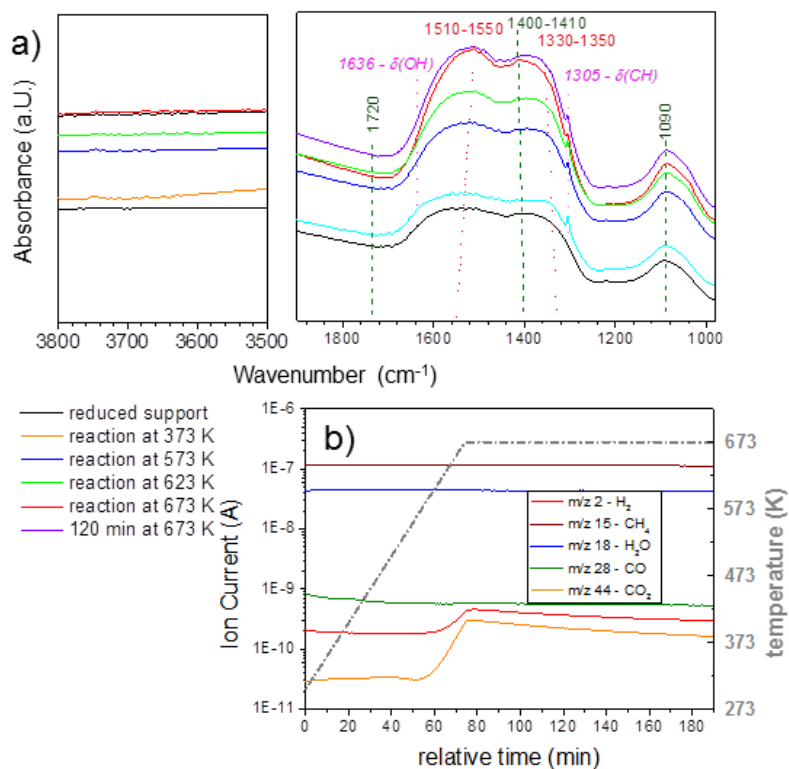


Fig. 46. a) operando FTIR and b) MS detected reactants and products during temperature programmed MSR over NiCeZr<sub>x</sub>\_comb up to 673 K.

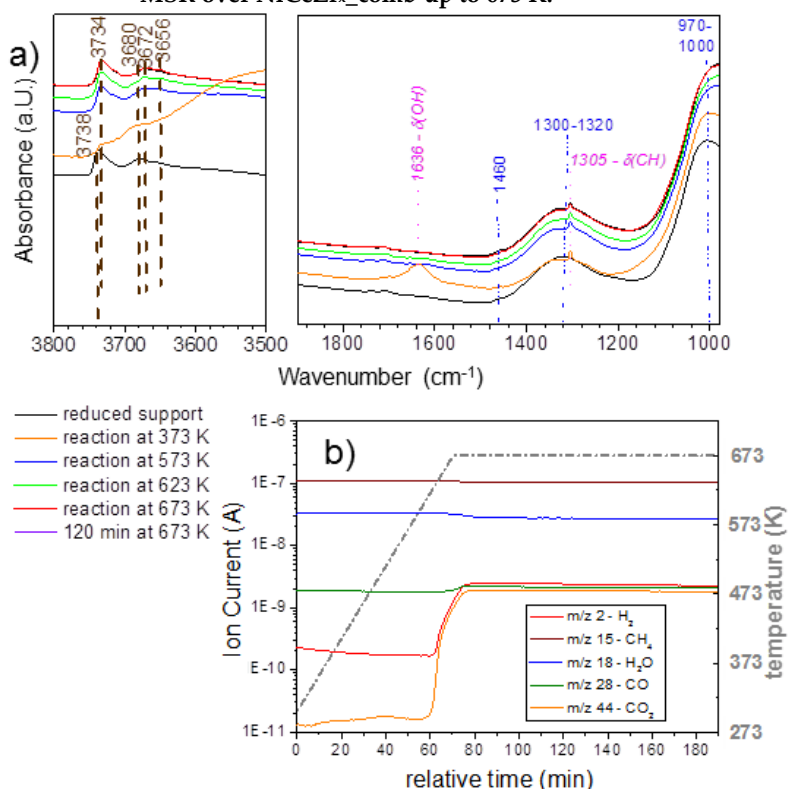


Fig. 47. a) operando FTIR and b) MS detected reactants and products during temperature programmed MSR over NiCeZr<sub>x</sub>\_cp up to 673 K.

Ni-Ce<sub>x</sub>Zr<sub>y</sub>O<sub>2</sub>\_cp shows about the same catalytic activity as Ni-ZrO<sub>2</sub> even though much less carbonates are observed over this catalyst, as shown in Fig. 47. Only a small amount of

monodentate carbonates at 1460 and 1300-1320 cm<sup>-1</sup> are observed and the catalytic activity remains stable during reaction. Both terminal and bridged OH bands are observed before and during reaction.

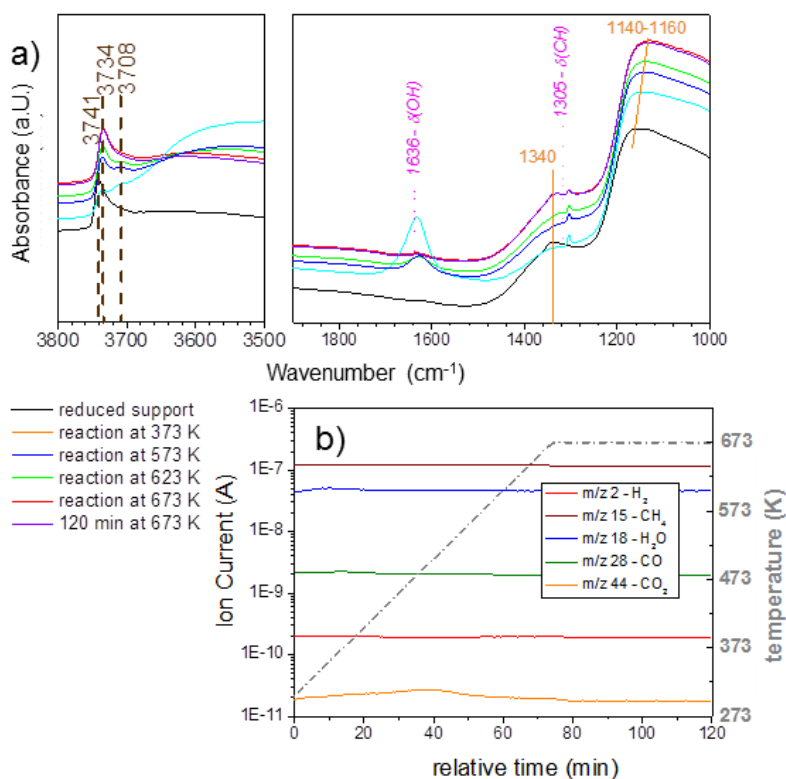


Fig. 48. a) operando FTIR and b) MS detected reactants and products during temperature programmed MSR over NiCeZr<sub>x</sub>\_ctab up to 673 K.

Ni-Ce<sub>x</sub>Zr<sub>y</sub>O<sub>2</sub>\_ctab, as shown in Fig. 48, is totally inactive besides of insignificant CO<sub>2</sub> evolution during heating in the reaction mixture. No formation of carbonates during interaction with the reactants and only terminal but no bridged hydroxyl groups are observed by FTIR.

Considering the FTIR spectra of all samples, a strong influence of the preparation method on the ability of carbonate formation and the presence of hydroxyl groups is observed. Except of Ni-Ce<sub>x</sub>Zr<sub>y</sub>O<sub>2</sub>\_ctab, all catalysts are active for MSR. The highest activity is observed for Ni-ZrO<sub>2</sub> Ni-CeZr and Ni-Ce<sub>x</sub>Zr<sub>y</sub>O<sub>2</sub>\_cp.

#### 4.4.5 Methane Dry Reforming

Ni-ZrO<sub>2</sub>, Ni-CeO<sub>2</sub> and the two catalysts supported on mixed oxides prepared by co-precipitation Ni-Ce<sub>x</sub>Zr<sub>y</sub>O<sub>2</sub>\_cp and Ni-Ce<sub>x</sub>Zr<sub>y</sub>O<sub>2</sub>\_ctab were tested for methane dry reforming (MDR). Prior to the reaction, the catalysts were oxidized at 773 K and reduced at 873 K. The results obtained for MDR reaction at 873 K for 24 hours are presented in Fig. 49. The direct measure of the thermal stability of a given catalyst is its catalytic activity and stability. It can be observed that the CH<sub>4</sub> and CO<sub>2</sub> conversion over Ni-ZrO<sub>2</sub> hardly changed over time while the conversion over Ni-CeO<sub>2</sub> rapidly and over Ni-Ce<sub>x</sub>Zr<sub>y</sub>O<sub>2</sub>\_cp continuously decreased. Ni-

Ce<sub>x</sub>Zr<sub>y</sub>O<sub>2-ctab</sub> was rarely active during the first 30 minutes before it completely deactivated. The H<sub>2</sub>:CO ratio achieved was below 1 due to reverse water-gas-shift reaction as a side reaction. The highest value was achieved over Ni-CeO<sub>2</sub> with strong decrease with time on stream. C-Balance as indication for coke formation when below 1 is increasing to 1 or nearly-1 after the first 2 hours. The H<sub>2</sub> and CO production rates are, in agreement with the reactant conversions, stable over Ni-ZrO<sub>2</sub> and decreasing with time on stream over Ni-CeO<sub>2</sub> and Ni-Ce<sub>x</sub>Zr<sub>y</sub>O<sub>2-cp</sub>. Over Ni-Ce<sub>x</sub>Zr<sub>y</sub>O<sub>2-ctab</sub> only little initial H<sub>2</sub> and CO production is observed before the catalyst is completely deactivated for methane dry reforming. The H<sub>2</sub> selectivity was around 75 % over both Ni-ZrO<sub>2</sub> and Ni-Ce<sub>x</sub>Zr<sub>y</sub>O<sub>2-cp</sub> during the whole time on stream indicating permanent H<sub>2</sub>O production during reaction while over Ni-CeO<sub>2</sub> the H<sub>2</sub> selectivity changes with time.

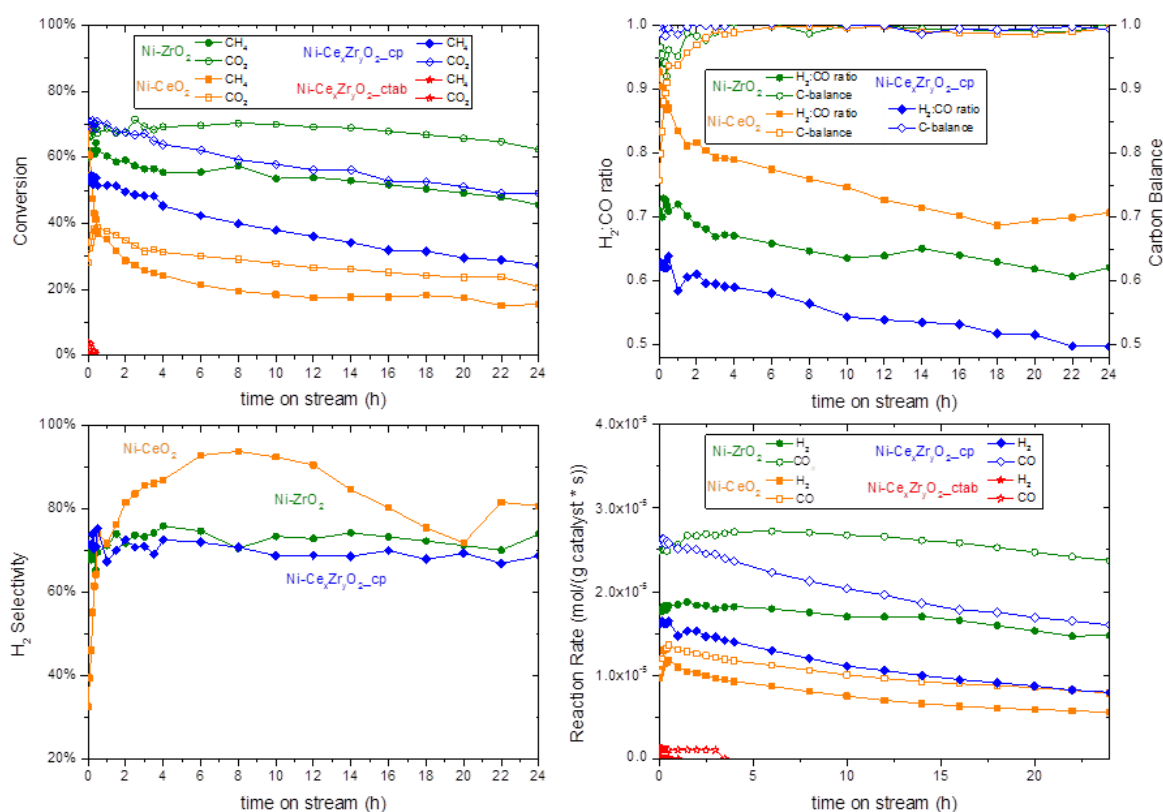


**Fig. 49.** Screening of Ni-ZrO<sub>2</sub>, Ni-CeO<sub>2</sub>, Ni-Ce<sub>x</sub>Zr<sub>y</sub>O<sub>2-cp</sub> and Ni-Ce<sub>x</sub>Zr<sub>y</sub>O<sub>2-ctab</sub> catalysts for methane dry reforming reaction at 873 K; feed composition: CH<sub>4</sub>:CO<sub>2</sub>:Ar = 10/10/80; feed flow rate = 25 ml/min.

The turn-over-frequency (TOF) for H<sub>2</sub> production rate based on the metallic Ni surface area after reduction at 600 °C are given in Table 8 normalized to the number of surface nickel atoms assuming  $1.59 \cdot 10^{19}$  nickel atoms/m<sup>2</sup>[186].

Table 8. Turn-over frequencies for methane conversion normalized to the number of surface nickel atoms during MDR.

sample	turn-over frequency (TOF) (s <sup>-1</sup> )		
	initial	after 3 hours	after 24 hours
Ni-ZrO <sub>2</sub>	12.1	4.2	4.4
Ni-CeO <sub>2</sub>	11.4	1.6	4.0
Ni-Ce <sub>x</sub> Zr <sub>y</sub> O <sub>2</sub> _cp	9.2	1.0	2.2

Since the reaction mixture consists of an oxidizing (CO<sub>2</sub>) and reducing (CH<sub>4</sub>) reactant, the question arises how the oxidation state of nickel in the beginning of the reaction affects the catalytic activity. The results shown above were obtained when the reactants were introduced to the quartz flow reactor directly after reduction at 873 K followed by inert gas flow for about 20 minutes at 873 K to completely remove the H<sub>2</sub> from the system. In a second experiment, the catalysts were *ex situ* oxidized and exposed to air at room temperature before heating again to 873 K in Ar gas flow with 10 K/min where the reaction was performed. As observed by TEM (4.4.2) and XAS (4.4.6) of these catalysts after *ex situ* reduction, nickel is completely re-oxidized due to exposure to air at room temperature.

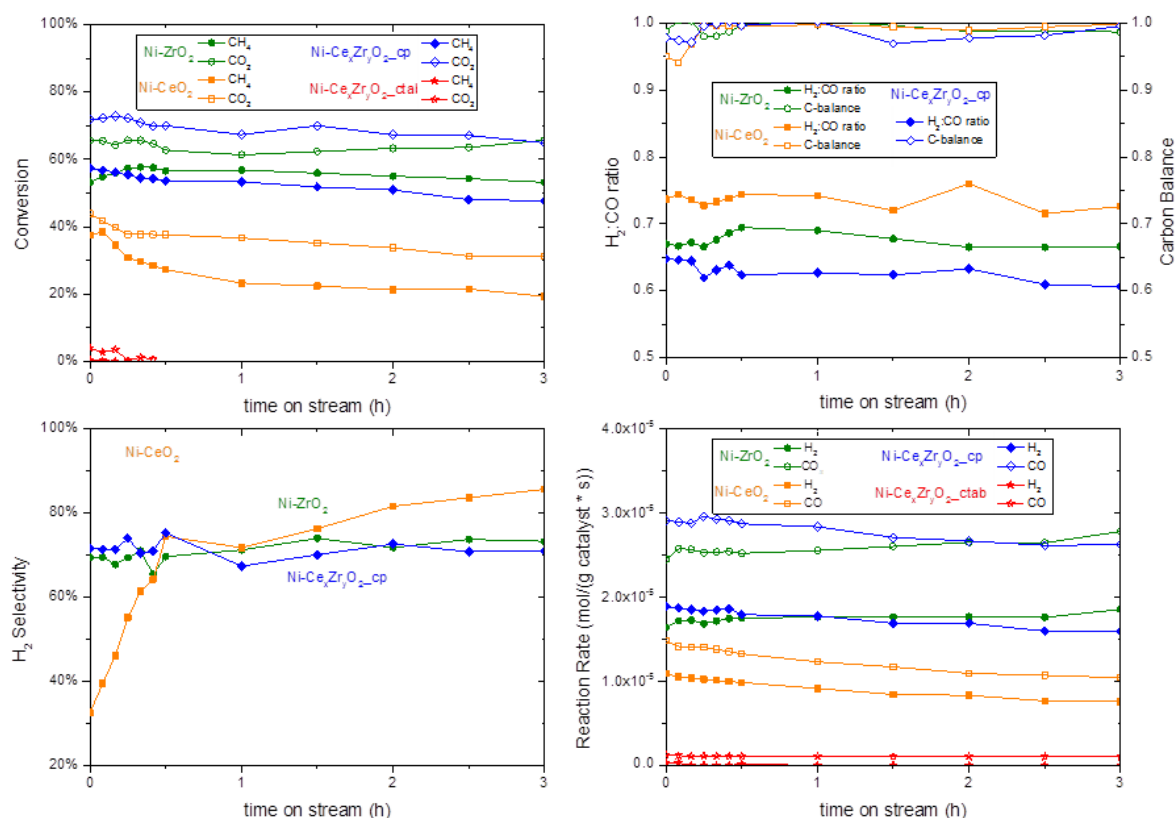


Fig. 50. Screening of Ni-ZrO<sub>2</sub>, Ni-CeO<sub>2</sub>, Ni-Ce<sub>x</sub>Zr<sub>y</sub>O<sub>2</sub>\_cp and Ni-Ce<sub>x</sub>Zr<sub>y</sub>O<sub>2</sub>\_ctab catalysts for methane dry reforming reaction at 873 K; feed composition: CH<sub>4</sub>:CO<sub>2</sub>:Ar = 10/10/80; feed flow rate = 25 ml/min. In contrast to the screening shown in Fig. 49, the catalysts were exposed to air between pretreatment and reaction.

As shown in Fig. 50, differences to the *in situ* reduced catalysts are only observed during the first 30 minutes of reaction. The higher initial CO<sub>2</sub> conversion indicates, that CO<sub>2</sub> is consumed due to oxidation of nickel.

#### 4.4.6 Post-MDR-studies

Via temperature programmed oxidation the amount of coke produced during 3 hours was compared with that produced during 24 hours of reaction. Used catalysts after 3 hours MDR were further analysed via transmission electron microscopy and X-ray absorption spectroscopy. Temperature programmed oxidation (TPO) was formed to obtain insights into coke formation. The amount of carbon dioxide formed during TPO provides information about the amount of coke formed during after 24 hours reaction in CH<sub>4</sub> and CO<sub>2</sub> and the temperature which is needed to burn off the carbon species may be characteristic for the carbon bond strength to the catalyst's surface. Fig. 51 shows the production of carbon dioxide during TPO in 20 % O<sub>2</sub> in Ar after methane dry reforming reaction.

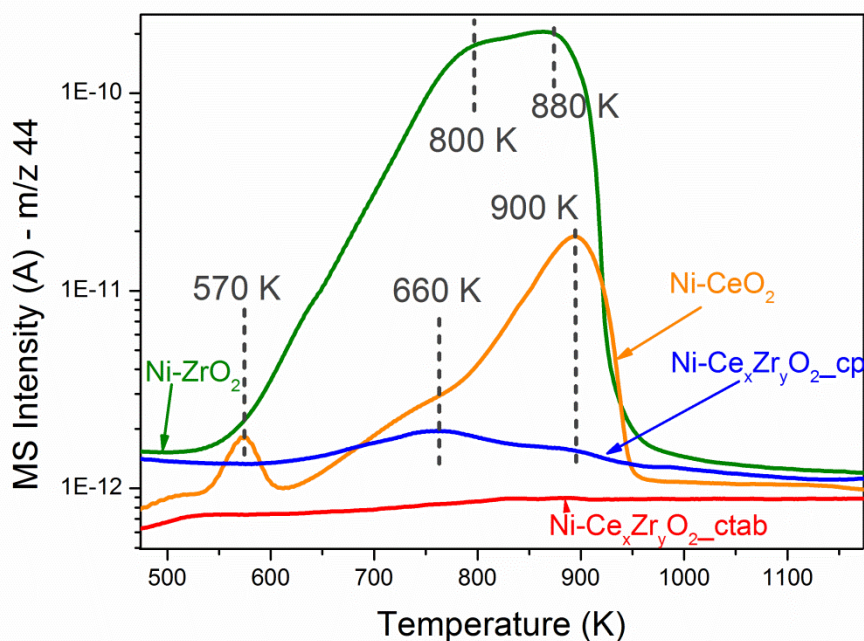


Fig. 51. Temperature Programmed Oxidation performed after 24 hours MDR with 20% O<sub>2</sub> in Ar.

Over Ni-ZrO<sub>2</sub> clearly the highest amount of coke was formed and temperatures of 880 K are needed to oxidize most of it. The small maximum of CO<sub>2</sub> evolution at 570 K over the Ni-CeO<sub>2</sub> catalyst can be assigned to the oxidation of amorphous carbon<sup>[187, 188]</sup> and around 800 K graphitic carbon is oxidized<sup>[35]</sup>. The CO<sub>2</sub> evolution around 880 K can be assigned to oxidation of whisker type carbon which does not deactivate the nickel surface but rather causes a breakdown of the catalyst by pore plugging<sup>[30]</sup>. The amount of CO<sub>2</sub> formed over Ni-ZrO<sub>2</sub> is about 20 times more than on Ni-CeO<sub>2</sub> and about 200 times more than on the almost inactive Ni-Ce<sub>x</sub>Zr<sub>y</sub>O<sub>2</sub>-cp. On Ni-Ce<sub>x</sub>Zr<sub>y</sub>O<sub>2</sub>-ctab as expected hardly any CO<sub>2</sub> is formed during TPO.

This is clearly a huge advantage of the Ni-Ce<sub>x</sub>Zr<sub>y</sub>O<sub>2</sub>-cp catalyst over the Ni-ZrO<sub>2</sub> even though the large amount of carbon formed during reaction apparently hardly affects the Ni-

ZrO<sub>2</sub> catalyst activity. The major problem of carbon deposition in a continuous flow reactor is the ability of blocking the reactor leading to physical blockage of the tube reactor. This was observed when increasing the amount of catalyst used for catalytic tests. Fig. 52 shows the CO<sub>2</sub> evolution during TPO after 3 hours MDR. The amount of coke formed on Ni-ZrO<sub>2</sub> and Ni-Ce<sub>x</sub>Zr<sub>y</sub>O<sub>2\_cp</sub> is only insignificantly smaller than after 24 hours MDR indicating that coke deposition mainly happens during the beginning of the reaction. In contrast, the amount of CO<sub>2</sub> over Ni-CeO<sub>2</sub> is definitely dependent of the reaction time.

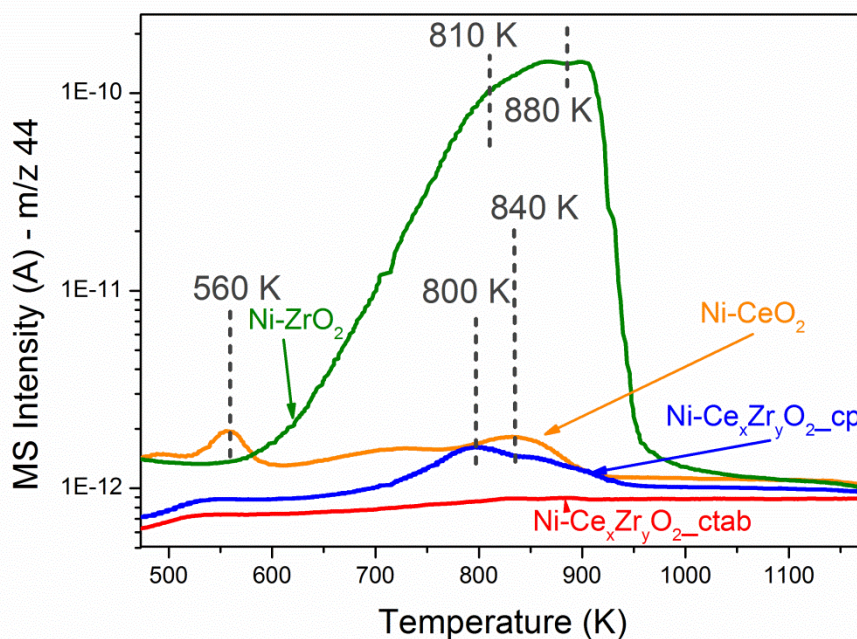


Fig. 52. Temperature Programmed Oxidation performed after 3 hours MDR with 20% O<sub>2</sub> in Ar.

Fig. 53 shows TEM images of Ni-ZrO<sub>2</sub> (a) and Ni-Ce<sub>x</sub>Zr<sub>y</sub>O<sub>2\_cp</sub> (b) dry reforming at 873 K for 3 hours. On both catalysts filamentous carbon has formed and some Ni particles are on top of these carbon nanofibers, tubes or rods. On Ni-CeO<sub>2</sub> and Ni-Ce<sub>x</sub>Zr<sub>y</sub>O<sub>2\_ctab</sub> no filamentous carbon was detected.

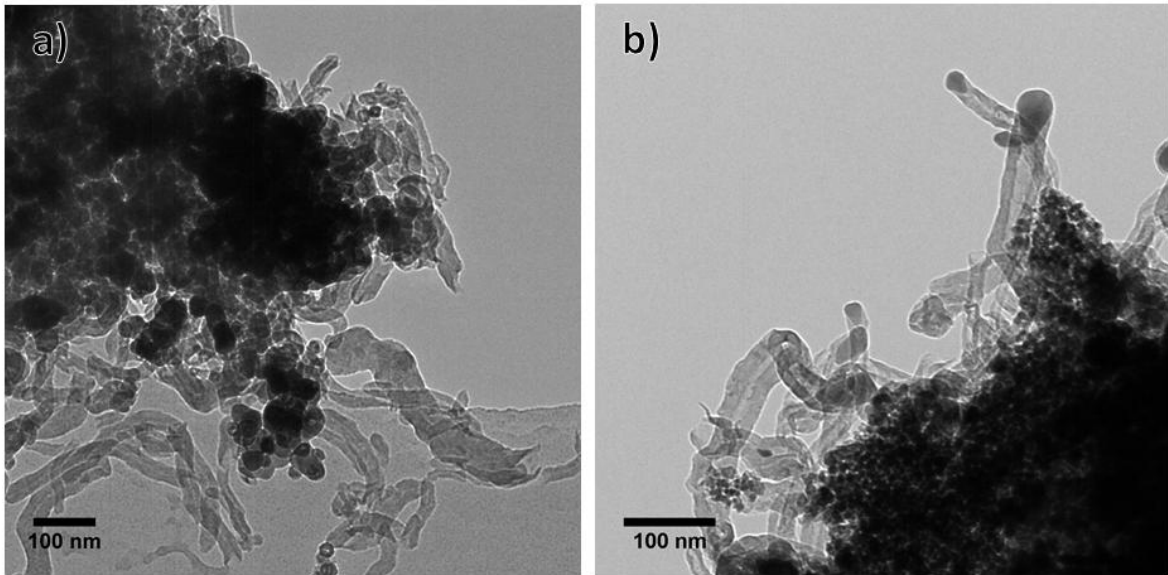


Fig. 53. TEM images of a) Ni-ZrO<sub>2</sub> and b) Ni-Ce<sub>x</sub>Zr<sub>y</sub>O<sub>2\_cp</sub> after exposure to methane and carbon dioxide at 600 °C for 3 hours.

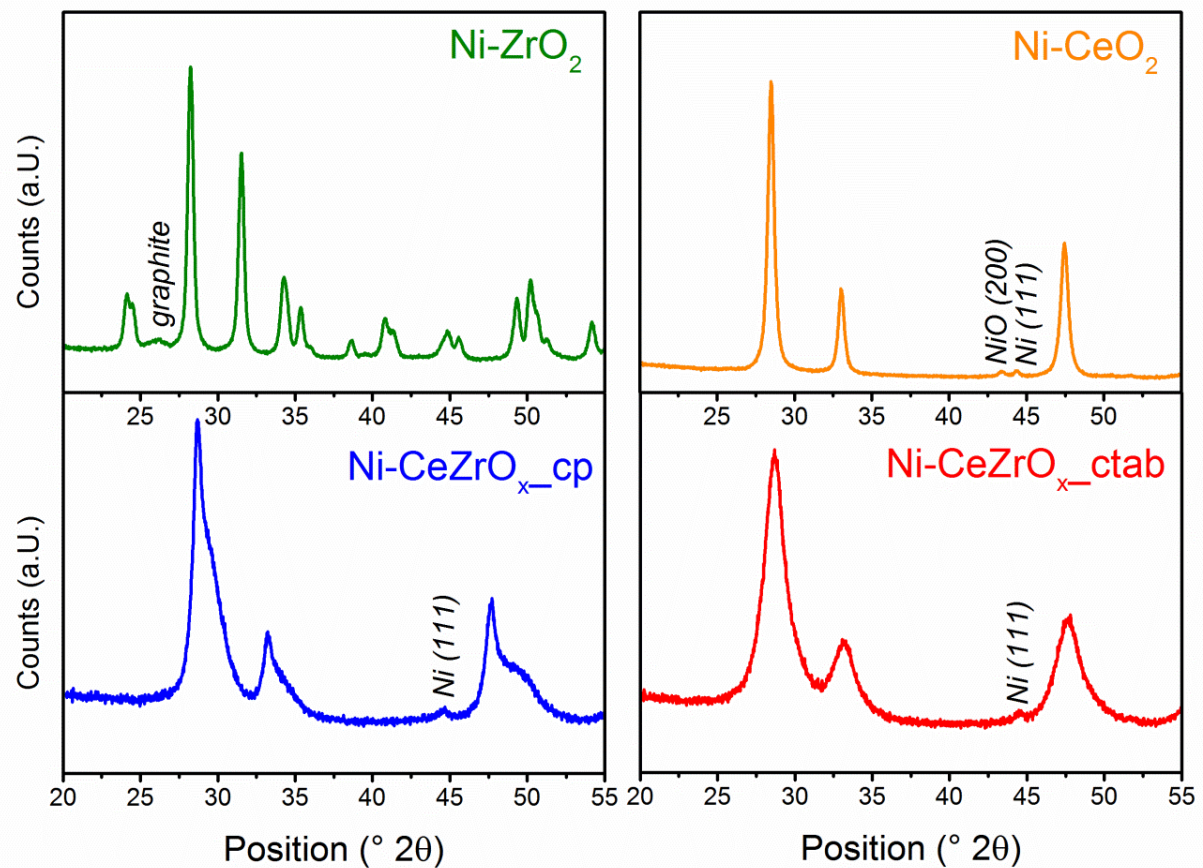


Fig. 54. XRD patterns of the Ni-ZrO<sub>2</sub>, Ni-CeO<sub>2</sub>, Ni-Ce<sub>x</sub>Zr<sub>y</sub>O<sub>2\_cp</sub> and Ni-Ce<sub>x</sub>Zr<sub>y</sub>O<sub>2\_ctab</sub> after MDR for 3 hours at 873 K

Fig. 54 shows a section of diffractograms of the samples after reaction at 600 °C. In contrast to the diffractograms shown in Fig. 54, the reflections of NiO have disappeared or – in case of

Ni-CeO<sub>2</sub> decreased in intensity and the reflection of Ni(111) at 44.3 ° 2θ is observed on Ni-CeO<sub>2</sub> and the mixed oxide supported samples. On Ni-ZrO<sub>2</sub> this reflection is overlapping with one of monoclinic ZrO<sub>2</sub>. The crystallite sizes calculated with Scherrer's equation are 27 nm, 23 nm and 21 nm on Ni-CeO<sub>2</sub>, Ni-Ce<sub>x</sub>Zr<sub>y</sub>O<sub>2\_cp</sub> and Ni-Ce<sub>x</sub>Zr<sub>y</sub>O<sub>2\_ctab</sub>, respectively and thus not much larger than the NiO crystallites of the catalysts after ex-situ reduction. The reflection at 26.1 ° 2θ in the diffractogram of the used Ni-ZrO<sub>2</sub> catalyst is assigned to graphite. On the other samples much less carbon was observed by TPO and it might be mainly amorphous.

Fig. 55 shows graphical representations of the Ni K-edge normalized  $\mu(E)$  in the XANES region (a) and the first derivative of the  $\mu(E)$  data in the XANES region (b). The latter reveal several local maxima with two larger ones around 8333 eV and/or 8343 eV. The position of the largest maximum value with the first derivative of the  $\mu(E)$  data was chosen as the value of  $E_0$ . With the Ni fcc reference foil the first maximum at 8333 eV is the highest one. With NiO reference and the pre-reduced samples the highest maximum is apparently at 8343 eV and with the used samples it is also at 8343 eV.

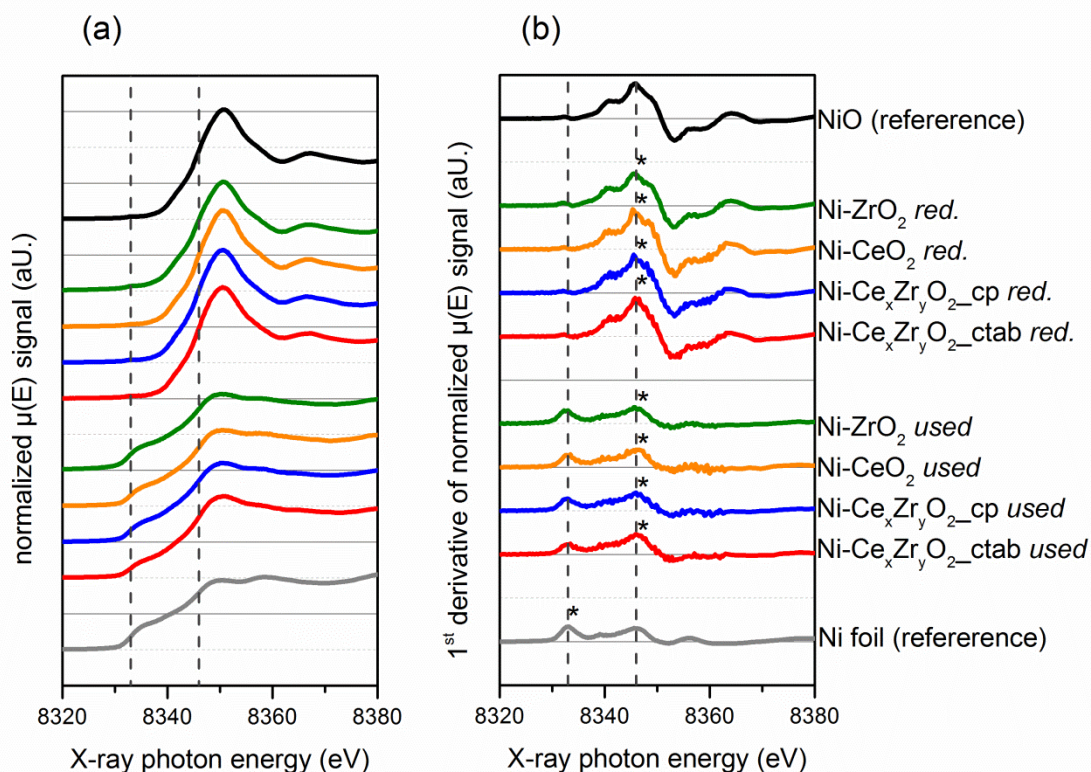
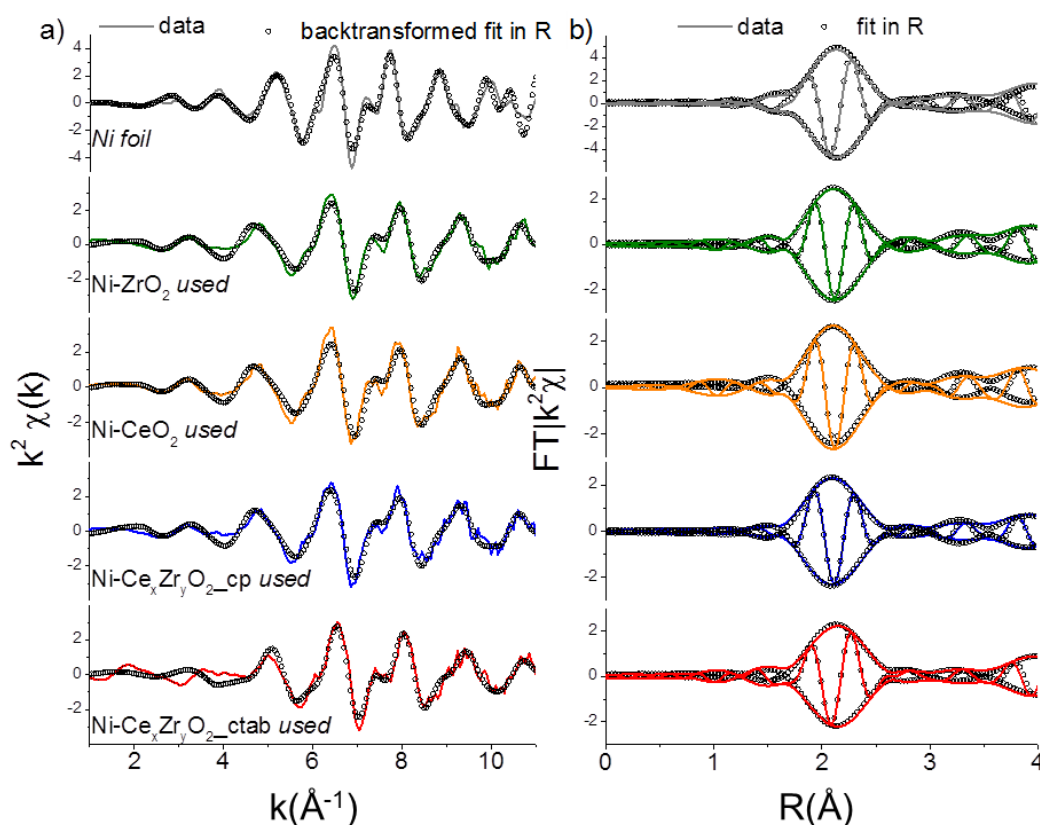


Fig. 55. a) normalized XANES spectra of reference samples and pre-reduced and used samples and b) first derivative of the spectra shown in a). The dashed lines in b) mark the positions of two local maxima at 8333 eV and 8343 eV. The asterisk (\*) labels the absolute maximum.

The XANES spectra of the reduced catalysts resemble that of NiO reference. Linear combination analysis of the spectra shown in Fig. 55 confirms that the Ni on all reduced

catalysts is oxidized. This proves that these catalysts are completely re-oxidized after exposure to air. Linear combination of the used catalysts, which were also exposed to air in between reaction and XAS measurement, resulted an amount of metallic nickel of 86 %, 84 %, 78 % and 70 % in Ni-ZrO<sub>2</sub>, Ni-CeO<sub>2</sub>, Ni-Ce<sub>x</sub>Zr<sub>y</sub>O<sub>2\_cp</sub> and Ni-Ce<sub>x</sub>Zr<sub>y</sub>O<sub>2\_ctab</sub>, respectively. In contrast to the reduced samples most of the Ni has remained metallic and did not get reoxidized. Since the Ni particles analysed in TEM and XRD were not significantly larger after reaction than before, sintering can be excluded. Possible explanations for the XANES spectra can be either that the carbon which has formed during reaction and deposited on the catalyst stabilizes the metallic state of nickel or a nickel carbide phase has formed. The XANES spectrum of Ni<sub>3</sub>C would more resemble the XANES of metallic Ni rather than NiO but show significant differences in the Fourier transforms of the  $\chi(k)$ . Ni<sub>3</sub>C was obtained and detected by XAS during Ni carburization<sup>[189, 190]</sup> and during low temperature steam reforming of ethanol over a ceria supported Ni catalyst<sup>[191]</sup>. Besides of carbon, nickel carbide formation is favored to form in the dry mixture of methane and carbon dioxide<sup>[106]</sup> and Ni<sub>3</sub>C formation was observed by Swaan et. al<sup>[192]</sup> while Goula et. al<sup>[193]</sup> discard any hypothesis of bulk nickel carbide formation during methane dry reforming.



**Fig. 56.**  $k^2$ -weighted EXAFS functions  $\chi(k)$  and magnitude and imaginary part of Fourier transforms (uncorrected for phase shifts) of  $\chi(k)$  of Ni-foil and the supported nickel catalysts after methane dry reforming reaction at 873 K. Solid lines: experimental data, hollowed spheres: fits in R-space and backtransformed into k-space.

The  $k^2$ -weighted  $k$  and  $R$  space EXAFS with their respective fits are shown in Fig. 56 and the best fitting structural parameters are presented in Table 9. According to these fittings, all

samples are well fitted by using Ni fcc. The formation of Ni<sub>3</sub>C could not be accredited due to the missing carbon signal from the first Ni-C coordination shell at the phase-uncorrected distance of  $R \sim 1.2 \text{ \AA}$ .

**Table 9.** Structural parameters resulting from multiple shell fits of the first Ni-Ni coordination shell in R-space to EXAFS data of Ni foil and post-reaction Ni supported catalysts.

<b>sample</b>	<b>R(Å)</b>	<b>CN</b>	<b><math>\sigma^2(\text{Å}^2)</math></b>	<b>R factor</b>
Ni foil	2.46 ± 0.00	12*	0.006	0.087
Ni-ZrO <sub>2</sub>	2.52 ± 0.05	9.6	0.005	0.073
Ni-CeO <sub>2</sub>	2.51 ± 0.05	11.1	0.006	0.084
Ni-Ce <sub>x</sub> Zr <sub>y</sub> O <sub>2</sub> _cp	2.55 ± 0.05	11.1	0.007	0.072
Ni-Ce <sub>x</sub> Zr <sub>y</sub> O <sub>2</sub> _ctab	2.53 ± 0.05	10.9	0.006	0.065

\* constrained for Ni foil

## Chapter 5

# Discussion

---

Alloy formation on bimetallic copper-nickel catalysts supported on  $\text{ZrO}_2$  was observed during reduction of the catalysts. Adsorption of CO was applied to determine the oxidation state and available surface sites. Copper-nickel alloy formation was indicated by the red-shift of the CO stretching frequency on metallic nickel by about  $30\text{ cm}^{-1}$  as well as by X-ray absorption measurements which revealed a lower reduction temperature of NiO and CuO in bimetallic alloyed samples as compared to monometallic catalysts. The extent of the red-shift of the Ni-CO band depends on the bulk composition. In addition, the composition affected the desorption temperature of CO on copper, resulting in significantly higher thermal stability on all the bimetallic samples.

Both hydrogen chemisorption and FTIR spectroscopy of CO adsorption clearly demonstrated that the very surface layer of the bimetallic particles was strongly enriched in Cu for the samples with different nominal copper:nickel bulk compositions.

With respect to the partial oxidation of methane, there was no advantage of adding Cu to Ni- $\text{ZrO}_2$  catalysts since Cu promoted the total oxidation of methane towards  $\text{CO}_2$  and  $\text{H}_2\text{O}$ .

$\text{CH}_4$  decomposition was studied on bimetallic CuNi- $\text{ZrO}_2$  catalysts by temperature programmed reaction, TPO and NAP-XPS in order to get insights into the *in situ* stability of CuNi compounds and the effect of Cu addition on the carbon chemistry. In contrast to monometallic Ni- $\text{ZrO}_2$ , an irreversible activation step was observed in methane at around 700 K, with the exact onset temperature depending on the composition, reduction temperature and metal loading. In the following we will discuss the potential origin and the factors affecting this surface modification process responsible for the onset of catalytic activity and take a closer look at the bimetallic Cu-Ni system.

The question arises what is the origin of the observed activation process occurring in methane between 650 and 735 K and leading to an irreversible modification of the catalytic performance of all bimetallic catalysts towards a Ni-like behaviour. Previous work on these materials allowed us to conclude that after reduction the surface of the bimetallic catalysts appears enriched in Cu<sup>[1]</sup> as indicated by selective  $\text{H}_2$  chemisorption on Ni and by FTIR spectroscopy of adsorbed CO. Since Cu is practically inactive in methane decomposition a

change in surface composition e.g. by Ni segregating to the surface is a potential reason for the drastic change in CH<sub>4</sub> decomposition activity. The interaction of Ni with C and/or CH<sub>x</sub> would be a likely driving force for the proposed surface segregation of Ni.

In contrast to H<sub>2</sub> chemisorption experiments at room temperature<sup>[1]</sup> showing that the surface is enriched in copper after reduction, the surface Cu:Ni ratio observed by XPS at 673 K was nearly similar to the overall Cu:Ni ratio of the catalyst. According to literature a copper-enriched top surface layer is in agreement with the lower surface free energy of copper compared to nickel<sup>[194]</sup>. According to Sachtler et al., the Gibbs free energy of a copper-nickel mixture at 475 K has a maximum at about 30 % copper and a minimum at 80 % and at 2 % copper<sup>[195]</sup> in the bulk. Therefore, we expect co-existing phases present at lower temperatures. Since the surface energy is lower for Cu compared to Ni the Cu-rich alloy phase is likely present at the surface and the Ni-rich alloy phase underneath (core-shell like structure). For Cu surfaces with Ni monolayers deposited on top it was reported in Refs.<sup>[196, 197]</sup> that Ni segregates into the first subsurface layer of Cu(100) as well as Cu(111)<sup>[198]</sup>. By theoretical calculations Pourovskii et al.<sup>[199]</sup> found a rather sharp minimum of the surface energy corresponding to the arrangement of a Ni layer in the second layer of Cu(100). Anyway, this surface composition is only present at low temperature. At elevated temperature the two phases become miscible. According to the Cu-Ni phase diagram, CuNi forms a single-phase alloy above 600 K.

As revealed by XPS measurements under reaction conditions, the increase of activity is clearly accompanied by an increase of the concentration of *metallic* Ni at the surface. Catalytic activity for methane decomposition therefore depends on the alloy surface composition, specifically on the presence of a sufficiently high concentration of metallic Ni at the surface.

Studt et al.<sup>[200]</sup> reported Ni segregation to the surface of CuNi alloys due to the higher bond strength towards CO. Li et al.<sup>[201]</sup> reported that the dissociative adsorption of methane and the formation of carbon flakes would be a plausible cause for their observation of reconstruction of Ni-Cu metal particles during methane decomposition reaction.<sup>[201]</sup> During methane decomposition reaction at 773 K recrystallization of the Ni-Cu alloy on copper-nickel-alumina catalysts was observed during induction of carbon formation in methane decomposition.<sup>[93]</sup> In a similar way, Ni could segregate to the very surface layer at elevated temperatures induced by the presence of methane and/or carbon, which consequently leads to an onset of catalytic activity for methane decomposition. Thus, the surface initially enriched in Cu at low temperatures exhibits low methane decomposition activity until the activation step changes the surface concentration of reduced Ni.

Ni segregation to the top surface is a potential explanation for the observed activation step. However, this could not be confirmed by quantitative analysis of the core level spectra, which is complicated by the (very likely) preferential decoration of Ni by carbon species formed over Ni during the reaction of methane. Nevertheless, there is clear evidence by the

XPS data that the sudden increase of reactivity can be linked to the higher concentration of reduced Ni at the surface.

When TPMD was carried out after applying a higher reduction temperature of 773 K an activation step was observed as well although the activation step temperature was lowered compared to the catalyst reduced at 673 K. Since reduction at 673 K leads to only partially reduced Ni<sup>[1]</sup> the ratio Ni:NiO is increased after reduction at higher temperature. The higher amount of metallic Ni (at or near the surface) after applying a higher reduction temperature could be a likely reason for the down-shift of the activation temperature.

Cu addition to Ni helps in the desired lowering of carbon deposition. TPO measurements showed a reduction of the amount of coke burnt off as CO<sub>2</sub> by about 50% when comparing Ni and the Ni-rich 13CuNi-ZrO<sub>2</sub> catalyst exhibiting similar catalytic activity (Table 3). Another effect of the Cu modification, which influences the carbon chemistry and coking behavior, is the decrease of the carbon oxidation temperature, probably due to a weaker bonding of carbon on the CuNi alloy surface.

Thus, Cu addition to Ni-ZrO<sub>2</sub> catalysts caused the formation of a CuNi alloy with high potential towards decreasing coke formation. However, since the CuNi alloy system is stable only in a limited range of conditions (temperatures up to around 700 K depending on the composition and pretreatment) the impact on methane reforming reactions, which usually occur at higher temperature, is strongly limited.

As a second part of this work, promotion of Ni-ZrO<sub>2</sub> via addition of ceria was studied. A strong dependence of the preparation method towards properties and catalytic performance was observed. As mentioned above, the addition of ceria via impregnation didn't cause any changes compared to Ni-ZrO<sub>2</sub>. Due to impregnation no interaction between zirconia and ceria can be expected and probably the amount of only 5 %w/w is too low for causing significant changes. The support material prepared by combustion synthesis consisted of rather small crystallites but had low specific surface area. Therefore, the chance for a better dispersion of nickel over the support is rather low. In terms of catalytic activity, no enhancement compared to Ni-ZrO<sub>2</sub> was observed and the already low catalytic activity decreased fast during catalytic methane steam reforming. Support preparation via co-precipitation yielded a material with small crystallite size and high surface area. Since the co-precipitation support Ce<sub>x</sub>Zr<sub>y</sub>O<sub>2\_cp</sub> consists of two mixed oxide phases, one tetragonal which is enriched in zirconia and one cubic which is enriched in ceria, surfactant assisted co-precipitation was performed. The addition of a surfactant during co-precipitation should increase the miscibility and therefore promote the formation of a single mixed oxide phase. Additionally, a larger surface area and higher coke resistance and sintering resistance has been observed due to the effect of surface assistance<sup>[72]</sup>. Even though a catalyst with high surface area consisting of one-phase ceria-zirconia mixed oxide was prepared, this catalyst showed no catalytic activity for the studied methane reforming reactions.

Huge differences in the catalytic performance of the two mixed oxide supported catalysts with same elemental composition were observed. The catalyst prepared by surfactant assisted co-precipitation showed promising textural properties such as high surface area what is correlated with good metal dispersion. Nevertheless, after reduction at 600 °C hardly any H<sub>2</sub> could adsorb, as shown with hydrogen chemisorption measurements, what indicates that no accessible metallic nickel is on the catalyst.

Considering the active Ni-Ce<sub>x</sub>Zr<sub>y</sub>O<sub>2</sub>\_cp catalyst, no advantage compared to Ni-ZrO<sub>2</sub> in terms of conversion or H<sub>2</sub>-selectivity was observed but the formation of filamentous carbon was strongly suppressed. As reported in Literature, the mixed oxide support material leads to acceleration of gasification of coke deposits on Pt particles which is related to the increase of the oxygen mobility on the surface<sup>[202]</sup> and the higher surface density of active sites on the ternary catalyst<sup>[6]</sup>.

The inactivity of the Ni-Ce<sub>x</sub>Zr<sub>y</sub>O<sub>2</sub>\_ctab catalyst could be explained by the inaccessibility of metallic Ni for hydrogen adsorption after reduction at 873 K. Since the surfactant was CTAB, which was used for the synthesis of the mixed oxide support material, residual bromide was considered to affect the catalytic activity. Residual chloride from Cl-containing Pt precursors was reported to have an enormous effect towards selectivity of the catalyst<sup>[203]</sup>, a similar effect of other halogens could be possible. Even though no bromide was detected by elemental analysis, an additional catalyst was prepared by impregnating the co-precipitation support with ammonium bromide (MERCK) before adding Ni. The amount of Br was the same as used for the preparation of Ni-Ce<sub>x</sub>Zr<sub>y</sub>O<sub>2</sub>\_ctab. The methane conversion over this brominated catalyst was about the same as over Ni-Ce<sub>x</sub>Zr<sub>y</sub>O<sub>2</sub>\_cp, namely 56.7 % initially (57.4 % over Ni-Ce<sub>x</sub>Zr<sub>y</sub>O<sub>2</sub>\_cp) and 46.5 % after 3 h time on stream (47.7 % over Ni-Ce<sub>x</sub>Zr<sub>y</sub>O<sub>2</sub>\_cp). Therefore, a negative effect due to the utilization of the bromide containing surfactant can be excluded. Thus, the only sensible explanation for the lack of catalytic activity or extremely fast deactivation of Ni-Ce<sub>x</sub>Zr<sub>y</sub>O<sub>2</sub>\_ctab can be assigned to the inaccessible Ni surface area observed by H<sub>2</sub>-Chemisorption and the observation in TEM, that Ni particles were always surrounded by support. The absence of catalytic activity of the Ni-Ce<sub>x</sub>Zr<sub>y</sub>O<sub>2</sub>\_ctab catalyst, which is in contrast to reports in the literature<sup>[72, 74, 75, 77]</sup>, is not attributed to this synthesis method in general, but the complex nature of this kind of synthesis compared to the rather simple impregnation, combustion and co-precipitation catalysts.

Considering the most active mixed oxide supported catalyst Ni-Ce<sub>x</sub>Zr<sub>y</sub>O<sub>2</sub>\_cp no improvement of catalytic activity for MSR or MDR could be achieved but the stability against coke formation was strongly increased and especially the formation of filamentous carbon was strongly suppressed compared to Ni-ZrO<sub>2</sub>. The suppression of formation of filamentous carbon, which can be certainly achieved by using ceria-zirconia as a support material, is beneficial to reduce the probability of blockage of the reactor tube in a flow-through system.

## Chapter 6

# Summary and Conclusions

---

The effect of modification of a Ni-ZrO<sub>2</sub> catalyst in order to prevent coke deposition during methane reforming reactions was examined via different approaches. In the first part of this thesis, the modification of the metallic Ni component with copper was studied and in the second part, the support was modified by ceria-addition. In both cases, significant differences in terms of catalytic activity and stability were observed.

CuNi alloy formation on the bimetallic supported catalysts was observed by infrared spectroscopy with CO as a probe molecule and with X-ray absorption spectroscopy. Via CO adsorption, a shift of the Ni<sup>0</sup>-CO band on the bimetallic catalyst compared to Ni-ZrO<sub>2</sub> was attributed to a strong interaction of neighbouring Cu atoms and therefore, formation of a CuNi alloy. Via X-ray absorption spectroscopy, alloy formation was indicated with strongly decreased reduction temperature of nickel in the bimetallic catalyst compared to monometallic nickel-zirconia. In addition to the FTIR studies, an enrichment of the very surface with copper was observed by H<sub>2</sub>-Chemisorption. Transmission electron microscopy showed particles containing both nickel and copper but also small copper containing no nickel.

The catalytic activity for partial oxidation of methane was studied in a repeated temperature programmed experiments. Addition of copper didn't cause any enhancement of this reaction since copper directed the selectivity towards complete oxidation of methane.

During methane decomposition, the bimetallic catalysts didn't show any catalytic activity until an activation step occurred, which irreversibly changed the catalytic performance to a state very similar to that of monometallic Ni-ZrO<sub>2</sub>. As observed by temperature programmed oxidation after methane decomposition, Cu addition to Ni improved the desired resistance against carbon deposition by lowering the amount of coke formed. Also lower temperature was required to burn off carbon from the bimetallic catalysts, as compared to Ni-ZrO<sub>2</sub>.

By *in situ* (operando) synchrotron-based near ambient pressure XPS the composition of the surface was determined and correlated with the catalytic performance. A sudden increase of catalytic activity could be explained by an increase of the concentration of reduced Ni atoms at the catalyst surface in the active state, likely as a consequence of the interaction with

methane. XPS showed the appearance of an additional Cu species on the catalyst surface, when catalytic activity sets in. This species could not be conclusively identified, but is related to the catalyst surface according to the depth profiles recorded.

C 1s core level spectra revealed the presence of various carbonaceous species. The signal attributed to carbon nanotubes increased when activity sets in, while the amount of graphite and carbide decreased again.

As a key result on the Cu-modification of Ni catalysts, we conclude that the CuNi alloy shows limited stability under reaction conditions. This system is stable only in a limited range of temperature up to ~700K in hydrocarbon atmosphere. Above this temperature, the alloy phase becomes unstable, and carbon-induced segregation of Ni species induces a fast increase of methane decomposition rate. In view of the applicability of this system, a detailed understanding of the stability and surface composition of the bimetallic phases present and the influence of the Cu promoter on the surface chemistry under actual reaction conditions are essential.

Support materials consisting of ceria, zirconia and mixed ceria-zirconia oxides prepared via different synthesis routes showed very different properties. Only support prepared by impregnation didn't show any significant differences to Ni-ZrO<sub>2</sub>. According to X-ray diffraction data, pure ZrO<sub>2</sub> consists of monoclinic crystallites. The crystallite size of all prepared mixed oxides was smaller than that of monoclinic ZrO<sub>2</sub>. In case of the co-precipitation support Ce<sub>x</sub>Zr<sub>y</sub>O<sub>2</sub>\_cp two ceria-zirconia mixed oxide phases were found. The support prepared by combustion synthesis consisted of small tetragonal mixed oxide crystallites but the lowest surface area. This kind of synthesis was least controllable due to the highly exothermic reaction which formed the mixed oxide. The highest specific surface area was observed for the two catalysts prepared by co-precipitation.

FTIR spectroscopy with CO as a probe molecule observed that, as on Ni-ZrO<sub>2</sub>, both oxidized and reduced nickel are present on the surface of the mixed oxide supported catalysts. In contrast, on Ni-CeO<sub>2</sub> only reduced Ni was present on the surface.

Catalytic methane steam and dry reforming showed that only with Ni-Ce<sub>x</sub>Zr<sub>y</sub>O<sub>2</sub>\_cp a performance comparable with that of Ni-ZrO<sub>2</sub> was observed. Besides of the inactive Ni-Ce<sub>x</sub>Zr<sub>y</sub>O<sub>2</sub>\_ctab catalyst, all catalysts were active for methane reforming.

Except of the surfactant assisted synthesis route, which was used for the preparation of Ce<sub>x</sub>Zr<sub>y</sub>O<sub>2</sub>\_ctab, only facile preparation routes were applied for the synthesis of the various mixed oxide supports. The advantage of these routes is the easy realization without complex precursors which need to be removed after the synthesis.

It could be shown that the catalytic activity of a supported catalyst depends not only on the active metallic site but also strongly on the support. When considering the support material,

not only the nature or composition of this oxide material is relevant but the method applied for support preparation plays an important role, too.

Even though no enhancement of the catalytic activity was observed for these mixed oxide supported catalyst, a strong decrease in terms of coke formation was observed by temperature programmed oxidation after methane dry reforming. The amount of carbon formed on the active mixed oxide supported catalyst Ni-Ce<sub>x</sub>Zr<sub>y</sub>O<sub>2\_cp</sub> was about 200 times lower than that on Ni-ZrO<sub>2</sub> which is a great advantage for a catalyst working at 873 K which is a low temperature for methane dry reforming.

# List of Abbreviations

---

BET	Method for determining pore size and volume by gas adsorption or desorption developed by Barret, Joyner and Halenda <sup>[185]</sup>
BJH	Method for determining the surface area by gas adsorption named after its inventors Brunauer, Emmett and Teller <sup>[184]</sup>
CTAB	Cetyltrimethylammonium Bromide
EDX	Energy Dispersive X-Ray Spectroscopy
EXAFS	Extended Absorption Fine Structure
FFT	Fast Fourier Transform
FID	Flame Ionization detector
FTIR	Fourier Transformed Infrared
GC	Gas Chromatograph
HERFD-XAS	High Energy Resolution Fluorescence Detected X-Ray Absorption Spectroscopy
MDR	Methane Dry Reforming
MFC	Mass Flow Controller
MS	Mass spectrometer
MSR	Methane Steam Reforming
NAP-XPS	Near Ambient Pressure X-Ray Photoelectron Spectroscopy
STP	Standard Temperature and Pressure
TCD	Thermal Conductivity Detector
TEM	Transmission Electron Microscopy
TPD	Temperature Programmed Desorption
TPMD	Temperature Programmed Methane Decomposition
TPO	Temperature Programmed Oxidation
XANES	X-Ray Near Edge Structure
XAS	X-Ray Absorption Spectroscopy
XPS	X-Ray Photoelectron Spectroscopy
XRD	X-Ray Diffraction

# List of Figures

---

Fig. 1.	Simplified mechanism of CO <sub>2</sub> reforming on Ni(111). Adopted from Wang et al. <sup>[108]</sup> .....	6
Fig. 2.	Schematic illustration of the experimental setup for FTIR measurement.....	13
Fig. 3.	Scheme of the Kinetic setup .....	15
Fig. 4.	Schematic illustration of the setup for <i>in situ</i> XAS measurements. Adopted from Kleymenov et al. <sup>[112]</sup>	18
Fig. 5.	Schematic illustration of near-ambient pressure XPS. The incident X-rays interact both with the sample surface (photoelectrons e <sub>s</sub> ) and part of the gas phase molecules in front of the sample (photoelectrons e <sub>g</sub> ) which are directed via a differentially pumped electrostatic lens system to the electron detector. ....	20
Fig. 6.	XRD pattern of ZrO <sub>2</sub> .....	22
Fig. 7.	FTIR spectra at room temperature of ZrO <sub>2</sub> after oxidation at 773 K and after reduction at 673 K.	23
Fig. 8.	Temperature Programmed Desorption of H <sub>2</sub> O from ZrO <sub>2</sub> powder. ....	24
Fig. 9.	FTIR Spectra of ZrO <sub>2</sub> after oxidation at 775 K and during adsorption of 0.05, 0.1, 0.5, 1, 2 and 5 mbar D <sub>2</sub> O at room temperature. ....	24
Fig. 10.	TPD profiles of D <sub>2</sub> O, OD, H <sub>2</sub> O and OH desorbed from ZrO <sub>2</sub> performed 3 times in a row. ....	25
Fig. 11.	TPD profiles of CO <sub>2</sub> desorbed from ZrO <sub>2</sub> two times in a row. ....	26
Fig. 12.	Temperature programmed desorption of carbonates followed by FTIR spectroscopy on ZrO <sub>2</sub> .	26
Fig. 13.	TEM micrographs of Ni-ZrO <sub>2</sub> after <i>ex-situ</i> reduction at 673 K. ....	27
Fig. 14.	TEM micrographs of Ni-ZrO <sub>2</sub> after <i>ex-situ</i> reduction at 873 K. ....	28
Fig. 15.	IR Spectra of CO on Ni-ZrO <sub>2</sub> , oxidized in 100 mbar O <sub>2</sub> at 773 K, in a) 0.005, b) 0.2, c) 0.5, d) 1.0, e) 3.0, f) 5.0 mbar CO pressure and g) after evacuation. Published in <sup>[1]</sup> . ....	29
Fig. 16.	IR Spectra of CO on Ni-ZrO <sub>2</sub> , reduced in 5 mbar H <sub>2</sub> at 673 K, in a) 0.005, b) 0.2, c) 0.5, d) 1.0, e) 3.0, f) 5.0 mbar CO pressure and g) after evacuation. Published in <sup>[1]</sup> . ....	30

- Fig. 17. TEM micrographs of Cu-ZrO<sub>2</sub> after *ex-situ* reduction at 673 K. The Cu particles identified by EDX are marked with a cycle. .... 31
- Fig. 18. IR Spectra of CO on Cu-Zr, reduced in 5 mbar H<sub>2</sub> at 673 K, in a) 0.005, b) 0.2, c) 0.5, d) 1.0, e) 3.0, f) 5.0 mbar CO pressure and g) after evacuation. .... 31
- Fig. 19. XANES spectra at the Ni K edge of a) Ni-ZrO<sub>2</sub> and b) 11CuNi-ZrO<sub>2</sub> during reduction in 5% hydrogen in helium and amount of reduced versus oxidized nickel calculated by linear combination of reference spectra for c) Ni-ZrO<sub>2</sub> and d) 11CuNi-ZrO<sub>2</sub>. Published in<sup>[1]</sup>. .... 32
- Fig. 20. HERFD-XAS spectra at the Cu K $\alpha$  edge of a) Cu-ZrO<sub>2</sub> and b) 11CuNi-ZrO<sub>2</sub> during reduction in 5% hydrogen in helium and amount of reduced versus oxidized copper calculated by linear combination of reference spectra for c) Cu-ZrO<sub>2</sub> and d) CuNi-ZrO<sub>2</sub>. Published in<sup>[1]</sup>. .... 33
- Fig. 21. TEM image of 11CuNi-ZrO<sub>2</sub>. The particle inside the circle was identified via EDX as Cu- and Ni-containing. Published in<sup>[2]</sup>. .... 34
- Fig. 22. a) Elemental map of the region shown in the rectangle in b) for the K edge energies of Ni, Cu, Zr and O recorded on 11CuNi-ZrO<sub>2</sub>. Full arrows: particles containing both Ni and Cu, dashed arrows: Cu but no Ni detected. Published in<sup>[2]</sup>. .... 34
- Fig. 23. XRD patterns of ZrO<sub>2</sub>, 13CuNi-Zr and 13 CuNi-Zr50 ..... 35
- Fig. 24. Infrared carbonyl spectra of reduced catalysts under 5 mbar CO pressure and after evacuation of CO: a) Cu-ZrO<sub>2</sub>, b) 31CuNi-ZrO<sub>2</sub>, c) 11CuNi-ZrO<sub>2</sub>, d) 13CuNi-ZrO<sub>2</sub> and e) Ni-ZrO<sub>2</sub>. Published in<sup>[1]</sup>. .... 36
- Fig. 25. Schematic illustration of CO adsorption on CuNi alloys. Donation of d-electrons from copper to nickel leads to reinforcement of the  $\pi$ -backbonding from nickel to antibonding  $7 \pi^*$  orbitals of CO. This leads to a weaker C–O bond and a red-shift of the CO stretch vibration band in infrared spectra. Published in<sup>[1]</sup>. .... 37
- Fig. 26. Temperature programmed desorption of CO followed by FTIR spectroscopy on 13CuNi-ZrO<sub>2</sub>. Published in<sup>[1]</sup>. .... 39
- Fig. 27. Temperature programmed desorption of CO followed by FTIR spectroscopy on 11CuNi-ZrO<sub>2</sub>. Published in<sup>[1]</sup>. .... 40
- Fig. 28. Temperature programmed desorption of CO followed by FTIR spectroscopy on 31CuNi-ZrO<sub>2</sub>. Published in<sup>[1]</sup>. .... 40
- Fig. 29. Area change of the integrated Cu-CO peak area of Cu-ZrO<sub>2</sub>, 31CuNi-ZrO<sub>2</sub>, 11CuNi-ZrO<sub>2</sub> and 13CuNi-ZrO<sub>2</sub> with temperature. Published in<sup>[1]</sup>. .... 41
- Fig. 30. Methane Conversion monitored by MS detection of CH<sub>3</sub> (m/z 15) on a) Cu-ZrO<sub>2</sub>, b) Ni-ZrO<sub>2</sub>, c) 31CuNi-ZrO<sub>2</sub>, d) 11CuNi-ZrO<sub>2</sub> and e) 13CuNi-ZrO<sub>2</sub> during 3 heating-cooling cycles between 573 and 773, K in methane/oxygen/argon. The temperature was ramped with 5 K/min. .... 42

- Fig. 31. Hydrogen evolution during TPMD on a) Ni-ZrO<sub>2</sub>, b) 13CuNi-ZrO<sub>2</sub>, c) 11CuNi-ZrO<sub>2</sub>, d) 31CuNi-ZrO<sub>2</sub>, e) Cu-ZrO<sub>2</sub> and f) 13CuNi-ZrO<sub>2</sub>50. The samples a)-f) were reduced at 673 K followed by 3 heating-cooling cycles between 573 and 773 K in methane/Ar. For f) only one heating cycle is shown. The temperature was ramped at 5 K/min. Published in<sup>[2]</sup>. ..... 44
- Fig. 32. Cu 2p<sub>3/2</sub> region of 13CuNi-ZrO<sub>2</sub> 50 in a) 0.10 mbar O<sub>2</sub> at 573 K and b) 0.25 mbar H<sub>2</sub> at 673 K for 30 min. The incident photon energy was 1100 eV. Published in<sup>[2]</sup>. ..... 46
- Fig. 33. Ni 2p<sub>3/2</sub> region of 13CuNi-ZrO<sub>2</sub> 50 in a) 0.10 mbar O<sub>2</sub> at 573 K and b) 0.25 mbar H<sub>2</sub> at 673 K for 30 min. The incident photon energy was 1010 eV. Published in<sup>[2]</sup>. ..... 47
- Fig. 34. a) Cu 2p<sub>3/2</sub> and b) Ni 2p<sub>3/2</sub> core level regions of 13CuNi-ZrO<sub>2</sub> in 0.25 mbar CH<sub>4</sub> at rising temperature from 523 to 723 K. The incident photon energies were 1100 eV (Cu) and 1010 eV (Ni). Published in<sup>[2]</sup>. ..... 49
- Fig. 35. C 1s core level region of 13CuNi-ZrO<sub>2</sub> in 0.25 mbar CH<sub>4</sub> at rising temperature from 523 to 723 K. The incident photon energy was 425 eV. Published in<sup>[2]</sup> ..... 50
- Fig. 36. Depth profile of a) Ni, b) Cu and c) C species based on the total amount of a) Ni, b) Cu and c) C, respectively. Spectra in the core level regions Ni 2p<sub>3/2</sub>, Cu 2p<sub>3/2</sub> and C 1s with kinetic energies of 150, 350 and 550 eV were consulted for the calculations. For clarity of the diagram error bars were left out in c). Published in<sup>[2]</sup>. ..... 51
- Fig. 37. TPO performed after the methane decomposition reaction over Ni and all CuNi catalysts (shown in Fig. 3). The mass spec trace of CO<sub>2</sub> (m/z 44) is displayed upon heating in 20 vol% O<sub>2</sub>/Ar at a rate of 5 K/min. .... 53
- Fig. 38. XRD patterns of a) Ni-ZrO<sub>2</sub>, b) ZrO<sub>2</sub>, c) Ni-CeZr, d) CeZr, e) Ni-Ce<sub>x</sub>Zr<sub>y</sub>O<sub>2</sub>\_comb, f) Ce<sub>x</sub>Zr<sub>y</sub>O<sub>2</sub>\_comb, g) Ni-Ce<sub>x</sub>Zr<sub>y</sub>O<sub>2</sub>\_cp, h) Ce<sub>x</sub>Zr<sub>y</sub>O<sub>2</sub>\_cp, i) Ni-Ce<sub>x</sub>Zr<sub>y</sub>O<sub>2</sub>\_ctab, j) Ce<sub>x</sub>Zr<sub>y</sub>O<sub>2</sub>\_cp, k) Ni-CeO<sub>2</sub> and l) CeO<sub>2</sub>. ZrO<sub>2</sub> and CeZr support show characteristics of monoclinic zirconia, CeO<sub>2</sub> and Ce<sub>x</sub>Zr<sub>y</sub>O<sub>2</sub>\_ctab show characteristics of cubic CeO<sub>2</sub> and cubic Ce-Zr-oxide, respectively and Ce<sub>x</sub>Zr<sub>y</sub>O<sub>2</sub>\_comb shows characteristics of tetragonal Ce-Zr-oxide. Ce<sub>x</sub>Zr<sub>y</sub>O<sub>2</sub>\_cp shows both reflections of cubic and tetragonal Ce-Zr-oxides. .... 54
- Fig. 39. XRD pattern of Ni-Ce<sub>x</sub>Zr<sub>y</sub>O<sub>2</sub>\_cp with assignment of the cubic and tetragonal phase. .... 55
- Fig. 40. a) TEM image of Ni-Ce<sub>x</sub>Zr<sub>y</sub>O<sub>2</sub>\_cp and b) Elemental map of the region shown in the rectangle in a) for the K-edge energies of O, Ce, Ni and Zr. Regions containing Ni are marked in a), I and II are shown in Fig. 41 with higher magnification. .... 56
- Fig. 41. TEM images of a) the region marked with I and b) the region marked with II in Fig. 40 a. ... 57
- Fig. 42. a) TEM image of Ni-Ce<sub>x</sub>Zr<sub>y</sub>O<sub>2</sub>\_ctab and b) FFT of a) ..... 57
- Fig. 43. IR spectra of a) 5 mbar CO adsorbed on reduced Ni-ZrO<sub>2</sub>, Ni-CeO<sub>2</sub>, Ni-Ce<sub>x</sub>Zr<sub>y</sub>O<sub>2</sub>\_cp and Ni-Ce<sub>x</sub>Zr<sub>y</sub>O<sub>2</sub>\_ctab at room temperature and b) after evacuation below 10<sup>-5</sup> mbar. .... 58

Fig. 44. a) operando FTIR and b) MS detected reactants and products during temperature programmed MSR over Ni-ZrO <sub>2</sub> up to 673 K.....	59
Fig. 45. a) operando FTIR and b) MS detected reactants and products during temperature programmed MSR over NiCeO <sub>2</sub> up to 673 K. ....	60
Fig. 46. a) operando FTIR and b) MS detected reactants and products during temperature programmed MSR over NiCeZr <sub>x</sub> _comb up to 673 K.....	61
Fig. 47. a) operando FTIR and b) MS detected reactants and products during temperature programmed MSR over NiCeZr <sub>x</sub> _cp up to 673 K. ....	61
Fig. 48. a) operando FTIR and b) MS detected reactants and products during temperature programmed MSR over NiCeZr <sub>x</sub> _ctab up to 673 K. ....	62
Fig. 49. Screening of Ni-ZrO <sub>2</sub> , Ni-CeO <sub>2</sub> , Ni-Ce <sub>x</sub> Zr <sub>y</sub> O <sub>2</sub> _cp and Ni-Ce <sub>x</sub> Zr <sub>y</sub> O <sub>2</sub> _ctab catalysts for methane dry reforming reaction at 873 K; feed composition: CH <sub>4</sub> :CO <sub>2</sub> :Ar = 10/10/80; feed flow rate = 25 ml/min. 63	
Fig. 50. Screening of Ni-ZrO <sub>2</sub> , Ni-CeO <sub>2</sub> , Ni-Ce <sub>x</sub> Zr <sub>y</sub> O <sub>2</sub> _cp and Ni-Ce <sub>x</sub> Zr <sub>y</sub> O <sub>2</sub> _ctab catalysts for methane dry reforming reaction at 873 K; feed composition: CH <sub>4</sub> :CO <sub>2</sub> :Ar = 10/10/80; feed flow rate = 25 ml/min. In contrast to the screening shown in Fig. 49, the catalysts were exposed to air between pretreatment and reaction.....	64
Fig. 51. Temperature Programmed Oxidation performed after 24 hours MDR with 20% O <sub>2</sub> in Ar. ...	65
Fig. 52. Temperature Programmed Oxidation performed after 3 hours MDR with 20% O <sub>2</sub> in Ar. ....	66
Fig. 53. TEM images of a) Ni-ZrO <sub>2</sub> and b) Ni-Ce <sub>x</sub> Zr <sub>y</sub> O <sub>2</sub> _cp after exposure to methane and carbon dioxide at 600 °C for 3 hours. ....	67
Fig. 54. XRD patterns of the Ni-ZrO <sub>2</sub> , Ni-CeO <sub>2</sub> , Ni-Ce <sub>x</sub> Zr <sub>y</sub> O <sub>2</sub> _cp and Ni-Ce <sub>x</sub> Zr <sub>y</sub> O <sub>2</sub> _ctab after MDR for 3 hours at 873 K.....	67
Fig. 55. a) normalized XANES spectra of reference samples and pre-reduced and used samples and b) first derivative of the spectra shown in a). The dashed lines in b) mark the positions of two local maxima at 8333 eV and 8343 eV. The asterisk (*) labels the absolute maximum. ....	68
Fig. 56. k <sup>2</sup> -weighted EXAFS functions $\chi(k)$ and magnitude and imaginary part of Fourier transforms (uncorrected for phase shifts) of $\chi(k)$ of Ni-foil and the supported nickel catalysts after methane dry reforming reaction at 873 K. Solid lines: experimental data, hollowed spheres: fits in R-space and backtransformed into k-space. ....	69

# List of Tables

---

Table 1. Composition of Cu/Ni-CeO <sub>2</sub> /ZrO <sub>2</sub> catalysts.....	10
Table 2. CO stretching vibration on bimetallic CuNi-ZrO <sub>2</sub> samples at different CO pressures. Published in <sup>[1]</sup> .....	38
Table 3. Hydrogen yields and initial reaction rates during methane decomposition at 773 K in 5 % CH <sub>4</sub> and 95 % Ar with a total flow of 50 ml/min. ....	45
Table 4. Peak positions obtained in XPS measurements on 13CuNi-ZrO <sub>2</sub> 50.....	47
Table 5. Proportion of NiO and Ni in Ni 2p <sub>3/2</sub> spectra fitted by linear combination of reference spectra. 48	48
Table 6. BET surface area, BJH average pore size and volume and crystallite size of ZrO <sub>2</sub> , CeO <sub>2</sub> , CeZr, Ce <sub>x</sub> Zr <sub>y</sub> O <sub>2</sub> _comb, Ce <sub>x</sub> Zr <sub>y</sub> O <sub>2</sub> _cp and Ce <sub>x</sub> Zr <sub>y</sub> O <sub>2</sub> _ctab. ....	56
Table 7. Ni dispersion and Ni surface area of Ni-ZrO <sub>2</sub> , Ni-CeO <sub>2</sub> , Ni-Ce <sub>x</sub> Zr <sub>y</sub> O <sub>2</sub> _cp and Ni- Ce <sub>x</sub> Zr <sub>y</sub> O <sub>2</sub> _ctab after reduction at 673 K and 873 K.....	59
Table 8. Turn-over frequencies for methane conversion normalized to the number of surface nickel atoms during MDR. ....	64
Table 9. Structural parameters resulting from multiple shell fits of the first Ni-Ni coordination shell in R-space to EXAFS data of Ni foil and post-reaction Ni supported catalysts.....	70

# References

---

1. Kitla, A.; Safonova, O. V.; Foettinger, K., Infrared studies on bimetallic copper/nickel catalysts supported on zirconia and ceria/zirconia. *Catal. Lett.* **2013**, 143, 517.
2. Wolfbeisser, A.; Kloetzer, B.; Mayr, L.; Rameshan, R.; Zemlyanov, D.; Bernardi, J.; Foettinger, K.; Rupprechter, G., Surface modification processes during methane decomposition on Cu-promoted Ni-ZrO<sub>2</sub> catalysts. *Catal. Sci. Technol.* **2015**, 5, (2), 967.
3. Roh, H.-S.; Eum, I.-H.; Jeong, D.-W., Low temperature steam reforming of methane over Ni-Ce(1-x)Zr(x)O<sub>2</sub> catalysts under severe conditions. *Renewable Energy* **2012**, 42, (0), 212.
4. Matsumura, Y.; Nakamori, T., Steam reforming of methane over nickel catalysts at low reaction temperature. *Appl. Catal., A* **2004**, 258, 107.
5. Roh, H.-S.; Platon, A.; Wang, Y.; King, D. L., Catalyst deactivation and regeneration in low temperature ethanol steam reforming with Rh/CeO<sub>2</sub>-ZrO<sub>2</sub> catalysts. *Catal. Lett.* **2006**, 110, (1-2), 1.
6. Kambolis, A.; Matralis, H.; Trovarelli, A.; Papadopoulou, C., Ni/CeO<sub>2</sub>-ZrO<sub>2</sub> catalysts for the dry reforming of methane. *Appl. Catal., A* **2010**, 377, 16.
7. Montoya, J. A.; Romero-Pascual, E.; Gimón, C.; Del, A. P.; Monzon, A., Methane reforming with CO<sub>2</sub> over Ni/ZrO<sub>2</sub>-CeO<sub>2</sub> catalysts prepared by sol-gel. *Catal. Today* **2000**, 63, 71.
8. Pompeo, F.; Nichio, N. N.; Souza, M. M. V. M.; Cesar, D. V.; Ferretti, O. A.; Schmal, M., Study of Ni and Pt catalysts supported on  $\alpha$ -Al<sub>2</sub>O<sub>3</sub> and ZrO<sub>2</sub> applied in methane reforming with CO<sub>2</sub>. *Appl. Catal., A* **2007**, 316, 175.
9. Souza, M. M. V. M.; Aranda, D. A. G.; Schmal, M., Reforming of Methane with Carbon Dioxide over Pt/ZrO<sub>2</sub>/Al<sub>2</sub>O<sub>3</sub> Catalysts. *J. Catal.* **2001**, 204, 498.
10. Bradford, M. C. J.; Vannice, M. A.; Ruckenstein, E., CO<sub>2</sub> reforming of CH<sub>4</sub>. *Catal. Rev. - Sci. Eng.* **1999**, 41, 1.
11. Bitter, J. H.; Seshan, K.; Lercher, J. A., The state of zirconia supported platinum catalysts for CO<sub>2</sub>/CH<sub>4</sub> reforming. *J. Catal.* **1997**, 171, 279.
12. Berrocal, G. P.; Da, S. A. L. M.; Assaf, J. M.; Alborno, A.; Rangel, M. d. C., Novel supports for nickel-based catalysts for the partial oxidation of methane. *Catal. Today* **2010**, 149, 240.

13. Otsuka, K.; Wang, Y.; Sunada, E.; Yamanaka, I., Direct partial oxidation of methane to synthesis gas by cerium oxide. *J. Catal.* **1998**, 175, 152.
14. Li, Y.; Li, D.; Wang, G., Methane decomposition to CO<sub>x</sub>-free hydrogen and nano-carbon material on group 8–10 base metal catalysts: A review. *Catal. Today* **2011**, 162, (1), 1.
15. Chen, J.; Li, X.; Li, Y.; Oin, Y., Production of hydrogen and nanocarbon from direct decomposition of undiluted methane on high-nickeled Ni-Cu-alumina catalysts. *Chem. Lett.* **2003**, 32, (5), 424.
16. Lazaro, M. J.; Echegoyen, Y.; Suelves, I.; Palacios, J. M.; Moliner, R., Decomposition of methane over Ni-SiO<sub>2</sub> and Ni-Cu-SiO<sub>2</sub> catalysts: Effect of catalyst preparation method. *Appl. Catal., A* **2007**, 329, 22.
17. Horn, R.; Schloegl, R., Methane Activation by Heterogeneous Catalysis. *Catal. Lett.* **2015**, 145, (1), 23.
18. Haghofer, A.; Ferri, D.; Foettinger, K.; Rupprechter, G., Who Is Doing the Job? Unraveling the Role of Ga<sub>2</sub>O<sub>3</sub> in Methanol Steam Reforming on Pd<sub>2</sub>Ga/Ga<sub>2</sub>O<sub>3</sub>. *ACS Catal.* **2012**, 2, (11), 2305.
19. Haghofer, A.; Foettinger, K.; Girgsdies, F.; Teschner, D.; Knop-Gericke, A.; Schloegl, R.; Rupprechter, G., In situ study of the formation and stability of supported Pd<sub>2</sub>Ga methanol steam reforming catalysts. *J. Catal.* **2012**, 286, 13.
20. Foettinger, K.; van Bokhoven, J. A.; Nachtegaal, M.; Rupprechter, G., Dynamic Structure of a Working Methanol Steam Reforming Catalyst: In Situ Quick-EXAFS on Pd/ZnO Nanoparticles. *J. Phys. Chem. Lett.* **2011**, 2, (5), 428.
21. Yang, J.; Lukashuk, L.; Akbarzadeh, J.; Stoeger-Pollach, M.; Peterlik, H.; Foettinger, K.; Rupprechter, G.; Schubert, U., Different Synthesis Protocols for Co<sub>3</sub>O<sub>4</sub>-CeO<sub>2</sub> Catalysts-Part 1: Influence on the Morphology on the Nanoscale. *Chem. - Eur. J.* **2015**, 21, (2), 885.
22. Yang, J.; Lukashuk, L.; Li, H.; Foettinger, K.; Rupprechter, G.; Schubert, U., High Surface Area Ceria for CO Oxidation Prepared from Cerium t-Butoxide by Combined Sol-Gel and Solvothermal Processing. *Catal. Lett.* **2014**, 144, (3), 403.
23. Barrabes, N.; Cornado, D.; Foettinger, K.; Dafinov, A.; Llorca, J.; Medina, F.; Rupprechter, G., Hydrodechlorination of trichloroethylene on noble metal promoted Cu-hydroxalcite-derived catalysts. *J. Catal.* **2009**, 263, (2), 239.
24. Barrabes, N.; Foettinger, K.; Llorca, J.; Dafinov, A.; Medina, F.; Sa, J.; Hardacre, C.; Rupprechter, G., Pretreatment Effect on Pt/CeO<sub>2</sub> Catalyst in the Selective Hydrodechlorination of Trichloroethylene. *J. Phys. Chem. C* **2010**, 114, (41), 17675.

25. Fischer, F.; Tropsch, H., Conversion of methane into hydrogen and carbon monoxide. *Brennst.-Chem.* **1928**, *9*, 39.
26. Ashcroft, A. T.; Cheetham, A. K.; Green, M. L. H.; Vernon, P. D. F., Partial oxidation of methane to synthesis gas using carbon dioxide. *Nature (London)* **1991**, *352*, (6332), 225.
27. Rostrup-Nielsen, J. R.; Bak, H. J. H., Carbon dioxide-reforming of methane over transition metals. *J. Catal.* **1993**, *144*, 38.
28. Sakai, Y.; Saito, H.; Sodesawa, T.; Nozaki, F., Catalytic reactions of hydrocarbons with carbon dioxide over metallic catalysts. *React. Kinet. Catal. Lett.* **1984**, *24*, (3-4), 253.
29. Solymosi, F.; Kutsan, G.; Erdohelyi, A., Catalytic reaction of methane with carbon dioxide over alumina-supported platinum metals. *Catal. Lett.* **1991**, *11*, (2), 149.
30. Ginsburg, J. M.; Piña, J.; El Solh, T.; de Lasa, H. I., Coke Formation over a Nickel Catalyst under Methane Dry Reforming Conditions: Thermodynamic and Kinetic Models. *Ind. Eng. Chem. Res.* **2005**, *44*, (14), 4846.
31. Bitter, J. H.; Seshan, K.; Lercher, J. A., Mono and bifunctional pathways of CO<sub>2</sub>/CH<sub>4</sub> reforming over Pt and Rh based catalysts. *J. Catal.* **1998**, *176*, 93.
32. Lercher, J. A.; Bitter, J. H.; Hally, W.; Niessen, W.; Seshan, K., Design of stable catalysts for methane-carbon dioxide reforming. *Stud. Surf. Sci. Catal.* **1996**, *101*, 463.
33. Seshan, K.; ten Barge, H. W.; Hally, W.; van Keulen, A. N. J.; Ross, J. R. H., Carbon dioxide reforming of methane in the presence of nickel and platinum catalysts supported on ZrO<sub>2</sub>. *Stud. Surf. Sci. Catal.* **1994**, *81*, 285.
34. Nagaoka, K.; Seshan, K.; Aika, K.-i.; Lercher, J. A., Carbon deposition during carbon dioxide reforming of methane-comparison between Pt/Al<sub>2</sub>O<sub>3</sub> and Pt/ZrO<sub>2</sub>. *J. Catal.* **2001**, *197*, 34.
35. Bradford, M. C. J.; Vannice, M. A., Catalytic reforming of methane with carbon dioxide over nickel catalysts. I. Catalyst characterization and activity. *Appl. Catal., A* **1996**, *142*, (1), 73.
36. McIntosh, S.; Gorte, R. J., Direct Hydrocarbon Solid Oxide Fuel Cells. *Chem. Rev.* **2004**, *104*, 4845.
37. Rostrup-Nielsen, J. R., Industrial relevance of coking. *Catal. Today* **1997**, *37*, (3), 225.
38. Kim, J. H.; Suh, D. J.; Park, T. J.; Kim, K. L., Effect of metal particle size on coking during CO<sub>2</sub> reforming of CH<sub>4</sub> over Ni-alumina aerogel catalysts. *Appl. Catal., A* **2000**, *197*, (2), 191.

39. Triantafyllopoulos, N. C.; Neophytides, S. G., Dissociative adsorption of CH<sub>4</sub> on NiAu/YSZ: The nature of adsorbed carbonaceous species and the inhibition of graphitic C formation. *J. Catal.* **2006**, 239, (1), 187.
40. Li, Y.; Chen, J.; Qin, Y.; Chang, L., Simultaneous Production of Hydrogen and Nanocarbon from Decomposition of Methane on a Nickel-Based Catalyst. *Energy Fuels* **2000**, 14, (6), 1188.
41. Xu, J.; Saeys, M., Improving the coking resistance of Ni-based catalysts by promotion with subsurface boron. *J. Catal.* **2006**, 242, (1), 217.
42. Gavrielatos, I.; Drakopoulos, V.; Neophytides, S. G., Carbon tolerant Ni–Au SOFC electrodes operating under internal steam reforming conditions. *J. Catal.* **2008**, 259, (1), 75.
43. Molenbroek, A. M.; Norskov, J. K.; Clausen, B. S., Structure and Reactivity of Ni-Au Nanoparticle Catalysts. *J. Phys. Chem. B* **2001**, 105, (23), 5450.
44. Hyldtoft, J.; Norskov, J. K.; Clausen, B. S., Process for steam reforming of hydrocarbons. In *United States Patent*, Haldor Topsoe A/S: Denmark, 1999.
45. Ashok, J.; Subrahmanyam, M.; Venugopal, A., Hydrotalcite structure derived Ni-Cu-Al catalysts for the production of H<sub>2</sub> by CH<sub>4</sub> decomposition. *Int. J. Hydrogen Energy* **2008**, 33, 2704.
46. Park, E. W.; Moon, H.; Park, M.-s.; Hyun, S. H., Fabrication and characterization of Cu-Ni-YSZ SOFC anodes for direct use of methane via Cu-electroplating. *Int. J. Hydrogen Energy* **2009**, 34, 5537.
47. Suelves, I.; Lazaro, M. J.; Moliner, R.; Echegoyen, Y.; Palacios, J. M., Characterization of NiAl and NiCuAl catalysts prepared by different methods for hydrogen production by thermo catalytic decomposition of methane. *Catal. Today* **2006**, 116, (3), 271.
48. Echegoyen, Y.; Suelves, I.; Lazaro, M. J.; Moliner, R.; Palacios, J. M., Hydrogen production by thermocatalytic decomposition of methane over Ni-Al and Ni-Cu-Al catalysts: Effect of calcination temperature. *J. Power Sources* **2007**, 169, (1), 150.
49. Monzón, A.; Latorre, N.; Ubieto, T.; Royo, C.; Romeo, E.; Villacampa, J. I.; Dussault, L.; Dupin, J. C.; Guimon, C.; Montieux, M., Improvement of activity and stability of Ni–Mg–Al catalysts by Cu addition during hydrogen production by catalytic decomposition of methane. *Catal. Today* **2006**, 116, (3), 264.
50. Cunha, A. F.; Órfão, J. J. M.; Figueiredo, J. L., Methane decomposition on Ni-Cu alloyed Raney-type catalysts. *Int. J. Hydrogen Energy* **2009**, 34, (11), 4763.
51. Li, Z.; Chen, J.; Zhang, X.; Li, Y.; Fung, K. K., Catalytic synthesized carbon nanostructures from methane using nanocrystalline Ni. *Carbon* **2002**, 40, (3), 409.

52. Chen, J.; Li, Y.; Li, Z.; Zhang, X., Production of CO<sub>x</sub>-free hydrogen and nanocarbon by direct decomposition of undiluted methane on Ni-Cu-alumina catalysts. *Appl. Catal. A* **2004**, 269, (1-2), 179.
53. Liu, H.; Zhang, R.; Yan, R.; Li, J.; Wang, B.; Xie, K., Insight into CH<sub>4</sub> dissociation on NiCu catalyst: A first-principles study. *Appl. Surf. Sci.* **2012**, 258, 8177.
54. Stadlmayr, W.; Rameshan, C.; Weilach, C.; Lorenz, H.; Haevecker, M.; Blume, R.; Rocha, T.; Teschner, D.; Knop-Gericke, A.; Zemlyanov, D.; Penner, S.; Schloegl, R.; Rupprechter, G.; Kloetzer, B.; Memmel, N., Temperature-Induced Modifications of PdZn Layers on Pd(111). *J. Phys. Chem. C* **2010**, 114, (24), 10850.
55. Holzapfel, H. H.; Wolfbeisser, A.; Rameshan, C.; Weilach, C.; Rupprechter, G., PdZn Surface Alloys as Models of Methanol Steam Reforming Catalysts: Molecular Studies by LEED, XPS, TPD and PM-IRAS. *Top. Catal.* **2014**, 57, (14-16), 1218.
56. Foettinger, K.; Rupprechter, G., In Situ Spectroscopy of Complex Surface Reactions on Supported Pd-Zn, Pd-Ga, and Pd(Pt)-Cu Nanoparticles. *Acc. Chem. Res.* **2014**, 47, (10), 3071.
57. Haghofer, A.; Foettinger, K.; Nachtegaal, M.; Armbruster, M.; Rupprechter, G., Microstructural Changes of Supported Intermetallic Nanoparticles under Reductive and Oxidative Conditions: An in Situ X-ray Absorption Study of Pd/Ga<sub>2</sub>O<sub>3</sub>. *J. Phys. Chem. C* **2012**, 116, (41), 21816.
58. Armbruster, M.; Behrens, M.; Cinquini, F.; Foettinger, K.; Grin, Y.; Haghofer, A.; Kloetzer, B.; Knop-Gericke, A.; Lorenz, H.; Ota, A.; Penner, S.; Prinz, J.; Rameshan, C.; Revay, Z.; Rosenthal, D.; Rupprechter, G.; Sautet, P.; Schloegl, R.; Shao, L.; Szentmiklosi, L.; Teschner, D.; Torres, D.; Wagner, R.; Widmer, R.; Wowsnick, G., How to Control the Selectivity of Palladium-based Catalysts in Hydrogenation Reactions: The Role of Subsurface Chemistry. *ChemCatChem* **2012**, 4, (8), 1048.
59. Sa, J.; Barrabes, N.; Kleymentov, E.; Lin, C.; Foettinger, K.; Safonova, O. V.; Szlachetko, J.; van Bokhoven, J. A.; Nachtegaal, M.; Urakawa, A.; Crespo, G. A.; Rupprechter, G., The oxidation state of copper in bimetallic (Pt-Cu, Pd-Cu) catalysts during water denitration. *Catal. Sci. Technol.* **2012**, 2, (4), 794.
60. Foettinger, K.; Schloegl, R.; Rupprechter, G., The mechanism of carbonate formation on Pd-Al<sub>2</sub>O<sub>3</sub> catalysts. *Chem. Commun. (Cambridge, U. K.)* **2008**, (3), 320.
61. Rupprechter, G., A surface science approach to ambient pressure catalytic reactions. *Catal. Today* **2007**, 126, (1-2), 3.
62. Rupprechter, G.; Weilach, C., Spectroscopic studies of surface-gas interactions and catalyst restructuring at ambient pressure: mind the gap! *J. Phys.: Condens. Matter* **2008**, 20, (18), 184019/1.

63. Wei, J.; Iglesia, E., Mechanism and Site Requirements for Activation and Chemical Conversion of Methane on Supported Pt Clusters and Turnover Rate Comparisons among Noble Metals. *J. Phys. Chem. B* **2004**, 108, 4094.
64. Wang, Y.-H.; Liu, H.-M.; Xu, B.-Q., Durable Ni/MgO catalysts for CO<sub>2</sub> reforming of methane: Activity and metal–support interaction. *J. Mol. Catal. A: Chem.* **2009**, 299, (1–2), 44.
65. Guerrero-Ruiz, A.; Sepulveda-Escribano, A.; Rodriguez-Ramos, I., Cooperative action of cobalt and MgO for the catalyzed reforming of CH<sub>4</sub> with CO<sub>2</sub>. *Catal. Today* **1994**, 21, (2-3), 545.
66. Verykios, X. E., Catalytic dry reforming of natural gas for the production of chemicals and hydrogen. *Int. J. Hydrogen Energy* **2003**, 28, 1045.
67. Barroso-Quiroga, M. M.; Castro-Luna, A. E., Catalytic activity and effect of modifiers on Ni-based catalysts for the dry reforming of methane. *Int. J. Hydrogen Energy* **2010**, 35, (11), 6052.
68. Juan-Juan, J.; Román-Martínez, M. C.; Illán-Gómez, M. J., Nickel catalyst activation in the carbon dioxide reforming of methane: Effect of pretreatments. *Appl. Catal., A* **2009**, 355, (1–2), 27.
69. Takahashi, R.; Sato, S.; Sodesawa, T.; Tomiyama, S., CO<sub>2</sub>-reforming of methane over Ni/SiO<sub>2</sub> catalyst prepared by homogeneous precipitation in sol-gel-derived silica gel. *Appl. Catal., A* **2005**, 286, (1), 142.
70. Gonzalez-Dela, C. V. M.; Holgado, J. P.; Pereniguez, R.; Caballero, A., Morphology changes induced by strong metal-support interaction on a Ni-ceria catalytic system. *J. Catal.* **2008**, 257, 307.
71. Wei, J. M.; Xu, B. Q.; Li, J. L.; Cheng, Z. X.; Zhu, Q. M., Highly active and stable Ni/ZrO<sub>2</sub> catalyst for syngas production by CO<sub>2</sub> reforming of methane. *Appl. Catal., A* **2000**, 196, (2), L167.
72. Chen, J.; Wu, Q.; Zhang, J.; Zhang, J., Effect of preparation methods on structure and performance of Ni/Ce<sub>0.75</sub>Zr<sub>0.25</sub>O<sub>2</sub> catalysts for CH<sub>4</sub>-CO<sub>2</sub> reforming. *Fuel* **2008**, 87, (13-14), 2901.
73. Ebiad, M. A.; Abd, E.-H. D. R.; Elsalamony, R. A.; Mohamed, L. S., Ni supported high surface area CeO<sub>2</sub>-ZrO<sub>2</sub> catalysts for hydrogen production from ethanol steam reforming. *RSC Adv.* **2012**, 2, 8145.
74. Kumar, P.; Sun, Y.; Idem, R. O., Nickel-Based Ceria, Zirconia, and Ceria-Zirconia Catalytic Systems for Low-Temperature Carbon Dioxide Reforming of Methane. *Energy Fuels* **2007**, 21, 3113.

75. Kumar, P.; Sun, Y.; Idem, R. O., Comparative Study of Ni-based Mixed Oxide Catalyst for Carbon Dioxide Reforming of Methane. *Energy Fuels* **2008**, *22*, 3575.
76. Roh, H.-S.; Potdar, H. S.; Jun, K.-W., Carbon dioxide reforming of methane over co-precipitated Ni-CeO<sub>2</sub>, Ni-ZrO<sub>2</sub> and Ni-Ce-ZrO<sub>2</sub> catalysts. *Catal. Today* **2004**, *93-95*, 39.
77. Sukonket, T.; Khan, A.; Saha, B.; Ibrahim, H.; Tantayanon, S.; Kumar, P.; Idem, R., Influence of the Catalyst Preparation Method, Surfactant Amount, and Steam on CO<sub>2</sub> Reforming of CH<sub>4</sub> over 5Ni/Ce<sub>0.6</sub>Zr<sub>0.4</sub>O<sub>2</sub> Catalysts. *Energy Fuels* **2011**, *25*, 864.
78. Horvath, A.; Stefler, G.; Geszti, O.; Kienneman, A.; Pietraszek, A.; Gucci, L., Methane dry reforming with CO<sub>2</sub> on CeZr-oxide supported Ni, NiRh and NiCo catalysts prepared by sol-gel technique: Relationship between activity and coke formation. *Catal. Today* **2011**, *169*, 102.
79. Ocampo, F.; Louis, B.; Kiennemann, A.; Roger, A. C., CO<sub>2</sub> methanation over Ni-Ceria-Zirconia catalysts: effect of preparation and operating conditions. *IOP Conf. Ser.: Mater. Sci. Eng.* **2011**, *19*, 012007/1.
80. Hori, C. E.; Permana, H.; Ng, K. Y. S.; Brenner, A.; More, K.; Rahmoeller, K. M.; Belton, D., Thermal stability of oxygen storage properties in a mixed CeO<sub>2</sub>-ZrO<sub>2</sub> system. *Appl. Catal., B* **1998**, *16*, (2), 105.
81. Minami, K.; Masui, T.; Imanaka, N.; Dai, L.; Pacaud, B., Redox behavior of CeO<sub>2</sub>-ZrO<sub>2</sub>-Bi<sub>2</sub>O<sub>3</sub> and CeO<sub>2</sub>-ZrO<sub>2</sub>-Y<sub>2</sub>O<sub>3</sub> solid solutions at moderate temperatures. *J. Alloys Compd.* **2006**, *408-412*, 1132.
82. Reddy, B. M.; Khan, A.; Lakshmanan, P.; Aouine, M.; Loridant, S.; Volta, J.-C., Structural Characterization of Nanosized CeO<sub>2</sub>-SiO<sub>2</sub>, CeO<sub>2</sub>-TiO<sub>2</sub>, and CeO<sub>2</sub>-ZrO<sub>2</sub> Catalysts by XRD, Raman, and HREM Techniques. *J. Phys. Chem. B* **2005**, *109*, 3355.
83. Sanchez, E. V.; Fernandez, L. E.; Panizza, M.; Resini, C.; Gallardo, A. J. M.; Busca, G., Characterization of cubic ceria-zirconia powders by X-ray diffraction and vibrational and electronic spectroscopy. *Solid State Sci.* **2003**, *5*, 1369.
84. Zhang, F.; Chen, C.-H.; Hanson, J. C.; Robinson, R. D.; Herman, I. P.; Chan, S.-W., Phases in ceria-zirconia binary oxide (1-x)CeO<sub>2</sub>-xZrO<sub>2</sub> nanoparticles: the effect of particle size. *J. Am. Ceram. Soc.* **2006**, *89*, 1028.
85. Otsuka, K.; Wang, Y.; Nakamura, M., Direct conversion of methane to synthesis gas through gas-solid reaction using CeO<sub>2</sub>-ZrO<sub>2</sub> solid solution at moderate temperature. *Appl. Catal., A* **1999**, *183*, 317.
86. Khan, A.; Sukonket, T.; Saha, B.; Idem, R., Catalytic Activity of Various 5 wt.% Ni/Ce<sub>0.5</sub>Zr<sub>0.33</sub>M<sub>0.17</sub>O<sub>2-δ</sub> Catalysts for the CO<sub>2</sub> Reforming of CH<sub>4</sub> in the Presence and Absence of Steam. *Energy Fuels* **2012**, *26*, 365.

87. Terribile, D.; Trovarelli, A.; Llorca, J.; de Leitenburg, C.; Dolcetti, G., The preparation of high surface area CeO<sub>2</sub>-ZrO<sub>2</sub> mixed oxides by a surfactant-assisted approach. *Catal. Today* **1998**, 43, (1-2), 79.
88. Cabanas, A.; Darr, J. A.; Lester, E.; Poliakoff, M., Continuous hydrothermal synthesis of inorganic materials in a near-critical water flow reactor; the one-step synthesis of nano-particulate Ce<sub>1-x</sub>Zr<sub>x</sub>O<sub>2</sub> (x = 0-1) solid solutions. *J. Mater. Chem.* **2001**, 11, 561.
89. Hirano, M.; Suda, A., Oxygen storage capacity, specific surface area, and pore-size distribution of ceria-zirconia solid solutions directly formed by thermal hydrolysis. *J. Am. Ceram. Soc.* **2003**, 86, 2209.
90. Srinivas, D.; Satyanarayana, C. V. V.; Potdar, H. S.; Ratnasamy, P., Structural studies on NiO-CeO<sub>2</sub>-ZrO<sub>2</sub> catalysts for steam reforming of ethanol. *Appl. Catal., A* **2003**, 246, 323.
91. Rossignol, S.; Gerard, F.; Duprez, D., Effect of the preparation method on the properties of zirconia-ceria materials. *J. Mater. Chem.* **1999**, 9, 1615.
92. Dong, X.-F.; Zou, H.-B.; Lin, W.-M., Effect of preparation conditions of CuO-CeO<sub>2</sub>-ZrO<sub>2</sub> catalyst on CO removal from hydrogen-rich gas. *Int. J. Hydrogen Energy* **2006**, 31, (15), 2337.
93. Li, Y.; Chen, J.; Ma, Y.; Zhao, J.; Qin, Y.; Chang, L., Formation of bamboo-like nanocarbon and evidence for the quasi-liquid state of nanosized metal particles at moderate temperatures. *Chem. Commun.* **1999**, (12), 1141.
94. Li, Y.; Chen, J.; Chang, L.; Qin, Y., The doping effect of copper on the catalytic growth of carbon fibers from methane over a Ni/Al<sub>2</sub>O<sub>3</sub> catalyst prepared from Feitknecht compound precursor. *J. Catal.* **1998**, 178, (1), 76.
95. Li, Y.; Chen, J.; Chang, L., Catalytic growth of carbon fibers from methane on a nickel-alumina composite catalyst prepared from Feitknecht compound precursor. *Appl. Catal. A* **1997**, 163, (1-2), 45.
96. Piao, L.; Li, Y.; Chen, J.; Chang, L.; Lin, J. Y. S., Methane decomposition to carbon nanotubes and hydrogen on an alumina supported nickel aerogel catalyst. *Catal. Today* **2002**, 74, (1-2), 145.
97. Zhang, X. X.; Li, Z. Q.; Wen, G. H.; Fung, K. K.; Chen, J.; Li, Y., Microstructure and growth of bamboo-shaped carbon nanotubes. *Chem. Phys. Lett.* **2001**, 333, (6), 509.
98. Li, Y.; Chen, J.; Chang, L.; Zhao, J., Feitknecht compound used as the precursor of the catalyst for the catalytic growth of carbon fibers from methane. *Stud. Surf. Sci. Catal.* **1998**, 118, 321.
99. Liao, M.-S.; Zhang, Q.-E., Dissociation of methane on different transition metals. *J. Mol. Catal. A: Chem.* **1998**, 136, 185.

100. Au, C.-T.; Ng, C.-F.; Liao, M.-S., Methane dissociation and syngas formation on Ru, Os, Rh, Ir, Pd, Pt, Cu, Ag, and Au: A theoretical study. *J. Catal.* **1999**, 185, 12.
101. Jones, G.; Jakobsen, J. G.; Shim, S. S.; Kleis, J.; Andersson, M. P.; Rossmeisl, J.; Abild-Pedersen, F.; Bligaard, T.; Helveg, S.; Hinnemann, B.; Rostrup-Nielsen, J. R.; Chorkendorff, I.; Sehested, J.; Norskov, J. K., First principles calculations and experimental insight into methane steam reforming over transition metal catalysts. *J. Catal.* **2008**, 259, (1), 147.
102. Wei, J.; Iglesia, E., Isotopic and kinetic assessment of the mechanism of reactions of CH<sub>4</sub> with CO<sub>2</sub> or H<sub>2</sub>O to form synthesis gas and carbon on nickel catalysts. *J. Catal.* **2004**, 224, (2), 370.
103. Enger, B. C.; Loedeng, R.; Holmen, A., A review of catalytic partial oxidation of methane to synthesis gas with emphasis on reaction mechanisms over transition metal catalysts. *Appl. Catal., A* **2008**, 346, (1-2), 1.
104. Alyea, E. C.; He, D.; Wang, J., Alcohol synthesis from syngas. I. Performance of alkali-promoted Ni-Mo(MOVS) catalysts. *Appl. Catal., A* **1993**, 104, (1), 77.
105. Burch, R.; Petch, M. I., Investigation of the synthesis of oxygenates from carbon monoxide/hydrogen mixtures on supported rhodium catalysts. *Appl. Catal., A* **1992**, 88, (1), 39.
106. Wang, S.; Lu, G. Q.; Millar, G. J., Carbon Dioxide Reforming of Methane To Produce Synthesis Gas over Metal-Supported Catalysts: State of the Art. *Energy Fuels* **1996**, 10, 896.
107. German, E. D.; Sheintuch, M., Predicting CH<sub>4</sub> Dissociation Kinetics on Metals: Trends, Sticking Coefficients, H Tunneling, and Kinetic Isotope Effect. *J. Phys. Chem. C* **2013**, 117, (44), 22811.
108. Wang, S.-G.; Liao, X.-Y.; Hu, J.; Cao, D.-B.; Li, Y.-W.; Wang, J.; Jiao, H., Kinetic aspect of CO<sub>2</sub> reforming of CH<sub>4</sub> on Ni(1 1 1): A density functional theory calculation. *Surf. Sci.* **2007**, 601, (5), 1271.
109. Birks, L. S.; Friedman, H., Particle-size determination from x-ray line broadening. *J. Appl. Phys.* **1946**, 17, 687.
110. Webb, P. A.; Orr, C., *Analytical Methods in Fine Particle Technology*. Micromeritics Instrument Cooperation: Norcross, 1997.
111. Micromeritics, *ASAP 2020 Chemi Accelerated Surface Area and Porosimetry System Operator's Manual*. Micromeritics Instrument Corporation: U.S.A., 2010.
112. Kleymentov, E.; Sa, J.; Abu-Dahrieh, J.; Rooney, D.; van, B. J. A.; Troussard, E.; Szlachetko, J.; Safonova, O. V.; Nachtegaal, M., Structure of the methanol synthesis

- catalyst determined by in situ HERFD XAS and EXAFS. *Catal. Sci. Technol.* **2012**, *2*, 373.
113. Sa, J.; Barrabes, N.; Kleymentov, E.; Lin, C.; Föttinger, K.; Safonova, O. V.; Szlachetko, J.; van, B. J. A.; Nachtegaal, M.; Urakawa, A.; Crespo, G. A.; Rupprechter, G., The oxidation state of copper in bimetallic (Pt-Cu, Pd-Cu) catalysts during water denitration. *Catal. Sci. Technol.* **2012**, *2*, 794.
114. Kleymentov, E.; van Bokhoven, J. A.; David, C.; Glatzel, P.; Janousch, M.; Alonso-Mori, R.; Studer, M.; Willmann, M.; Bergamaschi, A.; Henrich, B.; Nachtegaal, M., Five-element Johann-type x-ray emission spectrometer with a single-photon-counting pixel detector. *Rev. Sci. Instrum.* **2011**, *82*, 065107/1.
115. Klysubun, W.; Thanawan, S.; Thamasirianunt, P.; Radabutra, S.; Sombunchoo, P., Determination of chlorine content in chlorinated, vulcanized natural rubber by XANES. *Nucl. Instrum. Methods Phys. Res., Sect. A* **2007**, *582*, (1), 242.
116. Newville, M., IFEFFIT: interactive XAFS analysis and FEFF fitting. *J. Synchrotron Radiat.* **2001**, *8*, 322.
117. Ravel, B.; Newville, M., ATHENA, ARTEMIS, HEPHAESTUS: data analysis for X-ray absorption spectroscopy using IFEFFIT. *J. Synchrotron Radiat.* **2005**, *12*, (4), 537.
118. Jaeger, N. I., Perspectives: Surface science: Bridging gaps and opening windows. *Science (Washington, DC, U. S.)* **2001**, *293*, (5535), 1601.
119. Campbell, C. T., Surface science: Catalysts under pressure. *Science (Washington, DC, U. S.)* **2001**, *294*, (5546), 1471.
120. Bukhtiyarov, V. I.; Prosvirin, I. P.; Tikhomirov, E. P.; Kaichev, V. V.; Sorokin, A. M.; Evstigneev, V. V., In situ study of selective oxidation of methanol to formaldehyde over copper. *React. Kinet. Catal. Lett.* **2003**, *79*, (1), 181.
121. Joyner, R. W.; Roberts, M. W.; Yates, K., A "high-pressure" electron spectrometer for surface studies. *Surf. Sci.* **1979**, *87*, (2), 501.
122. Ruppender, H. J.; Grunze, M.; Kong, C. W.; Wilmers, M., In situ x-ray photoelectron spectroscopy of surfaces at pressures up to 1 mbar. *SIA, Surf. Interface Anal.* **1990**, *15*, (4), 245.
123. Bluhm, H.; Haevecker, M.; Knop-Gericke, A.; Kleimenov, E.; Schloegl, R.; Teschner, D.; Bukhtiyarov, V. I.; Ogletree, D. F.; Salmeron, M., Methanol Oxidation on a Copper Catalyst Investigated Using in Situ X-ray Photoelectron Spectroscopy. *J. Phys. Chem. B* **2004**, *108*, 14340.
124. Kaichev, V. V.; Prosvirin, I. P.; Bukhtiyarov, V. I.; Unterhalt, H.; Rupprechter, G.; Freund, H.-J., High-pressure studies of CO adsorption on Pd(111) by x-ray

- photoelectron spectroscopy and sum-frequency generation. *J. Phys. Chem. B* **2003**, 107, (v 15), 3522.
125. Yeh, J. J.; Lindau, I., Atomic subshell photoionization cross sections and asymmetry parameters:  $1 \leq Z \leq 103$ . *At. Data Nucl. Data Tables* **1985**, 32, 1.
126. Tsyganenko, A. A.; Filimonov, V. N., Infrared spectra of surface hydroxyl groups and crystalline structure of oxides. *J. Mol. Struct.* **1973**, 19, (2), 579.
127. Pozdnyakova, O.; Teschner, D.; Wootsch, A.; Kröhnert, J.; Steinhauer, B.; Sauer, H.; Toth, L.; Jentoft, F. C.; Knop-Gericke, A.; Paál, Z.; Schlögl, R., Preferential CO oxidation in hydrogen (PROX) on ceria-supported catalysts, part I: Oxidation state and surface species on Pt/CeO<sub>2</sub> under reaction conditions. *J. Catal.* **2006**, 237, (1), 1.
128. Hertl, W., Surface chemistry of zirconia polymorphs. *Langmuir* **1989**, 5, (1), 96.
129. Li, C.; Sakata, Y.; Arai, T.; Domen, K.; Maruya, K.; Onishi, T., Carbon monoxide and carbon dioxide adsorption on cerium oxide studied by Fourier-transform infrared spectroscopy. 1. Formation of carbonate species on dehydroxylated cerium dioxide at room temperature. *J. Chem. Soc., Faraday Trans. 1* **1989**, 85, 929.
130. Davydov, A. A., *Infrared Spectroscopy of Adsorbed Species on the Surface of Transition Metal Oxides*. John Wiley & Sons: Novosibirsk, USSR, 1984.
131. Collins, S. E.; Baltanas, M. A.; Bonivardi, A. L., An infrared study of the intermediates of methanol synthesis from carbon dioxide over Pd/ $\beta$ -Ga<sub>2</sub>O<sub>3</sub>. *J. Catal.* **2004**, 226, 410.
132. Bolis, V.; Magnacca, G.; Cerrato, G.; Morterra, C., Microcalorimetric and IR-spectroscopic study of the room temperature adsorption of CO<sub>2</sub> on pure and sulphated t-ZrO<sub>2</sub>. *Thermochim. Acta* **2001**, 379, 147.
133. Daturi, M.; Binet, C.; Lavalley, J.-C.; Galtayries, A.; Sporcken, R., Surface investigation on CexZr1-xO<sub>2</sub> compounds. *Phys. Chem. Chem. Phys.* **1999**, 1, 5717.
134. Mihaylov, M.; Chakarova, K.; Hadjiivanov, K., Formation of carbonyl and nitrosyl complexes on titania- and zirconia-supported nickel: FTIR spectroscopy study. *J. Catal.* **2004**, 228, 273.
135. Ryczkowski, J., IR spectroscopy in catalysis. *Catal. Today* **2001**, 68, 263.
136. Bandara, A.; Dobashi, S.; Kubota, J.; Onda, K.; Wada, A.; Domen, K.; Hirose, C.; Kano, S. S., Adsorption of CO and NO on NiO(111)/Ni(111) surface studied by infrared-visible sum frequency generation spectroscopy. *Surf. Sci.* **1997**, 387, 312.
137. Busca, G.; Lorenzelli, V.; Sanchez, E. V., Preparation, solid-state characterization, and surface chemistry of high-surface-area nickel-aluminum (Ni<sub>x</sub>Al<sub>2-2x</sub>O<sub>3-2x</sub>) mixed oxides. *Chem. Mater.* **1992**, 4, 595.

138. Platero, E. E.; Coluccia, S.; Zecchina, A., Carbon monoxide and nitrogen oxide (NO) adsorption on nickel oxide (NiO): a spectroscopic investigation. *Langmuir* **1985**, *1*, 407.
139. Hadjiivanov, K.; Knoezinger, H.; Mihaylov, M., FTIR Study of CO Adsorption on Ni-ZSM-5. *J. Phys. Chem. B* **2002**, *106*, 2618.
140. Hadjiivanov, K.; Mihaylov, M.; Abadjieva, N.; Klissurski, D., Characterization of Ni/TiO<sub>2</sub> catalysts prepared by successive adsorption-reduction of Ni<sup>2+</sup> ions. *J. Chem. Soc., Faraday Trans.* **1998**, *94*, 3711.
141. Kasal, P. H.; Bishop, R. J., Jr.; McLeod, D., Jr., Ligand effects on the redox reactions in nickel- and copper-exchanged zeolites. *J. Phys. Chem.* **1978**, *82*, 279.
142. Kermarec, M.; Olivier, D.; Richard, M.; Che, M.; Bozon-Verduraz, F., Electron paramagnetic resonance and infrared studies of the genesis and reactivity toward carbon monoxide of nickel(1+) ions in a NiCa-X zeolite. *J. Phys. Chem.* **1982**, *86*, 2818.
143. Bonneviot, L.; Cai, F. X.; Che, M.; Kermarec, M.; Legendre, O.; Lepetit, C.; Olivier, D., Preparation of mono- or zerovalent nickel by single or successive one-electron-transfer steps in the photoreduction of silica-supported nickel catalysts. *J. Phys. Chem.* **1987**, *91*, 5912.
144. Dalmon, J. A.; Primet, M.; Martin, G. A.; Imelik, B., Magnetic and infrared study of carbon monoxide chemisorption of silica supported nickel-copper alloys. *Surf. Sci.* **1975**, *50*, 95.
145. Hadjiivanov, K.; Mihaylov, M.; Klissurski, D.; Stefanov, P.; Abadjieva, N.; Vassileva, E.; Mintchev, L., Characterization of Ni/SiO<sub>2</sub> Catalysts Prepared by Successive Deposition and Reduction of Ni<sup>2+</sup> Ions. *J. Catal.* **1999**, *185*, 314.
146. Vesecky, S. M.; Xu, X.; Goodman, D. W., Infrared study of CO on NiO(100). *J. Vac. Sci. Technol., A* **1994**, *12*, 2114.
147. Yoshinobu, J.; Ballinger, T. H.; Xu, Z.; Jaensch, H. J.; Zaki, M. I.; Xu, J.; Yates, J. T., Jr., Ultraviolet photodesorption of carbon monoxide from nickel(II) oxide as measured by infrared spectroscopy. *Surf. Sci.* **1991**, *255*, 295.
148. Blyholder, G., Molecular orbital view of chemisorbed carbon monoxide. *J. Phys. Chem.* **1964**, *68*, 2772.
149. Alvarez-Rodriguez, J.; Cerro-Alarcon, M.; Guerrero-Ruiz, A.; Rodriguez-Ramos, I.; Arcoya, A., Effect of nickel precursor and the copper addition on the surface properties of Ni/KL-supported catalysts for selective hydrogenation of citral. *Appl. Catal., A* **2008**, *348*, 241.
150. Cangiano, M. d. I. A.; Ojeda, M. W.; Carreras, A. C.; Gonzalez, J. A.; Ruiz, M. d. C., A study of the composition and microstructure of nanodispersed Cu-Ni alloys obtained by different routes from copper and nickel oxides. *Mater. Charact.* **2010**, *61*, 1135.

151. Pérez-Hernández, R.; Mondragón Galicia, G.; Mendoza Anaya, D.; Palacios, J.; Angeles-Chavez, C.; Arenas-Alatorre, J., Synthesis and characterization of bimetallic Cu–Ni/ZrO<sub>2</sub> nanocatalysts: H<sub>2</sub> production by oxidative steam reforming of methanol. *Int. J. Hydrogen Energy* **2008**, *33*, (17), 4569.
152. Wu, Q.; Duchstein, L. D. L.; Chiarello, G. L.; Christensen, J. M.; Damsgaard, C. D.; Elkjaer, C. F.; Wagner, J. B.; Temel, B.; Grunwaldt, J.-D.; Jensen, A. D., In Situ Observation of Cu-Ni Alloy Nanoparticle Formation by X-Ray Diffraction, X-Ray Absorption Spectroscopy, and Transmission Electron Microscopy: Influence of Cu/Ni Ratio. *ChemCatChem* **2014**, *6*, 301.
153. Morterra, C.; Giamello, E.; Cerrato, G.; Centi, G.; Perathoner, S., Role of surface hydration state on the nature and reactivity of copper ions in Cu-ZrO<sub>2</sub> catalysts: N<sub>2</sub>O decomposition. *J. Catal.* **1998**, *179*, 111.
154. Chen, S.; Zou, H.; Liu, Z.; Lin, W., DRIFTS study of different gas adsorption for CO selective oxidation on Cu-Zr-Ce-O catalysts. *Appl. Surf. Sci.* **2009**, *255*, 6963.
155. Manzoli, M.; Di, M. R.; Boccuzzi, F.; Coluccia, S.; Kaspar, J., CO oxidation over CuOx-CeO<sub>2</sub>-ZrO<sub>2</sub> catalysts: Transient behaviour and role of copper clusters in contact with ceria. *Appl. Catal., B* **2005**, *61*, 192.
156. Eischens, R. P., Infrared spectra of chemisorbed molecules. An introductory lecture. *Z. Elektrochem.* **1956**, *60*, 782.
157. Kozlov, S. M.; Kovacs, G.; Ferrando, R.; Neyman, K. M., How to determine accurate chemical ordering in several nanometer large bimetallic crystallites from electronic structure calculations. *Chem. Sci.* **2015**, Ahead of Print.
158. Choudhary, T. V.; Sivadinarayana, C.; Chusuei, C. C.; Klinghoffer, A.; Goodman, D. W., Hydrogen Production via Catalytic Decomposition of Methane. *J. Catal.* **2001**, *199*, (1), 9.
159. Ferreira-Aparicio, P.; Rodríguez-Ramos, I.; Guerrero-Ruiz, A., Methane interaction with silica and alumina supported metal catalysts. *Appl. Catal. A* **1997**, *148*, (2), 343.
160. Jones, S. D.; Neal, L. M.; Hagelin-Weaver, H. E., Steam reforming of methanol using Cu-ZnO catalysts supported on nanoparticle alumina. *Appl. Catal., B* **2008**, *84*, 631.
161. Espinos, J. P.; Morales, J.; Barranco, A.; Caballero, A.; Holgado, J. P.; Gonzalez-Eliphe, A. R., Interface Effects for Cu, CuO, and Cu<sub>2</sub>O Deposited on SiO<sub>2</sub> and ZrO<sub>2</sub>. XPS Determination of the Valence State of Copper in Cu/SiO<sub>2</sub> and Cu/ZrO<sub>2</sub> Catalysts. *J. Phys. Chem. B* **2002**, *106*, 6921.
162. Ghijsen, J.; Tjeng, L. H.; Van, E. J.; Eskes, H.; Westerink, J.; Sawatzky, G. A.; Czyzyk, M. T., Electronic structure of cuprous and cupric oxides. *Phys. Rev. B: Condens. Matter Mater. Phys.* **1988**, *38*, 11322.

163. Liu, Z.; Amiridis, M. D.; Chen, Y., Characterization of CuO Supported on Tetragonal ZrO<sub>2</sub> Catalysts for N<sub>2</sub>O Decomposition to N<sub>2</sub>. *J. Phys. Chem. B* **2005**, 109, 1251.
164. Tong, W.; West, A.; Cheung, K.; Yu, K.-M.; Tsang, S. C. E., Dramatic Effects of Gallium Promotion on Methanol Steam Reforming Cu-ZnO Catalyst for Hydrogen Production: Formation of 5 Å Copper Clusters from Cu-ZnGaOx. *ACS Catal.* **2013**, 3, 1231.
165. Wagner, C. D.; Riggs, W. M.; Davis, L. E.; Moulder, J. F.; G.E., M., *Handbook of X-Ray Photoelectron Spectroscopy*. Perkin-Elmer Corporation, Physical Electronics Division, Eden Prairie, Minn. 5534: 1979.
166. Chen, L.-C.; Lin, S. D., The ethanol steam reforming over Cu-Ni/SiO<sub>2</sub> catalysts: Effect of Cu/Ni ratio. *Appl. Catal., B* **2011**, 106, (3–4), 639.
167. Naghash, A. R.; Etsell, T. H.; Xu, S., XRD and XPS Study of Cu-Ni Interactions on Reduced Copper-Nickel-Aluminum Oxide Solid Solution Catalysts. *Chem. Mater.* **2006**, 18, 2480.
168. Koschel, H.; Held, G.; Steinruck, H. P., The growth of thin Cu layers on Ni(111) studied by CO titration and photoelectron spectroscopy. *Surf. Sci.* **2000**, 453, (1-3), 201.
169. Preda, I.; Gutierrez, A.; Abbate, M.; Yubero, F.; Mendez, J.; Alvarez, L.; Soriano, L., Interface effects in the Ni 2p x-ray photoelectron spectra of NiO thin films grown on oxide substrates. *Phys. Rev. B: Condens. Matter Mater. Phys.* **2008**, 77, (7), 075411/1.
170. Guzzi, L.; Stefler, G.; Geszti, O.; Sajo, I.; Paszti, Z.; Tompos, A.; Schay, Z., Methane dry reforming with CO<sub>2</sub>: A study on surface carbon species. *Appl. Catal., A* **2010**, 375, 236.
171. Chia-Ching, W.; Cheng-Fu, Y., Investigation of the properties of nanostructured Li-doped NiO films using the modified spray pyrolysis method. *Nanoscale Res Lett* **2013**, 8, (1), 33.
172. Powell, C. J., Recommended Auger parameters for 42 elemental solids. *J. Electron Spectrosc. Relat. Phenom.* **2012**, 185, 1.
173. Pawelec, B.; Damyanova, S.; Arishtirova, K.; Fierro, J. L. G.; Petrov, L., Structural and surface features of PtNi catalysts for reforming of methane with CO<sub>2</sub>. *Appl. Catal., A* **2007**, 323, (0), 188.
174. Grosvenor, A. P.; Biesinger, M. C.; Smart, R. S. C.; McIntyre, N. S., New interpretations of XPS spectra of nickel metal and oxides. *Surf. Sci.* **2006**, 600, (9), 1771.
175. Bastl, Z., X-Ray photoelectron spectroscopic studies of palladium dispersed on carbon surfaces modified by ion beams and plasmatic oxidation. *Collect. Czech. Chem. Commun.* **1995**, 60, 383.

176. Kovács, G. J.; Bertóti, I.; Radnóczy, G., X-ray photoelectron spectroscopic study of magnetron sputtered carbon–nickel composite films. *Thin Solid Films* **2008**, 516, (21), 7942.
177. Laidani, N.; Calliari, L.; Speranza, G.; Micheli, V.; Galvanetto, E., Mechanical and structural properties of Ni-C films obtained by RF sputtering. *Surf. Coat. Technol.* **1998**, 100-101, 116.
178. Rodriguez, N. M.; Anderson, P. E.; Wootsch, A.; Wild, U.; Schlögl, R.; Paál, Z., XPS, EM, and Catalytic Studies of the Accumulation of Carbon on Pt Black. *J. Catal.* **2001**, 197, (2), 365.
179. Evans, S.; Thomas, J. M., The chemical nature of ion-bombarded carbon: a photoelectron spectroscopic study of 'cleaned' surfaces of diamond and graphite. *Proc. R. Soc. London, Ser. A* **1977**, 353, 103.
180. Wilson, J. I. B.; Walton, J. S.; Beamson, G., Analysis of chemical vapour deposited diamond films by X-ray photoelectron spectroscopy. *J. Electron Spectrosc. Relat. Phenom.* **2001**, 121, 183.
181. Jackson, S. T.; Nuzzo, R. G., Determining hybridization differences for amorphous carbon from the XPS C 1s envelope. *Appl. Surf. Sci.* **1995**, 90, (2), 195.
182. Savva, P. G.; Polychronopoulou, K.; Ryzkov, V. A.; Efstathiou, A. M., Low-temperature catalytic decomposition of ethylene into H<sub>2</sub> and secondary carbon nanotubes over Ni/CNTs. *Appl. Catal., B* **2010**, 93, 314.
183. Belton, D. N.; Schmieg, S. J., Electron spectroscopic identification of carbon species formed during diamond growth. *J. Vac. Sci. Technol., A* **1990**, 8, 2353.
184. Brunauer, S.; Emmett, P. H.; Teller, E., Adsorption of gases in multimolecular layers. *J. Am. Chem. Soc.* **1938**, 60, 309.
185. Barrett, E. P.; Joyner, L. G.; Halenda, P. P., The determination of pore volume and area distributions in porous substances. I. Computations from nitrogen isotherms. *J. Am. Chem. Soc.* **1951**, 73, 373.
186. Satterfield, C. N., *Heterogeneous Catalysis in Industrial Practice*. Krieger Pub.: 1996.
187. Herrera, J. E.; Resasco, D. E., In situ TPO/Raman to characterize single-walled carbon nanotubes. *Chem. Phys. Lett.* **2003**, 376, (3,4), 302.
188. Chen, J.; Yang, X.; Li, Y., Investigation on the structure and the oxidation activity of the solid carbon produced from catalytic decomposition of methane. *Fuel* **2010**, 89, (5), 943.
189. Uhlig, S.; Struis, R.; Schmid-Engel, H.; Bock, J.; Probst, A.-C.; Freitag-Weber, O.; Zizak, I.; Chernikov, R.; Schultes, G., Piezoresistive Ni:a-C:H thin films containing

- hcp-Ni or Ni<sub>3</sub>C investigated by XRD, EXAFS, and wavelet analysis. *Diamond Relat. Mater.* **2013**, 34, (0), 25.
190. Struis, R. P. W. J.; Bachelin, D.; Ludwig, C.; Wokaun, A., Studying the Formation of Ni<sub>3</sub>C from CO and Metallic Ni at T = 265°C in Situ Using Ni K-Edge X-ray Absorption Spectroscopy. *J. Phys. Chem. C* **2009**, 113, (6), 2443.
191. Moraes, T. S.; Neto, R. C. R.; Ribeiro, M. C.; Mattos, L. V.; Kourtelesis, M.; Ladas, S.; Verykios, X.; Bellot Noronha, F., The study of the performance of PtNi/CeO<sub>2</sub>-nanocube catalysts for low temperature steam reforming of ethanol. *Catal. Today* **2015**, 242, Part A, (0), 35.
192. Swaan, H. M.; Kroll, V. C. H.; Martin, G. A.; Mirodatos, C., Deactivation of supported nickel catalysts during the reforming of methane by carbon dioxide. *Catal. Today* **1994**, 21, (2-3), 571.
193. Goula, M. A.; Lemonidou, A. A.; Efstathiou, A. M., Characterization of Carbonaceous Species Formed during Reforming of CH<sub>4</sub> with CO<sub>2</sub> over Ni/CaO-Al<sub>2</sub>O<sub>3</sub> Catalysts Studied by Various Transient Techniques. *J. Catal.* **1996**, 161, (2), 626.
194. Zhu, L.; Depristo, A. E., Microstructures of bimetallic clusters: bond order metal simulator for disordered alloys. *J. Catal.* **1997**, 167, 400.
195. Sachtler, W. M. H.; Van, d. P. P., Role of individual surface atoms in chemisorption and catalysis by nickel-copper alloys. *Surf. Sci.* **1969**, 18, 62.
196. Kim, S. H.; Lee, K. S.; Min, H. G.; Seo, J.; Hong, S. C.; Rho, T. H.; Kim, J.-S., Subsurface growth of Ni atoms deposited on a Cu(001) surface. *Phys. Rev. B: Condens. Matter Mater. Phys.* **1997**, 55, (12), 7904.
197. Alkemade, P. F. A.; Fortuin, H.; Balkenende, R.; Habraken, F. H. P. M.; Van der Weg, W. F., The growth of nickel-copper surface alloys by decomposition of nickel carbonyl on copper(100). *Surf. Sci.* **1990**, 225, (3), 307.
198. Tzeng, Y. R.; Wu, H. T.; Shiang, D.; Tsong, T. T., Behavior of nickel atoms on the copper(111) surface: a study by high-resolution electron-energy-loss spectroscopy. *Phys. Rev. B: Condens. Matter Mater. Phys.* **1993**, 48, (8), 5549.
199. Pourovskii, L. V.; Skorodumova, N. V.; Vekilov, Y. K.; Johansson, B.; Abrikosov, I. A., Calculated properties of surface and subsurface nickel monolayers on copper. *Surf. Sci.* **1999**, 439, (1-3), 111.
200. Studt, F.; Abild-Pedersen, F.; Wu, Q.; Jensen, A. D.; Temel, B.; Grunwaldt, J.-D.; Nørskov, J. K., CO hydrogenation to methanol on Cu-Ni catalysts: Theory and experiment. *J. Catal.* **2012**, 293, (0), 51.

201. Li, D.; Chen, J.; Li, Y., Evidence of composition deviation of metal particles of a Ni–Cu/Al<sub>2</sub>O<sub>3</sub> catalyst during methane decomposition to CO<sub>x</sub>-free hydrogen. *Int. J. Hydrogen Energy* **2009**, *34*, (1), 299.
202. Damyanova, S.; Pawelec, B.; Arishtirova, K.; Huerta, M. V. M.; Fierro, J. L. G., The effect of CeO<sub>2</sub> on the surface and catalytic properties of Pt/CeO<sub>2</sub>–ZrO<sub>2</sub> catalysts for methane dry reforming. *Appl. Catal., B* **2009**, *89*, (1–2), 149.
203. Barrabes, N.; Fottinger, K.; Llorca, J.; Dafinov, A.; Medina, F.; Sa, J.; Hardacre, C.; Rupprechter, G., Pretreatment Effect on Pt/CeO<sub>2</sub> Catalyst in the Selective Hydrodechlorination of Trichloroethylene. *J. Phys. Chem. C* **2010**, *114*, 17675.

# Appendix

---

## **Infrared Studies on Bimetallic Copper/Nickel Catalysts Supported on Zirconia and Ceria/Zirconia**

Astrid Kitla, Olga V. Safonova, Karin Föttinger

Published in: Catalysis Letters (2013) 143, 517-530

## **Surface modification processes during methane decomposition on Cu-promoted Ni-ZrO<sub>2</sub> catalysts**

Astrid Wolfbeisser, Bernhard Klötzer, Lukas Mayr, Raffael Rameshan, Dmitry Zemlyanov, Johannes Bernardi, Karin Föttinger, Günther Rupprechter

Published in: Catalysis Science and Technology (2015) 5, 967-978

# Infrared Studies on Bimetallic Copper/Nickel Catalysts Supported on Zirconia and Ceria/Zirconia

Astrid Kitla · Olga V. Safonova · Karin Föttinger

Received: 16 January 2013 / Accepted: 26 March 2013 / Published online: 6 April 2013  
© The Author(s) 2013. This article is published with open access at Springerlink.com

**Abstract** Infrared spectroscopy has been employed for a detailed characterization of  $ZrO_2$  and  $CeO_2/ZrO_2$  supported nickel and copper/nickel catalysts to be utilized for methane decomposition. Adsorption of CO at 303 K was performed in order to determine the surface composition and accessible adsorption sites. Alloy formation occurred during reduction, as indicated by a red-shift of the vibrational band of CO on Ni: by  $27\text{ cm}^{-1}$  on nickel-rich CuNi alloy, by  $34\text{ cm}^{-1}$  on 1:1 Cu:Ni and by  $36\text{ cm}^{-1}$  on copper-rich CuNi alloy. CuNi alloy formation was confirmed by X-ray absorption spectroscopy during reduction revealing a considerably lower reduction temperature of NiO in the bimetallic catalyst compared to the monometallic one. However, hydrogen chemisorption indicated that after reduction at 673 K copper was enriched at the surface of the all bimetallic catalysts, in agreement with IR spectra of adsorbed CO. In situ IR studies of methane decomposition at 773 K demonstrated that the addition of Cu to Ni strongly reduced coking occurring preferentially on nickel, while maintaining methane activation. Modification of the zirconia by ceria did not have much effect on the adsorption and reaction properties. Ceria-zirconia and zirconia supported samples exhibited very similar properties and surface chemistry. The main difference was an additional IR band of CO adsorbed on metallic copper pointing to an interaction of part of the Cu with the ceria.

**Keywords** CuNi alloy · Bimetallic catalyst · Methane conversion · Coke · Infrared spectroscopy · CO adsorption

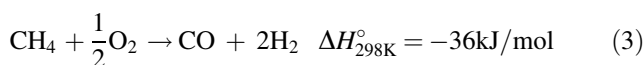
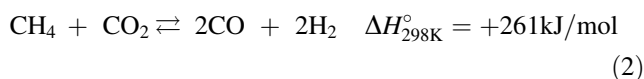
A. Kitla · K. Föttinger (✉)  
Institute of Materials Chemistry, Vienna University of  
Technology, Getreidemarkt 9 BC01, 1060 Vienna, Austria  
e-mail: karin.foettinger@tuwien.ac.at

O. V. Safonova  
Paul Scherrer Institut, 5232 Villigen PSI, Switzerland

## 1 Introduction

The global need of energy, rising oil prices and environmental requirements to reduce  $CO_2$  emissions increase the interest in alternative energy generation, such as fuel cells as clean and efficient means of energy production. There are a number of different types of fuel cells with those operating via a proton-exchange membrane receiving the largest attention [1]. Fuel cells that run directly on hydrogen are considered clean because the exhaust is only water, but this ignores the fact that the vast majority of  $H_2$  is generated by reforming of hydrocarbons, such as methane, [2] producing CO or  $CO_2$  by-product. Furthermore, the storage of gaseous hydrogen or liquefied hydrogen is difficult and dangerous. Thus, the production of hydrogen from hydrocarbons by internal reforming in solid oxide fuel cells (SOFCs) represents a good alternative.

Catalysis plays an important role during all involved processes. Catalysts are used for the production of  $H_2$  from hydrocarbons (preferentially from sustainable sources), and catalysts are also used directly in solid oxide fuel cells for e.g. methane reforming or oxygen activation. Methane as a feedstock can be obtained from different sources, such as from natural gas or biogas.  $H_2$  can then be produced by methane steam reforming [3–5], (1), dry reforming [4, 6–13], (2) or partial oxidation [14, 15], (3) of methane.



Commercially used catalysts for methane reforming are based on Ni. The active nickel particles, however, tend to form coke, leading to deactivation of the catalysts [16]. Improved stability against coke formation was observed for NiAu catalysts [17–19] and was explained by the reduced stability of adsorbed carbon on nickel atoms in the vicinity of a gold atom. In the current work Cu was used to dilute Ni, in order to improve the stability against coke formation while maintaining the high activity of nickel catalysts for methane activation. The interaction of Ni with methane is the key step in methane reactions and of fundamental importance in coke formation. Methane decomposition was therefore examined in the absence of H<sub>2</sub>O, CO<sub>2</sub> or O<sub>2</sub>.

Liao et al. [20] calculated dissociation enthalpies and activation energies of the sequential dehydrogenation of methane for various transition metals, including nickel and copper. The total dissociation of methane on Cu and the other coinage metals was found to be very endothermic. Nickel was one of the most efficient catalysts for the methane dissociation described by sequential dehydrogenation of CH<sub>4</sub>:



In this work Cu–Ni bimetallic combinations with different Cu:Ni ratios were investigated with respect to their activity for methane activation and their tendency towards coking. The catalysts were thoroughly characterized regarding the Cu–Ni interaction by X-ray absorption and FTIR spectroscopy to confirm alloy formation. FTIR spectroscopy was utilized to characterize the surface composition and available adsorption sites by CO adsorption after oxidation and reduction in H<sub>2</sub> as well as after methane exposure, in order to obtain insights into the effect of Cu addition to Ni catalysts. Cu addition to Ni/ZrO<sub>2</sub> strongly reduced coking, while modification of the support surface by CeO<sub>2</sub> addition did not have an effect in the present investigations.

## 2 Materials and Methods

### 2.1 Sample Preparation

Starting from Ni/ZrO<sub>2</sub>, materials of increasing complexity in composition were synthesized. First, Cu was added in different molar ratios. Additionally, the support surface was modified by CeO<sub>2</sub>. The Cu/Ni–CeO<sub>2</sub>/ZrO<sub>2</sub> catalysts of different compositions as summarized in Table 1 were prepared by impregnation. One sample was obtained by another synthesis route, the combustion synthesis, to evaluate the influence of the synthesis procedure.

Commercial Zr(OH)<sub>4</sub> (MEL chemicals XZO 880/01) was calcined with a heating rate of 2 K/min from room

**Table 1** Composition of Cu/Ni–CeO<sub>2</sub>/ZrO<sub>2</sub> catalysts

Sample name	ZrO <sub>2</sub> (wt%)	CeO <sub>2</sub> (wt%)	Cu (wt%)	Ni (wt%)
Cu–Zr	95	–	5	–
31CuNi–Zr	95	–	3.75	1.25
11CuNi–Zr	95	–	2.5	2.5
13CuNi–Zr	95	–	1.25	3.75
Ni–Zr	95	–	–	5
Cu–CeZr	90	5	5	–
31CuNi–CeZr	90	5	3.75	1.25
11CuNi–CeZr	90	5	2.5	2.5
13CuNi–CeZr	90	5	1.25	3.75
Ni–CeZr	90	5	–	5

temperature to 973 K and kept at this temperature for 2 h. After calcination the zirconia support (Zr) was cooled down to room temperature.

For obtaining ceria/zirconia, Ce(NO<sub>3</sub>)<sub>3</sub>·6H<sub>2</sub>O was dissolved in water and ZrO<sub>2</sub> was suspended in this solution to obtain a powder with 5.3 wt% CeO<sub>2</sub>. The suspension was dried over night at 373 K. Then the yellowish ceria/zirconia powder (CeZr) was heated to 723 K with a heating rate of 5 K/min and held there for 2 h. Addition of ceria by impregnation is expected to result in a modification of the oxide support surface, with the ceria mostly present on the surface.

Bimetallic CuNi samples were prepared by coimpregnation. Cu(NO<sub>3</sub>)<sub>2</sub>·3H<sub>2</sub>O and Ni(NO<sub>3</sub>)<sub>2</sub>·6H<sub>2</sub>O were mixed to obtain the following Cu:Ni molar ratios: 1:0, 3:1, 1:1, 1:3 and 0:1. The nitrates were dissolved in water and in each case 4.75 g ZrO<sub>2</sub> or CeO<sub>2</sub>/ZrO<sub>2</sub> powder was suspended in these solutions. Every solution contained as much metal nitrate to obtain 5 wt% metal in the final catalyst powder.

One catalyst sample was produced by a combustion synthesis route adapted from Ringuedé et al. [21]. The combustion catalyst had the same composition as sample 11CuNi–CeZr and will be designated CuNi–CeZr\_C in the following. In this procedure, ZrO(NO<sub>3</sub>)<sub>2</sub>·6H<sub>2</sub>O, Ce(NO<sub>3</sub>)<sub>3</sub>·6H<sub>2</sub>O, Ni(NO<sub>3</sub>)<sub>2</sub>·6H<sub>2</sub>O and Cu(NO<sub>3</sub>)<sub>2</sub>·3H<sub>2</sub>O were mixed together and melted. Water was admixed to the molten mass and urea was added. Only half of the urea was necessary for the reaction while the rest was used as a fuel. After the addition of urea the mixture was placed into the preheated oven, where it was kept for 15 min at 873 K. After the impetuous reaction greenish agglomerates with a texture different from that of the other samples were obtained. Finally, fine powder was gained by hand-milling of the agglomerates.

### 2.2 Characterization

X-ray diffraction (XRD) studies were carried out on an XPERT-PRO diffractometer with Cu K<sub>α</sub> radiation

operating at 40 kV and 40 mA with a  $2\theta$  scanning from  $5^\circ$  to  $90^\circ$  and a step size of  $0.02^\circ$ .

In situ X-ray absorption spectroscopy (XAS) measurements were carried out in fluorescence mode at the SuperXAS beamline [22] at the Swiss Light Source in Villigen, Switzerland using a Johann-type high-energy-resolution X-ray emission spectrometer and a single-photon-counting Pilatus 100 pixel detector. The spectrometer and experimental setup are described in detail in [23, 24]. The catalyst was placed between two plugs of quartz wool in a quartz plug flow reactor [25] which could be heated by an air blower heater. High energy resolution fluorescence detected X-ray absorption spectroscopy (HERFD-XAS) was measured at the maximum of the Cu  $K_\alpha$  edge using a spherically bent Si(111) analyser crystal ( $R = 1,000$  mm). The spectra of the X-ray absorption near edge structure (XANES) at the Ni K edge were acquired in total fluorescence yield mode using a PIPS diode. The catalyst was heated in a mixture of 5 % hydrogen in helium with a heating rate of 10 K/min from room temperature up to 660 K in case of Ni–Zr and up to 560 K for Cu–Zr and CuNi–Zr. Spectra were recorded at 300, 360, 430, 500, 560 and in case of Ni–Zr at 660 K. The sample was kept for about 20 min at each temperature while spectra were recorded. After cooling down to room temperature another spectrum at 300 K was recorded. X-ray absorption data were processed and analyzed using the IFEFFIT [26] software package.

The specific surface areas (BET) and porosity of calcined samples were calculated from  $N_2$  adsorption data acquired at liquid  $N_2$  temperature on a Micromeritics ASAP 2020 instrument. The powders were first outgassed at 573 K and  $<13 \times 10^{-3}$  mbar for 60 min to ensure a clean surface prior to acquisition of the adsorption isotherm.

In order to determine the specific surface area of nickel measurements of hydrogen chemisorption were performed on a Micromeritics ASAP 2020C. Prior to analysis the samples were heated in an oxygen flow up to 773 K and kept at that temperature for 60 min. After cooling down in vacuum to 573 K the samples were heated in a hydrogen flow up to 673 K. After 30 min reduction the samples were evacuated for 30 min at 673 K. Chemisorption was performed at 308 K at hydrogen pressures between 75 and 775 mbar and repeated once in order to isolate the chemisorption isotherm.  $H_2$  was chosen as analysis gas because it adsorbs irreversibly on nickel but not on copper. Between the first and the repeated analysis the samples were evacuated at 308 K to remove reversibly adsorbed  $H_2$ . The difference of the first isotherm data (reversible + irreversible adsorption) and the repeated isotherm data (only reversible adsorption) was utilized to calculate the quantity of irreversibly adsorbed hydrogen. For the

determination of the metal dispersion hydrogen pressures of 150, 177, 212, 245 and 277 mbar were selected.

Surface sites and oxidation states of the metals were investigated by FTIR spectroscopy of chemisorbed CO. IR spectra were recorded in transmission using a Bruker Vertex 70 spectrometer with a mercury cadmium telluride (MCT) detector. Samples were pressed to small discs and placed in the IR cell. All infrared spectra were collected at a resolution of  $4\text{ cm}^{-1}$  in the  $4,000\text{--}900\text{ cm}^{-1}$  range by averaging 128 scans to achieve good signal to noise ratios. The results shown herein are difference spectra where the spectrum of the clean sample before adsorption was taken as a background.

The oxidation treatment was carried out in the IR cell by heating at  $10\text{ K min}^{-1}$  from room temperature to 773 K under 100 mbar  $O_2$  pressure and holding that temperature for 1 h. Then, the IR cell was evacuated, and spectra were recorded before and after exposure to 5 mbar CO at 303 K. For measuring CO adsorption on reduced catalysts, the samples were heated in 50 mbar  $H_2$  and 900 mbar  $N_2$  at 10 K/min to 673 K after oxidation and kept at that temperature for 30 min. Then, the samples were outgassed at 673 K for 30 min ( $p \sim 10^{-6}$  mbar). Spectra before and after exposure to 5 mbar CO were recorded at 303 K.

IR spectra before and after exposure to 5 mbar CO were also recorded after heating a pre-oxidized sample in 5 mbar  $CH_4$  and 900 mbar  $N_2$  at  $2\text{ K min}^{-1}$  to 773 K. The same procedure was applied to the pre-reduced samples.

### 3 Results and Discussion

#### 3.1 Structural and Textural Properties

The crystalline structure was determined by XRD. The X-ray diffractograms of the samples Zr, 11CuNi–Zr, 11CuNi–CeZr and CuNi–CeZr\_C after calcination are shown in Fig. 1. The pure  $ZrO_2$  support and the catalysts produced by impregnation show reflections assigned to monoclinic  $ZrO_2$ , whereas the diffractogram of CuNi–CeZr\_C is characteristic of tetragonal  $ZrO_2$ . Apart from the different support phase the diffractograms also differ in reflection width. The much broader reflections of the combustion catalyst originate from a smaller support crystallite size, which is reasonable in light of the preparation procedure. Bulk CuO and NiO were not detected in the diffractograms, though. Both species seem to have too small crystallite size. Furthermore, bulk CuO has reflections very close to the characteristic reflections of monoclinic  $ZrO_2$  (monoclinic  $ZrO_2$ :  $35.4^\circ$  and  $38.7^\circ$ ; CuO:  $35.6^\circ$  and  $38.8^\circ$ ).

In order to determine the oxidation state of the analysed copper and nickel containing samples, Ni K edge XANES

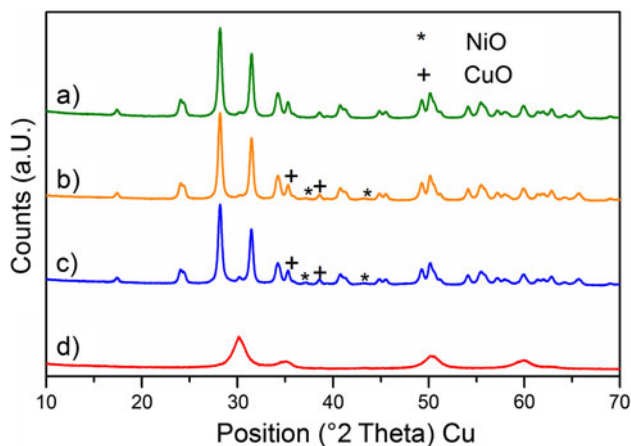
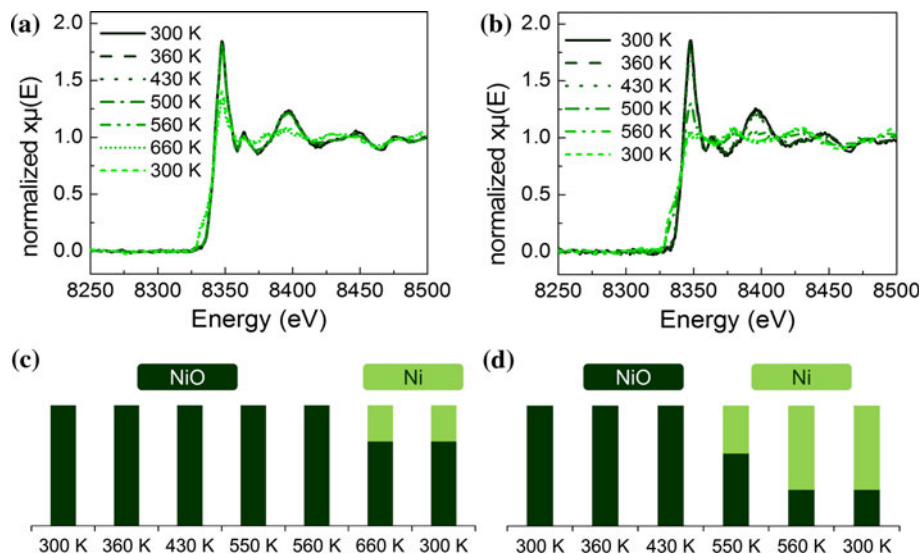


**Fig. 1** XRD patterns of *a* Zr, *b* 11CuNi-Zr, *c* 11CuNi-CeZr and *d* CuNi-CeZr\_C after calcination. *a*–*c* show characteristics of monoclinic zirconia whereas *d* shows characteristics of a tetragonal structure

and Cu K-edge HERFD-XAS spectra were recorded. NiO and Ni foil as well as CuO, Cu<sub>2</sub>O and Cu foil were analysed and served as reference spectra. The spectra obtained on the catalysts during reduction were fitted by a linear combination of these reference spectra to estimate the fraction of atoms in the respective oxidation states.

Figure 2 shows XANES spectra in H<sub>2</sub>/He at different temperatures during reduction. Both the Ni in Ni-Zr and in 11CuNi-Zr is completely oxidized until 430 K. On Ni-Zr nickel reduction starts at 660 K and the linear combination analysis indicates about 30 % of nickel atoms in the reduced (metallic) state. On the bimetallic catalyst 11CuNi-Zr reduction already sets in at 500 K. The amount of reduced nickel increases from 40 % at 500 K to 70 % at 560 K. This indicates that an alloy between Cu and Ni has formed under these conditions and Cu causes a decrease of the reduction temperature of Ni.

**Fig. 2** XANES spectra at the Ni K edge of **a** Ni-Zr and **b** 11CuNi-Zr during reduction in 5 % hydrogen in helium and amount of reduced versus oxidized nickel calculated by linear combination of reference spectra for **c** Ni-Zr and **d** 11CuNi-Zr



Considering Cu-Zr and CuNi-Zr, a similar effect of lowering the reduction temperature of Cu was found as shown in Fig. 3. Up to 360 K copper was completely in the +II oxidation state in both mono- and bimetallic samples. After reduction at 430 K about 10 % of the monometallic copper was reduced to Cu(I)oxide while on the bimetallic sample 10 % were already reduced to Cu<sup>0</sup>, 40 % were in +I and 50 % in +II oxidation state. After reduction at 550 K the amount of Cu(I)oxide increased to 30 % in the monometallic sample, whereas 50 % Cu<sup>0</sup>, 20 % Cu<sub>2</sub>O and 30 % CuO were present in the bimetallic sample. Finally, after reduction at 660 K both catalysts were reduced to the same extent with 50 % Cu<sup>0</sup>.

The surface area analysis by N<sub>2</sub> physisorption was carried out for the samples Zr, 11CuNi-Zr, 11CuNi-CeZr and CuNi-CeZr\_C. The results of the calculations of the specific surface areas using the method of Brunauer, Emmet, and Teller (BET) and of the pore size and pore volume using the method of Barret, Joyner and Halenda (BJH) [27] are shown in Table 2.

The highest surface area was found for ZrO<sub>2</sub>. By adding metal oxides by impregnation the specific surface area decreased by around 4–7 % likely due to blocking of some pores. The surface area of the combustion catalyst was significantly lower. The mesopores volume, calculated by the BJH method, was higher for the pure support and the impregnation catalysts than for the combustion catalyst.

## 3.2 Adsorption Properties

### 3.2.1 H<sub>2</sub> Chemisorption

The accessible nickel surface area was determined by selective chemisorption of H<sub>2</sub>. The active nickel surface areas per gram sample and per gram nickel are shown in

**Fig. 3** HERFD-XAS spectra at the Cu K edge of **a** Cu–Zr and **b** 11CuNi–Zr during reduction in 5 % hydrogen in helium and amount of reduced versus oxidized copper species calculated by linear combination of reference spectra for **c** Cu–Zr and **d** 11CuNi–Zr

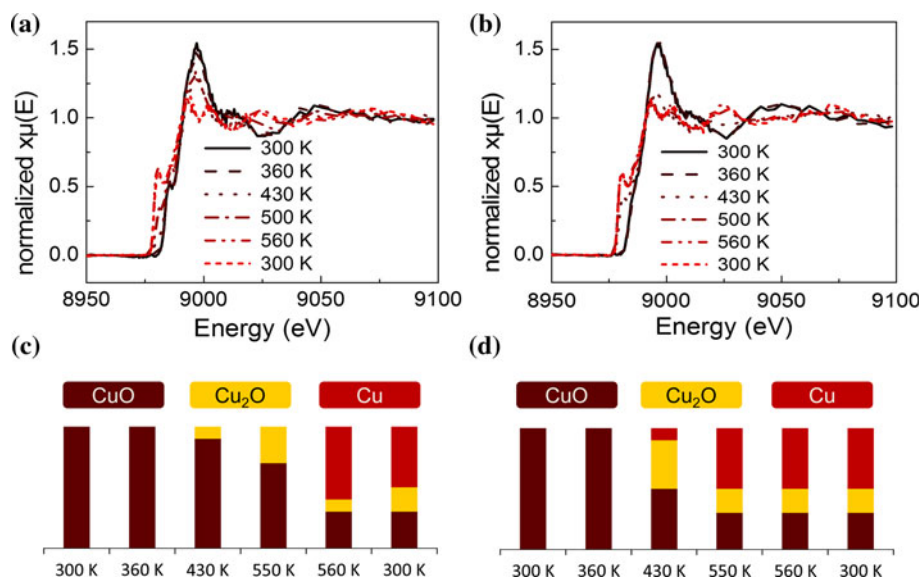


**Table 2** BET surface area und BJH average pore size and volume of Zr, 11CuNi–Zr, 11CuNi–CeZr and CuNi–CeZr\_C

Sample name	BET surface area (m <sup>2</sup> /g)	BJH average pore size (nm)	BJH average pore volume (cm <sup>3</sup> /g)
Zr	36.6	21	0.18
11CuNi–Zr	35.1	20	0.17
11CuNi–CeZr	34.2	17	0.14
CuNi–CeZr_C	32.4	11	0.05

Table 3. As expected, on the catalyst Cu–Zr no hydrogen adsorbs irreversibly, since this sample does not contain nickel. When comparing the accessible nickel surface area per gram nickel there is an enormous decrease for samples containing copper compared to Ni–Zr, while there is hardly any difference between the samples containing different Cu:Ni ratios (1:3, 1:1 and 3:1). The decrease of the nickel surface area per gram sample is not that enormous but also significant. These results can be explained by enrichment of Cu at the surface of the bimetallic materials in hydrogen after a reduction treatment at 673 K.

When applying H<sub>2</sub> chemisorption measurements for characterizing bimetallic catalysts, one has to be aware of complications that can arise from spillover processes. Evidence had been presented by Goodman and co-workers [28–30] that hydrogen can spillover from Ru or Re to Cu on Cu/Ru(0001) and Cu/Re(0001) surfaces. Hydrogen spilling over from Ni to Cu would imply more adsorbed hydrogen than nickel surface atoms. However, we detected a strongly reduced amount of hydrogen that can be adsorbed. Even though the results of the H<sub>2</sub> chemisorption measurements are probably not fully accurate due to potential spillover effects, semi-quantitative information can be obtained and the Cu enrichment at the surface is clearly observed. To confirm this conclusion

**Table 3** Nickel surface area determined by Hydrogen Chemisorption

Sample name	wt% Ni	Nickel surface area (m <sup>2</sup> /g of sample)	Nickel surface area (m <sup>2</sup> /g of nickel)
Ni–Zr	5.00	1.570	31.40
13CuNi–Zr	3.75	0.140	3.74
11CuNi–Zr	2.50	0.067	2.67
31CuNi–Zr	1.25	0.036	2.84
Cu–Zr	0	–	–
CuNi–CeZr_C	2.50	–	–

additional information was obtained from utilizing spectroscopic methods (see Sect. 3.2.3). On the catalyst CuNi–CeZr\_C prepared by combustion synthesis no irreversible hydrogen adsorption is observed, in contrast to the impregnation catalysts. That implies that no reduced nickel is present on the surface of this sample after reduction in hydrogen at 673 K. By this synthesis procedure NiO, CuO, ZrO<sub>2</sub> and CeO<sub>2</sub> were formed simultaneously in one step. This may mean that NiO and CuO are incorporated into the support oxide lattice, and hydrogen is not able to reduce NiO at 673 K to Ni. XRD patterns in Fig. 1 did not show any reflections for NiO, but a different ZrO<sub>2</sub> modification for CuNi–CeZr\_C, which supports this interpretation. For Pt/CeO<sub>2</sub> adsorption and reaction properties of materials prepared by combustion synthesis were found to be different than those of impregnated samples [31, 32].

### 3.2.2 Infrared Spectroscopy of CO Adsorption on Ni–Zr Catalysts

Infrared spectra of room temperature CO adsorption on oxidized Ni–Zr are shown in Fig. 4a. According to literature data [8, 9, 33–35] adsorption of CO on ZrO<sub>2</sub> results in

a band at about  $2,190\text{ cm}^{-1}$ . Ni in different oxidation states can be distinguished by the vibration frequencies of adsorbed CO. Bands ascribed to  $\text{Ni}^{n+}\text{-CO}$  surface complexes cover a broad spectral range including, besides linear monocarbonyls, also bridged, di- and tricarbonyl species.  $\text{Ni}^{2+}\text{-CO}$  produces a weak band at around  $2,150\text{--}2,180\text{ cm}^{-1}$  [8, 34, 36–38]. CO forms stable monocarbonyls with  $\text{Ni}^+$  ( $2,160\text{--}2,100\text{ cm}^{-1}$ ) [39–42], which may be converted into dicarbonyls ( $\nu_s(\text{CO})$  at  $2,131\text{--}2,145$  and  $\nu_{as}(\text{CO})$  at  $2,100\text{--}2,083\text{ cm}^{-1}$ ) [39, 41–43] with increasing CO pressure. The stretching vibrations of  $\text{Ni}^+(\text{CO})_3$  are expected at about  $2,156$ ,  $2,124$  and  $2,109\text{ cm}^{-1}$  [39]. Linear carbonyls of metallic nickel appear at  $2,050\text{--}2,094\text{ cm}^{-1}$  [36, 42–48] and bridged carbonyls are visible below  $1,960\text{ cm}^{-1}$  [36, 44, 48].

Figure 4a displays spectra obtained in different CO background pressures to deduce additional information from changes with increasing CO coverage. At 0.05 mbar CO pressure two bands are visible: The  $\text{Zr}^{4+}\text{-CO}$

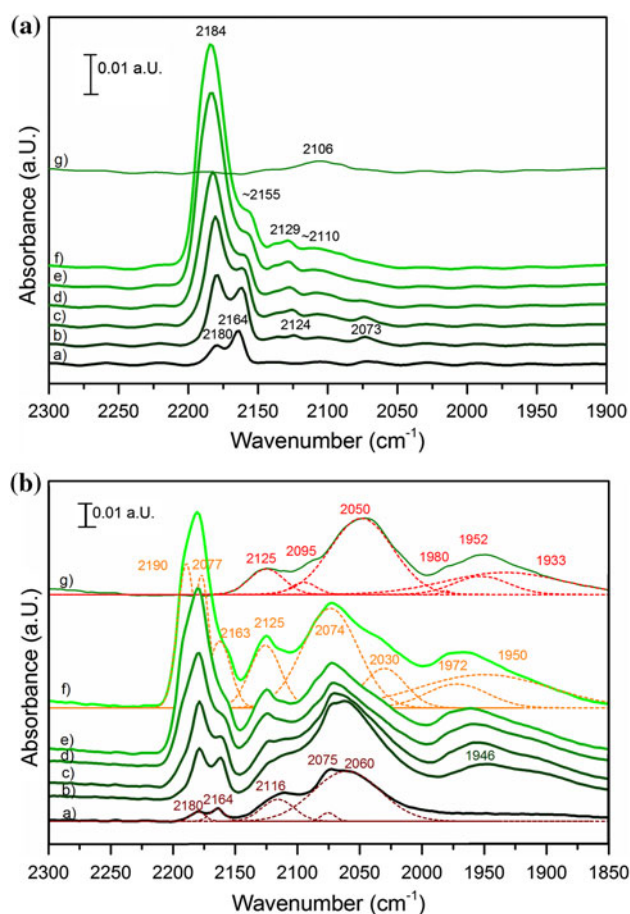


**Fig. 4** **A** IR Spectra of CO on Ni-Zr oxidized in 100 mbar  $\text{O}_2$  at 773 K: in *a* 0.005, *b* 0.2, *c* 0.5, *d* 1.0, *e* 3.0, *f* 5.0 mbar CO pressure and *g* after evacuation. **B** IR Spectra of CO on Ni-Zr reduced in 5 mbar  $\text{H}_2$  at 673 K: in *a* 0.005, *b* 0.2, *c* 0.5, *d* 1.0, *e* 3.0, *f* 5.0 mbar CO pressure and *g* after evacuation

interaction at  $2,180\text{ cm}^{-1}$  and the  $\text{Ni}^{2+}\text{-CO}$  interaction at  $2,164\text{ cm}^{-1}$ . At 0.2 mbar besides these two bands, absorption peaks at  $2,124$  and at  $2,073\text{ cm}^{-1}$  can be observed. Those bands are attributed to the symmetric and antisymmetric CO stretching vibrations of  $\text{Ni}^+(\text{CO})_2$ . With increasing pressure the low frequency band shifts to higher wavenumber and disappears. The three bands at about  $2,155$ ,  $2,129$  and  $2,110\text{ cm}^{-1}$  are attributed to  $\text{Ni}^+(\text{CO})_3$ . The band of the  $\text{Ni}^{2+}\text{-CO}$  interaction is covered by the  $2,155\text{ cm}^{-1}$ -band of  $\text{Ni}^+(\text{CO})_3$  and the  $\text{Zr}^{4+}\text{-CO}$  interaction, which increased strongly with increasing CO pressure and shifted to  $2,184\text{ cm}^{-1}$ . After evacuation only one band at  $2,106\text{ cm}^{-1}$  remains. This band is attributed to  $\text{Ni}^+\text{-CO}$ , which is known to be stable against evacuation [39, 41–43]. In summary, various CO on  $\text{Ni}^{2+}$  and  $\text{Ni}^+$  adsorption complexes can be observed in the spectra.

Infrared spectra of CO adsorption at various pressures obtained after reduction of Ni-Zr at 673 K are shown in Fig. 4b. Like on the oxidized sample, a  $\text{Ni}^{2+}\text{-CO}$  peak at  $2,164\text{ cm}^{-1}$  and a  $\text{Zr}^{4+}\text{-CO}$  peak at  $2,180\text{ cm}^{-1}$  are observed at 0.05 mbar CO pressure. With increasing CO pressure, the  $\text{Zr}^{4+}\text{-CO}$  peak grows and covers the  $\text{Ni}^{2+}\text{-CO}$  peak.

The band at  $2,075\text{ cm}^{-1}$  appearing in 0.05 mbar CO is attributed to linearly adsorbed CO on  $\text{Ni}^0$ , while the band at  $1,946\text{ cm}^{-1}$ , which starts to show up at 0.2 mbar, is attributed to bridge-bonded CO on  $\text{Ni}^0$ . This band blue-shifts with increasing CO pressure. The vibration at  $2,116\text{ cm}^{-1}$  shifting to  $2,125\text{ cm}^{-1}$  with increasing pressure is attributed to  $\text{Ni}^+\text{-CO}$ . The unusual oxidation state  $\text{Ni}^+$  can be stabilized by the ligand CO [41]. After evacuation  $\text{Ni}^+\text{-CO}$  as well as linear and bridged CO on  $\text{Ni}^0$  remain on the surface. Overall, CO adsorption indicates that both reduced and oxidized Ni species are present on the surface. In agreement with the XAS measurements presented in Fig. 2, NiO reduction is not complete at 673 K.

### 3.2.3 Infrared Spectroscopy of CO Adsorption on Bimetallic Catalysts: Influence of Composition

Infrared spectra of room temperature CO adsorption on the various oxidized samples are compared in Fig. 5. The spectra obtained in 5 mbar CO atmosphere are displayed in bold lines, fine lines characterize the CO which remains adsorbed after evacuation of gas phase CO at room temperature. Starting from Ni-Zr the effect of Cu addition and of the modification of the support by adding  $\text{CeO}_2$  on the surface adsorption sites was investigated.

First, CO was adsorbed on the pure zirconia and the ceria-zirconia. In good agreement with literature data [8, 9, 33–35] adsorption of CO on pure  $\text{ZrO}_2$  gives rise to a band at about  $2,190\text{ cm}^{-1}$ , which characterizes  $\text{Zr(IV)-CO}$

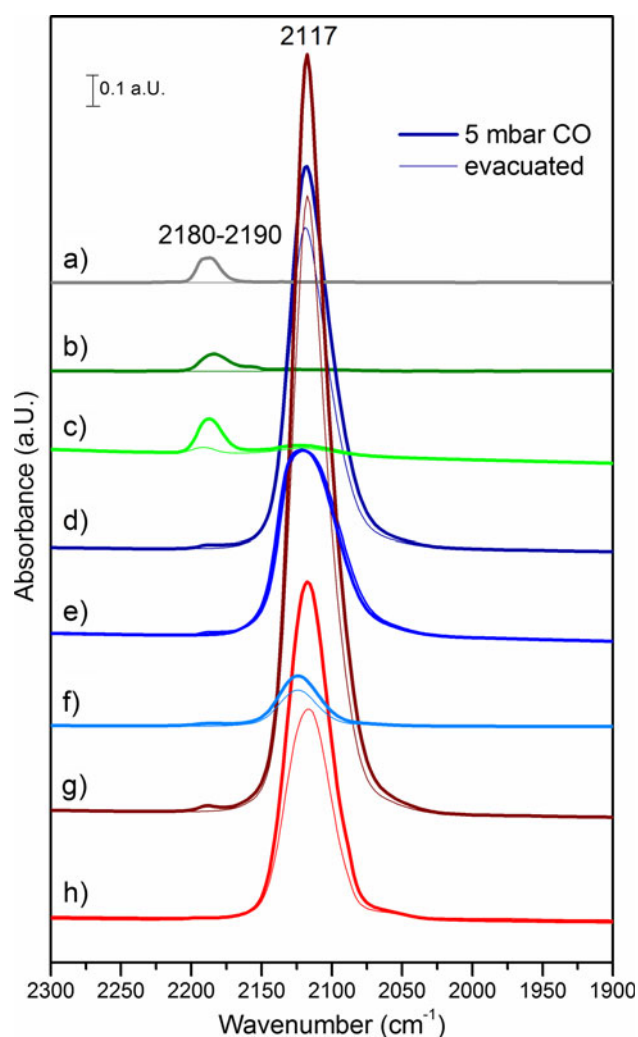


**Fig. 5** IR spectra of 5 mbar CO adsorbed on *a* Zr, *b* Ni–Zr, *c* Ni–CeZr, *d* 11CuNi–Zr, *e* 11CuNi–CeZr, *f* CuNi–CeZr\_C, *g* Cu–Zr and *h* Cu–CeZr after oxidation in 100 mbar O<sub>2</sub> at 773 K for 1 h

adsorption complexes [8, 33, 34]. The addition of CeO<sub>2</sub> should cause a red-shift of this peak due to the lower vibrational frequency of CO on CeO<sub>2</sub> [33], but as in this case the amount of ceria is rather low, the peak shift is negligible (spectrum not shown for brevity).

At about 2,150–2,180 cm<sup>-1</sup> the absorption band of the weak Ni(II)–CO [8, 34, 36–38] interaction should appear, but as the weak bands of Ni(II)–CO and Zr(IV)–CO are very close to each other they cannot be distinguished at a CO pressure of 5 mbar. This was shown in more detail in Sect. 3.2.2 where different CO-species on oxidized Ni–Zr were detected by performing CO adsorption at lower CO pressures and coverages.

The only strongly interacting CO species observed on oxidized samples is the Cu<sup>+</sup>–CO interaction at around 2,115–2,120 cm<sup>-1</sup>. The Cu<sup>+</sup>–CO band was reported at around 2,120–2,143 cm<sup>-1</sup> [49–51]. This interaction is

much stronger than Cu<sup>0</sup>–CO appearing below 2,110 cm<sup>-1</sup> [49–52] and Cu<sup>2+</sup>–CO at around 2,170–2,175 cm<sup>-1</sup> [51]. On the bimetallic catalysts an absorption band of strongly adsorbed CO appears at around 2,120 cm<sup>-1</sup> like on the copper monometallic catalyst, but the peaks are broader, and a slight shift to higher wavenumber can be observed. This may indicate an interaction of copper with neighbouring nickel atoms. The broader peaks suggest that there is a distribution of Cu(I) sites with slightly different electronic properties or chemical environment on the surface.

On the CuNi–CeZr\_C sample the CO absorption band is even broader than on the 11CuNi–CeZr sample, and there is also a larger shift to higher wavenumbers with the CO vibrational band appearing at 2,124 cm<sup>-1</sup>.

Overall, CO adsorbed on Cu<sup>+</sup> is the predominant species observed in the IR spectra on all Cu-containing samples.

Infrared spectra of room temperature CO adsorption on reduced samples are shown in Fig. 6. Compared to the spectra of CO on oxidized samples, new bands have appeared. However, bands of CO on oxidized Cu and Ni species, which already existed on the oxidized samples, are still present indicating incomplete reduction.

On the monometallic nickel samples Ni–Zr and Ni–CeZr several new bands appeared, which are attributed to carbonyls on Ni<sup>0</sup> and Ni<sup>+</sup>, as described in Sect. 3.2.2. On the copper containing samples the much weaker CO interaction with reduced Cu<sup>0</sup> is observed in addition to the Cu<sup>+</sup>–CO band. CO on reduced Cu–Zr shows beside the Zr<sup>4+</sup>–CO interaction only one peak at around 2,111 cm<sup>-1</sup> consisting of both Cu<sup>0</sup>–CO and Cu<sup>+</sup>–CO contributions, which shifts to 2,123 cm<sup>-1</sup> after evacuation with mostly the more stable Cu<sup>+</sup>–CO remaining adsorbed at the surface.

Upon Cu addition to Ni catalysts the Ni<sup>0</sup>–CO peak, which appears at about 2,070 cm<sup>-1</sup> in 5 mbar CO and at about 2,050 cm<sup>-1</sup> upon evacuation of gas phase CO on the Ni–Zr, red-shifts by approximately 50–70 cm<sup>-1</sup> on the bimetallic samples to 2,012–2,023 cm<sup>-1</sup> (Fig. 6). According to Blyholder's scheme [48], the CO stretching vibration is predicted to shift from pure Ni as compared to Ni–Cu, because metallic Cu is expected to donate electrons to Ni. This should increase back-donation into the π\* orbitals of CO with consequently lowering of the CO stretching frequency. Simultaneously, the electron donation reinforces the bond between CO and Ni. This is illustrated in Scheme 1. Compared to pure Ni, the CO bands on CuNi alloy were reported to shift to lower frequencies by about 40 cm<sup>-1</sup> [48, 53]. Dalmon et al. [44] observed band of the irreversibly adsorbed Ni–CO at 2,058 cm<sup>-1</sup> on monometallic nickel, at 2,028 cm<sup>-1</sup> on a 36.6 % and at 2,005 cm<sup>-1</sup> on a 72 % copper containing alloy, in good agreement with the present work. The fact that there is no shift of the

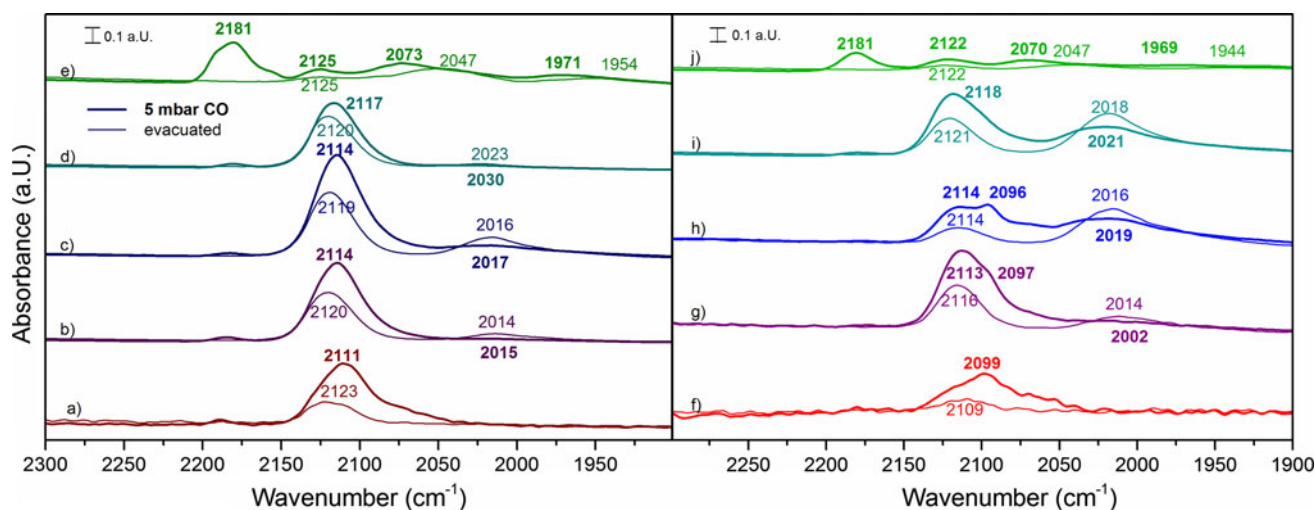
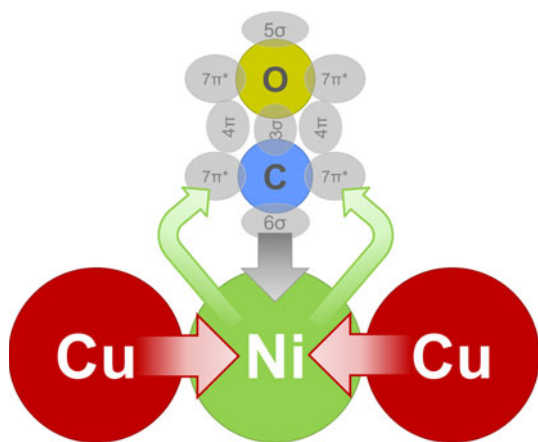


**Fig. 6** Infrared spectra of reduced catalysts in 5 mbar CO pressure and after evacuation of CO: *a* Cu–Zr, *b* 31CuNi–Zr, *c* 11CuNi–Zr, *d* 13CuNi–Zr and *e* Ni–Zr; *f* Cu–CeZr, *g* 31CuNi–CeZr, *h* 11CuNi–CeZr, *i* 13CuNi–CeZr and *j* Ni–CeZr



**Scheme 1** Schematic illustration of CO adsorption on CuNi alloys. Donation of d-electrons from copper to nickel leads to reinforcement of the  $\pi$ -backbonding from nickel to antibonding  $7\pi^*$  orbitals of CO. This leads to a weaker C–O bond and a red-shift of the CO stretch vibration band in infrared spectra

$\text{Cu}^+$ –CO vibration with composition indicates that Ni is interacting with  $\text{Cu}^0$ , but not with  $\text{Cu}^+$ .

CO adsorption spectra were again recorded in different CO pressures to obtain information on coverage dependence of CO bands/species, as on the monometallic Ni–Zr catalyst. The band positions of the CO stretching vibrations on the bimetallic catalysts are summarized in Table 4. Beside the blue-shift of CO on nickel by 50–70  $\text{cm}^{-1}$  with increasing Ni content, as described above, a blue-shift of 7–26  $\text{cm}^{-1}$  with increasing CO coverage is observed. The vibration frequency of CO on the alloyed  $\text{Ni}^0$  blue-shifts by 7  $\text{cm}^{-1}$  on copper-rich and up to 34  $\text{cm}^{-1}$  on nickel-rich alloys with increasing CO coverage. After evacuation the CO vibration frequency is observed in between 2012 and 2,023  $\text{cm}^{-1}$  on all samples. The stretching frequency of

CO on  $\text{Cu}^+$  stays at about 2,110–2,120  $\text{cm}^{-1}$  on all zirconia based catalysts and seems only little pressure dependent.

In general, hardly any differences are observed between the zirconia and the ceria-zirconia supported catalysts. When comparing the zirconia supported catalysts with the ceria-zirconia based materials, which are shown on the left and right panel of Fig. 6, respectively, the shape of the peaks attributed to  $\text{Cu}^+$ –CO and  $\text{Cu}^0$ –CO is different. The CO stretching vibration on Cu–CeZr appears at a lower wavenumber than on Cu–Zr. After evacuation the band on Cu–CeZr blue-shifts from 2,099 to 2,109  $\text{cm}^{-1}$  and decreases almost completely, while on Cu–Zr the band shifts from 2,111 to 2,123  $\text{cm}^{-1}$  upon evacuation. This indicates that copper particles on reduced Cu–CeZr are interacting with  $\text{CeO}_2$ , which seems to result in different electronic properties. Chen et al. [50] reported two peaks at 2,106  $\text{cm}^{-1}$  and 2,078  $\text{cm}^{-1}$  on Cu–Ce–O, which were assigned to the CO adsorption on two different linear adsorption sites. By doping with  $\text{ZrO}_2$  only one peak at 2,113  $\text{cm}^{-1}$  was reported [50]. A band at 2,097  $\text{cm}^{-1}$  was found by Manzoli et al. [52] and attributed to CO on small three dimensional metallic copper particles.

On the bimetallic samples 31CuNi–CeZr and 11CuNi–Ce–Zr two CO bands below and above 2,100  $\text{cm}^{-1}$  are clearly visible, while the spectra on Ni–CeZr and 13CuNi–CeZr show hardly any difference to the zirconia supported samples. At low CO coverage a shoulder appeared at approximately 2,071–2,076  $\text{cm}^{-1}$  on the nickel-rich ceria/zirconia supported samples 13CuNi–CeZr and 11CuNi–CeZr. This feature is in between the band at 2,078  $\text{cm}^{-1}$  on Ce–Cu–O reported by Chen et al. [50] and the peak at 2,067  $\text{cm}^{-1}$  on ceria and ceria/zirconia supported catalysts reported by Manzoli. In both cases this band was only

**Table 4** CO stretch vibration frequencies on bimetallic CuNi–ZrO<sub>2</sub> samples at different CO pressures

Sample	CO pressure (mbar)	CO on Cu/Cu <sup>+</sup> (cm <sup>-1</sup> )	CO on Ni (cm <sup>-1</sup> )	Sample	CO pressure (mbar)	CO on Cu/Cu <sup>+</sup> (cm <sup>-1</sup> )	CO on Ni (cm <sup>-1</sup> )
31CuNi–Zr	0.05	2,110	–	31CuNi–CeZr	0.05	2,104	1,995
	0.2	2,110	2,001		0.2	2,104/2,096	2,000
	0.5	2,111	2,011		0.5	2,107/2,097	2,005
	1	2,113	2,016		1	2,110/2,097	2,001
	3	2,113	2,018		3	2,110/2,097	2,000
	5	2,114	2,015		5	2,113/2,097	2,002
	Evacuated to <10 <sup>-5</sup>	2,120	2,014		Evacuated to <10 <sup>-5</sup>	2,116	2,012
11CuNi–Zr	0.05	2,110	–	11CuNi–CeZr	0.05	2,104	1,989
	0.2	2,110	2,000		0.2	2,114/2,095/2,076	2,000
	0.5	2,110	2,007		0.5	2,114/2,095/2,074	2,008
	1	2,113	2,014		1	2,112/2,096	2,013
	3	2,114	2,018		3	2,113/2,096	2,014
	5	2,114	2,017		5	2,114/2,096	2,019
	Evacuated to <10 <sup>-5</sup>	2,119	2,016		Evacuated to <10 <sup>-5</sup>	2,115	2,016
13CuNi–Zr	0.05	2,111	–	13CuNi–CeZr	0.05	2,107	1,997
	0.2	2,111	2,004		0.2	2,111/2,096/2,071	2,013
	0.5	2,112	2,013		0.5	2,115/2,096/2,073	2,015
	1	2,113	2,021		1	2,117/2,098	2,015
	3	2,116	2,025		3	2,117/2,098	2,017
	5	2,117	2,030		5	2,119	2,021
	Evacuated to <10 <sup>-5</sup>	2,120	2,023		Evacuated to <10 <sup>-5</sup>	2,121	2,019

found in presence of ceria. According to the interpretation of Manzoli et al. [52] this band is attributed to very small copper clusters, in close contact to reduced ceria. It seems as if ceria may give rise to copper sites with different electronic properties or even cause reduction of copper to a greater extent than on zirconia supported samples. Nickel properties were not changed by the addition of ceria.

Regarding the influence of the preparation procedure, the infrared spectra of CO on the reduced combustion catalyst CuNi–CeZr\_C, which are not shown here, appear to be identical as after oxidation. This is in agreement with H<sub>2</sub>-chemisorption, where no indication of reduction of Ni under these conditions was found.

Clearly, in all samples the CO spectra are dominated by the signals of CO adsorbed on Cu. This implies a Cu enriched surface on the bimetallic samples, which is in agreement with chemisorption measurements.

### 3.2.4 Temperature Stability of CO Adsorption Complexes

Temperature stability of the adsorbed CO species on different samples was followed by recording IR spectra during heating with a rate of 10 K/min in vacuum. CO desorbed from Ni–Zr at about 450 K and from Cu–Zr at 410 K. On all bimetallic samples the desorption temperatures were higher, as shown in Fig. 7a–c.

With decreasing coverage the peak of CO adsorbed on copper species does not shift in frequency, but a second CO peak at about 2,100 cm<sup>-1</sup> from Cu<sup>0</sup>–CO, which might be obscured by the Cu<sup>+</sup>–CO peak at about 2,120 cm<sup>-1</sup> at room temperature due to the higher coverage, becomes visible with increasing temperature. On 13CuNi–Zr these two CO species are still present on the surface at 550 K, but disappear at about 565 K. On 11CuNi–Zr those peaks disappear between 540 and 550 K, and on 31CuNi–Zr they already vanish at about 450–460 K. Thus, with increasing copper content the CO desorption temperature is more similar to the monometallic copper sample. The usually unstable Cu–CO interaction seems to be reinforced by nickel.

To visualize the different CO desorption properties of alloyed and monometallic copper, difference quotients of the integrated peak areas of the copper peak between 2,160 and 2,080 cm<sup>-1</sup> are shown in Fig. 7d. Most of the CO desorbs from Cu–Zr and the copper-rich sample 31CuNi–Zr slightly above room temperature. Only a small amount of CO remains on the surface of Cu–Zr before desorbing at around 390 K. On the samples 11CuNi–Zr and 13CuNi–Zr most of the CO desorbs at 440 K and above, while on 31CuNi–Zr a small shoulder at 440 K can be observed. Beside the Cu–CO interaction of low temperature stability, which already vanishes after rising the temperature slightly

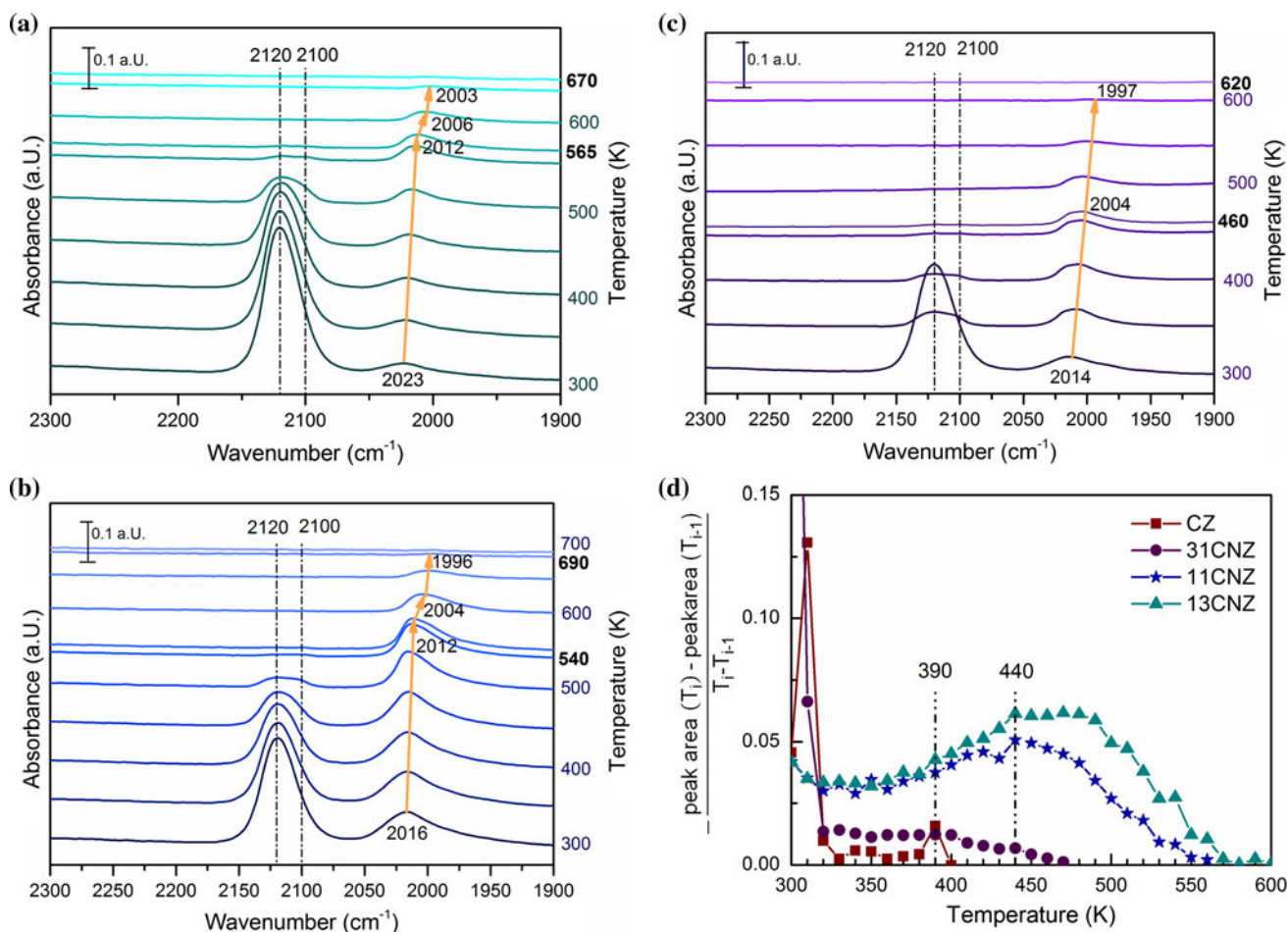


**Fig. 7** **a** Temperature programmed desorption of CO followed by FTIR spectroscopy on 13CuNi-Zr, **b** on 11CuNi-Zr and **c** on 31CuNi-Zr. **d** Area change of the integrated Cu-CO peak area of Cu-Zr, 31CuNi-Zr, 11CuNi-Zr and 13CuNi-Zr with temperature

above room temperature, a second Cu-CO species is observed starting to desorb at 440 K. This species might be attributed to CO on copper surrounded by nickel. As copper tends to donate d-electrons to nickel strengthening the interaction between CO and nickel [48], the electron density in copper is reduced, which normally has its d-band completely filled. Less electrons in the d-band may reinforce the  $\sigma$ -bonding between CO and the metal and thus lead to a higher stability of this complex.

In parallel with the disappearance of the CO peak on copper, the CO peak on nickel shows a sudden shift to a lower wavenumber on 11CuNi-Zr and 13CuNi-Zr. This seems to be a coverage effect, as much CO desorbs from the catalyst at this stage. The Ni-CO peak completely disappears at about 670 K on 13CuNi-Zr and at about 700 K on 11CuNi-Zr. On 31CuNi-Zr the position of the Ni-CO band does not seem to be affected by the complete disappearance of the Cu-CO band, as only a small amount of CO is present and thus desorbs from 31CuNi-Zr at

elevated temperatures. Furthermore, Ni-CO desorbs already around 620 K from this sample.

The total band shift of about  $20\text{ cm}^{-1}$  from room temperature to desorption temperature is also observed on Ni-Zr and is attributed to a coverage effect, probably accompanied by a temperature effect on the CO vibration frequency.

To sum up, the adsorption strength of CO on copper increases with decreasing copper content. The Ni-CO band shows the highest stability on the 11CuNi-Zr sample. On 31CuNi-Zr it is more stable than on Ni-Zr, but less stable than on the nickel-rich sample.

### 3.3 Methane Decomposition

After a detailed characterization of the materials, which confirmed Cu-Ni alloy formation but suggesting a Cu enrichment at the surface for all bimetallic Cu:Ni compositions, the reaction with methane, for which these catalysts

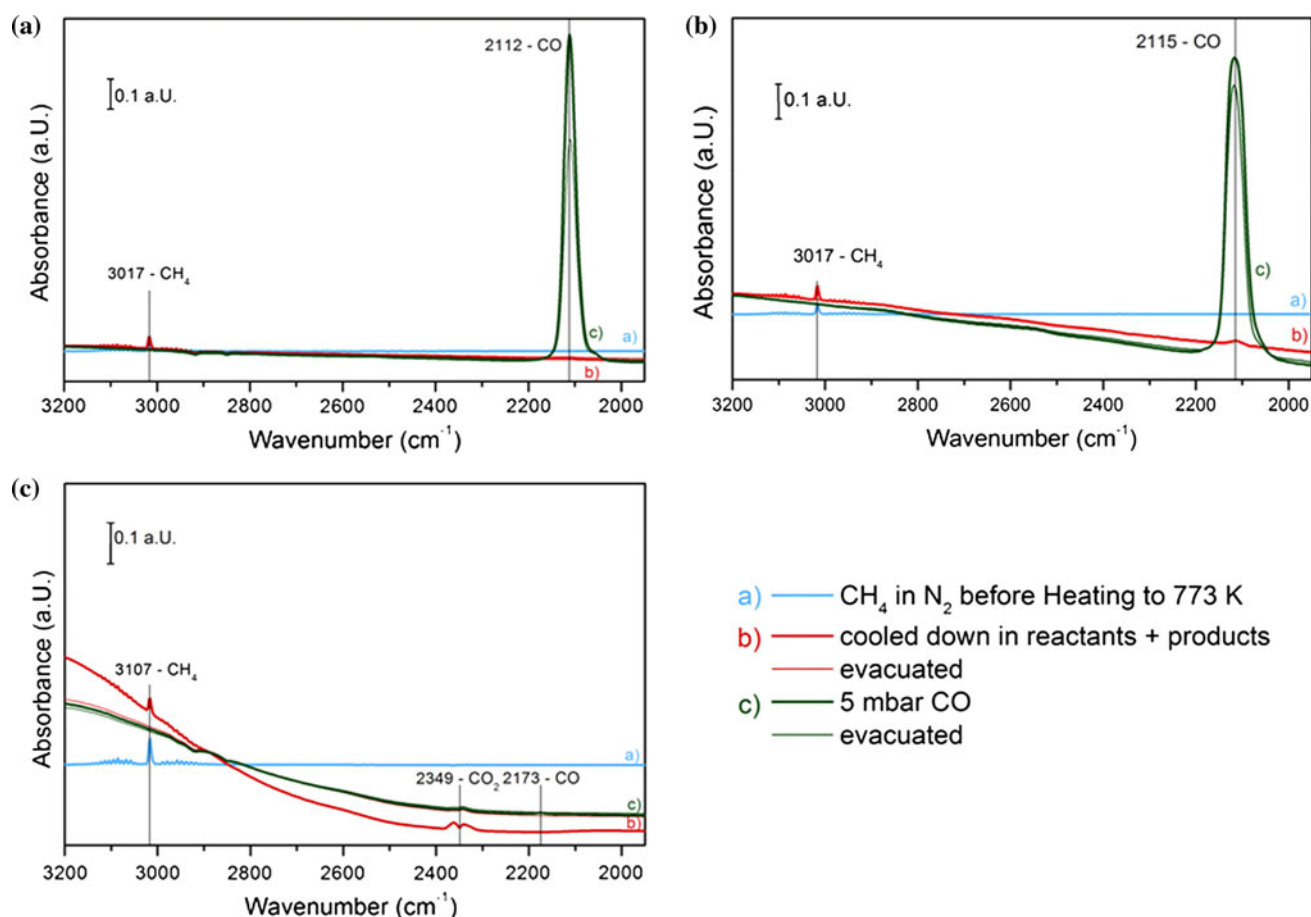


**Fig. 8** IR spectra recorded at room temperature before and after the methane heating ramp and subsequent CO adsorption on oxidized **a** Cu–CeZr, **b** 11CuNi–CeZr and **c** Ni–CeZr

are typically used, was followed again by utilizing infrared spectroscopy.

### 3.3.1 Methane Decomposition Followed by CO Adsorption on Pre-oxidized Catalysts

Pre-oxidized samples were heated in 5 mbar methane and 900 mbar nitrogen up to 773 K and then cooled down to room temperature in the reaction mixture. Afterwards, the chamber was evacuated and CO adsorption was applied another time in order to compare the oxidation state of the catalysts before and after methane conversion and to detect available versus affected CO adsorption sites on the surface.

Figure 8 shows infrared spectra before and after methane decomposition and during CO adsorption on pre-oxidized Cu–CeZr, 11CuNi–CeZr and Ni–CeZr. Generally, no difference was observed in zirconia supported samples, which are therefore not shown here.

On Ni–CeZr a strong change of the baseline is clearly visible in the FTIR spectra. This change in total absorption

indicates a change of the sample's colour most probably due to significant coke formation. A small amount of CO<sub>2</sub> is formed during the reaction of methane giving rise to the characteristic IR band of CO<sub>2</sub> in the gas phase. After methane exposure at 773 K CO adsorption is strongly decreased (Fig. 8c). Only about 6 % of the initially already small amount of CO adsorbing on a fresh oxidized sample were determined after this procedure. Since also the peak of the Zr<sup>4+</sup>–CO interaction decreases strongly, this could imply that not only nickel but also the support is partially covered by coke. In contrast, the IR spectra on Cu–CeZr before and after heating in methane to 773 K do not show differences as no IR active products are formed, and the baseline of the spectra is about the same. Compared to the fresh oxidized sample, 85 % CO can be adsorbed on this catalyst. The slight decrease may be attributed to copper sintering. On 11CuNi–CeZr little change in the total absorbance is observed and a small amount of CO is produced. Adsorption of CO is still possible after methane exposure, and compared to the fresh oxidized sample, 90 % CO adsorbs on the sample.

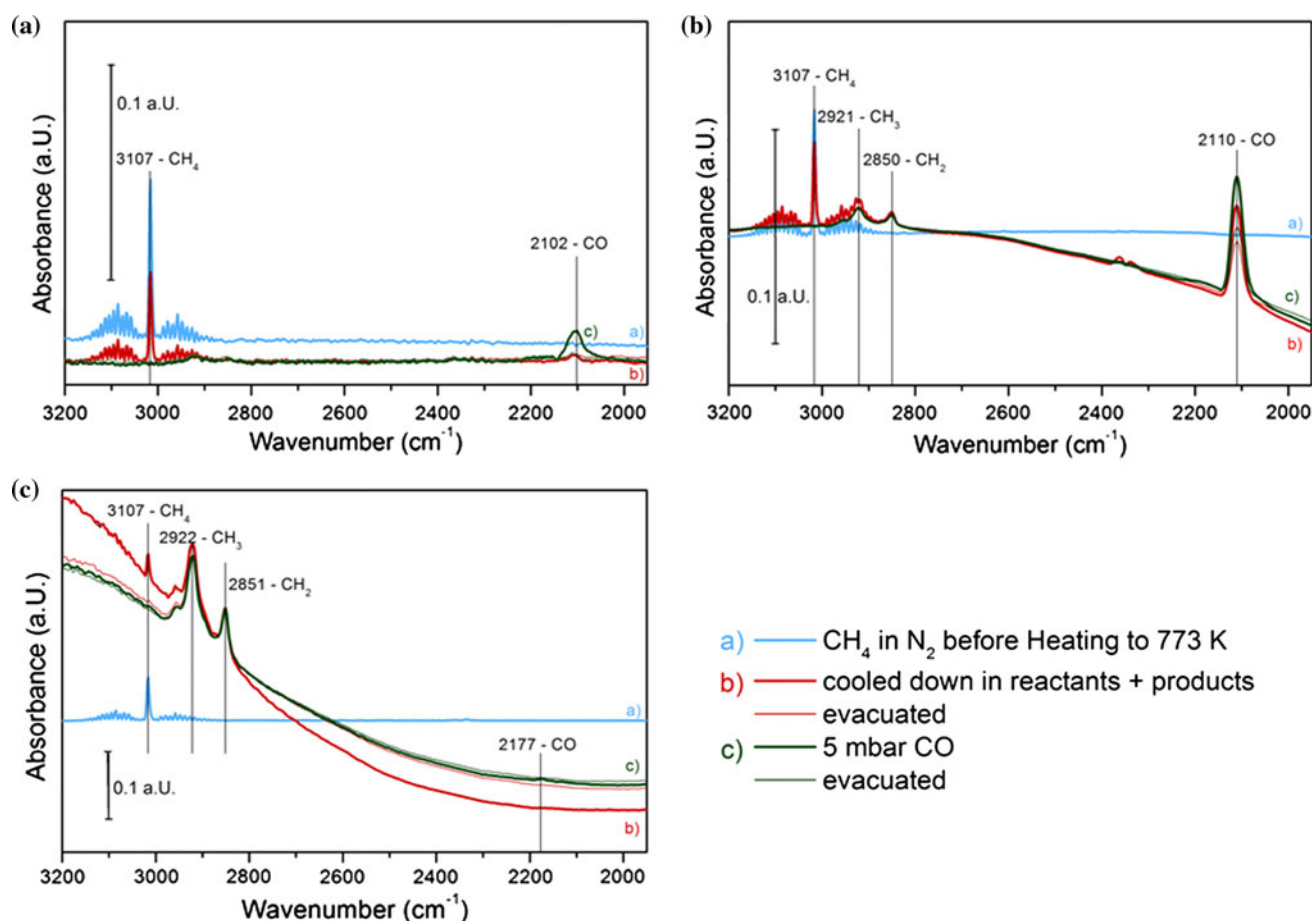


**Fig. 9** IR spectra recorded at room temperature before and after the methane heating ramp and subsequent CO adsorption on reduced **a** Cu–CeZr, **b** 11CuNi–CeZr and **c** Ni–CeZr

### 3.3.2 Methane Decomposition Followed by CO Adsorption on Pre-reduced Catalysts

The same procedure as described in Sect. 3.3.1 was applied to the catalysts after reduction in  $H_2/N_2$ . IR spectra of pre-reduced Ni–CeZr, 11CuNi–CeZr and Cu–CeZr before and after methane decomposition followed by CO adsorption are shown in Fig. 9. The total absorption of the Ni–CeZr changed completely over the whole spectral range after methane decomposition, which again indicates considerable coke formation. Besides, a large amount of adsorbed  $CH_3$  and  $CH_2$  species formed. These species are intermediates of the partial dehydrogenation of methane. CO adsorption is practically impossible on the Ni sample. Only 1 % compared to the fresh reduced sample is adsorbed on Ni–CeZr after exposure to methane.

As on the pre-oxidized samples, Cu–CeZr appears to be much less reactive than Ni–CeZr and 11CuNi–CeZr. On Cu–CeZr a small amount of CO is produced out of methane. Compared to the sample directly after reduction in  $H_2/N_2$  40 % CO can adsorb after evacuation. Most probably,

this can again be attributed to sintering of the now reduced copper taking place upon heating to 773 K. This suggests that on Cu–CeZr another mechanism of methane activation occurs than on nickel. On Cu–CeZr partial oxidation of methane occurs most probably with oxygen atoms from the support oxide while on nickel methane (partial) dehydrogenation is the main reaction.

On the bimetallic catalyst 11CuNi–CeZr CO,  $CO_2$  and adsorbed  $CH_3$  and  $CH_2$  are observed upon heating in methane (Fig. 9b). The amount of produced CO is much larger than on Cu–CeZr. Coking is apparently strongly reduced when regarding absorption over the whole spectral range recorded. When dosing CO after the methane exposure, in total about 40 % of the amount of CO that was adsorbed on a freshly reduced 11CuNi–CeZr sample was adsorbed on the used catalyst. From this it can be concluded that the bimetallic 11CuNi–CeZr catalyst is active for methane dehydrogenation but much less coke formation is detected than on Ni catalysts. On the bimetallic Cu–Ni catalyst both pathways are observed, but (partial) oxidation is favoured and dehydrogenation down to elemental carbon is strongly reduced.

This is in line with the observed enrichment of the surface in copper, breaking up larger nickel ensembles, which are supposed to be responsible for coke formation, and/or changing the electronic properties of nickel resulting in reduced C–H bond breaking.

Gavrielatos et al. [18] and Triantafyllopoulos and Neophytides [19] reported reduced coke formation on Ni–YSZ modified with Au compared with unmodified Ni–YSZ. Generally, two parameters can be considered for the graphite development on nickel surfaces. Firstly, a critical ensemble on Ni is needed for graphite formation [54]. Au was found to be enriched on the surface breaking up larger Ni ensembles [18, 19]. Secondly, Besenbacher et al. [55] showed by DFT calculations and experimental measurements that small amounts of Au on the Ni surface increase the resistance toward carbon formation either by increasing the activation barrier of methane dehydrogenation reaction or by decreasing the binding energy of the resulting CH<sub>x</sub> and C species on the Ni surface.

Liu et al. [56] recently performed DFT calculations for the methane dissociation on copper-rich NiCu(111) compared to Cu(111) and Ni(111). A decreased coke deposition on the copper-rich alloy surface was predicted, because on the one hand the activation barrier of the rate-determining step of methane dissociation is higher by 0.27 eV on copper-rich NiCu(111) than on Ni(111) but lower by 0.58 eV than on Cu(111), which means that a Cu-rich NiCu surface can suppress carbon deposition [56]. Another feature which was found to prevent the building up of a graphite layer was the decrease of C adsorption energy on copper-rich NiCu(111) compared to Ni(111) [56].

## 4 Conclusions

In this work a detailed FTIR spectroscopic study of Cu and Ni bimetallic combinations supported on zirconia and ceria–zirconia is presented. Starting from Ni–Zr, the complexity in composition of the materials investigated was increased by adding Cu to the Ni particles and by modification of the support with ceria.

Adsorption of CO was applied to determine the oxidation state and available surface sites. Copper–nickel alloy formation was indicated by the red-shift of the CO stretching frequency on metallic nickel by about 30 cm<sup>-1</sup> as well as by X-ray absorption measurements which revealed a lower reduction temperature of NiO and CuO in bimetallic alloyed samples as compared to monometallic catalysts. The extent of the red-shift of the Ni–CO band depends on the bulk composition. In addition, the composition affected the desorption temperature of CO on copper, resulting in significantly higher temperature stability on all the bimetallic samples.

Both hydrogen chemisorption and FTIR spectroscopy of CO adsorption clearly demonstrated that the surface of the bimetallic particles was strongly enriched in Cu with about the same composition for samples with different nominal copper:nickel bulk compositions.

Upon exposure to methane at 773 K, coke formation occurred over Ni–CeO<sub>2</sub>/ZrO<sub>2</sub> resulting in a strong change in total absorption. In addition, CH<sub>3</sub> and CH<sub>2</sub> species were formed on the Ni catalyst, which proves (partial) dehydrogenation of methane. In contrast, on Cu–CeO<sub>2</sub>/ZrO<sub>2</sub> CO production was observed with no further changes in the IR spectra. On the bimetallic 11CuNi–CeZr sample after reduction both CH<sub>2</sub>, CH<sub>3</sub> and CO formation took place coming along with strongly reduced coke formation compared to Ni.

While Cu strongly influenced the reaction and adsorption properties of the Ni samples, ceria–zirconia materials exhibited very similar properties and surface chemistry as zirconia-supported samples in the present study. The main difference was an additional IR band of CO adsorbed on metallic copper pointing to an interaction of part of the Cu with the ceria.

**Acknowledgments** This work was supported by the Austrian Science Fund (FWF): (F4502-N16) via SFB FOXSI. We thank Dr. K. Hradil (TU Vienna) for XRD measurements and the Swiss Light Source (Villigen, Switzerland) for providing beamtime at the Super-XAS beamline. Work supported by the European Community's Seventh Framework Programme (FP7/2007-2013) under Grant agreement no. 226716.

**Open Access** This article is distributed under the terms of the Creative Commons Attribution License which permits any use, distribution, and reproduction in any medium, provided the original author(s) and the source are credited.

## References

- Agrell J, Birgersson H, Boutonnet M, Melian-Cabrera I, Navarro RM, Fierro JLG (2003) *J Catal* 219:389
- Armor JN (1999) *Appl Catal A Gen* 176:159
- Matsumura Y, Nakamori T (2004) *Appl Catal A Gen* 258:107
- Wei J, Iglesia E (2004) *J Catal* 224:370
- Rostrup-Nielsen JR, Sehested J, Nørskov JK (2002) *Adv Catal* 47:65
- Kambolis A, Matralis H, Trovarelli A, Papadopoulou C (2010) *Appl Catal A Gen* 377:16
- Montoya JA, Romero-Pascual E, Gimon C, Del AP, Monzon A (2000) *Catal Today* 63:71
- Pompeo F, Nichio NN, Souza MMVM, Cesar DV, Ferretti OA, Schmal M (2007) *Appl Catal A Gen* 316:175
- Souza MMVM, Aranda DAG, Schmal M (2001) *J Catal* 204:498
- Silverwood IP, Hamilton NG, McFarlane AR, Kapitan J, Hecht L, Norris EL, Ormerod RM, Frost CD, Parker SF, Lennon D (2012) *Phys Chem Chem Phys* 14:15214
- Silverwood IP, Hamilton NG, Staniforth JZ, Laycock CJ, Parker SF, Ormerod RM, Lennon D (2010) *Catal Today* 155:319

12. Bitter JH, Seshan K, Lercher JA (1998) *J Catal* 176:93
13. Bradford MCJ, Vannice MA (1996) *Appl Catal A Gen* 142:97
14. Berrocal GP, Silva ALMD, Assaf JM, Albornoz A, Rangel MdC (2010) *Catal Today* 149:240
15. Otsuka K, Wang Y, Sunada E, Yamanaka I (1998) *J Catal* 175:152
16. McIntosh S, Gorte RJ (2004) *Chem Rev* 104:4845
17. Rostrup-Nielsen JR, Alstrup I (1999) *Catal Today* 53:311
18. Gavrielatos I, Drakopoulos V, Neophytides SG (2008) *J Catal* 259:75
19. Triantafyllopoulos NC, Neophytides SG (2006) *J Catal* 239:187
20. Liao M-S, Zhang Q-E (1998) *J Mol Catal A: Chem* 136:185
21. Ringuede A, Labrincha JA, Frade JR (2001) *Solid State Ionics* 141–142:549
22. Abdala PM, Safonova OV, Wiker G, van Beek W, Emerich H, van Bokhoven JA, Sa J, Szlachetko J, Nachttegaal M (2012) *Chimia* 66:699
23. Sa J, Barrabes N, Kleymenov E, Lin C, Föttinger K, Safonova OV, Szlachetko J, van Bokhoven JA, Nachttegaal M, Urakawa A, Crespo GA, Rupprechter G (2012) *Catal Sci Technol* 2:794
24. Kleymenov E, van Bokhoven JA, David C, Glatzel P, Janousch M, Alonso-Mori R, Studer M, Willmann M, Bergamaschi A, Henrich B, Nachttegaal M (2011) *Rev Sci Instrum* 82:065107
25. van Beek W, Safonova OV, Wiker G, Emerich H (2011) *Phase Transitions* 84:726
26. Newville M (2001) *J Synchrotron Radiat* 8:322
27. Barrett EP, Joyner LG, Halenda PP (1951) *J Am Chem Soc* 73:373
28. Goodman DW, Peden CHF (1985) *J Catal* 95:321
29. Rodriguez JA, Campbell RA, Goodman DW (1991) *Surf Sci* 244:211
30. Rodriguez JA, Goodman DW (1991) *J Phys Chem* 95:4196
31. Gayen A, Boaro M, Leitenburg CD, Llorca J, Trovarelli A (2010) *J Catal* 270:285
32. Barrabés N, Föttinger K, Llorca J, Dafinov A, Medina F, Sá J, Hardacre C, Rupprechter G (2010) *J Phys Chem C* 114:17675
33. Daturi M, Binet C, Lavalley J-C, Galtayries A, Sporken R (1999) *Phys Chem Chem Phys* 1:5717
34. Mihaylov M, Chakarova K, Hadjiivanov K (2004) *J Catal* 228:273
35. Ryczkowski J (2001) *Catal Today* 68:263
36. Bandara A, Dobashi S, Kubota J, Onda K, Wada A, Domen K, Hirose C, Kano SS (1997) *Surf Sci* 387:312
37. Busca G, Lorenzelli V, Sanchez EV (1992) *Chem Mater* 4:595
38. Platero EE, Coluccia S, Zecchina A (1985) *Langmuir* 1:407
39. Hadjiivanov K, Knoezinger H, Mihaylov M (2002) *J Phys Chem B* 106:2618
40. Hadjiivanov K, Mihaylov M, Abadjieva N, Klissurski D (1998) *J Chem Soc Faraday Trans* 94:3711
41. Kasal PH, Bishop RJ Jr, McLeod D Jr (1978) *J Phys Chem* 82:279
42. Kermarec M, Olivier D, Richard M, Che M, Bozon-Verduraz F (1982) *J Phys Chem* 86:2818
43. Bonneviot L, Cai FX, Che M, Kermarec M, Legendre O, Lepetit C, Olivier D (1987) *J Phys Chem* 91:5912
44. Dalmon JA, Primet M, Martin GA, Imelik B (1975) *Surf Sci* 50:95
45. Hadjiivanov K, Mihaylov M, Klissurski D, Stefanov P, Abadjieva N, Vassileva E, Mintchev L (1999) *J Catal* 185:314
46. Vesecky SM, Xu X, Goodman DW (1994) *J Vac Sci Technol, A* 12:2114
47. Yoshinobu J, Ballinger TH, Xu Z, Jaensch HJ, Zaki MI, Xu J, Yates JT Jr (1991) *Surf Sci* 255:295
48. Blyholder G (1964) *J Phys Chem* 68:2772
49. Morterra C, Giamello E, Cerrato G, Centi G, Perathoner S (1998) *J Catal* 179:111
50. Chen S, Zou H, Liu Z, Lin W (2009) *Appl Surf Sci* 255:6963
51. Davydov AA (1984) *Infrared spectroscopy of adsorbed species on the surface of transition metal oxides*. Wiley, Novosibirsk
52. Manzoli M, Di MR, Boccuzzi F, Coluccia S, Kaspar J (2005) *Appl Catal B Environ* 61:192
53. Eischens RP (1956) *Z Elektrochem* 60:782
54. Andersen NT, Topsøe F, Alstrup I, Rostrup-Nielsen JR (1987) *J Catal* 104:454
55. Besenbacher F, Chorkendorff I, Clausen BS, Hammer B, Molenbroek AM, Norskov JK, Stensgaard I (1998) *Science* 279:1913
56. Liu H, Zhang R, Yan R, Li J, Wang B, Xie K (2012) *Appl Surf Sci* 258:8177

## PAPER

CrossMark  
click for updatesCite this: *Catal. Sci. Technol.*, 2015,  
5, 967Surface modification processes during methane  
decomposition on Cu-promoted Ni–ZrO<sub>2</sub> catalystsAstrid Wolfbeisser,<sup>a</sup> Bernhard Klötzer,<sup>b</sup> Lukas Mayr,<sup>b</sup> Raffael Rameshan,<sup>b</sup>  
Dmitry Zemlyanov,<sup>c</sup> Johannes Bernardi,<sup>d</sup> Karin Föttinger<sup>\*a</sup>  
and Günther Rupprechter<sup>a</sup>

The surface chemistry of methane on Ni–ZrO<sub>2</sub> and bimetallic CuNi–ZrO<sub>2</sub> catalysts and the stability of the CuNi alloy under reaction conditions of methane decomposition were investigated by combining reactivity measurements and *in situ* synchrotron-based near-ambient pressure XPS. Cu was selected as an exemplary promoter for modifying the reactivity of Ni and enhancing the resistance against coke formation. We observed an activation process occurring in methane between 650 and 735 K with the exact temperature depending on the composition which resulted in an irreversible modification of the catalytic performance of the bimetallic catalysts towards a Ni-like behaviour. The sudden increase in catalytic activity could be explained by an increase in the concentration of reduced Ni atoms at the catalyst surface in the active state, likely as a consequence of the interaction with methane. Cu addition to Ni improved the desired resistance against carbon deposition by lowering the amount of coke formed. As a key conclusion, the CuNi alloy shows limited stability under relevant reaction conditions. This system is stable only in a limited range of temperature up to ~700 K in methane. Beyond this temperature, segregation of Ni species causes a fast increase in methane decomposition rate. In view of the applicability of this system, a detailed understanding of the stability and surface composition of the bimetallic phases present and the influence of the Cu promoter on the surface chemistry under relevant reaction conditions are essential.

Received 30th July 2014,  
Accepted 3rd October 2014

DOI: 10.1039/c4cy00988f

www.rsc.org/catalysis

## Introduction

Hydrogen is known as a promising source of energy and fuel. Up to now hydrogen is mostly produced out of hydrocarbons such as methane. *Via* steam reforming<sup>1–4</sup> or partial oxidation<sup>5,6</sup> of methane, CO or CO<sub>2</sub> is formed as a by-product. For many applications such as the use of hydrogen in PEM fuel cells CO needs to be removed because it is a catalyst poison. One possibility to overcome the problem of CO or CO<sub>2</sub> formation is the direct production of hydrogen out of methane by catalytic decomposition in the absence of air or oxygen. The by-product of this process is carbon in the form of layers, filaments, fibres or nanotubes. Especially, the formation of useful nanocarbons<sup>7–14</sup> is of high interest. Li *et al.*<sup>15</sup> published a comprehensive review about this topic discussing the effect of

the nature of the catalyst and feed composition on the catalytic activity, stability and the influence on the morphology of the produced carbon.

During methane decomposition, methane is adsorbed on the catalyst followed by C–H bond breaking, deposition of carbon and generation of hydrogen. Transition metals such as Ni,<sup>16–18</sup> Fe<sup>17</sup> and Co<sup>19</sup> are known to be effective for methane decomposition to hydrogen and carbon nanofibres. Ni catalysts are known for their high activity but are easily deactivated due to carbon deposition. However, nickel-based catalysts have been proven to be sensitive to doping and structure modification by other metals, such as Cu, which affects the structure and morphology of the produced carbon.<sup>8</sup> Improved stability against deactivation has been achieved by adding a second metal component; for example, Au<sup>20–23</sup> and Cu<sup>13,24–32</sup> have been studied for this aim. The Ni–Au surface alloy was active for steam reforming and more resistant toward carbon formation than the pure Ni, which was explained by blocking of highly reactive Ni edge and kink sites by Au atoms.<sup>21</sup> The addition of Cu to nickel-based catalysts has several effects such as an easier reducibility of Ni. Cu is rich in d-electrons which may exert an electronic effect on Ni and furthermore affect the affinity of the metal surface to graphite.<sup>15</sup> Ashok *et al.* observed that addition of Cu to Ni

<sup>a</sup> Institute of Materials Chemistry, Vienna University of Technology, Getreidemarkt 9, 1020 Wien, Austria. E-mail: karin.foettinger@tuwien.ac.at; Fax: +43 1 58801 16599; Tel: +43 1 165110

<sup>b</sup> Institute of Physical Chemistry, University of Innsbruck, Innrain 52a, 6020 Innsbruck, Austria

<sup>c</sup> Purdue University, Brick Nanotechnology Center, 1205 West State Street, West Lafayette, IN 47907-2057, USA

<sup>d</sup> University Service Center for Transmission Electron Microscopy, Vienna University of Technology, Wiedner Hauptstraße 8-10, 1040 Wien, Austria

enhanced the methane decomposition activity of hydrotalcite-like Ni–Cu–Al catalysts when added in an appropriate amount.<sup>26</sup> Suelves *et al.* showed that doping of Cu has a strong influence on the dispersion of nickel and enhances the catalyst activity.<sup>30</sup> Similarly, Monzón found that promoting Ni with a small amount of Cu improves the activity and stability of the catalyst.<sup>31</sup> Cunha *et al.* reported that doping with Cu improves the catalyst stability.<sup>32</sup> Li *et al.* observed that in Cu<sub>0.25</sub>Ni<sub>0.75</sub>Al<sub>2</sub>O<sub>4</sub> Cu is acting as a dispersive agent to prevent Ni from growing<sup>24</sup> and enhances the catalyst stability when employed in a suitable amount.<sup>13</sup> Lazaro *et al.* found that the presence of copper in NiCu–SiO<sub>2</sub> catalysts led to higher methane conversion,<sup>28</sup> and Park *et al.* observed that on Cu–Ni–YSZ anode materials for the direct use of methane fuel in solid oxide fuel cells (SOFC) carbon deposition decreased compared to the amount of carbon on Ni–YSZ.<sup>29</sup> DFT-based computational studies by Liu *et al.* compared methane dissociation on NiCu(111) bimetallic alloy surfaces. Their calculations indicated that C is easily formed on a uniform 1:1 NiCu surface but unfavourable on a Cu-rich NiCu surface.<sup>33</sup> Therefore, the surface composition on a NiCu alloy catalyst under reaction conditions is expected to play the key role in determining the catalytic activity and stability.

One prerequisite for a successful promoter is *in situ* stability under relevant reaction conditions, *i.e.* high temperatures and reactive surrounding gas atmosphere. Therefore, understanding the stability of the bimetallic phases and the influence of the promoter on the surface chemistry are essential. We have studied CH<sub>4</sub>- and methanol reforming activities and selectivities on Ni-, Cu- and Pd-based catalyst systems by combining *in situ* spectroscopic techniques such as XPS, FTIR and XAS.<sup>25,34–39</sup> In the present work, we have selected Cu as an exemplary compound for modifying the reactivity of Ni in methane decomposition and enhancing the resistance against coke formation.

In this work we focus on the surface chemistry of methane on Ni–ZrO<sub>2</sub> catalysts during methane decomposition at temperatures up to 773 K and study the stability of the CuNi alloy under reaction conditions. By *in situ* synchrotron-based near-ambient pressure (NAP)-XPS we determined the surface composition of the catalysts and the nature of the carbonaceous species present and correlated these data with the catalytic performance. Cu addition to Ni improved the desired reduction of carbon deposition,<sup>40</sup> but only in a limited range of temperature due to the limited stability of this system.

## Experimental

### Sample preparation

Ni–ZrO<sub>2</sub> and bimetallic CuNi–ZrO<sub>2</sub> catalysts were synthesized by impregnation of ZrO<sub>2</sub> using nitrate precursor salts. Prior to impregnation, commercial Zr(OH)<sub>4</sub> (MEL Chemicals XZO 880/01) was calcined at a heating rate of 2 K min<sup>−1</sup> from room temperature to 973 K and kept at this temperature for 2 h. After calcination the zirconia support exhibits a specific surface area of 36.6 m<sup>2</sup> g<sup>−1</sup>.

Bimetallic CuNi samples were prepared by coimpregnation. Cu(NO<sub>3</sub>)<sub>2</sub>·3H<sub>2</sub>O (Fluka, p.a.) and Ni(NO<sub>3</sub>)<sub>2</sub>·6H<sub>2</sub>O (Merck, p.a.) were mixed to obtain the following Cu : Ni molar ratios: 1 : 0, 3 : 1, 1 : 1, 1 : 3 and 0 : 1. The nitrates were dissolved in water, and in each case 4.75 g of ZrO<sub>2</sub> powder was suspended in these solutions. Every solution contained as much metal nitrate to obtain 5 wt% metal loading in the final catalyst powder. Additionally, a 5 wt% Cu–ZrO<sub>2</sub> reference material was synthesized by the same procedure.

For *in situ* X-ray photoelectron spectroscopy (XPS) investigations an additional sample was prepared *via* the same synthesis route with a higher overall metal loading of 50 wt% in order to prevent sample charging.

All catalysts and their respective compositions are summarized in Table 1.

### Characterization

Transmission electron microscopy (TEM) was utilized to obtain information about the size, morphology and distribution of the metal particles on the zirconia support. For TEM measurements the samples were deposited on carbon-coated Cu grids (Ni–ZrO<sub>2</sub>) or Au grids (all copper-containing samples). The catalysts were oxidized at 773 K and reduced at 673 K prior to the experiment. TEM measurements were performed using an analytical TECNAI F20 instrument connected to an EDX detector. EDX was used to identify Cu, Ni or bimetallic CuNi particles. For the bimetallic catalyst elemental mapping was additionally carried out.

### Reactivity for methane decomposition

Temperature-programmed methane decomposition (TPMd) experiments were performed in a quartz flow reactor. Part of the effluent was directed to a mass spectrometer (Pfeiffer QMS 200) *via* a differentially pumped capillary. Thereby the main products (H<sub>2</sub>, CO, CO<sub>2</sub> and CH<sub>4</sub>) were detected. 50 mg of the catalyst was loaded into the glass reactor in-between two plugs of quartz wool. The catalysts were oxidized at 773 K and reduced at 673 K prior to the reaction. Then the samples were heated up to 773 K and cooled down to 573 K in a mixture of 5% CH<sub>4</sub> and 95% Ar with a total flow of 50 ml min<sup>−1</sup>. The heating and cooling rate was set to 5 K min<sup>−1</sup> and the heating–cooling cycle was repeated thrice. After the TPMd experiment the sample was cooled down to room temperature in Ar. Subsequently, temperature-programmed oxidation (TPO) was performed in 20% O<sub>2</sub> in Ar applying a heating rate of 5 K min<sup>−1</sup> up to 673 K.

Table 1 Composition of CuNi–ZrO<sub>2</sub> catalysts

Sample name	ZrO <sub>2</sub> (wt%)	Cu (wt%)	Ni (wt%)
Ni–ZrO <sub>2</sub>	95	—	5
13CuNi–ZrO <sub>2</sub>	95	1.25	3.75
11CuNi–ZrO <sub>2</sub>	95	2.5	2.5
31CuNi–ZrO <sub>2</sub>	95	3.75	1.25
Cu–ZrO <sub>2</sub>	95	5	—
13CuNi–ZrO <sub>2</sub> 50	50	12.5	37.5

For the quantitative determination of the reaction rates the reaction products were analyzed under steady-state conditions by a gas chromatograph equipped with a thermal conductivity detector (TCD) and flame ionization detector (FID).

### *In situ* XPS measurements

*In situ* synchrotron-based near-ambient pressure (NAP)-XPS measurements were carried out at the ISSIS-PGM beamline at the Helmholtz-Zentrum Berlin using a high-pressure XPS station constructed at the FHI Berlin. Details of the setup are described elsewhere.<sup>41</sup> Briefly, the setup uses a differentially pumped electrostatic lens system and a SPECS hemispherical electron analyser.

The sample was placed inside a reaction cell with adjustable gas flow and a total pressure up to the millibar range. The composition of the gas phase was analysed by MS. Heating was done by an IR laser from the back side. The sample was *in situ* oxidized in 0.1 mbar O<sub>2</sub> at 573 K and reduced in 0.25 mbar H<sub>2</sub> at 673 K prior to exposure to 0.25 mbar CH<sub>4</sub> at temperatures ranging from 523 up to 723 K.

The catalyst 13CuNi-ZrO<sub>2</sub>50 with 50 wt% total metal loading was used for these experiments which prevented sample charging. The calcined powder was pressed onto a copper plate and reduced in 0.25 mbar H<sub>2</sub> at 773 K prior to placing it into the *in situ* reaction cell. Measurements were performed at photon energies of 1100 eV for the Cu 2p, 1010 eV for the Ni 2p and 425 eV for the C 1s XP spectra, yielding a photoelectron kinetic energy of 150 eV. For depth profiling the photon energies were varied to obtain additional photoelectron kinetic energies of 350 eV and 550 eV. All spectra were corrected for synchrotron beam current, incident photon flux and energy-dependent photo-ionization cross sections.<sup>42</sup> Binding energies (BEs) were referenced to the Fermi edge recorded after each core-level measurement. The measured signal envelopes were fitted to Gauss-Lorentzian peaks by using Casa XPS software after subtraction of a Shirley background.

## Results

### Transmission electron microscopy

Fig. 1 shows transmission electron micrographs of Ni-ZrO<sub>2</sub>, Cu-ZrO<sub>2</sub> and 11CuNi-ZrO<sub>2</sub> after *ex situ* reduction.

The size of the ZrO<sub>2</sub> particles was between 50 and 100 nm. In general the metal particles were found to be evenly

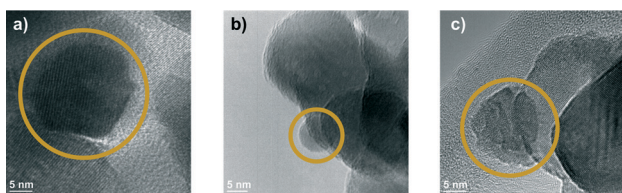


Fig. 1 TEM images of a) Ni-ZrO<sub>2</sub>, b) Cu-ZrO<sub>2</sub> and c) 11CuNi-ZrO<sub>2</sub>. The particles inside the circles were identified *via* EDX as Ni in a), Cu in b) and CuNi in c).

distributed on the oxide support. The Ni particles in Ni-ZrO<sub>2</sub> exhibit a homogeneous size distribution of approximately 20 nm mean size and are of polyhedral shape. The Cu particles in Cu-ZrO<sub>2</sub> are spherical and about 5 nm in size. In contrast, the metal particles on the bimetallic 11CuNi-ZrO<sub>2</sub> with average sizes of around 20 nm are polycrystalline and rather irregular in shape. EDX spectra showed that those particles contained both Cu and Ni, although not in the expected 1 : 1 ratio, but they were enriched in nickel. To get a better understanding of the Cu and Ni distribution on the bimetallic catalyst, elemental maps were recorded. The results are displayed in Fig. 2.

While Ni was always accompanied by the simultaneous presence of Cu as demonstrated with full arrows in Fig. 2, Cu was additionally found finely distributed in regions where no or hardly any nickel was detected (dashed arrows in Fig. 2). Thus, the elemental maps revealed the presence of Ni-rich bimetallic particles as well as monometallic Cu particles. XANES spectra of the same catalyst during reduction confirmed the presence of bimetallic CuNi particles.<sup>25</sup> The observation that the presence of copper improves the reducibility of nickel and lowers its reduction temperature is in agreement with TPR experiments reported in the literature.<sup>9,26,27,43–45</sup>

### Temperature-programmed methane decomposition

The reactivity of the catalysts for decomposition of methane was investigated by TPMd measurements. The results obtained over Ni-ZrO<sub>2</sub> are shown in Fig. 3a).

The production of hydrogen started at around 625 K, increased further with increasing temperature and decreased again reversibly when the sample was cooled down to 573 K. Upon heating again to 773 K, the hydrogen production rate remained approximately the same as in the first cycle. Thus, no deactivation of H<sub>2</sub> production activity was observed. Besides H<sub>2</sub> formation, carbon dioxide evolution occurred during the first heating cycle in methane up to ~700 K. In the second and third heating cycles a small CO<sub>2</sub> desorption peak was observed with a maximum at 630 K. The detected CO<sub>2</sub>

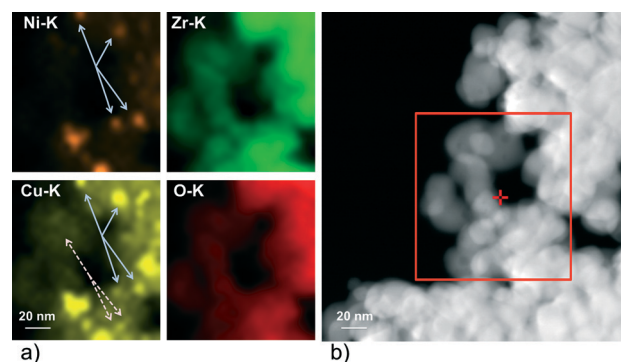
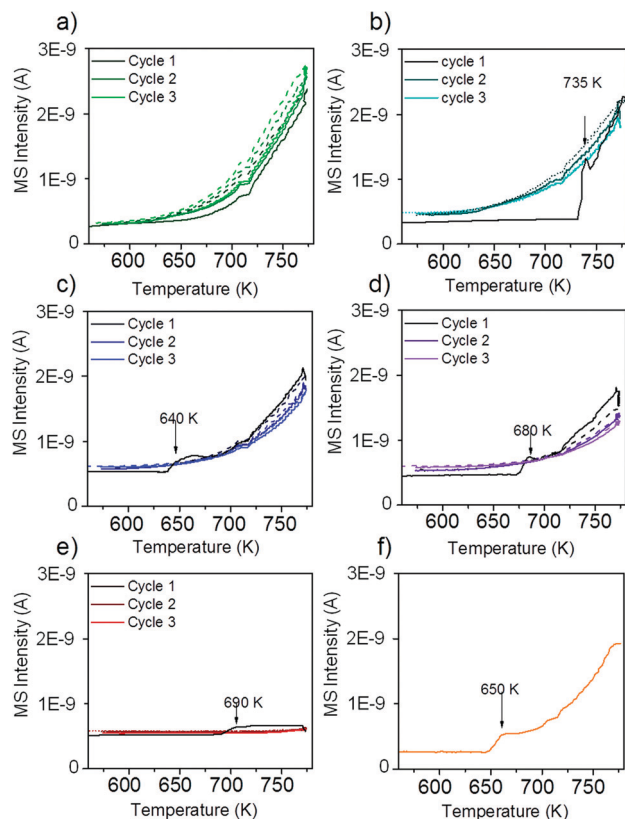


Fig. 2 a) Elemental map of the region shown in the rectangle in b) for the K edge energies of Ni, Cu, Zr and O recorded on 11CuNi-ZrO<sub>2</sub>. Full arrows: particles containing both Ni and Cu, dashed arrows: Cu but no Ni detected.



**Fig. 3** Hydrogen evolution during methane TPMd on a) Ni-ZrO<sub>2</sub>, b) 13CuNi-ZrO<sub>2</sub>, c) 11CuNi-ZrO<sub>2</sub>, d) 31CuNi-ZrO<sub>2</sub>, e) Cu-ZrO<sub>2</sub> and f) 13CuNi-ZrO<sub>2</sub>.50. The samples a)–f) were reduced at 673 K followed by 3 heating-cooling cycles between 573 and 773 K in methane/Ar. For f) only one heating cycle is shown. The temperature was ramped at 5 K min<sup>-1</sup>.

likely originates from the reaction of methane with surface oxygen and carbonates of zirconia or with NiO present due to incomplete reduction.

Fig. 3b) shows the rate of hydrogen production over 13CuNi-ZrO<sub>2</sub> under the same conditions. Over this sample no catalytic activity was found up to 735 K. At this temperature, the amount of produced hydrogen increased rapidly up to a level similar to that over Ni-ZrO<sub>2</sub>. The onset of H<sub>2</sub> production was accompanied by a small amount of CO<sub>2</sub> evolving which occurred only in the first heating cycle. During the second and third reaction cycles about the same amount of hydrogen was detected than that over Ni-ZrO<sub>2</sub>. This indicates an irreversible surface modification process on the bimetallic 13CuNi-ZrO<sub>2</sub> sample occurring during the first heating cycle in methane which significantly changed the catalytic performance of the catalyst.

On 11CuNi-ZrO<sub>2</sub> and 31CuNi-ZrO<sub>2</sub> as well as 13CuNi-ZrO<sub>2</sub>.50, shown in Fig. 3c), d) and f), a behaviour was observed similar to that on 13CuNi-ZrO<sub>2</sub> but the activation step occurred at 640 K, 680 K and 650 K, respectively, and the activity for H<sub>2</sub> formation was lower than that on the Ni-rich sample. Over Cu-ZrO<sub>2</sub>, shown in Fig. 3e), hardly any hydrogen production was observed. During the first heating cycle a small amount of hydrogen was produced above 690 K

but decreased again during the isothermal period at 773 K. A small amount of CO<sub>2</sub> was also detected during the first heating cycle. Afterwards, Cu-ZrO<sub>2</sub> was completely inactive. The low initial activity can likely be attributed to the reaction of methane with surface oxygen and hydroxide species from zirconia or incompletely reduced Cu species and are not available anymore in the second and third reaction cycles. Often CO is reported as a by-product of the reaction between methane and oxygen species on the support or the incompletely reduced metal oxides.<sup>46,47</sup> However, formation of various surface carbonate species was observed from CO on zirconia and all zirconia-supported catalysts by IR spectroscopy, which likely decompose to CO<sub>2</sub>.

In order to find out whether hydrogen evolution occurs because of further reduction of the catalyst in methane, the measurement was repeated with the same sample but after reduction at 773 K instead of 673 K. The sudden onset in hydrogen formation accompanied by carbon dioxide evolution was also observed, but the onset temperature was lowered to 650 K.

For quantitative comparison of the catalytic activity the amount of produced hydrogen was determined by GC-TCD.

Table 2 shows the hydrogen yields and reaction rates for hydrogen production during steady-state methane decomposition at 773 K.

The initial reaction rate  $r$  calculated per gram catalyst decreased with decreasing overall Ni content. However, the rate  $R$  normalized per gram Ni is of about the same order of magnitude for Ni and all bimetallic samples containing 5 wt% total loading. In agreement with TPMd measurements, similar rates of hydrogen formation were detected on Ni-rich 13CuNi-ZrO<sub>2</sub> compared to those on Ni-ZrO<sub>2</sub>. Cu is almost inactive and the reaction rate decreases fast to zero with time on-stream while it stays constant for the other catalysts for at least 1 hour. The rate  $r$  of the catalyst containing 50 wt% metals, 13CuNi-ZrO<sub>2</sub>.50, is about the same as that of 13CuNi-ZrO<sub>2</sub> with 5 wt% metal loading, which results in a reaction rate  $R$  per gram nickel of one order of magnitude lower. This can probably be explained by a lower Ni dispersion at such high loading. In general, we did not observe an enhancement of the catalytic activity by addition of copper to the Ni-ZrO<sub>2</sub> catalyst.

### Temperature-programmed oxidation

To obtain insights into coke formation, temperature-programmed oxidation (TPO) was performed after reaction in methane. The amount of carbon dioxide formed during TPO provides information about the amount of coke formed during the reaction, and the temperature, which is needed to burn off the carbon species, may be characteristic of the carbon bond strength to the catalyst's surface. Fig. 4 shows the production of carbon dioxide observed during TPO in 20% O<sub>2</sub> in Ar performed directly after methane decomposition (described in the previous section). Over Ni-ZrO<sub>2</sub> the highest amount of coke was formed and temperatures of 770 K were

**Table 2** Hydrogen yields and initial reaction rates during methane decomposition at 773 K in 5% CH<sub>4</sub> and 95% Ar with a total flow of 50 ml min<sup>-1</sup>

Sample	H <sub>2</sub> yield	Reaction rate <i>r</i> per g catalyst (mol H <sub>2</sub> /(g <sub>catalyst</sub> s <sup>-1</sup> ))	Reaction rate <i>R</i> per g nickel (mol H <sub>2</sub> /(g <sub>nickel</sub> s <sup>-1</sup> ))
Ni-ZrO <sub>2</sub>	63.3%	2.4 × 10 <sup>-5</sup>	4.8 × 10 <sup>-4</sup>
13CuNi-ZrO <sub>2</sub>	49.8%	1.9 × 10 <sup>-5</sup>	5.0 × 10 <sup>-4</sup>
11CuNi-ZrO <sub>2</sub>	16.9%	6.4 × 10 <sup>-6</sup>	2.6 × 10 <sup>-4</sup>
31CuNi-ZrO <sub>2</sub>	13.6%	5.1 × 10 <sup>-6</sup>	4.1 × 10 <sup>-4</sup>
Cu-ZrO <sub>2</sub>	1.5%	5.6 × 10 <sup>-7</sup>	—
13CuNi-ZrO <sub>2</sub> 50	40.0%	1.5 × 10 <sup>-5</sup>	3.9 × 10 <sup>-5</sup>

needed to oxidize most of it. On the nickel-rich bimetallic catalyst 13CuNi-ZrO<sub>2</sub> the amount of formed CO<sub>2</sub> was lower by about 50% compared to that on Ni-ZrO<sub>2</sub>. Furthermore, much lower temperatures of around 700 K were required to remove carbon by oxidation. At about 750 K a second smaller CO<sub>2</sub> evolution peak was observed in the TPO. Over 11CuNi-ZrO<sub>2</sub> the amount of coke was reduced to 30% compared to that over Ni-ZrO<sub>2</sub>, and the maximum of CO<sub>2</sub> formation was detected at 650 K. Over the Cu-rich catalyst 31CuNi-ZrO<sub>2</sub> the amount of carbon was reduced to only 20% compared to that over Ni-ZrO<sub>2</sub>. Here, one needs to keep in mind the lower activity of the Cu-rich compositions compared to that of Ni-ZrO<sub>2</sub>. The maximum of the CO<sub>2</sub> formation rate was observed at 660 K. When considering the differences in H<sub>2</sub> production rate (Table 2) and the CO<sub>2</sub> peak areas observed in the TPO measurements, the addition of Cu lowered the amount of coke formed. A major effect of Cu was, however, the down-shift of the carbon oxidation temperature. Since hardly any methane decomposition reaction took place over the Cu-ZrO<sub>2</sub> reference material, no coke was burnt off during TPO over this catalyst.

The TPO curves show large CO<sub>2</sub> desorption peaks in a narrow temperature range as well as broader peaks of CO<sub>2</sub> formation over a broad temperature range. The narrow peaks were always accompanied by a small peak of water (*m/z* 18) which indicates oxidation of CH<sub>x</sub> species in this temperature range. The much broader peak underneath might originate from other carbonaceous species such as filamentous carbon.

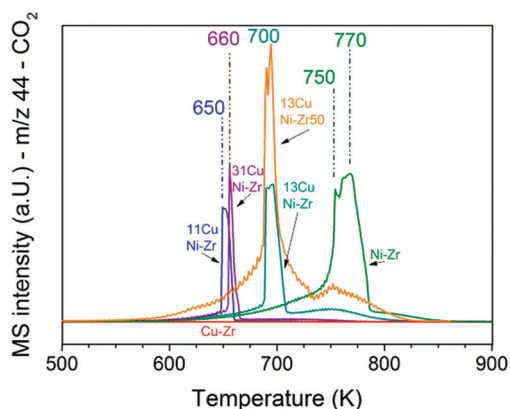


**Fig. 4** TPO performed after the methane decomposition reaction over Ni and all CuNi catalysts (shown in Fig. 3). The mass spectrometry trace of CO<sub>2</sub> (*m/z* 44) is displayed upon heating in 20 vol% O<sub>2</sub>/Ar at a rate of 5 K min<sup>-1</sup>.

The presence of CH<sub>x</sub> species indicates that part of the adsorbed methane dissociated incompletely.

In summary, the highest C and CH<sub>x</sub> oxidation temperature was observed on monometallic nickel at 750–770 K. Since the oxidation temperature decreased on the bimetallic catalysts we conclude that C species are less strongly bonded to the bimetallic surface. A similar trend with the composition was noticed as for the activity onset temperature described in the section about TPMd. The highest temperature required to burn off coke was observed for 13CuNi-ZrO<sub>2</sub>, with a CO<sub>2</sub> evolution maximum at 700 K, while 11CuNi-ZrO<sub>2</sub> exhibited the lowest carbon oxidation temperature with a CO<sub>2</sub> evolution maximum at 650 K.

#### *In situ* X-ray photoelectron spectroscopy

In order to learn more about the surface composition, oxidation states and carbonaceous species present under the reaction atmosphere, *in situ* XPS at millibar pressures was employed. The bimetallic Ni-rich 1:3 composition which showed the most pronounced increase in methane decomposition activity was investigated further by synchrotron-based *in situ* XPS aiming at understanding the nature of the irreversible surface modification process. To avoid further complication of the (already complex) spectra by charging effects, a catalyst with a higher overall metal loading of 50 wt% was utilized after carefully checking the comparability of this material to the respective 5 wt% sample.

#### XP spectra during reduction in H<sub>2</sub>

Fig. 5 shows the Cu 2p<sub>3/2</sub> binding energy region of 13CuNi-ZrO<sub>2</sub>50 during a) oxidation and b) reduction. The peak positions and full width at half-maximum (FWHM) are listed in Table 3.

The broad peak at 933.3 eV is attributed to CuO<sup>48–53</sup> with two characteristic shake-up satellite peaks at 940.7 and 943.3 eV. The structure seen in the satellite line is due to the multiplet splitting in the 2p 3d final state.<sup>50</sup> The small peak located at 932.3 eV is characteristic of Cu<sub>2</sub>O and/or metallic Cu.<sup>48,50,52,53</sup> During reduction at 673 K the CuO peak decreased in intensity while the signal of reduced Cu species strongly increased. Since the shift of alloyed Cu in CuNi has been reported to be only about 0.2 eV compared to that in monometallic Cu<sup>54–56</sup> we could not resolve this species.

Fig. 6 shows the Ni 2p<sub>3/2</sub> core levels of 13CuNi-ZrO<sub>2</sub>50 measured during a) oxidation and b) reduction. The peak at

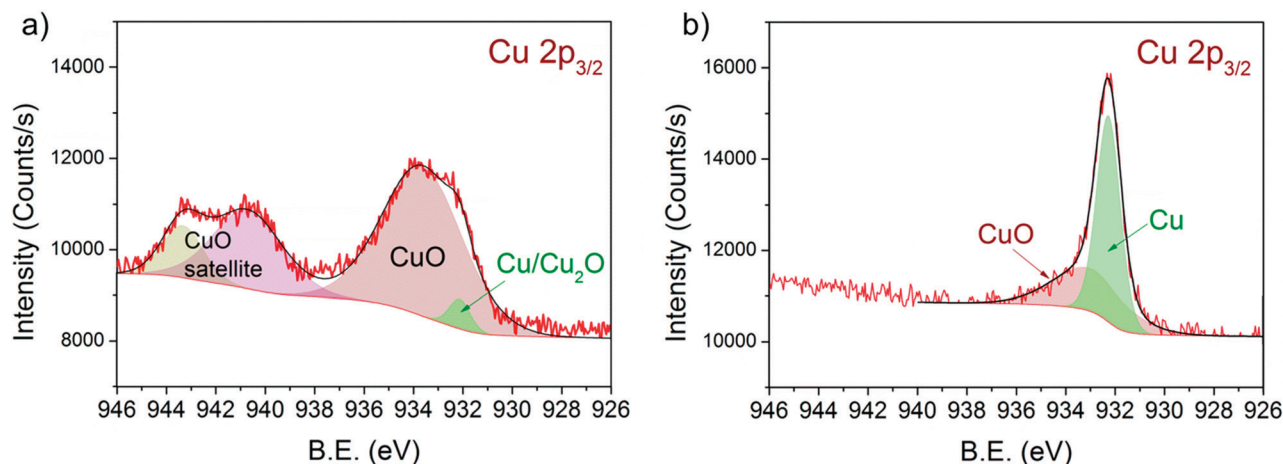


Fig. 5 Cu  $2p_{3/2}$  region of  $^{13}\text{CuNi-ZrO}_2$  50 in a) 0.10 mbar  $\text{O}_2$  at 573 K and b) 0.25 mbar  $\text{H}_2$  at 673 K for 30 min. The incident photon energy was 1100 eV.

Table 3 Peak positions obtained in XPS measurements on  $^{13}\text{CuNi-ZrO}_2$  50

Species	Peak position (eV)	FWHM (eV)
CuO satellite 2	$943.3 \pm 0.2$	$1.9 \pm 0.2$
CuO satellite 1	$940.7 \pm 0.2$	$3.3 \pm 0.2$
CuO	$933.3 \pm 0.4$	$3.7 \pm 0.3$
New Cu species	$933.6 \pm 0.2$	$1.1 \pm 0.1$
Cu and $\text{Cu}_2\text{O}$	$932.3 \pm 0.1$	$0.9 \pm 0.1$
NiO	$854.2 \pm 0.2$	
Ni	$852.6 \pm 0.1$	
Carbonates/carbon oxygenates	$290.1 \pm 0.1, 288.8 \pm 0.1, 287.8 \pm 0.2$	$1.1 \pm 0.2$
C–O or C–OH	$286.3 \pm 0.1$	$0.9 \pm 0.1$
$\text{C}_x\text{H}_y$ species	$285.4 \pm 0.1$	$0.8 \pm 0.1$
C $\text{sp}^2$	$284.8 \pm 0.1$	$0.6 \pm 0.1$
Graphitic carbon	$284.3 \pm 0.1$	$0.8 \pm 0.1$
$\text{Ni}_x\text{C}$	$283.4 \pm 0.1$	$0.9 \pm 0.1$

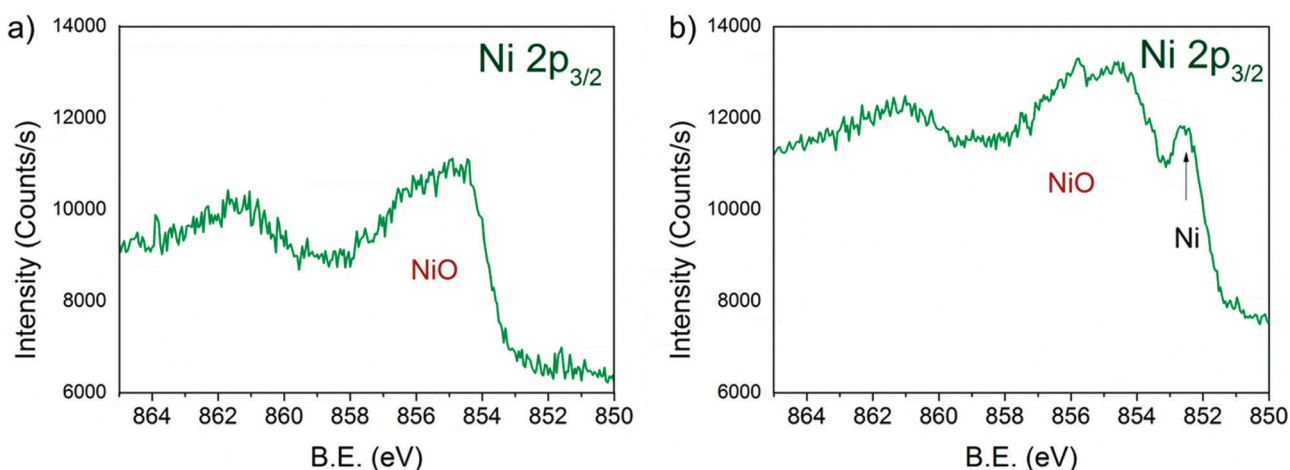


Fig. 6 Ni  $2p_{3/2}$  region of  $^{13}\text{CuNi-ZrO}_2$  50 in a) 0.10 mbar  $\text{O}_2$  at 573 K and b) 0.25 mbar  $\text{H}_2$  at 673 K for 30 min. The incident photon energy was 1010 eV.

854.3 eV is attributed to the main line of NiO.<sup>23,53,57–59</sup> In a reducing atmosphere an additional peak appeared at 852.6 eV, which is ascribed to metallic nickel.<sup>53,60,61</sup> Again, it is not possible to distinguish between nickel interacting with

copper and non-interacting with copper due to the small chemical shift of about 0.2 eV<sup>54–56</sup> which would be expected for Ni alloyed with Cu. In agreement with previously reported findings by IR spectroscopy of CO adsorption on reduced

CuNi both oxidized and reduced Ni species are present at the surface after reduction at 673 K, although the bulk consists predominantly of reduced Ni species according to XANES measurements.

Due to the high complexity of the NiO spectrum consisting of shake-up peaks and multiplet states<sup>57,62</sup> we fitted Ni 2p<sub>3/2</sub> spectra by the linear combination of reference spectra of NiO and completely reduced Ni. The resulting Ni-to-NiO ratios are summarized in Table 4.

Overall, the XP spectra reveal the coexistence of reduced Cu and a mixture of oxidized and metallic Ni species in the near-surface region after reduction.

### XP spectra during methane decomposition

Fig. 7 shows a) the Cu 2p<sub>3/2</sub> region and b) the Ni 2p<sub>3/2</sub> region of 13CuNi-ZrO<sub>2</sub> during exposure to 0.25 mbar methane at temperatures from 523 to 723 K directly after reduction in H<sub>2</sub>.

At 523 K mainly metallic copper and small amounts of CuO were present in the Cu 2p<sub>3/2</sub> region. By increasing the

temperature the metallic Cu peak became broader and shifted to a slightly higher binding energy indicating further alloy formation between copper and nickel. The amount of nickel oxide decreased with temperature, while the signal of metallic nickel increased. At 723 K a new Cu species at 933.6 eV appeared at the highest temperature. A potential assignment of this species is Cu interacting with surface carbonates;<sup>53</sup> however, a larger shift to higher binding energies would be expected compared to CuO. CuO core levels have been observed over a broad binding energy range, but in the XP spectrum at 723 K no satellite peaks characteristic of CuO are found, which rather excludes the assignment of the peak at 933.6 eV to CuO. Currently, the nature of this peak remains an open question.

Between 698 and 723 K the biggest changes were observed in the Ni 2p<sub>3/2</sub> region as well. The amount of NiO decreased significantly, while the concentration of metallic nickel increased in the near-surface region. Note that in the temperature range between 698 and 723 K where the strongest spectral changes occurred the catalytic activity of this catalyst increases dramatically, as shown by TPMd and in agreement with the simultaneously recorded mass spectrometry data.

Fig. 8 shows the C 1s core level region during exposure of 13CuNi-ZrO<sub>2</sub> to methane at temperatures increasing from 523 to 723 K. A number of different carbon-containing surface species were present in methane. Polycarbonates, carbonates and carbon oxygenates above 287 eV hardly changed with temperature. Various carbonate species were also observed by infrared spectroscopy on ZrO<sub>2</sub>. C-O<sup>63-66</sup> or C-OH<sup>64,65</sup> at 286.3 eV increased with temperature, indicating an interaction of carbon with the oxide support or NiO and CuO which had not been reduced up to that temperature.

**Table 4** Proportion of NiO and Ni in Ni 2p<sub>3/2</sub> spectra fitted by linear combination of reference spectra

Atmosphere and temperature (K)	NiO	Ni
O <sub>2</sub> – 573	100%	
H <sub>2</sub> – 573	77 ± 3%	23 ± 3%
CH <sub>4</sub> – 523	79 ± 3%	21 ± 3%
CH <sub>4</sub> – 573	80 ± 2%	20 ± 2%
CH <sub>4</sub> – 623	79 ± 3%	21 ± 3%
CH <sub>4</sub> – 673	77 ± 3%	23 ± 3%
CH <sub>4</sub> – 697	75 ± 3%	25 ± 3%
CH <sub>4</sub> – 723	66 ± 3%	34 ± 3%

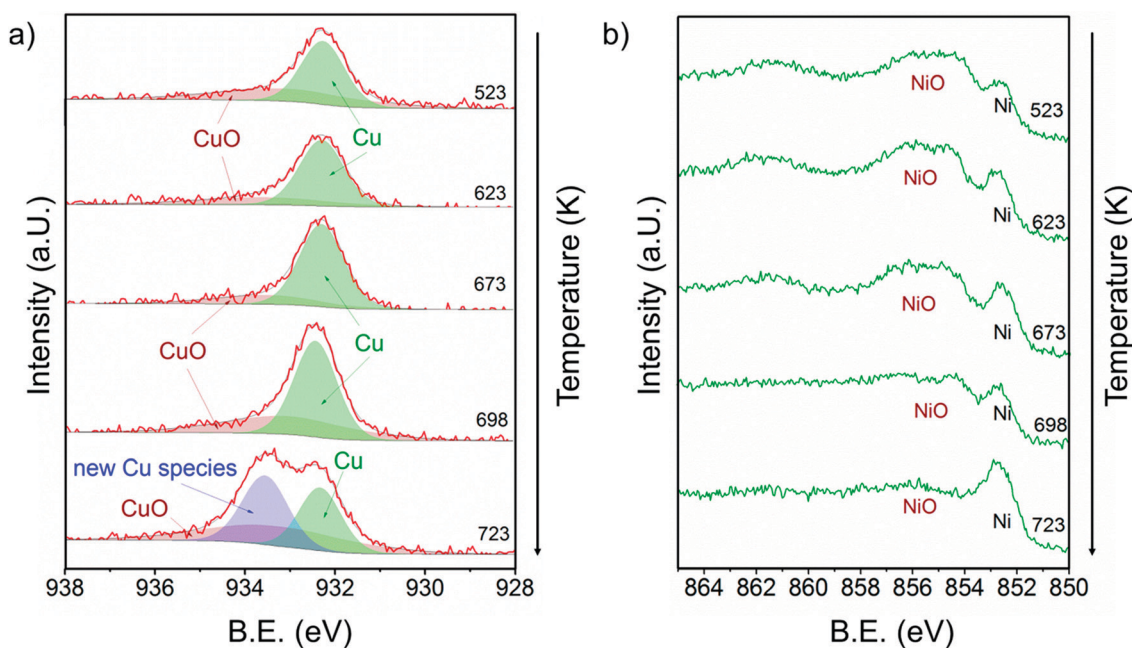


**Fig. 7** a) Cu 2p<sub>3/2</sub> and b) Ni 2p<sub>3/2</sub> core level regions of 13CuNi-ZrO<sub>2</sub> in 0.25 mbar CH<sub>4</sub> at rising temperature from 523 to 723 K. The incident photon energies were 1100 eV (Cu) and 1010 eV (Ni).

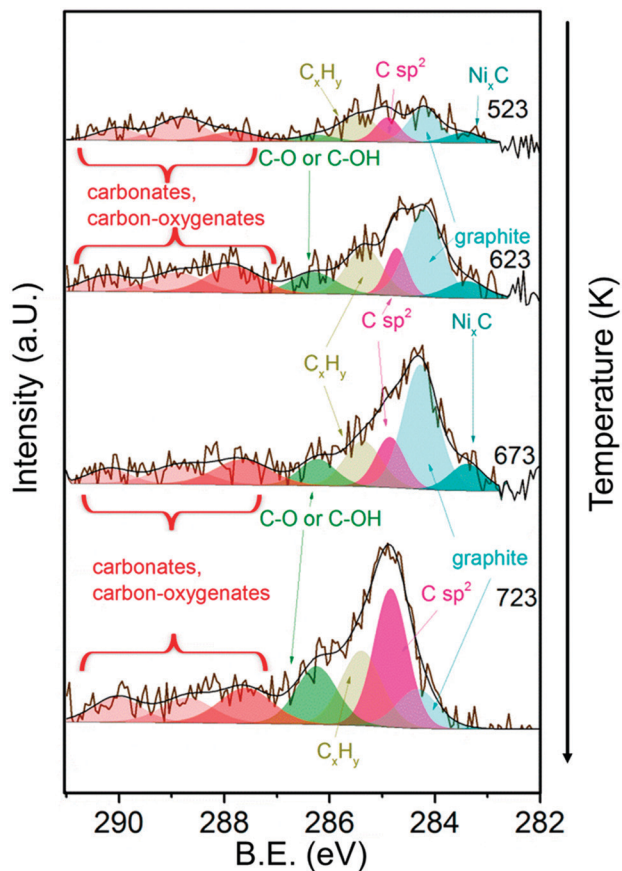


Fig. 8 C 1s core level region of  $^{13}\text{CuNi-ZrO}_2$  in 0.25 mbar  $\text{CH}_4$  at increasing temperature from 523 to 723 K. The incident photon energy was 425 eV.

The amount of graphitic carbon<sup>63,67,68</sup> at 284.3 eV binding energy increased until 673 K but then decreased again at 723 K. The peak at 284.8 eV attributed to C having  $\text{sp}^2$  hybridization<sup>64,68–70</sup> indicates the formation of carbon nanotubes (CNTs) and increased with increasing temperature. The signal at 285.4 eV corresponds to  $\text{C}_x\text{H}_y$  species.<sup>66,71</sup> These species increased upon heating as well. Alternatively, the signal could indicate the presence of structural defects on carbon nanotubes.<sup>70</sup>  $\text{Ni}_x\text{C}$ <sup>64,65</sup> appeared at 283.4 eV and increased at first with rising temperature but then completely vanished at 723 K.

In summary, the amount of several carbon species increased during methane decomposition. In particular, the growth of CNTs is significantly enhanced at the highest temperature at which catalytic activity sets in at the same time, while graphitic carbon decreases, either by transformation to CNTs or dissolution in the bulk of the particles.

### Depth profiling

To get more insights into the distribution of Ni, Cu and C species in the surface and subsurface region XP spectra were recorded using different photon energies. The photon energies were varied to obtain photoelectron kinetic energies of

150 eV, 350 eV and 550 eV for each set of spectra of the relevant core level regions (Ni 2p, Cu 2p, C 1s). These depth profiles were performed at 523, 673 and 723 K in methane.

Fig. 9 visualizes the relative core level peak areas of the various Cu, Ni and C species based on the respective total areas of Cu, Ni and C signals. Upon heating from 523 to 673 K,

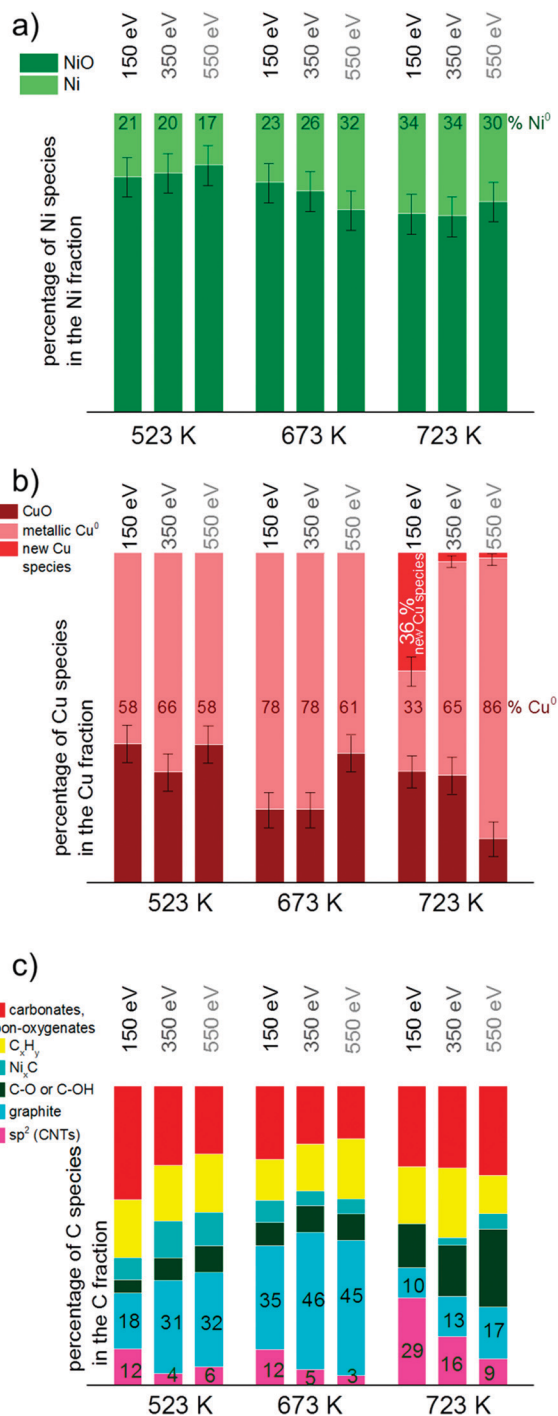


Fig. 9 Depth profile of a) Ni, b) Cu and c) C species based on the total amount of Ni, Cu and C, respectively. Spectra in the core level regions Ni 2p<sub>3/2</sub>, Cu 2p<sub>3/2</sub> and C 1s with kinetic energies of 150, 350 and 550 eV were consulted for the calculations. For clarity of the diagram error bars were left out in c).

the relative amount of metallic Ni increases mainly in the deeper (near-surface) layers. After further heating from 673 to 723 K an increased amount of reduced Ni is present on the surface as well. The amount of metallic Cu increases with temperature. At 723 K the new Cu species appeared which cannot be identified yet (as discussed in the results section). Interestingly, this species is related to the surface of the catalyst and appears only when using photon energies yielding photoelectrons of 150 eV kinetic energies, *i.e.* when measuring with the highest surface sensitivity.

In general, the total amount of carbon species decreases with increasing kinetic energy, indicating that the carbon species are present mostly at the surface of the catalyst. As shown in Fig. 9c), the relative proportion of CNTs increases significantly at 723 K, in particular in the surface-sensitive measurement, as shown by the strongly decreasing amount of  $sp^2$  hybridized carbon with increasing kinetic energy. Nickel carbide disappeared at 723 K in the most surface-sensitive spectra recorded at 150 eV kinetic energy, while a small amount of carbide is still present in the somewhat deeper near-surface layers. The relative amount of graphitic carbon is highest at 673 K reaction temperature and then decreases considerably at 723 K. This is observed for all photoelectron kinetic energies that were analyzed. The proportion of carbon present as carbonates, carbon-oxygenates and hydrocarbon species does not depend much on reaction temperature and photon energy.

## Discussion

$CH_4$  decomposition was studied on bimetallic CuNi–ZrO<sub>2</sub> catalysts by temperature-programmed reaction, TPO and NAP-XPS in order to get insights into the *in situ* stability of CuNi compounds and the effect of Cu addition on the carbon chemistry. In contrast to monometallic Ni–ZrO<sub>2</sub>, an irreversible activation step was observed in methane at around 700 K, with the exact onset temperature depending on the composition, reduction temperature and metal loading. In the following we will discuss the potential origin and the factors affecting this surface modification process responsible for the onset of catalytic activity and take a closer look at the bimetallic Cu–Ni system.

The question arises as to what is the origin of the observed activation process occurring in methane between 650 and 735 K and leading to an irreversible modification of the catalytic performance of all bimetallic catalysts towards a Ni-like behaviour. Previous work on these materials allowed us to conclude that after reduction the surface of the bimetallic catalysts appears enriched in Cu<sup>25</sup> as indicated by selective H<sub>2</sub> chemisorption on Ni and by FTIR spectroscopy of adsorbed CO. Since Cu is practically inactive in methane decomposition a change in surface composition, *e.g.* by Ni segregating to the surface, is a potential reason for the drastic change in  $CH_4$  decomposition activity. The interaction of Ni with C and/or  $CH_4$  would be a likely driving force for the proposed surface segregation of Ni.

In contrast to H<sub>2</sub> chemisorption experiments at room temperature<sup>25</sup> showing that the surface is enriched in copper after reduction, the surface Cu:Ni ratio observed by XPS at 673 K was nearly similar to the overall Cu:Ni ratio of the catalyst. According to the literature, a copper-enriched top surface layer is in agreement with the lower surface free energy of copper compared to that of nickel.<sup>72</sup> According to Sachtler *et al.*, the Gibbs free energy of a copper–nickel mixture at 475 K has a maximum at about 30% copper and a minimum at 80% and at 2% copper<sup>73</sup> in the bulk. Therefore, we expect coexisting phases to be present at lower temperatures. Since the surface energy is lower for Cu compared to that for Ni the Cu-rich alloy phase is likely present at the surface and the Ni-rich alloy phase underneath (core–shell-like structure). For Cu surfaces with Ni monolayers deposited on top it was reported in ref. 74 and 75 that Ni segregates into the first subsurface layer of Cu(100) as well as Cu(111).<sup>76</sup> By theoretical calculations, Pourovskii *et al.*<sup>77</sup> found a rather sharp minimum of the surface energy corresponding to the arrangement of a Ni layer in the second layer of Cu(100). Anyway, this surface composition is only present at low temperature. At elevated temperature the two phases become miscible. According to the Cu–Ni phase diagram, CuNi forms a single-phase alloy above 600 K.

As revealed by XPS measurements under reaction conditions, the increase in activity is clearly accompanied by an increase in the concentration of *metallic* Ni at the surface. Catalytic activity for methane decomposition therefore depends on the alloy surface composition, specifically on the presence of a sufficiently high concentration of metallic Ni at the surface.

Studt *et al.*<sup>78</sup> reported Ni segregation to the surface of CuNi alloys due to the higher bond strength towards CO. Li *et al.*<sup>79</sup> reported that the dissociative adsorption of methane and the formation of carbon flakes would be a plausible cause for their observation of reconstruction of Ni–Cu metal particles during methane decomposition reaction.<sup>79</sup> In a remarkable study, Li *et al.* observed a recrystallization of the Ni–Cu alloy on copper–nickel–alumina catalysts during induction of carbon formation in methane decomposition at 773 K.<sup>7</sup> In a similar way, Ni could be segregated to the very surface layer at elevated temperatures induced by the presence of methane and/or carbon, which consequently leads to an onset of catalytic activity for methane decomposition. Thus, the surface initially enriched in Cu at low temperatures exhibits low methane decomposition activity until the activation step changes the surface concentration of reduced Ni.

Ni segregation to the top surface is a potential explanation for the observed activation step. However, this could not be confirmed by quantitative analysis of the core level spectra, which is complicated by the (very likely) preferential decoration of Ni by carbon species formed over Ni during the reaction of methane. Nevertheless, there is clear evidence by the XPS data that the sudden increase of reactivity can be linked to the higher concentration of reduced Ni at the surface.

When TPMd was carried out after applying a higher reduction temperature of 773 K an activation step was observed as well, although the activation step temperature was lower compared to that for the catalyst reduced at 673 K. Since reduction at 673 K leads to only partially reduced Ni,<sup>25</sup> the Ni:NiO ratio is increased after reduction at higher temperature. The higher amount of metallic Ni (at or near the surface) after applying a higher reduction temperature could be a likely reason for the down-shift of the activation temperature.

Cu addition to Ni helps in the desired lowering of carbon deposition. TPO measurements showed a reduction of the amount of coke burnt off as CO<sub>2</sub> by about 50% when comparing Ni and the Ni-rich 13CuNi-ZrO<sub>2</sub> catalyst exhibiting similar catalytic activity (Table 2). Another effect of the Cu modification, which influences the carbon chemistry and coking behavior, is the decrease in the carbon oxidation temperature, probably due to a weaker bonding of carbon on the CuNi alloy surface.

However, the CuNi system is stable only in a limited range of conditions (temperatures up to around 700 K depending on the composition and pretreatment). Therefore, a key result of this work is the detection of the instability of CuNi under hydrocarbon-rich conditions at higher temperatures (> ~700 K).

## Conclusions

In this work we have investigated the surface chemistry of methane on Ni-ZrO<sub>2</sub> and bimetallic CuNi-ZrO<sub>2</sub> catalysts with a focus on the *in situ* stability under relevant reaction conditions, *i.e.* high temperatures and reactive surrounding gas atmosphere methane.

The activity of bimetallic CuNi-ZrO<sub>2</sub> catalysts for methane decomposition strongly increased after an irreversible activation step occurring at different temperatures depending on the Cu:Ni ratio. By *in situ* synchrotron-based near-ambient pressure (NAP-)XPS we determined the surface composition of the catalysts and the nature of the carbonaceous species present and correlated these data with the catalytic performance. The sudden increase in catalytic activity could be explained by an increase in the concentration of reduced Ni atoms at the catalyst surface in the active state, likely as a consequence of the interaction with methane. XPS showed the appearance of an additional Cu species on the catalyst surface, when catalytic activity sets in. This species could not be conclusively identified up to now, but is related to the catalyst surface according to the depth profiles recorded.

C 1s core level spectra revealed the presence of various carbonaceous species. The signal attributed to carbon nanotubes increased when activity sets in, while the amount of graphite and carbide decreased again. Cu addition to Ni improved the desired resistance against carbon deposition by lowering the amount of coke formed. A lower temperature was required to burn off carbon from the bimetallic catalysts compared to Ni-ZrO<sub>2</sub>.

As a key result on the Cu-modification of Ni catalysts, we conclude that the CuNi alloy shows limited stability under relevant reaction conditions. This system is stable only in a limited range of temperature up to ~700 K in a hydrocarbon atmosphere. Beyond this temperature, the alloy phase becomes unstable, and carbon-induced segregation of Ni species induces a fast increase in methane decomposition rate. In view of the applicability of this system, a detailed understanding of the stability and surface composition of the bimetallic phases present and the influence of the Cu promoter on the surface chemistry under actual reaction conditions are essential.

## Acknowledgements

This work was supported by the Austrian Science Fund (FWF) under the projects F4502-N16 and F4503-N16 (SFB FOXSI).

We thank HZB for the allocation of synchrotron radiation beamtime and we would like to thank the BESSY staff for assistance. The research leading to these results has received funding from the European Community's Seventh Framework Programme (FP7/2007-2013) under grant agreement no. 312284.

## Notes and references

- 1 B. Li, S. Kado, Y. Mukainakano, T. Miyazawa, T. Miyao, S. Naito, K. Okumura, K. Kunimori and K. Tomishige, *J. Catal.*, 2007, **245**, 144.
- 2 Y. Matsumura and T. Nakamori, *Appl. Catal., A*, 2004, **258**, 107.
- 3 J. R. Rostrup-Nielsen, J. Sehested and J. K. Nørskov, *Adv. Catal.*, 2002, **47**, 65.
- 4 J. R. H. Ross, A. N. J. van Keulen, M. E. S. Hegarty and K. Seshan, *Catal. Today*, 1996, **30**, 193.
- 5 G. P. Berrocal, S. A. L. M. Da, J. M. Assaf, A. Albornoz and M. D. C. Rangel, *Catal. Today*, 2010, **149**, 240.
- 6 K. Otsuka, T. Ushiyama and I. Yamanaka, *Chem. Lett.*, 1993, 1517.
- 7 Y. Li, J. Chen, Y. Ma, J. Zhao, Y. Qin and L. Chang, *Chem. Commun.*, 1999, 1141.
- 8 Y. Li, J. Chen, Y. Qin and L. Chang, *Energy Fuels*, 2000, **14**, 1188.
- 9 Y. Li, J. Chen, L. Chang and Y. Qin, *J. Catal.*, 1998, **178**, 76.
- 10 Y. Li, J. Chen and L. Chang, *Appl. Catal., A*, 1997, **163**, 45.
- 11 L. Piao, Y. Li, J. Chen, L. Chang and J. Y. S. Lin, *Catal. Today*, 2002, **74**, 145.
- 12 X. X. Zhang, Z. Q. Li, G. H. Wen, K. K. Fung, J. Chen and Y. Li, *Chem. Phys. Lett.*, 2001, **333**, 509.
- 13 J. Chen, Y. Li, Z. Li and X. Zhang, *Appl. Catal., A*, 2004, **269**, 179.
- 14 Y. Li, J. Chen, L. Chang and J. Zhao, *Stud. Surf. Sci. Catal.*, 1998, **118**, 321.
- 15 Y. Li, D. Li and G. Wang, *Catal. Today*, 2011, **162**, 1.
- 16 J. Ashok, S. N. Kumar, M. Subrahmanyam and A. Venugopal, *Catal. Lett.*, 2008, **121**, 283.
- 17 M. A. Ermakova and D. Y. Ermakov, *Catal. Today*, 2002, **77**, 225.

- 18 R. Guil-Lopez, V. La Parola, M. A. Pena and J. L. G. Fierro, *Int. J. Hydrogen Energy*, 2012, **37**, 7042.
- 19 X. Li, Y. Zhang and K. J. Smith, *Appl. Catal., A*, 2004, **264**, 81.
- 20 I. Gavrielatos, V. Drakopoulos and S. G. Neophytides, *J. Catal.*, 2008, **259**, 75.
- 21 A. M. Molenbroek, J. K. Norskov and B. S. Clausen, *J. Phys. Chem. B*, 2001, **105**, 5450.
- 22 J. R. Rostrup-Nielsen and I. Alstrup, *Catal. Today*, 1999, **53**, 311.
- 23 N. C. Triantafyllopoulos and S. G. Neophytides, *J. Catal.*, 2006, **239**, 187.
- 24 Z. Li, J. Chen, X. Zhang, Y. Li and K. K. Fung, *Carbon*, 2002, **40**, 409.
- 25 A. Kitla, O. V. Safonova and K. Foettinger, *Catal. Lett.*, 2013, **143**, 517.
- 26 J. Ashok, M. Subrahmanyam and A. Venugopal, *Int. J. Hydrogen Energy*, 2008, **33**, 2704.
- 27 Y. Echegoyen, I. Suelves, M. J. Lazaro, R. Moliner and J. M. Palacios, *J. Power Sources*, 2007, **169**, 150.
- 28 M. J. Lazaro, Y. Echegoyen, I. Suelves, J. M. Palacios and R. Moliner, *Appl. Catal., A*, 2007, **329**, 22.
- 29 E. W. Park, H. Moon, M.-S. Park and S. H. Hyun, *Int. J. Hydrogen Energy*, 2009, **34**, 5537.
- 30 I. Suelves, M. J. Lazaro, R. Moliner, Y. Echegoyen and J. M. Palacios, *Catal. Today*, 2006, **116**, 271.
- 31 A. Monzón, N. Latorre, T. Ubieta, C. Royo, E. Romeo, J. I. Villacampa, L. Dussault, J. C. Dupin, C. Guimon and M. Montiox, *Catal. Today*, 2006, **116**, 264.
- 32 A. F. Cunha, J. J. M. Órfão and J. L. Figueiredo, *Int. J. Hydrogen Energy*, 2009, **34**, 4763.
- 33 H. Liu, R. Zhang, R. Yan, J. Li, B. Wang and K. Xie, *Appl. Surf. Sci.*, 2012, **258**, 8177.
- 34 K. Föttinger, J. A. van Bokhoven, M. Nachttegaal and G. Rupprechter, *J. Phys. Chem. Lett.*, 2011, **2**, 428.
- 35 A. Haghofer, K. Foettinger, F. Girgsdies, D. Teschner, A. Knop-Gericke, R. Schloegl and G. Rupprechter, *J. Catal.*, 2012, **286**, 13.
- 36 K. Foettinger, *Catal. Today*, 2013, **208**, 106.
- 37 K. Foettinger and G. Rupprechter, *Acc. Chem. Res.*, 2014, **47**, 3071–3079.
- 38 C. Rameshan, W. Stadlmayr, S. Penner, H. Lorenz, N. Memmel, M. Haevecker, R. Blume, D. Teschner, T. Rocha, D. Zemlyanov, A. Knop-Gericke, R. Schloegl and B. Kloetzer, *Angew. Chem., Int. Ed.*, 2012, **51**, 3002.
- 39 C. Rameshan, W. Stadlmayr, C. Weilach, S. Penner, H. Lorenz, M. Haevecker, R. Blume, T. Rocha, D. Teschner, A. Knop-Gericke, R. Schloegl, N. Memmel, D. Zemlyanov, G. Rupprechter and B. Kloetzer, *Angew. Chem., Int. Ed.*, 2010, **49**, 3224.
- 40 C. Rameshan, L. Mayr, B. Kloetzer, A. Knop-Gericke, M. Haevecker, R. Blume, D. Zemlyanov and S. Penner, *Catal. Lett.*, submitted.
- 41 H. Bluhm, M. Haevecker, A. Knop-Gericke, E. Kleimenov, R. Schloegl, D. Teschner, V. I. Bukhtiyarov, D. F. Ogletree and M. Salmeron, *J. Phys. Chem. B*, 2004, **108**, 14340.
- 42 J. J. Yeh and I. Lindau, *At. Data Nucl. Data Tables*, 1985, **32**, 1.
- 43 J. Alvarez-Rodriguez, M. Cerro-Alarcon, A. Guerrero-Ruiz, I. Rodriguez-Ramos and A. Arcoya, *Appl. Catal., A*, 2008, **348**, 241.
- 44 M. D. L. A. Cangiano, M. W. Ojeda, A. C. Carreras, J. A. Gonzalez and M. D. C. Ruiz, *Mater. Charact.*, 2010, **61**, 1135.
- 45 R. Pérez-Hernández, G. Mondragón Galicia, D. Mendoza Anaya, J. Palacios, C. Angeles-Chavez and J. Arenas-Alatorre, *Int. J. Hydrogen Energy*, 2008, **33**, 4569.
- 46 T. V. Choudhary, C. Sivadinarayana, C. C. Chusuei, A. Klinghoffer and D. W. Goodman, *J. Catal.*, 2001, **199**, 9.
- 47 P. Ferreira-Aparicio, I. Rodríguez-Ramos and A. Guerrero-Ruiz, *Appl. Catal., A*, 1997, **148**, 343.
- 48 S. D. Jones, L. M. Neal and H. E. Hagelin-Weaver, *Appl. Catal., B*, 2008, **84**, 631.
- 49 J. P. Espinos, J. Morales, A. Barranco, A. Caballero, J. P. Holgado and A. R. Gonzalez-Elipse, *J. Phys. Chem. B*, 2002, **106**, 6921.
- 50 J. Ghijsen, L. H. Tjeng, E. J. Van, H. Eskes, J. Westerink, G. A. Sawatzky and M. T. Czyzyk, *Phys. Rev. B: Condens. Matter Mater. Phys.*, 1988, **38**, 11322.
- 51 Z. Liu, M. D. Amiridis and Y. Chen, *J. Phys. Chem. B*, 2005, **109**, 1251.
- 52 W. Tong, A. West, K. Cheung, K.-M. Yu and S. C. E. Tsang, *ACS Catal.*, 2013, **3**, 1231.
- 53 C. D. Wagner, W. M. Riggs, L. E. Davis, J. F. Moulder and G. E. Muilenberg, *Handbook of X-Ray Photoelectron Spectroscopy*, ed., Perkin-Elmer Corporation, Physical Electronics Division, Eden Prairie, Minn. 5534, 1979.
- 54 L.-C. Chen and S. D. Lin, *Appl. Catal., B*, 2011, **106**, 639.
- 55 A. R. Naghash, T. H. Etsell and S. Xu, *Chem. Mater.*, 2006, **18**, 2480.
- 56 H. Koschel, G. Held and H. P. Steinruck, *Surf. Sci.*, 2000, **453**, 201.
- 57 I. Preda, A. Gutierrez, M. Abbate, F. Yubero, J. Mendez, L. Alvarez and L. Soriano, *Phys. Rev. B: Condens. Matter Mater. Phys.*, 2008, **77**, 075411.
- 58 L. Guzzi, G. Stefler, O. Geszti, I. Sajo, Z. Paszti, A. Tompos and Z. Schay, *Appl. Catal., A*, 2010, **375**, 236.
- 59 W. Chia-Ching and Y. Cheng-Fu, *Nanoscale Res. Lett.*, 2013, **8**, 33.
- 60 C. J. Powell, *J. Electron Spectrosc. Relat. Phenom.*, 2012, **185**, 1.
- 61 B. Pawelec, S. Damyanova, K. Arishtirova, J. L. G. Fierro and L. Petrov, *Appl. Catal., A*, 2007, **323**, 188.
- 62 A. P. Grosvenor, M. C. Biesinger, R. S. C. Smart and N. S. McIntyre, *Surf. Sci.*, 2006, **600**, 1771.
- 63 Z. Bastl, *Collect. Czech. Chem. Commun.*, 1995, **60**, 383.
- 64 G. J. Kovács, I. Bertóti and G. Radnóczy, *Thin Solid Films*, 2008, **516**, 7942.
- 65 N. Laidani, L. Calliari, G. Speranza, V. Micheli and E. Galvanetto, *Surf. Coat. Technol.*, 1998, **100–101**, 116.
- 66 N. M. Rodriguez, P. E. Anderson, A. Wootsch, U. Wild, R. Schlögl and Z. Paál, *J. Catal.*, 2001, **197**, 365.
- 67 S. Evans and J. M. Thomas, *Proc. R. Soc. London, Ser. A*, 1977, **353**, 103.
- 68 J. I. B. Wilson, J. S. Walton and G. Beamson, *J. Electron Spectrosc. Relat. Phenom.*, 2001, **121**, 183.

- 69 S. T. Jackson and R. G. Nuzzo, *Appl. Surf. Sci.*, 1995, **90**, 195.
- 70 P. G. Savva, K. Polychronopoulou, V. A. Ryzkov and A. M. Efstathiou, *Appl. Catal., B*, 2010, **93**, 314.
- 71 D. N. Belton and S. J. Schmieg, *J. Vac. Sci. Technol., A*, 1990, **8**, 2353.
- 72 L. Zhu and A. E. Depristo, *J. Catal.*, 1997, **167**, 400.
- 73 W. M. H. Sachtler and D. P. P. Van, *Surf. Sci.*, 1969, **18**, 62.
- 74 S. H. Kim, K. S. Lee, H. G. Min, J. Seo, S. C. Hong, T. H. Rho and J.-S. Kim, *Phys. Rev. B: Condens. Matter Mater. Phys.*, 1997, **55**, 7904.
- 75 P. F. A. Alkemade, H. Fortuin, R. Balkenende, F. H. P. M. Habraken and W. F. Van der Weg, *Surf. Sci.*, 1990, **225**, 307.
- 76 Y. R. Tzeng, H. T. Wu, D. Shiang and T. T. Tsong, *Phys. Rev. B: Condens. Matter Mater. Phys.*, 1993, **48**, 5549.
- 77 L. V. Pourovskii, N. V. Skorodumova, Y. K. Vekilov, B. Johansson and I. A. Abrikosov, *Surf. Sci.*, 1999, **439**, 111.
- 78 F. Studt, F. Abild-Pedersen, Q. Wu, A. D. Jensen, B. Temel, J.-D. Grunwaldt and J. K. Nørskov, *J. Catal.*, 2012, **293**, 51.
- 79 D. Li, J. Chen and Y. Li, *Int. J. Hydrogen Energy*, 2009, **34**, 299.